

Electron Flow through Cytochrome P450

Thesis by
Maraia Emily Ener

In Partial Fulfillment of the Requirements for the
degree of
Doctor of Philosophy

CALIFORNIA INSTITUTE OF TECHNOLOGY

Pasadena, California

2014

(Defended December 16th, 2013)

© [2014]

Maraia Emily Ener

All Rights Reserved

for my aunt Mine, who first inspired me to pursue a PhD

ACKNOWLEDGMENTS

First I would like to thank my doctoral advisor, Harry Gray. Harry's charisma, irreverence, enthusiasm for life, and passion for chemistry are unparalleled, and I am honored to be a part of the extensive Gray Nation. I have greatly benefitted from the supportive, collaborative environment that Harry fosters in the group, and I am grateful for all of the opportunities he has given me to present my research to the bioinorganic community, including a number of international conferences. This Thesis, Harry, is for you. I love it!!!!!!

I would also like to thank Jay Winkler, who (whether he intended or not) has been every bit as much a mentor. I am constantly amazed by Jay's brilliance, wealth of knowledge, and ability to build almost anything. The work in this Thesis would not have been possible without his guidance and expertise, and I continue to strive to be a more thorough, more rigorous, (and sometimes more skeptical!) scientist because of it. *Don't panic. Just think.*

Many thanks also go out to my other committee members: Professors Mitchio Okumura, Theodor Agapie, and Doug Rees. I am lucky to have such a supportive team, and have benefitted from our conversations at my candidacy exam, 4th year meeting, props exam, and thesis defense. Extra thanks to Mitchio for being my committee chair, and for the five pounds of delicious green grapes that Kana and I picked at his home.

My graduate experience, scientific and personal, has greatly benefitted from interaction with a number of colleagues and friends. I want to begin by giving my heartfelt thanks to the trio who has been with me to the end: Jeff Warren, Oliver Shafaat, and Kana Takematsu. Somewhere along the line, Jeff became my big brother in lab. No one brings the ridiculous like Professor Dr. Jeffrey J. Warren

(PhD), *no one*. From tinfoil hands in the cold, dark laser room, to “what-to-do-with-my-life” morning discussions over coffee, Jeff has made me laugh, infuriated me, inspired me, and reminded me countless times that “it’s going to be okay.” No one else has so consistently and so vocally expressed confidence in my scientific abilities; for that, I am ever grateful. Oliver has been my little brother counterpart (this is *my* table quadrant, keep your feet out!). He is always around to lend a hand, share a drink (or five), enjoy a laugh, and has obligingly agreed to take over all of my BILRC duties - I am confident that they are in good hands (p.s. Oliver, you still owe me a beer). Kana has been a fantastic office mate, confidante, and friend. She has patiently fielded my questions in physical chemistry, laser operation, and diplomacy, has read numerous iterations of my research proposals, and has watered my plants when I’m not in town. Thanks, Kana!

And now, from the end... back to be beginning. Before I even joined the group, Nicole Bouley Ford, Gretchen Keller, and Bert Lai convinced me that Caltech was the place to be. Bert Lai became my office mate, and instantly made me feel I was part of the subbasement/bio crew. His advice that “there will *always* be one more experiment” has never felt more relevant than now, as I write this Thesis.

I am deeply grateful to Lionel Cheruzel, who, in his last few months at Caltech, was a patient and effective teacher, trained me on everything P450, and handed me a working project just as things were starting to get really interesting. I continue to benefit from communication and collaboration with The Frenchman.

I was incredibly fortunate to have a wonderful team of Ch153 TA/laser GLAs to jump-start my journey in the worlds of ligand field theory and nanosecond transient absorption. Jillian Dempsey is a fantastic teacher and role model. She gives me hope that there can be life, joy, and sanity in academia. Alec Durrell is also a wonderful

teacher and mentor. Our conversations across the BI hallway always made me think more deeply about fundamental aspects of inorganic chemistry. It was incredibly rewarding to teach Ch153 side-by-side. I still find myself trying to fill Jillian and Alec's enormous shoes.

In the realm of Ch153, Alexis Komor has been a wonderful Co-TA for Ch153 for the past two years, and Bryan Hunter has done a fantastic job taking up the reins. You got this, guys!

When I joined the Gray group, the BioInorganic subbasement was a particularly rockin' place to be. Special thanks go to Kyle Lancaster, Charlotte Whited, Nicole Bouley Ford, and Gretchen Keller for bringing, the class, the sass, the fast-talking and the shit-talking. Charlotte founded our two-person Team Subgroup for heme enzymes, and taught me that grad school is a balance between collaboration and independence: "It's *your* Thesis, you figure it out!" Through the chaos and darkness, Gretchen Keller reminds me that there is a world outside of grad school. Her creativity, artistry, and insights are an inspiration. It was fantastic to have another partner in crime in the world of heme enzymes (go Team Haem Team!), and I'm honored to have become her friend. In the twilight of the subbasement days, Peter Agbo's quiet presence, dry humor, and sharp intellect have been a comfort.

James McKone and Judith Lattimer have been amazing year-mates from the very beginning. Judy and I met on visit weekend, and she has consistently gone out of her way to include me in social gatherings. It's been sometimes difficult to feel connected to the Caltech community when I commute 30 miles (each direction), and this has made a huge difference. Judy is AWESOME!!! James and I joined the Gray group within a few weeks of each other (in the summer before grad school), not knowing that we had spent four years of college across the river from each other,

in a tiny town in Minnesota. I could never dream of being as cool as James. I've forgiven him for being a St. Olaf student, and he has shown himself to be a calm and patient teacher, and reliable resource to turn to. The farmers market trips and Saturday brunches with James, Judy and Co. made Caltech feel more like home my first year in California. Speaking of brunches, I also want to thank the other members of Team House: Alex Goldberg (and his delicious cardamom coffee) and Ethan Van Arnam.

I have had the opportunity to work with a number of talented undergraduate students, including Katja Luxem, Megan Jackson, Rocio Mercado. They continue to inspire me, and remind me that sometimes otter pops are the answer to everything. Special thanks to Katja Luxem for being my and Jeff's first SURF (a modicum of the data she collected is in this Thesis). Based on her record of international escapades thus far, I'm pretty sure Katja will take over the world - way to go, lady! Extra special thanks to Megan for the chocolate birthday cheesecake.

I've been fortunate to work closely with some fantastic postdocs in the Gray group. First, I want to thank Wes Sattler, who is rarely found without a smile on his face, and who has come through a number of lab dramas with optimism and resolve. I may never end up being an organometallic chemist, but it's not due to any lack of effort on his part! By extension, I want to thank his biological clone, Aaron Sattler. In particular, Aaron's collection of antique Macbook Pro dongles has saved me more than once. James Blakemore has been another wonderful addition to the Group, and I have benefitted immensely from our conversations on electrochemistry.

I have also benefitted from interactions with a number of other Gray group members, including (but not limited to): Morgan Cable, Tania Darnton, Paul

Bracher, Smaranda Marinescu, Hema Karunadasa, Tetsu Kimura, Bryan Stubbert, Astrid Mueller, Matt Hartings, Josh Palmer, Paul Oblad, Heather Williamson, Yan Choi, Melanie Yen, Carl Blumenfeld, Mike Rose, Mike Lichterman, Kate Pletneva. Seiji Yamada's time in our group is now the stuff of legend.

My graduate experience wouldn't have been complete without other members of the Caltech staff, and Chemistry Department. Catherine May, Rick Jackson, and Pat Anderson keep the world spinning. I will never forget Catherine's welcome on my first day "who are *you*?", Rick's magical cabinet stocked with tea and pick-me-up candies, and Pat's immaculate fashion sense. Joe Drew and Steve Gould keep us supplied, and a fantastic team keeps the BI sparkling. It goes without saying that the Caltech faculty are amazing. I'm giving John Bercaw a special shout-out here for knowing where Carleton is, and for saying hi to me in the hallway. A number of non-Gray group researchers have also made important contributions to my graduate experience, including (but again, not limited to): Leslie O'Leary, Ian Tonks, Samantha MacMillan, Rachel Klet, and Maddy Radlauer.

I also want to thank a number of collaborators in Frances Arnold's group. Pete Heinzelman was very helpful in my first few months at Caltech, Eric Brustad is a P450 BM3-crystallizing genius, and one of my proudest achievements in grad school (zero to reproducible air-sensitive redox titrations in < 30 days) came about because of collaborations with Eric, Pedro Coelho, and Jane Wang. Frances Arnold herself is an inspiration, and has been supportive of my efforts.

Last, but by no means least, I would like to thank my family and friends who have stood by me and waited patiently through the madness of graduate school. First, I must thank my parents, Ruth and Oran Ener, who have always supported education,

creative thought, the pursuit of knowledge, and the development of character (oh, the character...). Because of them, I have made it to the end of my PhD; because of them, I never considered that I couldn't. I have two phenomenal siblings, Cjuneyt and Amir Ener, who make me proud every day. Their beautiful and brilliant lady friends, Eloise Galligan and Lydia Larson, have been a wonderful addition to our family, and Eloise is now officially my sister-in-law! To my BFFs Jess Wenstrom and Erica Hoaglund – can't wait to see you again!

Finally, I want to thank Adam Goetz, my spouse and partner who moved across the country to be with me. Adam, for you, I try every day to be stronger, kinder and more forgiving. Thank you for being here for me all the way through my Thesis (and all the way through yours). I'm so excited for us to be real people again!

ABSTRACT

The cytochromes P450 (P450s) are a remarkable class of heme enzymes that catalyze the metabolism of xenobiotics and the biosynthesis of signaling molecules. Controlled electron flow into the thiolate-ligated heme active site allows P450s to activate molecular oxygen and hydroxylate aliphatic C–H bonds via the formation of high-valent metal-oxo intermediates (compounds I and II). Due to the reactive nature and short lifetimes of these intermediates, many of the fundamental steps in catalysis have not been observed directly. The Gray group and others have developed photochemical methods, known as “flash-quench,” for triggering electron transfer (ET) and generating redox intermediates in proteins in the absence of native ET partners. Photo-triggering affords a high degree of temporal precision for the gating of an ET event; the initial ET and subsequent reactions can be monitored on the nanosecond-to-second timescale using transient absorption (TA) spectroscopies. Chapter 1 catalogues critical aspects of P450 structure and mechanism, including the native pathway for formation of compound I, and outlines the development of photochemical processes that can be used to artificially trigger ET in proteins. Chapters 2 and 3 describe the development of these photochemical methods to establish electronic communication between a photosensitizer and the buried P450 heme. Chapter 2 describes the design and characterization of a Ru-P450-BM3 conjugate containing a ruthenium photosensitizer covalently tethered to the P450 surface, and nanosecond-to-second kinetics of the photo-triggered ET event are presented. By analyzing data at multiple wavelengths, we have identified the formation of multiple ET intermediates, including the catalytically relevant compound II; this intermediate is generated by oxidation of a bound water molecule in the ferric resting state enzyme. The work in Chapter 3 probes the role of a tryptophan residue situated between the

photosensitizer and heme in the aforementioned Ru-P450 BM3 conjugate. Replacement of this tryptophan with histidine does not perturb the P450 structure, yet it completely eliminates the ET reactivity described in Chapter 2. The presence of an analogous tryptophan in Ru-P450 CYP119 conjugates also is necessary for observing oxidative ET, but the yield of heme oxidation is lower. Chapter 4 offers a basic description of the theoretical underpinnings required to analyze ET. Single-step ET theory is first presented, followed by extensions to multistep ET: electron “hopping.” The generation of “hopping maps” and use of a hopping map program to analyze the rate advantage of hopping over single-step ET is described, beginning with an established rhenium-tryptophan-azurin hopping system. This ET analysis is then applied to the Ru-tryptophan-P450 systems described in Chapter 2; this strongly supports the presence of hopping in Ru-P450 conjugates. Chapter 5 explores the implementation of flash-quench and other phototriggered methods to examine the native reductive ET and gas binding events that activate molecular oxygen. In particular, TA kinetics that demonstrate heme reduction on the microsecond timescale for four Ru-P450 conjugates are presented. In addition, we implement laser flash-photolysis of P450 ferrous-CO to study the rates of CO rebinding in the thermophilic P450 CYP119 at variable temperature. Chapter 6 describes the development and implementation of air-sensitive potentiometric redox titrations to determine the solution reduction potentials of a series of P450 BM3 mutants, which were designed for non-native cyclopropanation of styrene *in vivo*. An important conclusion from this work is that substitution of the axial cysteine for serine shifts the wild type reduction potential positive by 130 mV, facilitating reduction by biological redox cofactors in the presence of poorly-bound substrates. While this mutation abolishes oxygenation activity, these mutants are capable of catalyzing the cyclopropanation of styrene, even within the confines of an *E. coli* cell. Four appendices are also provided, including photochemical heme

oxidation in ruthenium-modified nitric oxide synthase (Appendix A), general protocols (Appendix B), Chapter-specific notes (Appendix C) and Matlab scripts used for data analysis (Appendix D).

TABLE OF CONTENTS

Acknowledgments	iv
Abstract.....	x
Table of Contents.....	xiii
List of Figures.....	xix
List of Tables	xxv
Chapter 1: Cytochrome P450: From pursuit of reactive intermediates to engineering novel reactivity	1
1.1 Cytochrome P450: a remarkable metabolic enzyme.....	2
1.2 P450: structural features that direct function.....	4
1.3 P450 activity: reactions and mechanisms	9
<i>Oxygen activation</i>	10
<i>P450 active hydroxylating agents: ferryl compounds I and II</i>	14
1.4 Photo-triggered electron transfer in proteins	15
<i>Photosensitizers</i>	18
<i>Small molecule quenchers</i>	21
1.5 Photo-triggered ET in P450: two pathways toward reactive heme species.....	23
<i>Precedence for photochemical heme oxidation</i>	24
<i>P450 considerations: the buried heme</i>	26
1.6 New Frontiers: Novel P450 Active Species for Non-Native Catalysis ..	26
1.7 Conclusions	30
1.8 References	31
Chapter 2: Photo-triggered oxidation of Ru-modified cytochrome P450 ...	35
2.1 Background: Toward high-valent P450 intermediates.....	36
2.2 Motivation and selection of the photochemical system	40
<i>Photosensitizer</i>	40
<i>Exogenous oxidative quencher</i>	41
<i>P450 mutants</i>	41
2.3 Results.....	43
2.3.1 Characterization.....	43
<i>UV-visible absorbance</i>	43
<i>Steady-state luminescence</i>	44
<i>X-ray crystal structure analysis</i>	45
2.3.2 Laser flash-quench experiments.....	49
<i>Time-resolved luminescence</i>	49
<i>Transient absorption</i>	52
<i>Kinetics analysis of TA data</i>	57
2.4 Discussion	59
2.4.1 Kinetics Model	60

2.5 Concluding Remarks.....	65
2.6 Acknowledgments	65
2.7 Materials and Methods	66
<i>Chemicals</i>	66
<i>Procedures</i>	66
2.7.1 Ru photosensitizer	66
<i>Synthesis</i>	66
<i>Characterization</i>	67
2.7.2 Mutagenesis and expression of P450 BM3 mutants	67
<i>Plasmid</i>	67
<i>Mutagenesis</i>	67
<i>Expression</i>	68
<i>Extraction and purification</i>	68
2.7.3 Ru-P450 conjugation	69
2.7.4 Crystallization and structure determination.....	69
2.7.5 Preparation of laser samples	70
2.8 References	71
Chapter 3: Photo-triggered electron transfer through tryptophan in Ru-P450 systems	74
3.1 Background: Light to ET	75
3.1.1 P450 systems: Motivation and selection	80
3.2 Results and Analysis.....	84
3.2.1 Characterization of mutants	84
<i>UV-visible absorbance</i>	84
<i>X-ray crystal structure analysis of C97-BM3_(wH)</i>	85
3.2.2 Ru-P450 luminescence.....	88
3.2.3 Ru-P450 transient absorption.....	92
<i>P450-BM3 mutants: effect of tryptophan 96</i>	92
<i>ET reactivity of CYP119 mutants</i>	94
<i>Temperature dependence</i>	97
<i>Search for the tryptophan radical cation</i>	98
3.3 Discussion	99
<i>Final thoughts and avenues for future work</i>	101
3.4 Conclusions	102
3.5 Acknowledgments	102
3.6 Materials and Methods	102
<i>Materials</i>	102
<i>Procedures</i>	103
3.6.1 Photosensitizer synthesis.....	103
<i>Synthesis</i>	103
<i>Characterization</i>	104
3.6.2 Protein mutagenesis, expression and purification	104
<i>Plasmid</i>	104

<i>Mutagenesis</i>	104
<i>Overexpression in E. coli</i>	104
3.6.3 Conjugation of the Ru-photosensitizer.....	105
3.6.4 Crystallization and structure determination.....	105
3.6.5 Preparation of laser samples	106
3.7 References	107
Chapter 4: Multistep electron transfer: “hopping maps” tutorial and application.....	109
4.1 Electron transfer through proteins.....	110
<i>Method for examining photochemical ET in proteins: photochemical triggering</i>	112
4.2 Single step electron tunneling: semiclassical theory	114
<i>Experimental measurements</i>	118
4.3 Multistep electron transfer	119
4.4 Construction of hopping maps: an example for Re-azurin	124
4.5 ET parameters: selection process, effects, and limitations	129
<i>Temperature</i>	130
<i>Distance</i>	131
<i>Tunneling decay constant, β</i>	133
<i>Reorganization energy, λ</i>	134
<i>Driving forces</i>	136
4.6 Hopping map limitations	137
4.7 Application to the Ru-W-P450 system	138
<i>Estimates and challenges</i>	139
<i>Single-step tunneling</i>	141
<i>Hopping analysis</i>	142
<i>Varying distance</i>	143
<i>Varying β and λ</i>	145
4.8 Conclusions	147
4.9 Acknowledgments	147
4.10 References	148
Chapter 5: Photochemical heme reduction and gas binding in cytochrome P450	152
5.1 Background: reductive activation of dioxygen	153
5.2 Results and Analysis	159
5.2.1 Reductive flash-quench.....	159
<i>Luminescence</i>	159
<i>Single wavelength transient absorption</i>	161
<i>Assignment of intermediates</i>	163
<i>Fitting</i>	165
5.2.2 Reductive ET in the presence of CO.....	168
5.2.3 CO photolysis and rebinding.....	170
<i>Power dependence and yield of CO escape</i>	174

	xvi
<i>Temperature dependence (substrate free)</i>	175
<i>Temperature dependence in the presence of laurate</i>	176
<i>Picosecond transient absorption measurements</i>	178
<i>Non-negative least squares fitting</i>	179
<i>Eyring analysis</i>	185
5.3 Discussion, conclusions, and future work	186
5.4 Acknowledgments	187
5.5 Materials and Methods	187
<i>Chemicals</i>	187
<i>Ru-P450 conjugates</i>	188
<i>Synthesis/purification of reductive quencher</i>	188
<i>Preparation of samples for flash-quench heme reduction</i>	188
<i>Preparation of samples for CO photolysis and rebinding</i>	189
5.6 References	191
Chapter 6: Axial-ligand influence on P450 reduction potentials: implications for catalysis	194
6.1 Background: Controlled electron flow through P450.....	195
<i>Enzymes</i>	200
6.2 Methods development for redox titrations.....	202
<i>Spectrophotometric titration</i>	202
<i>Electrochemical titration</i>	205
<i>Potentiometric titration</i>	209
<i>Test: Wild-type P450 BM3</i>	210
6.3 Results	213
6.3.1 Wild-type Enzymes: P450 BM3 and CYP119	213
<i>Wild Type P450 BM3</i>	213
<i>Wild Type CYP119</i>	214
6.3.2 Potentiometric titration of mutants for <i>in vivo</i> cyclopropanation...216	
<i>C400S axial mutation</i>	217
<i>Engineered cyclopropanation mutants</i>	218
6.3.3 Additional axial mutants	219
6.4 Discussion	223
6.5 Conclusions and future work.....	224
6.6 Acknowledgments	225
6.7 Materials and Methods	225
<i>Chemicals</i>	225
<i>Instrumentation</i>	226
<i>Procedures</i>	226
<i>Preparation of samples for redox titration</i>	226
<i>Potentiometric redox titration</i>	227
6.8 References	228
Appendix A: Photochemical oxidation of nitric oxide synthase	230
A.1 Introduction to nitric oxide synthase	231

A.2 Results	235
A.2.1 Ru-photosensitizer conjugation	235
<i>Selection of NOS mutant and Ru photosensitizer</i>	235
<i>Characterization of RuNOS</i>	237
A.2.2 Ru-NOS Luminescence	239
<i>Luminescence quenching</i>	242
A.2.3 Transient Absorption.....	244
A.3 Discussion	247
A.4 Conclusion	249
A.5 Acknowledgments	250
A.6 Materials and Methods	250
<i>Expression protocols</i>	250
<i>Extraction and purification</i>	250
<i>Ru-NOS conjugation and purification</i>	251
A.7 References.....	253
Appendix B: Common Protocols	254
B.1 Instrumentation.....	255
B.2 Site-directed mutagenesis	255
B.3 Transformation protocol	256
B.4. Amplification and purification of plasmid DNA.....	256
B.5 P450 overexpression in <i>E. coli</i> , extraction and purification	257
<i>Expression</i>	257
<i>Extraction and purification</i>	257
B.6 Ru-P450 conjugation	258
B.7 Preparation of laser samples	259
B.8 Laser details	260
<i>Nanosecond-to-second transient spectroscopies</i>	260
<i>Picosecond-to-nanosecond transient spectroscopy</i>	263
B.9 Data workup.....	265
Appendix C: Chapter-specific notes	266
C.1 Notes for Chapter 2	267
<i>Ru-P450 luminescence: dependence on concentration</i>	267
<i>Low temperature experiments</i>	267
C.2 Notes for Chapter 3	269
<i>Search for the tryptophan radical cation intermediate</i>	269
C.3 Notes for Chapter 5	271
<i>Selection of probe wavelength for CO rebinding kinetics</i>	271
<i>Overlay of PSI and NSI kinetics traces</i>	272
<i>Nonlinear least squares fitting of CO rebinding kinetics at various temperatures</i>	273
C.4 Notes for Chapter 6	275
<i>Determination of ferrous/ferric ratios</i>	275
<i>Reproducibility</i>	275

Appendix D: Matlab programs	277
D.1 Plotting x,y data: MEplotter	278
D.2 Time resolved single-wavelength data workup	279
D.2.1 Time-zero adjustment	279
<i>xadjuster</i>	279
D.2.2 Log-compression	281
<i>compress</i>	281
<i>logtimej</i>	283
D.3 Data splicing	285
<i>overlayer</i>	285
<i>combine</i>	288
D.4 Singular Value Decomposition	291
<i>svder1</i>	291
<i>svderMulti</i>	292
D.5 Multiexponential fitting.....	293
<i>nonlinear_fitter4</i>	293
<i>autoresider</i>	295
<i>MExpGFitter</i>	296
<i>MExpG</i>	297
<i>MExpGvalues</i>	298
D.6 Nonnegative least squares analysis	299
<i>npls_prep</i>	299
<i>npls_grad_reg_r2_KT</i>	301
<i>Panalyzer</i>	310
<i>Pmoments</i>	312
D.7 Hopping Maps.....	313
<i>MapMaker</i>	313
<i>MapPlotter</i>	315
<i>MapValues</i>	316
<i>tauM</i>	318
<i>tauETM</i>	319
D.8 Ferric/ferrous deconvolution.....	320
<i>SpectralDeconvoluter</i>	320

LIST OF FIGURES

<i>Number</i>	<i>Page</i>
Figure 1.1 Structures of P450 BM3 heme domain from <i>Bacillus megaterium</i> and CYP119 from <i>Sulfolobus acidocaldarius</i>	5
Figure 1.2 P450 BM3 active site	6
Figure 1.3 CYP119 active site	7
Figure 1.4 Overlay of substrate-free and substrate-bound forms of P450 BM3	8
Figure 1.5 Various reactions catalyzed by cytochrome P450.....	10
Figure 1.6 Canonical P450 catalytic cycle	11
Figure 1.7 Structure of P450 BM3 oxygenase and reductase domains.....	13
Figure 1.8 $[\text{Ru}(\text{bpy})_3]^{2+}$ absorption and emission spectra in water, at room temperature	16
Figure 1.9 $[\text{Ru}(\text{bpy})_3]^{2+}$ photochemistry	17
Figure 1.10 Redox active model proteins	18
Figure 1.11 An example of a perfluorinated ruthenium wire	19
Figure 1.12 Photosensitizers for site-specific surface labeling at amino acids	20
Figure 1.13 Flash-quench ET cycles	22
Figure 1.14 Paths for formation of high-valent CI and CII	24
Figure 1.15 Flash-quench oxidation of a heme protein active site.....	25
Figure 1.16 Histidine-ligated hemes	25
Figure 1.17 P450-catalyzed cyclopropanation of styrene	28
Figure 1.18 Native and engineered P450 catalytic schemes	28
Figure 2.1 Catalytic cycle for P450-catalyzed hydroxylation reactions.....	36
Figure 2.2 $[\text{Ru}^{\text{II}}(\text{bpy})_3]^{2+}$ flash-quench and oxidation of the a heme protein active site.....	39
Figure 2.3 $[\text{Ru}(\text{bpy})_2(\text{IAphen})]^{2+}$ tethering to cysteine, to form the conjugate Cys-Ru(bpy) ₂ (Aphen).....	40
Figure 2.4 K97 labeling site	42
Figure 2.5 Absorption spectra of $[\text{Ru}(\text{bpy})_2(\text{IAphen})]^{+2}$, P450-BM3 C62A/C156S/K97C, Ru _{K97C} -P450 _{BM3} at approximately equal concentrations	44
Figure 2.6 Steady-state luminescence spectra of Ru photosensitizers in deoxygenated water	45
Figure 2.7 The Ru _{K97C} -P450 _{BM3} structure.	47
Figure 2.8 Overlay of Ru _{K97C} -P450 _{BM3} with wild type substrate-free and substrate-bound forms	47
Figure 2.9 Stacking of Ru _{K97C} -P450 _{BM3} with an adjacent crystal unit	48

Figure 2.10 Time resolved 630 nm luminescence decays in the absence of quencher.....	50
Figure 2.11 Luminescence decays of Ru _{K97C} -P450 _{BM3} (pH 8) at various concentrations of [Ru(NH ₃) ₆] ³⁺ quencher.....	51
Figure 2.12 Stern-Volmer quenching of Ru _{K97C} -P450 _{BM3} with [Ru(NH ₃) ₆] ³⁺ at three pH values.....	52
Figure 2.13 Single-wavelength transient absorption of Ru ^{II} _{K97C} -Fe ^{III} _{P450} in the absence of quencher.....	53
Figure 2.14 Transient Absorption data for flash-quench of [Ru(bpy) ₂ (IAphen)] ²⁺ with 17 mM [Ru(NH ₃) ₆] ³⁺	54
Figure 2.15 Single-wavelength transient absorption following flash-quench (λ _{ex} = 480 nm) of Ru ^{II} _{K97C} -Fe ^{III} _{P450} at pH 8.....	55
Figure 2.16 pH dependence of Ru _{K97C} -P450 _{BM3} transient absorption features.....	56
Figure 2.17 tgSVD of TA data for Ru ^{II} _{K97C} -Fe ^{III} _{P450} with [Ru(NH ₃) ₆] ³⁺ at six wavelengths.....	57
Figure 2.18 Global fitting of Ru ^{II} _{K97C} -Fe ^{III} _{P450} TA data at pH 8.....	59
Figure 2.19 Scheme for photochemical oxidation of cytochrome P450....	60
Figure 2.20 Extracted difference spectra of intermediate species.....	61
Figure 2.21 Photo-triggered cycle for flash-quench oxidation of Ru ^{III} _{K97C} -Fe ^{III} _{P450}	64
Figure 3.1 Photo-excitation of P680 chromophores in Photosystem II triggers oxidation of the oxygen evolving complex (OEC).....	75
Figure 3.2 Photo-excitation of the tethered ruthenium complex triggers oxidation of the P450 heme active site.....	76
Figure 3.3 Formation of high-valent CI and CII.....	77
Figure 3.4 Multistep ET in rhenium-labeled azurin.....	79
Figure 3.5 Multistep ET in ruthenium-labeled cytochrome P450.....	80
Figure 3.6 Putative multistep ET pathway in Ru _{C97} -BM3(W).....	81
Figure 3.7 Structures of P450 BM3 and CYP119.....	83
Figure 3.8 Photosensitizer conjugation sites in P450-BM3 and CYP119..	84
Figure 3.9 UV-visible absorbance spectra of P450 mutants.....	85
Figure 3.10 Overlay of C97-BM3 _(WH) (purple) with open and closed WT BM3 structures.....	86
Figure 3.11 C97-BM3 _(WH) active site.....	87
Figure 3.12 Time-resolved luminescence decays of Ru-BM3 conjugates in the presence and absence of 17 mM [Ru(NH ₃) ₆] ³⁺ quencher.....	89
Figure 3.13 Time-resolved luminescence decays of Ru-CYP119 conjugates in the presence and absence of 17 mM [Ru(NH ₃) ₆] ³⁺ quencher.....	90
Figure 3.14 Overlay of luminescence decays for four Ru-P450 conjugates... ..	91
Figure 3.15 Single wavelength TA traces of Ru _{K97C} -P450 _{BM3} conjugates in the presence of [Ru(NH ₃) ₆] ³⁺ , following excitation at 480 nm.....	93

Figure 3.16 Flash-quench schemes.....	94
Figure 3.17 Single wavelength transient absorption traces of Ru-CYP119 conjugates in the presence of $[\text{Ru}(\text{NH}_3)_6]^{3+}$, following excitation at 480 nm	96
Figure 3.18 TA data of $\text{Ru}_{\text{C77}}\text{-CYP119}_{(\text{H}W)}$ at variable temperature	97
Figure 3.19 UV-visible absorbance spectra P450, Ru photosensitizer	99
Figure 4.1 Multistep ET in biological energy conversion systems.	110
Figure 4.2 Sequential ET steps in the photo-triggered oxidation of Ru-P450 conjugates.....	112
Figure 4.3 Photosensitizers and metallo-proteins.....	113
Figure 4.4 Ribonucleotide reductase from <i>E. coli</i>	114
Figure 4.5 Energy diagram illustrating thermodynamic parameters for an ET reaction	115
Figure 4.6 Energy diagram illustrating diabatic and adiabatic states, and the coupling parameter H_{AB}	116
Figure 4.7 Tunneling timetables for driving force optimized ET reactions.	118
Figure 4.8 The $\text{Re}_{\text{H124}}\text{-W122-Azurin}$ hopping system.....	124
Figure 4.9 Prompt #1: ET parameters.....	125
Figure 4.10 Prompt #2: Hopping Map parameters	126
Figure 4.11 Sample hopping map for $\text{Re}_{\text{H124}}\text{-W}_{122}\text{-Azurin}$	127
Figure 4.12 Temperature dependence of the $\text{Re}_{\text{H124}}\text{-W}_{122}\text{-Azurin}$ hopping map	130
Figure 4.13 Hopping maps for $\text{Re}_{\text{H124}}\text{-W}_{122}\text{-Azurin}$ with differing distance formulations.....	132
Figure 4.14 Hopping maps for $\text{Re}_{\text{H124}}\text{-W}_{122}\text{-Azurin}$ with differing values of β	133
Figure 4.15 Hopping maps for $\text{Re}_{\text{H124}}\text{-W}_{122}\text{-Azurin}$ with differing values of λ	135
Figure 4.16 Square scheme for tryptophan and tyrosine, including relevant reduction potentials and acid dissociation constants	137
Figure 4.17 Hopping system in $\text{Ru}_{\text{K97C}}\text{-W}_{96}\text{-P450}_{\text{BM3}}$	139
Figure 4.18 Model of the Ru-P450 surface.....	140
Figure 4.19 Hopping maps for $\text{Ru}_{\text{C97}}\text{-W}_{96}\text{-P450}_{\text{BM3}}$ heme oxidation: Distance formulations	144
Figure 4.20 Hopping maps for $\text{Ru}_{\text{K97C}}\text{-P450}_{\text{BM3}}$ photochemical heme oxidation: Altering β and λ	145
Figure 4.21 Hopping maps for $\text{Ru}_{\text{K97C}}\text{-P450}_{\text{BM3}}$ photochemical heme oxidation: Worst case hopping scenario	146
Figure 5.1 Canonical P450 catalytic scheme, highlighting the reductive ET events that activate dioxygen.....	153
Figure 5.2 Structure of the $\text{Ru-P450}_{\text{BM3}}$ conjugate	155
Figure 5.3 Flash-quench cycles for ET with the heme active site	156

Figure 5.4 Cartoon of CO photolysis and rebinding.....	157
Figure 5.5 Luminescence decay at 630 nm of four Ru-P450 conjugates in the presence and absence of <i>p</i> OMeDMA.....	160
Figure 5.6 Single-wavelength transient absorption data of Ru-P450 at various wavelengths.....	162
Figure 5.7 Single wavelength transient absorption data for flash-quench of four Ru-P450 mutants.....	163
Figure 5.8 Spectra of ferric and ferrous wild-type P450-BM3, and the ferrous – ferric difference spectrum.....	165
Figure 5.9 Normalized overlay of TA for the four Ru-P450 systems	167
Figure 5.10 Flash-quench scheme for heme reduction.....	168
Figure 5.11 UV-visible absorbance spectra of Fe ^{III} -P450 BM3 under argon, or CO before and after laser excitation.....	169
Figure 5.12 UV-visible absorbance spectra of five-coordinate, dithionite-reduced WT CYP119 and the corresponding six-coordinate ferrous CO species.....	171
Figure 5.13 Transient difference spectra following flash-photolysis of WT CYP119 ferrous-CO.....	172
Figure 5.14 Single-wavelength TA following flash-photolysis of WT CYP119	173
Figure 5.15 Power dependence of CO escape, 460 nm excitation	174
Figure 5.16 Temperature dependence of CO rebinding (no substrate)...	175
Figure 5.17 UV-visible absorption spectra of WT CYP119 with and without laurate.....	176
Figure 5.18 Temperature dependence of CO rebinding in the presence of laurate.....	177
Figure 5.19 Comparison of laurate-free and laurate-bound CO rebinding kinetics	178
Figure 5.20 Picosecond-to-millisecond TA data for CO rebinding in substrate-free CYP119 at various temperatures	179
Figure 5.21 Amplitude coefficients derived from nonnegative least squares fitting of CYP119 CO rebinding kinetics	180
Figure 5.22 Integration of rate constant amplitudes at varying temperature (substrate free)	181
Figure 5.23 First moment of populations at varying temperature (substrate free).....	181
Figure 5.24 Second centered moment of populations at varying temperature (substrate free)	182
Figure 5.25 Comparison of amplitude integrations for the slow population in substrate free and laurate-bound CYP119	183
Figure 5.26 Comparison of slow population first moment in substrate-free and laurate-bound CYP119.....	184

Figure 5.27 Comparison of slow population second centered moment (variance) in substrate-free and laurate-bound CYP119.....	184
Figure 5.28 Eyring plot for rebinding of escaped CO in CYP119.....	186
Figure 6.1 Structure of P450 BM3	195
Figure 6.2 P450-catalyzed cyclopropanation of styrene	196
Figure 6.3 Schemes for native and engineered P450 catalysis	197
Figure 6.4 P411 ₁₃ —Ser structure and activity	199
Figure 6.5 Structure of P450 ₁₃ -Cys, highlighting mutations in blue.....	201
Figure 6.6 Absorption spectrum of the methyl viologen radical cation...203	
Figure 6.7 Chemical titration of WT P450 BM3 with reduced MV	204
Figure 6.8 Spectroelectrochemical setup	205
Figure 6.9 Electron relay between the working electrode and the P450 heme	206
Figure 6.10 Absorption spectra taken during the spectroelectrochemical reduction of WT BM3	207
Figure 6.11 Absorption spectra taken during the spectroelectrochemical oxidation of dithionite-reduced WT BM3.....	207
Figure 6.12 Plot of the electrochemical titration of WT BM3	208
Figure 6.13 Absorption spectra of WT BM3 during reductive potentiometric titration.....	210
Figure 6.14 Absorption spectrum of WT BM3 during oxidative potentiometric titration.....	211
Figure 6.15 Open circuit potential measurements of WT BM3 during potentiometric titration.....	212
Figure 6.16 Redox titration plot of wild-type P450 BM3	213
Figure 6.17 Titration curve of WT P450 BM3	214
Figure 6.18 Absorbance spectra of WT CYP119 during potentiometric titration with dithionite.....	215
Figure 6.19 Open circuit potential measurements for WT CYP119	215
Figure 6.20 Potentiometric titration of WT CYP119 with overlaid Nernst function.....	216
Figure 6.21 Absorption spectra of P450 BM3 C400S.....	217
Figure 6.22 Redox titration curves of C400S and WT BM3 overlaid by one-electron Nernst functions	218
Figure 6.23 Titration curves for four mutants.....	219
Figure 6.24 Redox titration curve of C400M.....	220
Figure 6.25 Reduction of C400Y shows loss of isosbestic points	221
Figure 6.26 Spectra of C400A during potentiometric titration	222
Figure 6.27 Loss of isosbestic points in C400A absorption during titration	222
Figure 6.28 Spectra of C400H during potentiometric titration.....	223
Figure A1 Cartoon of the NOS homodimeric structure.....	231

Figure A.2 Dimeric structure of NOS from <i>Geobacillus stearothermophilus</i>	232
Figure A.3 NOS-catalyzed production of nitric oxide from L-arginine ..	233
Figure A.4 Proposed catalytic cycle for NOS.....	233
Figure A.5 Flash-quench cycle for oxidizing the heme active site	234
Figure A.6 Location of the photosensitizer tethering site.....	236
Figure A.7 UV-visible absorption of unlabeled and labeled Ru-NOS and free photosensitizer	237
Figure A.8 Structure of Ru-NOS.....	238
Figure A.9 Tryptophan 243 is located between the photosensitizer and heme in Ru-NOS.....	238
Figure A.10 Luminescence decay of Ru-NOS with fits	240
Figure A.11 Luminescence lifetimes of Ru-NOS at varying ionic strength	242
Figure A.12 ET quenching of Ru-NOS with $[\text{Ru}^{\text{III}}(\text{NH}_3)_6]^{3+}$	243
Figure A.13 Relative amplitudes of the major and minor decay components.....	243
Figure A.14 Transient absorption data at six wavelengths.....	245
Figure A.15 tgSVD of TA data for flash-quench of Ru-NOS	246
Figure A.16 Global fitting of TA data at six wavelengths	247
Figure A.17 Scheme for photochemical oxidation of the NOs heme.....	249
Figure B.1 Specialized cuvette for laser studies	259
Figure B.2 Nanosecond-pulsed single-wavelength transient luminescence and absorption setup: NSI	260
Figure B.3 Nanosecond-pulsed multi-wavelength transient absorption setup: NSII.....	261
Figure B.4 NSI instrument response to scattered laser light.....	262
Figure B.5 Picosecond-pulsed transient absorption setup: PSI.....	263
Figure B.6 PSI instrument response to scattered laser light.....	264
Figure C.1 Luminescence decays of RuK97C-BM3, varied conc.	267
Figure C.2 Luminescence decays at variable temperature.....	268
Figure C.3 TA at variable temperature	269
Figure C.4 Transient difference spectra of photosensitizers and Ru-P450 conjugates.....	270
Figure C.5 406 nm narrow band pass filter.....	272
Figure C.6 Overlay of PSI and NSI data for CO rebinding kinetics	273
Figure C.7 Rate constant amplitudes from nlns fitting.....	274
Figure C.8 Deconvolution of a spectrum into ferric and ferrous components using the script: spectraldeconvoluter.m	275
Figure C.9 Two separate potentiometric titrations of WT P450 BM3	276

LIST OF TABLES

<i>Number</i>	<i>Page</i>
Table 1.1 Relevant reduction potentials of wild type P450s and redox cofactors	12
Table 1.2 Parameters for a selection of oxidative quenchers	23
Table 2.1 X-ray crystallographic data collection, refinement statistics, and validation	46
Table 2.2 Observed rate constants (γ_{1-5} , s^{-1}) extracted from global fitting of single-wavelength TA at six wavelengths (390-440 nm)	59
Table 2.3 Extracted kinetics parameters	62
Table 3.1 Excited state lifetimes of four Ru-P450 conjugates in the absence and presence of 17 mM $[Ru(NH_3)_6]^{3+}$ quencher	91
Table 4.1 Experimentally-determined reorganization energies for various proteins	135
Table 4.2 Calculated single-step tunneling times for porphyrin oxidation, using a variety of ET parameters	141
Table 4.3 Minimum driving forces necessary to obtain an ET time of 1.3 μs for each hopping map.....	142
Table 5.1 Luminescence lifetimes, taken from biexponential (unquenched) and monoexponential (quenched) fits	160
Table 5.2 Rates of heme reduction extracted from global fitting of transient absorption data	166
Table 5.3 Thermodynamic activation parameters for CO rebinding in CYP119 and various heme enzymes	186
Table 6.1 Reduction potentials of ferric P450 and redox active cofactors	224
Table A.1 Luminescence lifetimes of Ru-NOS in 50 mM borate buffer, pH 8.....	241
Table A.2 Luminescence lifetimes of Ru-NOS in 500 mM sodium chloride, 50 mM borate buffer, pH 8.....	241
Table A.3 Rate constants extracted from global fitting of TA data.....	246

Chapter 1

**CYTOCHROME P450:
FROM PURSUIT OF REACTIVE INTERMEDIATES
TO
ENGINEERING NOVEL REACTIVITY**

1.1. Cytochrome P450: a remarkable metabolic enzyme

Every living organism is composed of cells that are alive with chemical reactions, the processes that allow them to grow, reproduce, and respond to the environment. Beneficial nutrients are broken down to provide energy and synthetic building blocks, new molecules are built from scratch or modified for specific purposes, and unwanted or harmful chemicals are detoxified and excreted. Each of these metabolic processes must be accomplished in a very precise, controlled fashion; this often requires surmounting a significant reaction barrier. Thus, cells employ enzymatic machinery to catalyze these reactions.

Metabolic enzymes face a number of significant challenges. Splitting up large molecules into smaller or more useful components requires activating, breaking, and functionalizing some of the strongest and most inert chemical bonds found in organic molecules. Additionally, a series of reduction and oxidation reactions (redox) is often required, in which electrons are specifically transferred out of one chemical bond and into a new one. All of these transformations must occur in a tightly controlled fashion in order to synthesize complex molecules with specific information encoded in the molecular structure. Furthermore, they must be accomplished on a wide variety of substrates; exposure to toxins and xenobiotics in the environment provides a constant variety of sizes, geometries, and functionalities.

A remarkable class of enzymes called cytochrome P450 (often abbreviated as just “P450”), plays a critical role in these metabolic processes. These enzymes possess three characteristics that make them indispensable. First, the P450 center houses a thiolate-ligated heme active site capable of generating extremely reactive iron-oxo species. These reactive species can react with alkane C–H bonds – the most

common and inert bonds found in organic molecules. Secondly, the amino acids that directly surround the active site orient substrates in proximity to the reactive center, allowing the enzyme to form new bonds in a controlled fashion with high levels of regio- and stereoselectivity. Finally, flexible protein architecture around the active site allows P450s to envelop substrates with a wide variety of sizes, geometries, and functionalities, and thus, metabolize myriad small molecules.

Because of these three features, P450s are found in every living organism, from bacteria and archaea, to plants, fungi, and animals; there are even a number of viruses that carry the P450 genetic code. Since their initial discovery in rat liver microsomes in the 1940s, advances in genomics have led to the discovery of over 20,000 versions of P450,¹ and this number keeps rising. The remarkable reactivity displayed by P450s has made them a highly active field of research, involving many disciplines from medicine and toxicology to molecular biology, biochemistry, and biophysics. In addition, they are inspiration for the development of inorganic catalysts and synthetic methodologies. A fundamental question continues to fascinate scientists: how do these enzymes catalyze such difficult transformations? Specifically, what is the nature of the catalytically active species? How does the enzyme control the fundamental electron transfer (ET) events that are required to form the active species, and for it to then react with substrates? Furthermore, can we harness and modify P450s to drive catalysis in an entirely new way?

This Chapter begins by discussing the key features of P450s that contribute to their remarkable reactivity, including the nature of reactive intermediates along the catalytic pathway. Two soluble, bacterial enzymes are highlighted in particular: P450 BM3 from the soil bacterium *Bacillus megaterium*, and CYP119 from the thermophilic hot-springs archaeum *Sulfolobus acidocaldarius*. These two variants are the focus of the experimental work that will be presented and analyzed in

Chapters 2-6. This first Chapter next addresses a rapid, photochemical method for triggering ET within enzyme systems in order to generate and investigate reactive species. Implementation of this method is discussed in Chapters 2-5. Finally, this Chapter discusses a recent report of engineered P450-catalyzed cyclopropanations. By manipulating electron flow, these artificial P450s can be reprogrammed to catalyze cyclopropanation of styrene within the context of an *E. coli cell*. Electrochemical measurements that quantify this electronic manipulation are presented in Chapter 6.

1.2. P450: structural features that direct function

The first X-ray crystallographic characterization of a P450 was achieved in 1987 for the soluble, bacterial P450_{CAM} from *Pseudomonas putida*.² Bacterial variants such as P450_{CAM} often are stable, soluble, and easier to study. In contrast, mammalian variants are delicate and frequently are membrane bound. Due in large part to improvements to crystallization techniques, there are almost 600 P450 structures in the protein data base (PDB) to date, including 107 structures of human variants. This increasing wealth of data allows identification of common features and individual peculiarities. Entire volumes have been written on the relationship between P450 structure and function,³ so this Chapter only briefly highlights the features that are pertinent to Chapters 2-6 of this Thesis.

Cytochrome P450s are largely α -helical proteins, with a tertiary structure that is highly conserved and unique to the superfamily; no non-P450 proteins share this fold.⁴ The structures of P450 BM3 and CYP119 are shown in **Figure 1.1**. It is perhaps unsurprising that the most highly conserved regions are those adjacent to the active site, while those associated with substrate specificity may differ significantly among P450 variants.

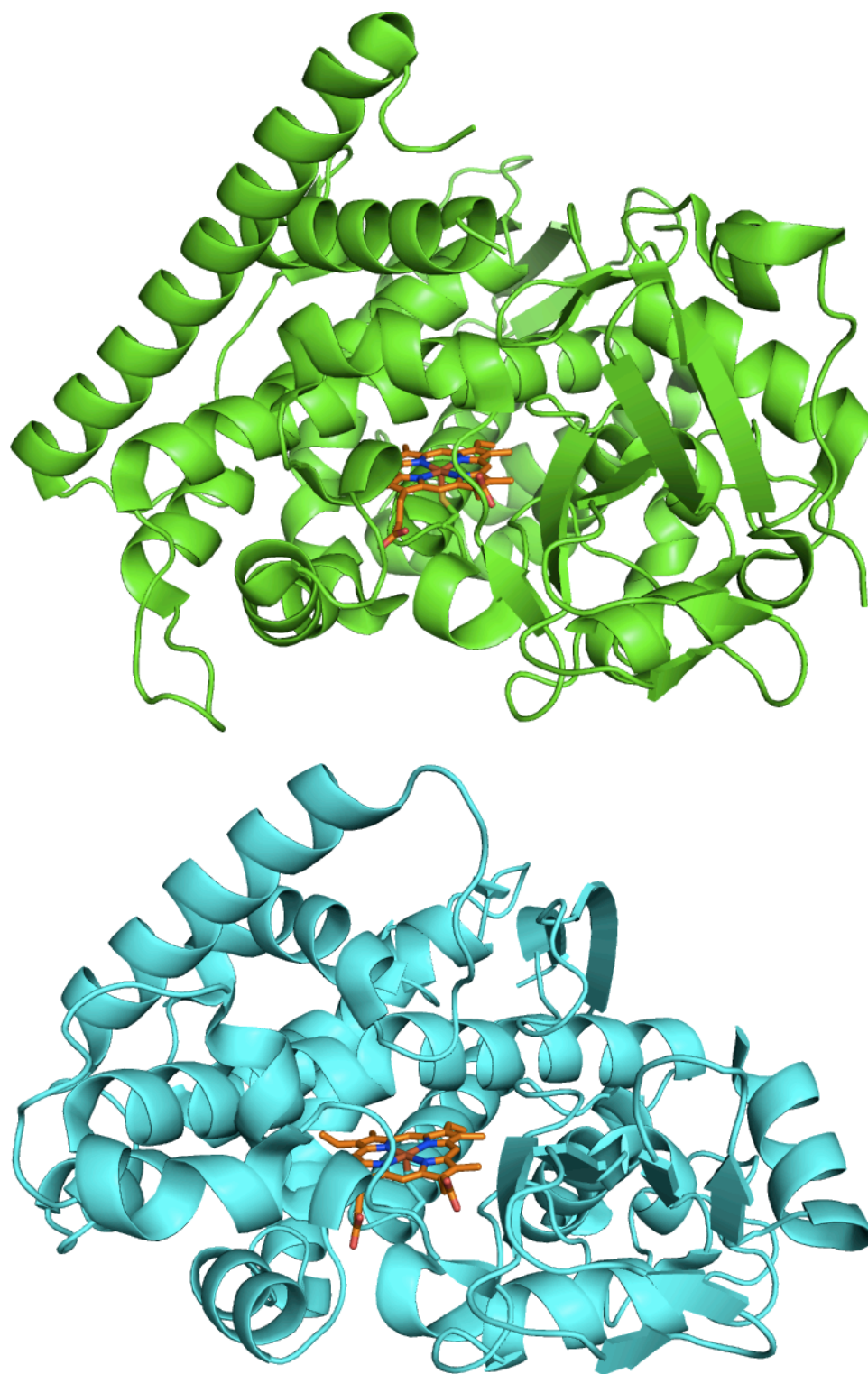


Figure 1.1. Structures of P450 BM3 heme domain from *Bacillus megaterium* and CYP119 from *Sulfolobus acidocaldarius*. BM3: top, green, PDB: 2IJ2. CYP119: bottom, cyan, PDB: 1IO7. Heme active sites are highlighted in orange. All figures in this Chapter were made using PyMol graphics software for Mac.

At the heart of cytochrome P450 lies the heme, iron protoporphyrin IX, that drives P450 chemistry. The iron center is ligated on the proximal face by an absolutely conserved cysteine (**Figure 1.2**, green); this ligation is absolutely critical for P450 function. This cysteine is part of a signature β -bulge containing the conserved sequence FxxGx(H/R)xCxG; this lies at the end of helix L, which runs beneath the heme (**Figure 1.2**, blue). This region of the protein fold is critical for holding the cysteine in place. Three hydrogen bonds from nearby backbone amide N-H donors also stabilize the thiolate ligand. This ligation and hydrogen bonding arrangement is shared with two other heme monooxygenases: chloroperoxidase and nitric oxide synthase.

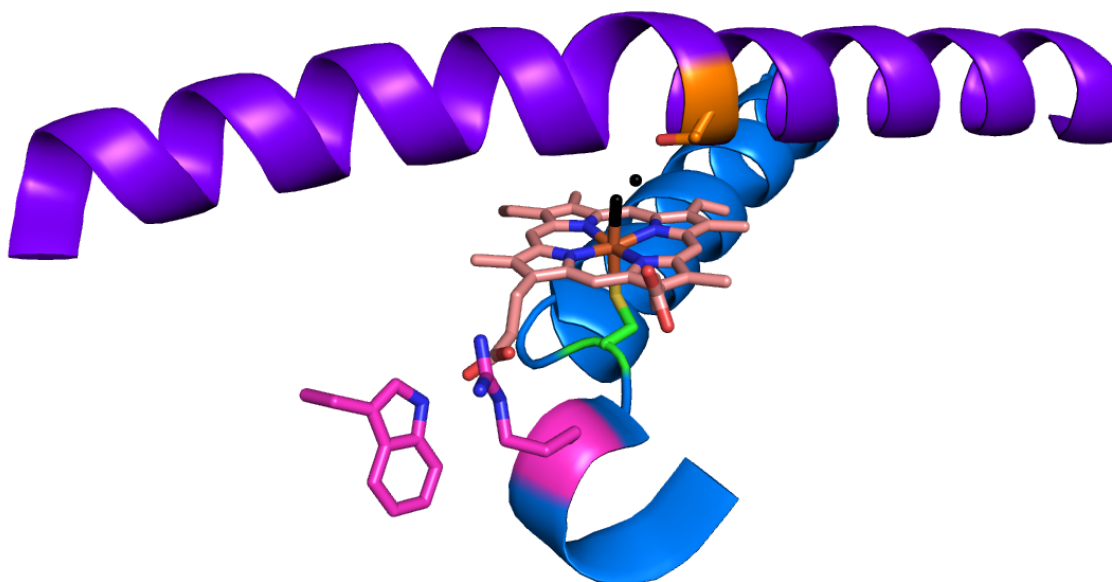


Figure 1.2. P450 BM3 active site. The heme is colored pale pink. The L helix (blue), and contains cysteine400 (green) which ligates the heme. In bright pink: arginine398 and tryptophan96 form hydrogen bonds with one of the heme propionates. The long I helix (purple) above the heme contains threonine268 (orange). The axial water molecule, and an additional, structured water molecule above the heme are shown as a black dot.

The P450 heme is not covalently bound to the protein structure, but rather is held in place by cysteine ligation, hydrophobic contacts, and hydrogen bonding

between the heme propionates and amino acid side chains. The precise nature of the hydrogen bonding partners differs among P450 variants. For P450 BM3, this includes a tryptophan96 and arginine398; site directed mutagenesis studies that replaced tryptophan96 with non-hydrogen bonding residues (e.g., alanine) saw greatly diminished heme incorporation in the expressed mutants. CYP119 contains a more extensive hydrogen bond network between the protein and the heme propionates (**Figure 1.3**). Histidine76, histidine315, and arginine80 form hydrogen bonds with one of the heme propionates, and arginine259 forms a hydrogen bond with the other.

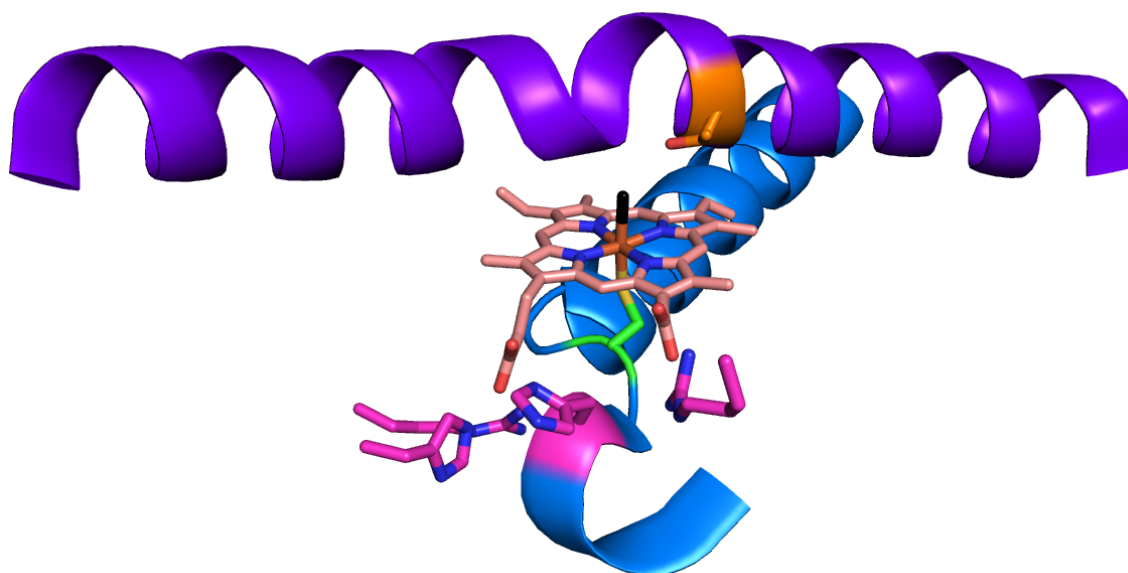


Figure 1.3. CYP119 active site. The heme is colored pale pink. The L helix (blue), and contains cysteine317 (green) which ligates the heme. In bright pink: histidine315, histidine76, and arginine80 form hydrogen bonds with one of the heme propionates, and arginine259 forms a hydrogen bond with the other. The long I helix (purple) above the heme contains threonine213 (orange). The axial water molecule is black.

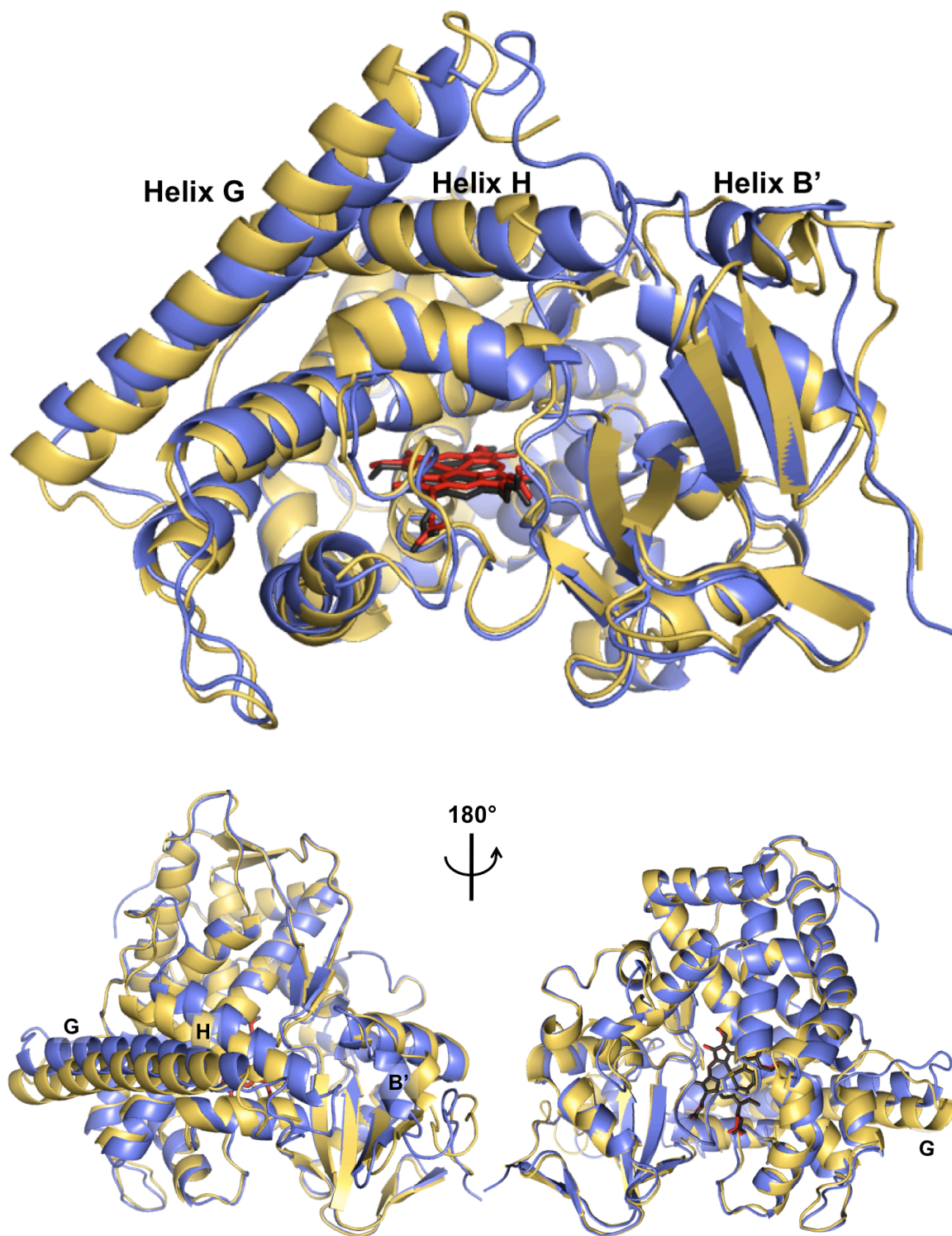


Figure 1.4. Overlay of substrate-free (open, gold) and substrate-bound (closed, blue) forms of P450 BM3. **Top:** view from the front. **Bottom:** views from distal (left) and proximal (right) faces.

The distal face of the P450 heme is in contact with the substrate binding pocket. In the absence of substrate, a water molecule acts as the distal axial ligand, making the iron center six coordinate and low spin. The long I helix (**Figure 1.2** and **Figure 1.3**, purple) runs along this distal face, and contains a conserved threonine side chain that is involved in oxygen activation, as discussed in Section 1.3. The substrate binding pocket of cytochrome P450 is largely hydrophobic, with key residues positioned to align substrate. While the heme active site is deeply buried, a long substrate-access channel provides a pathway for molecules to enter. Upon substrate binding, large conformation changes can be seen for many P450 variants. For example, in the presence of long chain fatty acids such as palmitic acid, the P450 BM3 G, H, and B' helices tighten down on the pocket (**Figure 1.4**).

1.3. P450 activity: reactions and mechanisms

Broadly, P450s catalyze the metabolism of xenobiotics and the biosynthesis of signaling molecules. The most common and well-studied transformations are monooxygenase reactions, such as hydroxylation of aliphatic and aromatic carbons or heteroatoms, and epoxidations.⁵ Dehydrations, ring formations and expansions, and reductive halogenations among many others have also been observed. As will be discussed in Section 1.6, the heme active site can also be engineered for non-native reactions including carbene transfer.

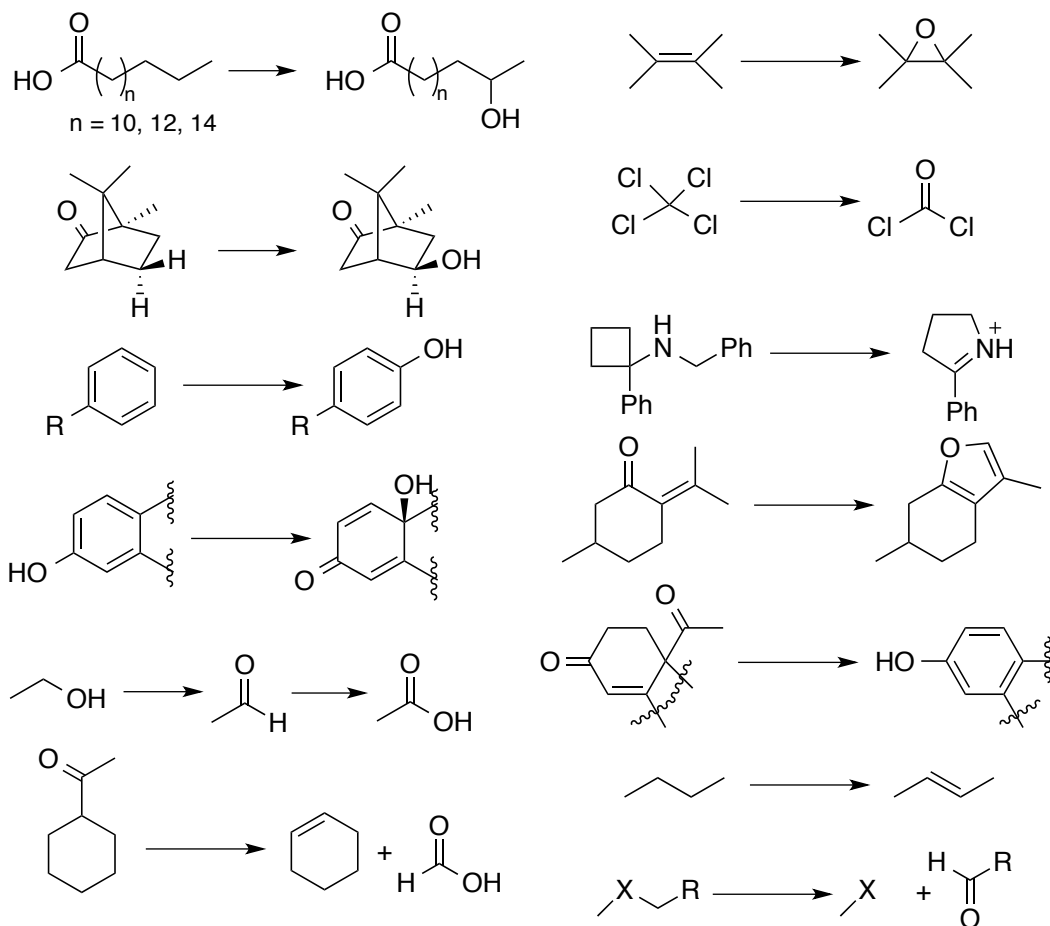


Figure 1.5. Various reactions catalyzed by cytochrome P450s.

Oxygen Activation

P450 monooxygenase activity requires binding and activation of molecular oxygen (O_2) with the input of high-energy electrons. Once the O–O bond is broken, a single oxygen atom is incorporated into an organic substrate molecule; the other is released as water. A canonical P450 catalytic cycle is shown in **Figure 1.6**; black rhombs represent the active site heme. Each step in this catalytic process relies on critical features in the P450 architecture.

The stepwise, reductive activation of dioxygen involves transient generation of reactive intermediates that include superoxide, peroxide, and high valent iron-

oxos. In order to prevent deleterious generation and release of these species, many P450s have an important gating mechanism prevents the flow of electrons, and thus, the activation of dioxygen, in the absence of substrate; both P450 BM3 and CYP119 fall into this class. In these enzymes, the resting state contains a six-coordinate, ferric (Fe^{III}) heme, which is ligated by the axial thiolate on the proximal face, and a loosely bound water molecule on the distal face (species 1 of **Figure 1.6**). Strong interactions of the iron $3d$ orbitals with these ligands cause the resting state to be low-spin.

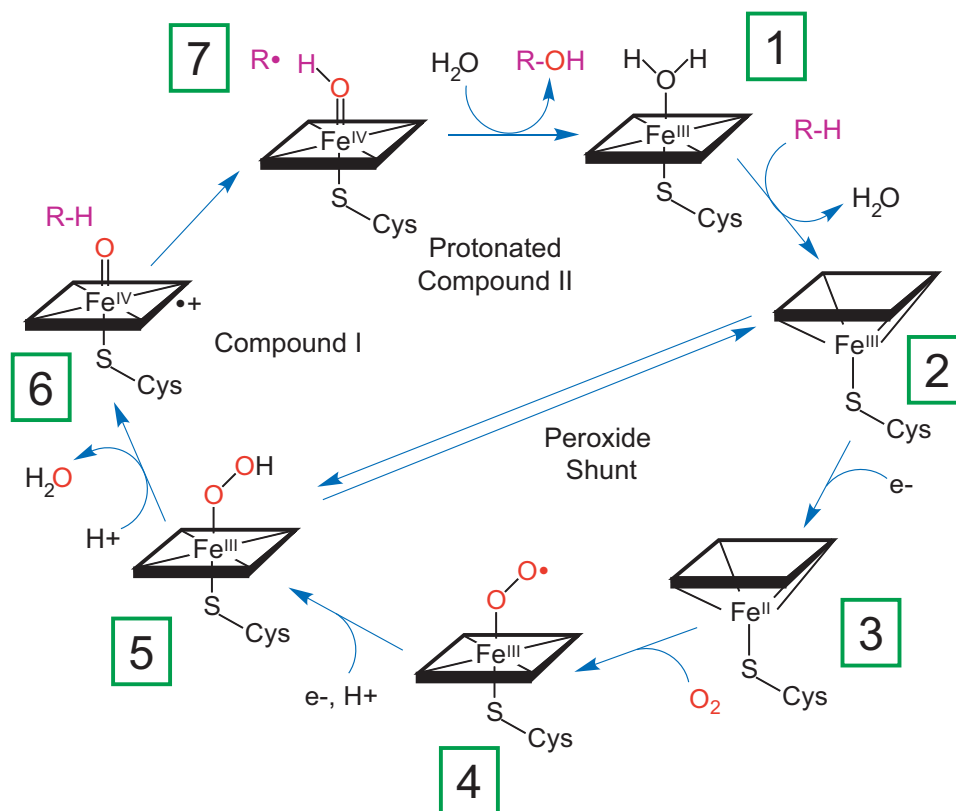


Figure 1.6. Canonical P450 catalytic cycle.

Due in large part to the strongly donating character of the axial thiolate, the resting state $\text{Fe}^{\text{III/II}}$ reduction potential is too negative to be reduced by native redox cofactors such as reduced nicotinamide adenine dinucleotide phosphate (NADPH), and reduced flavin adenine dinucleotide (FADH_2) (**Table 1.1**).

Substrate binding causes displacement of the axial water molecule,⁶ forming a five-coordinate, ferric heme in which the iron center is displaced below the ring of the porphyrin (species 2).⁷ The weaker ligand field in this geometry favors the high spin iron state, and shifts the $\text{Fe}^{\text{III/II}}$ reduction potential 50-150 mV positive,⁸ facilitating one-electron reduction of the heme (species 3).

Table 1.1. Relevant reduction potentials of wild type P450s and redox cofactors⁸⁻¹⁰

Enzyme/Cofactor	E° (mV vs. NHE)
NAD^+/NADH ($2e^-$)	-320 ^a
FAD/FADH_2 ($2e^-$)	-320 ^b
$\text{FAD}/\text{FADH}\cdot$	-264 ^b
$\text{FADH}\cdot/\text{FADH}_2$	-375 ^b
WT BM3 $\text{Fe}^{\text{III/II}}$	-430 ^{c,d}
WT BM3 $\text{Fe}^{\text{III/II}}$ (substrate bound)	-290 ^c
WT CYP119 $\text{Fe}^{\text{III/II}}$	-420 ^d

a: ref 9. b: ref 10. c: ref 8. d: Chapter 6 of this Thesis

The requisite electrons from NAD(P)H, and are transferred to the heme by various electron relays. For the subset of P450s known as “Class I” enzymes, a flavoprotein reductase acquires the two electrons from NADPH and dispatches them individually to an iron-sulfur protein, which in turn reduces the P450 oxygenase. Mammalian P450s associated with steroid synthesis and the majority of bacterial enzymes fall into this category. In Class II enzymes, a single flavoprotein reductase transfers the electrons from NADPH to the P450 oxygenase via the associated flavin mononucleotide cofactor (FMN).¹¹ The mammalian P450s involved in drug metabolism are an example of this class.¹¹ P450 BM3 belongs to a unique, “self-sufficient” class, in which the reductase and oxygenase domains are fused. This facilitates ET, and allows P450 BM3 to turnover product with some of the highest

rates: 930 min^{-1} for lauric acid, and 1470 min^{-1} for arachidonic acid.¹² For comparison, CYP119 oxidizes lauric acid at a rate of 11 min^{-1} .¹³

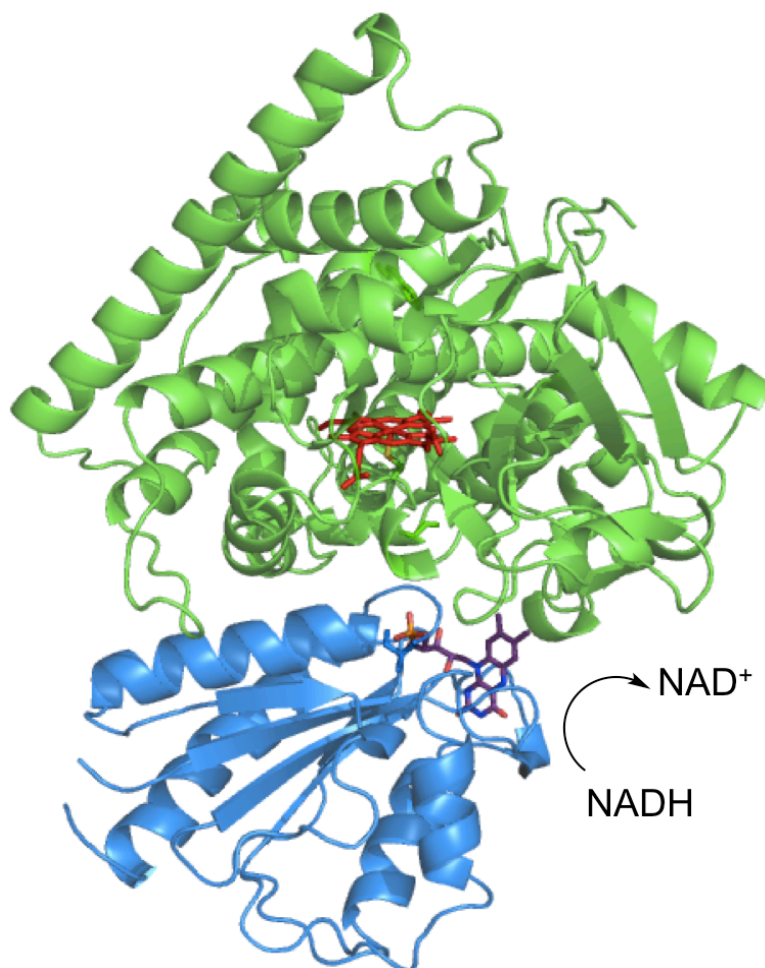


Figure 1.7. Structure of P450 BM3 oxygenase and reductase domains (PDB: 1BVY). The oxygenase domain is colored green (heme: red), and the reductase domain is colored blue (flavin: purple).

The ferrous heme readily binds oxygen, forming a ferric superoxide (species 4). Further reduction by one electron and protonated forms a hydroperoxy species (species 5). Two main factors affect heterolysis of the O–O bond at the heme active site. First, the “thiolate-push” from the strongly-donating thiolate ligand assists in heterolytic bond cleavage.¹⁴ Second, a well-organized proton relay facilitates selective protonation of the distal oxygen. This relay includes the conserved

threonine side chain on helix I, as well as organized water molecules within the active site (**Figure 1.2**). The doubly-protonated distal oxygen departs as a water molecule, generating a ferryl, ligand-radical-cation species known as Compound I (CI, **Figure 1.6**, species **6**).

P450 active hydroxylation agents: ferryl compounds I and II

CI is an extremely reactive oxidant, which allows P450 to functionalize strong and unactivated C–H bonds. CI abstracts a hydrogen atom from substrate to form Compound II (CII, **Figure 1.6 7**), which then undergoes radical recombination with substrate to produce hydroxylated product. Release of product from the active site and re-ligation by a water molecule returns the enzyme to its resting state.

The native steps of substrate binding, ET, and O–O bond cleavage are slower than the reaction of CI with substrate. However, CI can be generated from the resting state by reaction with chemical oxygen-atom donors, including *meta*-chloroperoxybenzoic acid (*m*CPBA). This chemical oxidation was accomplished cleanly for highly purified samples of CYP119, and CI was spectroscopically characterized by UV-visible absorption, Mössbauer, and electron paramagnetic resonance (EPR) spectroscopies.^{15,16} The apparent second order rate constant for reaction of CI with lauric acid (dodecanoic acid) is $1.1 \times 10^7 \text{ M}^{-1}\text{s}^{-1}$.¹⁵

It is remarkable that a wide range of specific chemical transformations can be achieved by very similar reactive heme-oxygen intermediates. It is equally remarkable that an enzyme can house a reactive species capable of activating aliphatic C–H bonds, and emerge unscathed. How does the enzyme house such a

reactive species without reacting with the much weaker bonds that make up the protein itself?

One factor is the gating mechanism described earlier; many P450s cannot be reduced (and therefore cannot activate dioxygen to form CI) in the absence of substrate. Another factor is the thiolate ligation; this causes CII to be more basic than other heme enzymes which are ligated by histidine. Characterization of chloroperoxidase and P450 CII by Mössbauer spectroscopy indicates a protonated, $\text{Fe}^{\text{IV}}\text{-OH}$ species.^{17,18} CII in CYP158 from *Streptomyces coelicolor* has a reported pK_a of almost 12,¹⁸ much higher than the pK_a of ~ 3.5 for histidine-ligated proteins such as horseradish peroxidase and myoglobin.¹⁹ Abstraction of the hydrogen atom from substrate requires transfer of both the electron and the proton. By facilitating proton transfer through basicity of CII, a less-oxidizing CI is required.

Much progress has been made to understand the native P450 catalytic cycle. Chemical generation, trapping, and spectroscopic characterization of the CI and CII active species have been huge steps in the understanding of cytochrome P450 reactivity. However, the fundamental nuclear reorganization that drives O–O bond scission to form CI, and the events of hydrogen atom abstraction and radical rebound to form hydroxylated substrate, have yet to be observed directly. Formation of these intermediates requires rapid and precisely controlled ET.

1.4. Photo-triggered electron transfer in proteins

Photo-triggered processes provide a high degree of temporal precision for the gating of reactions. Absorption of a photon occurs nearly instantaneously, and light energy can be delivered in discrete packets using pulsed lasers. In these cases, the precision of temporal gating is limited by the length of a laser pulse; this can be a few nanoseconds (as in the case of experimental instrumentation for this Thesis)

or as little as a few femtoseconds. In order to translate the energy from photons into a desired reaction, such as ET, an additional component is needed: a photosensitizer.

When photosensitizers absorb a photon of the appropriate wavelength, a reactive electronic excited state is generated. Ruthenium tris(2,2'-bipyridine) ($[\text{Ru}(\text{bpy})_3]^{2+}$) is a classic example.^{20,21} The metal-to-ligand charge transfer (MLCT) absorption band ($\lambda_{\text{max}} = 453 \text{ nm}$) is responsible for the orange-red color of this complex (**Figure 1.8**). Excitation into the MLCT band generates a reactive excited state that is both oxidizing at the metal center and reducing at the ligand (**Figure 1.9**, left). The excited state can relax by emission of a photon ($\lambda_{\text{max}} = 626 \text{ nm}$), or can be “quenched” by ET to or from a redox partner.

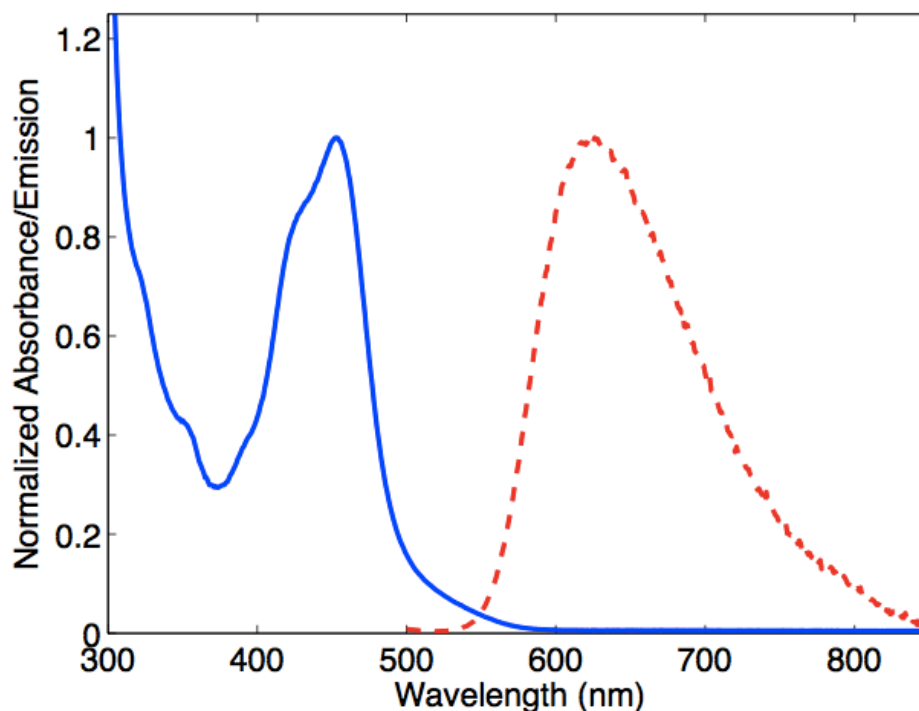


Figure 1.8. $[\text{Ru}(\text{bpy})_3]^{2+}$ absorption (blue, solid) and emission (red, dashed) spectra in water, at room temperature. The emission spectrum was generated using 480 nm excitation.

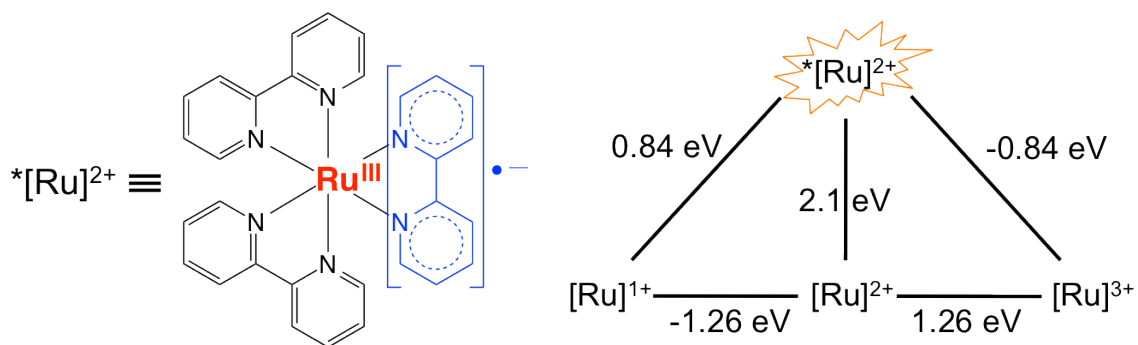


Figure 1.9. $[\text{Ru}(\text{bpy})_3]^{2+}$ photochemistry. **Left:** MLCT excited state of $[\text{Ru}(\text{bpy})_3]^{2+}$. **Right:** Modified Latimer diagram for $[\text{Ru}(\text{bpy})_3]^{2+}$; potentials are vs. the normal hydrogen electrode (NHE), in water.^{20,21}

In some cases, the photosensitizer's excited state reduction potential is sufficient to accomplish a desired ET reaction within the lifetime of the excited state (e.g., 600 ns for $[\text{Ru}(\text{bpy})_3]^{2+}$ in deoxygenated water). However, in cases where additional driving force is required, or where the ET reaction is slower than luminescent relaxation of the photosensitizer, a method called “flash-quench” can be employed. In our example of $[\text{Ru}(\text{bpy})_3]^{2+}$, a “flash” of light, such as a laser pulse, generates the photosensitizer excited state; this in turn is “quenched” by ET with exogenous small molecules. By selection of an appropriate quencher, either the more oxidizing $[\text{Ru}]^{3+}$ or more reducing $[\text{Ru}]^{1+}$ can be generated; this new species can be used to achieve ET with a system of interest. Flash-quench generates a photosensitizer state with additional driving force, and the separation of charges extends the lifetime of the reactive species.

By partnering photosensitizers with redox-active proteins, flash quench can be used to trigger biologically-relevant ET. In particular, the Gray lab has focused on systems in which the electron acceptor (or donor) is a metal center, such as copper in azurin, or heme iron in cytochromes, including cytochrome P450 (**Figure 1.10**). An advantage of these systems is that the metal center has strong absorbance in the

visible region. Furthermore, the absorption bands are sensitive to oxidation state of the metal center; ET reactions can be monitored using transient absorption spectroscopies. By varying the nature of the photosensitizer and the protein structure, the Gray lab and others have probed the mechanistic aspects of biological ET. Curious readers are directed toward a number of excellent reviews for further details.²²⁻²⁴ An extension of this analysis, multistep ET (“hopping”) is discussed in Chapter 4.

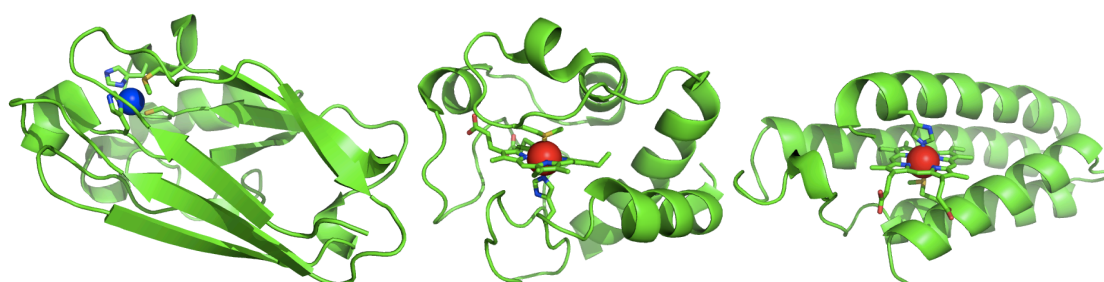


Figure 1.10. Redox active model proteins. Left to right: *P. aeruginosa* azurin (PDB: 1JZG, Cu in blue), horse heart cytochrome c (PDB: 1HRC, heme Fe in red), cytochrome b562 (PDB: 256B, heme Fe in red).

The bulk of this Thesis (Chapters 2-5) focus on the extension of these photo-triggered methods to generate redox intermediates and investigate ET mechanisms in cytochrome P450. To set the stage for the design of photosensitizer-P450 systems, we outline strategies for the selection of appropriate photochemical elements.

Photosensitizers

A wide variety of photosensitizers have been used for initiating ET within proteins. The Gray lab and others have employed ruthenium, rhenium, and osmium photosensitizers with a variety of ligand frameworks to study ET processes within metalloproteins, including heme proteins.^{22,25} Selection of an appropriate

photosensitizer for each specific application requires assessment of several photochemical and photophysical aspects.

Electronic communication between the protein and photosensitizer is critically important. For systems in which the protein redox cofactor is solvent exposed, simple photosensitizers such as $[\text{Ru}(\text{bpy})_3]^{2+}$ can be implemented. However, when the redox cofactor is buried inside the protein framework, more elaborate methods must be employed. Photosensitizer “wires” that bind noncovalently to the protein surface, or within the substrate channel, can be used (**Figure 1.11**).

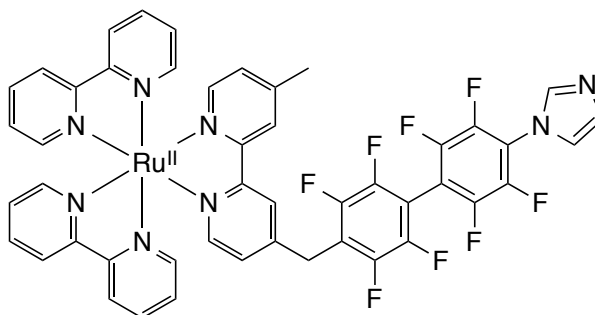


Figure 1.11. An example of a perfluorinated ruthenium wire.

A potential disadvantage of these wires is that noncovalent binding results in a distribution of free and bound photosensitizers. For enhanced control over binding location, the photosensitizer can be tethered to the protein surface (**Figure 1.12**).

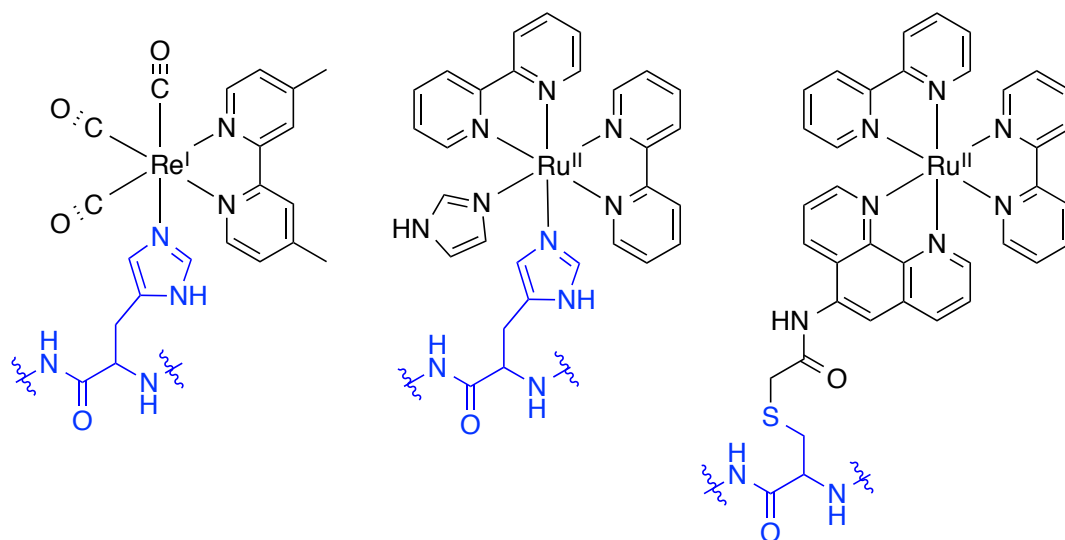


Figure 1.12. Photosensitizers for site-specific surface labeling at amino acids (blue). **Left:** $[\text{Re}(\text{dimethyl-bpy})(\text{CO})_3(\text{imidazole})]^{1+}$ is ligated by histidine. **Center:** $[\text{Ru}(\text{bpy})_2(\text{imidazole})]^{2+}$ is ligated by histidine. **Right:** $[\text{Ru}(\text{bpy})_2(\text{iodoacetamidophenanthroline})]^{2+}$ is tethered to cysteine.

This can be achieved by direct coordination of the photosensitizer metal center by histidine amino acids (**Figure 1.12** left and center). Alternatively, nucleophilic residues such as cysteine can be modified with an iodoacetamido linker attached to the photosensitizer ligand, in order to generate a covalent thioether bond between protein and photosensitizer (**Figure 1.12**, right). Selective photosensitizer conjugation to a specific site on the protein surface is accomplished by removal of native histidine/cysteine residues, and installation of a single labeling site, using site directed mutagenesis.

Selection of the photosensitizer/protein conjugation method is also important. The cysteine tethering reaction is more rapid, and can be accomplished at low temperature (4 °C) within the span of a few hours.²⁶ By comparison, histidine labeling often takes days or weeks, and may require room- or elevated temperature (37 °C).^{27,28} However, the more flexible iodoacetamido linker (cysteine-labeling) results in a photosensitizer-metalloprotein distance that is not fixed, as it is in

direct metal ligation by histidine. For experiments in which knowledge of discrete photosensitizer-protein distance is important, histidine labeling may be advantageous. Additionally, it is important to consider the native amino acid composition of the protein. For example, for large proteins that contain a high number of exposed histidine residues, cysteine labeling is more practical.

The photosensitizer must also provide sufficient driving force to accomplish the desired ET. Varying the metal center and the ligand framework provides a range of driving forces that span over 1 V.²⁹

Absorption (of both photosensitizer and protein) is another key factor. It is desirable to excite the photosensitizer at a wavelength that is not also absorbed by the protein or its cofactors. Protein absorption reduces the number of photons available to excite the photosensitizer; it could cause undesired sample heating as excited protein molecules relax by thermal processes; or (particularly in the case of heme enzymes) it could cause protein photochemistry or luminescence that interfere with observation of the desired ET processes.

Small molecule quenchers

Flash-quench methods require an exogenous small molecule ET quencher (Q). For protein experiments, Q must be water soluble up to millimolar concentrations at mild pH (6-8), and must have an appropriate reduction potential to rapidly (ideally, diffusion limited) oxidize or reduce the photosensitizer.

In addition, the quencher must not have significant absorbance at wavelengths of interest for the photosensitizer-protein system; this is analogous to what was described for protein absorbance. Laser-triggered flash-quench ET process can be probed by transient absorption spectroscopies, therefore it is also desirable that the

quencher not absorb at the probe wavelengths (e.g., the Soret region for heme proteins: 390 – 440 nm).

A final consideration for quencher selection is redox reversibility. In a reversible cycle (such as depicted in **Figure 1.13**), the stable, reduced quencher serves as an electron source to complete the ET cycle and return the system back to its resting state. In an ideal reversible system, the flash-quench cycle can be repeated *ad infinitum*, with no degradation or persistent accumulation of intermediates. Reversibility is most desirable for rapid transient absorption laser studies, in which the averaging of many shots is required to achieve a sufficient signal-to-noise ratio. Alternatively, irreversible quenchers serve as a sacrificial oxidant; this supplies more time for slow reaction events, and allows for accumulation (and detection) of oxidized species. Irreversible quenchers are usually desirable for steady-state flash-quench processes, such as light-driven catalysis. Parameters for three water-soluble ET quenchers are given in **Table 1.2**.

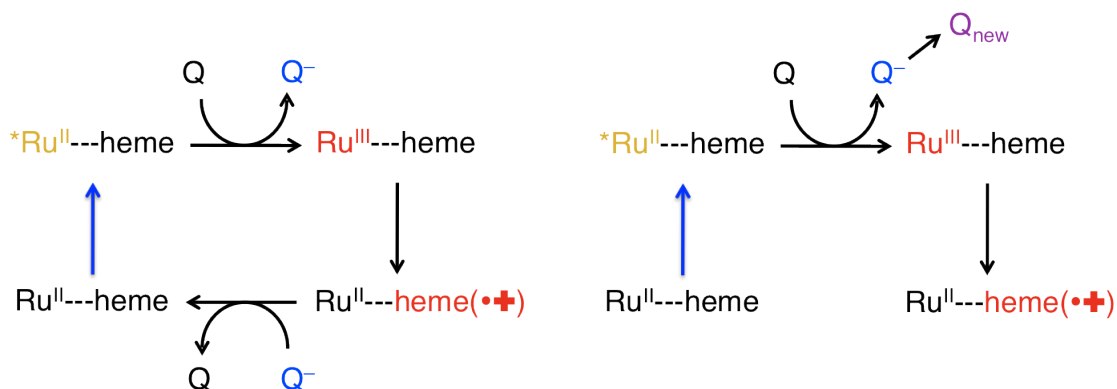


Figure 1.13. Flash-quench ET cycles. Oxidized species are highlighted in red, reduced species in blue. **Left:** Reversible flash-quench ET. **Right:** irreversible flash-quench.

Table 1.2. Parameters for a selection of oxidative quenchers.³⁰⁻³³ Potentials are reported vs. NHE.

Q	$E^\circ(Q/Q^-)$	ϵ (480 nm)	ϵ (400-440 nm)	solubility (pH 7)	reversibility
[Ru(NH ₃) ₆] ³⁺	0 V	<i>negligible</i>	<i>negligible</i>	> 50 mM	reversible
Methyl viologen	-0.45 V	<i>negligible</i>	<i>negligible</i>	> 50 mM	reversible
[Co(NH ₃)Cl] ²⁺	0.29 V	30 M ⁻¹ cm ⁻¹	15-25 M ⁻¹ cm ⁻¹	< 20 mM	irreversible

1.5. Photo-triggered ET in P450: two pathways toward reactive heme species

Photosensitizers and flash-quench can be used in place of native ET partners to generate and investigate the active species CI and CII. Reductive flash-quench supplies the electrons necessary to activate dioxygen (**Figure 1.14**, blue arrows), much more rapidly than the ET with native redox partners. Alternatively, assuming microscopic reversibility of reaction in the catalytic cycle, one could envision a novel pathway in which direct oxidation of the ferric aquo heme (loss of one electron and one proton) generates CII, followed by a second one-electron one-proton oxidation to generate CI (**Figure 1.14**, red arrows). An attractive aspect of this “reverse,” oxidative route is that the oxygen atom in CI, which would be incorporated into substrate, is derived not from dioxygen or reactive oxygen species, but from water. This method was previously implemented to generate CII and CI in histidine-ligated heme enzymes and model systems (vide infra). Inspired by these successes, we began the pursuit of P450 CI using the oxidative route; these experiments are discussed in Chapters 2-4. Reductive ET and associated reactions are discussed in Chapter 5.

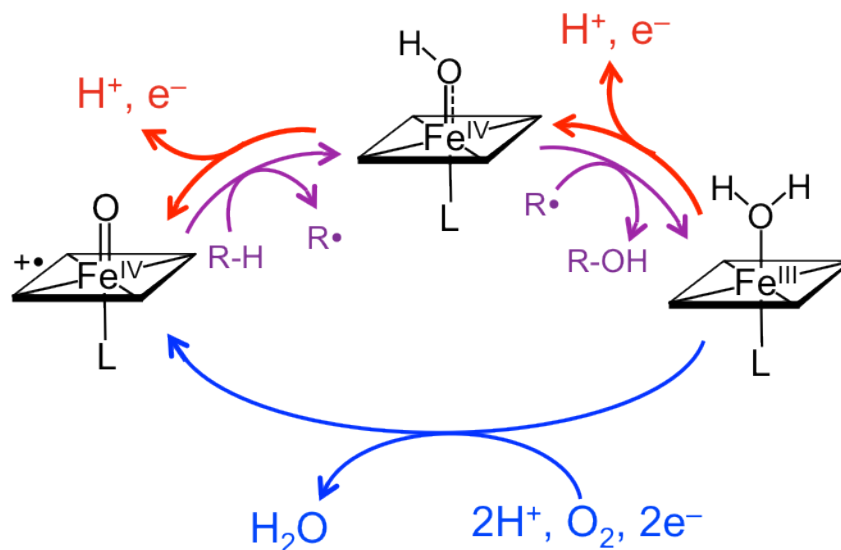


Figure 1.14. Pathways for formation of high valent C1 and C2. Blue arrows: reductive activation of dioxygen (native catalytic cycle). Red arrows: oxidative activation of water. Purple arrows: hydroxylation of substrate (RH).

Precedence for photochemical heme oxidation

Photochemical heme oxidation was first achieved for the model system microperoxidase-8 (MP8), the heme-containing 8-amino acid fragment of horseheart cytochrome *c* (**Figure 1.16**, right). Laser flash-photolysis of a sample composed of [Ru(bpy)₃]²⁺, an excess of [Ru(NH₃)₆]³⁺ as an oxidative quencher, and MP8 resulted in one-electron oxidation of the exposed heme. The position, shape, and intensity of the heme Soret and Q-bands are sensitive to oxidation state and heme environment. C2 formation was observed by a shift to higher energy of the Soret band at pH values above 7. In more acidic solutions, C2 was not produced, but rather an Fe^{III} porphyrin radical cation species was characterized by loss of the Soret absorbance (a “bleach”) (**Figure 1.15**). Analogous flash-quench oxidation was also achieved for the histidine-ligated enzyme horseradish peroxidase (HRP) (**Figure 1.16**, left).

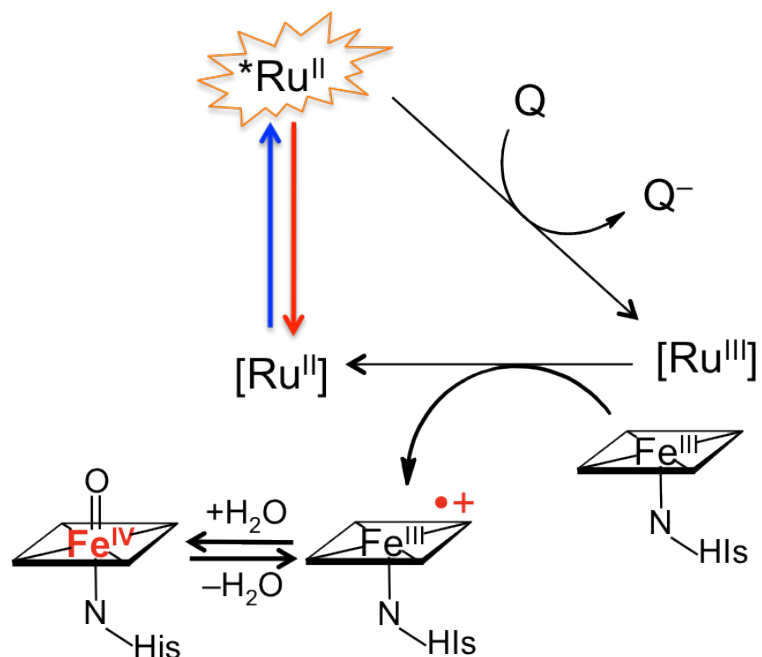


Figure 1.15. Flash-quench oxidation of a heme protein active site. Blue arrow indicates excitation with blue light (e.g., 480 nm), the red arrow indicates emission of red light (e.g., 630 nm).

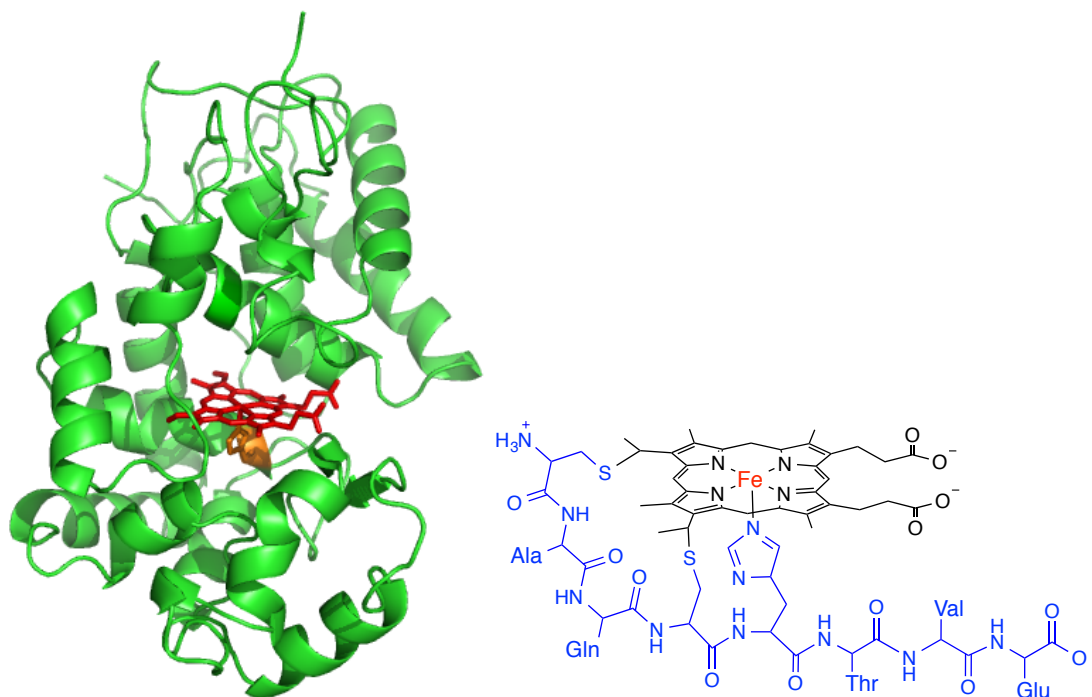


Figure 1.16. Histidine-ligated hemes. **Left:** Horseradish Peroxidase (HRP, PDB: 1HCH). **Right:** Microperoxidase-8 from horseheart cytochrome *c*.

P450 considerations: the buried heme

The analogous use of $[\text{Ru}(\text{bpy})_3]^{2+}$ was unsuccessful for oxidation of the P450 heme, likely due to deep burial of the active site within the protein scaffold. Ruthenium “wires” were synthesized as substrate mimics; rapid flash-quench heme reduction was accomplished using an imidazole-terminated perfluorinated ruthenium wire (**Figure 1.11**).³⁴ However, this method both blocks the substrate channel and displaces the axial water molecule that is necessary for oxidative formation of CII. Covalent tethering of the photosensitizer to the P450 surface has finally enabled the desired oxidative ET (Chapter 2).

1.6. New Frontiers: Novel P450 Active Species for Non-Native Catalysis

Cytochrome P450s offer a seemingly boundless platform in which to design and examine redox catalysis. As described earlier, the catalytic scope of native P450 catalysis is already vast (**Figure 1.5**). With small adjustments from directed evolution and rational design, P450 catalysis can be extended further to include the biodegradation of halocarbons,³⁵ and oxidation of gaseous hydrocarbons.^{36–38} By modifying the surface with photosensitizers, P450 catalysis can even be driven with light.^{39,40} As described in the previous section, the development of photochemical methods may be used to accomplish P450 catalysis by activating water, instead of oxygen or other reactive oxygen species.

However, the extent of catalysis is restricted by the nature of the active species; atom-transfer reactions catalyzed by CI are limited to oxygenation reactions. Development of alternative atom transfer methods would greatly expand utility of P450 catalysts for industrial transformations.

One particularly attractive new reaction target is enzymatic cyclopropanation. The controlled formation of new carbon-carbon bonds is one of the most fundamental challenges in synthetic chemistry. Specifically, generation of the strained cyclopropane motif often requires the formation of two new C–C bonds in a regioselective fashion, as well as control of the stereochemistry at all three carbon centers. Cyclopropanes are found in myriad organic compounds including natural products, pyrethroid insecticides, fragrances, and therapeutics,⁴¹ and the development of cheap, efficient, selective, and sustainable cyclopropanation methods is an active area of research.⁴² The development of enzymatic cyclopropanation routes can take advantage of selectivity imparted by the protein scaffold under mild temperatures and pressures. However, this reactivity requires formation of a novel active species.

Inspiration for P450-catalyzed carbene transfer came from small molecule late transition metal porphyrins (primarily Rh, Fe, Ru, Os), which catalyze the cyclopropanation of alkenes in the presence of diazo carbene precursors.^{43–47} The reaction is thought to proceed via initial formation of a metallo-carbenoid, followed by carbene transfer to the alkene.

Early in 2013, Coelho *et al.* reported carbene transfer from ethyldiazoacetate (EDA) to styrene to form cyclopropanated products catalyzed by cytochrome P450 BM3.⁴⁸ Both wild-type and engineered P450 mutants were capable of catalyzing the reaction, but specific mutants achieved high turnover numbers. In particular, the single T268A mutation was sufficient to raise the turnover number from 5 (wild-type) to 323, with high selectivity for *trans* 1:99 *cis:trans* ratio and 96% enantioselectivity for the *trans* *S,S* diastereomer. Additional mutations to the active site and periphery were used to reverse this *cis:trans* selectivity; the highest

selectivity was reported as 92:8 *cis:trans*, with 97% *S,S* enantioselectivity for the *cis* form.

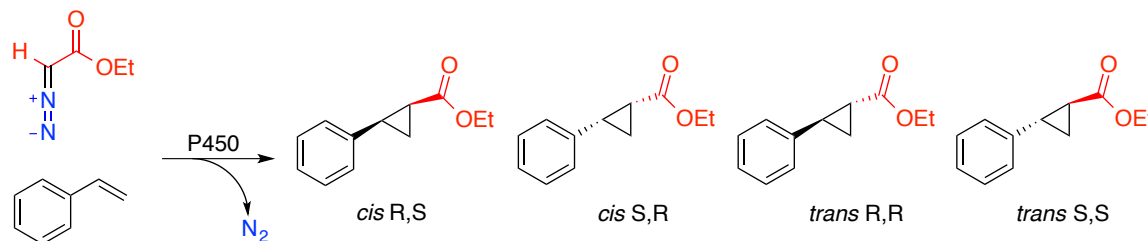


Figure 1.17. P450-catalyzed cyclopropanation of styrene.

In analogy to small molecule metalloporphyrin studies,⁴⁷ the authors proposed a mechanistic scheme that employs a high-valent carbenoid active species (**Figure 1.18, right**).

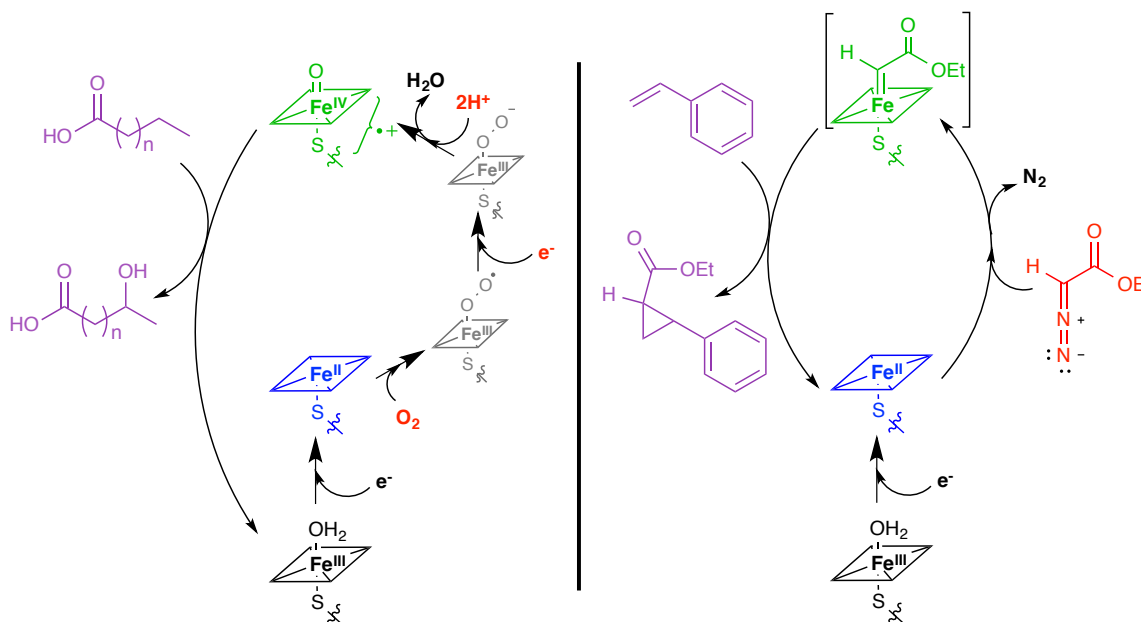


Figure 1.18. Native and engineered P450 catalytic schemes. **Left:** Consensus P450 catalytic cycle for oxygenations, showing hydroxylation of a fatty acid. **Right:** Proposed catalytic scheme for the cyclopropanation of styrene.

Many details of the proposed mechanism have yet to be experimentally verified, including the identity of the active cyclopropanating agent. However, there is

significant evidence that ferrous (not ferric) P450 is required to activate ethyldiazoacetate (EDA). Cyclopropanation activity required the presence of strong reductant, such as dithionite, and the net reaction is inhibited by carbon monoxide, which readily binds to ferrous hemes.⁴⁹

While this in method offers an exquisite proof-of-concept for the development of enzymatic cyclopropanations, the extension of this reactivity to *in vivo* systems would avoid time consuming isolation and purification steps. P450 BM3 is an ideal candidate for such development, as this “self-sufficient” enzyme contains both heme oxygenase and flavin reductase domains fused in a single polypeptide chain. No additional redox partner proteins are required. However, the biological electron source for heme reduction (a critical step for activation of EDA) is NADH. The aforementioned mutants show little to no cyclopropanation activity in the presence of this cofactor.

This observed inactivity is due to a substrate gating mechanism described previously (Section 1.3); styrene binds with low affinity ($K_M \sim 5 \text{ mM}$)⁴⁸ and is inefficient at effecting the low-to-high spin state change. Enzyme engineering to increase the binding affinity might facilitate gating; however, this would need to be achieved for every individual substrate. Incorporation of inert perfluorinated substrate mimics has been implemented to artificially prop the gate open and facilitate oxidation of tiny, ill-binding substrates such as ethane and methane.³⁸ However, use of these decoy molecules *in vitro* is expensive, and implementation for *in vivo* systems has not been established.

Alternatively, the enzyme could be reprogrammed to bypass this substrate gating mechanism by altering the resting state reduction potential. In Chapter 6, we

describe a series of electrochemical experiments that probe electron flow in a new generation of P450 mutants engineered for cyclopropanation.

1.7. Conclusions

Rapid and efficient ET is critical for the formation of the reactive P450 intermediates responsible for catalysis, as well as for their selective functionalization of organic substrates and biological molecules. The remaining Chapters in this Thesis explore the details of photochemical generation of high-valent heme intermediates in ruthenium-P450 conjugates, photochemical heme reduction and gas binding as ways to monitor the native P450 cycle, and electrochemical characterization of P450 axial mutants in relation to cyclopropanation activity.

1.8. References

- (1) Nelson, D. R. Cytochrome P450 Stats
<http://drnelson.uthsc.edu/P450.statsfile.html> (accessed Nov 23, 2013).
- (2) Poulos, T. L.; Finzel, B. C.; Howard, A.J. High Resolution Crystal Structure of Cytochrome P450cam. *J. Mol. Biol.* **1987**, *195*, 687–700.
- (3) Ortiz de Montellano, P. *Cytochrome P450: Structure, Mechanism and Biochemistry*; 3rd ed.; Kluwer Academic/Plenum Publishers: New York, 2005.
- (4) Poulos, T. L.; Johnson, E. F. Structures of Cytochrome P450 Enzymes. In *Cytochrome P450: Structure, Mechanism, and Biochemistry*; Kluwer Academic/Plenum Publishers: New York, 2005.
- (5) Guengerich, F. P. Common and Uncommon Cytochrome P450 Reactions Related to Metabolism and Chemical Toxicity. *Chem. Res. Toxicol.* **2001**, *14*, 611–650.
- (6) Denisov, I. G.; Makris, T. M.; Sligar, S. G.; Schlichting, I. Structure and Chemistry of Cytochrome P450. *Chem. Rev.* **2005**, *105*, 2253–2278.
- (7) Shaik, S.; De Visser, S. P. Computational Approaches to Cytochrome P450 Function. In *Cytochrome P450: Structure, Mechanism, and Biochemistry*; Kluwer Academic/Plenum Publishers: New York, 2005; pp. 45–80.
- (8) Ost, T. W. B.; Miles, C. S.; Munro, A. W.; Murdoch, J.; Reid, G. A.; Chapman, S. K. Phenylalanine 393 Exerts Thermodynamic Control over the Heme of Flavocytochrome P450 BM3. *Biochemistry* **2001**, *40*, 13421–13429.
- (9) Harris, D. C. *Quantitative Chemical Analysis*; 6th Edition.; W. H. Freeman and Company: New York, 2003.
- (10) Dunford, A. J.; Girvan, H. M.; Scrutton, N. S.; Munro, A. W. Probing the Molecular Determinants of Coenzyme Selectivity in the P450 BM3 FAD/NADPH Domain. *Biochim. Biophys. Acta* **2009**, *1794*, 1181–1189.
- (11) Meunier, B.; De Visser, S. P.; Shaik, S. Mechanism of Oxidation Reactions Catalyzed by Cytochrome P450 Enzymes. *Chem. Rev.* **2004**, *104*, 3947–3980.
- (12) Munro, A. W.; Daff, S.; Coggins, J. R.; Lindsay, J. G.; Chapman, S. K. Probing Electron Transfer in Flavocytochrome P-450 BM3 and Its Component Domains. *Eur. J. Biochem.* **1996**, *239*, 403–409.
- (13) Lim, Y.-R.; Eun, C.-Y.; Park, H.-G.; Han, S.; Han, J.-S.; Cho, K. S.; Chun, Y.-J.; Kim, D. Regioselective Oxidation of Lauric Acid by CYP119, an Orphan Cytochrome P450 from *Sulfolobus Acidocaldarius*. *J. Microbiol. Biotechnol.* **2010**, *20*, 574–578.
- (14) Dawson, J. H. Probing Structure-Function Relations in Heme-Containing Oxygenases and Peroxidases. *Science* **1988**, *240*, 433–439.

- (15) Rittle, J.; Green, M. T. Cytochrome P450 Compound I: Capture, Characterization, and C-H Bond Activation Kinetics. *Science* **2010**, *330*, 933–937.
- (16) Krest, C. M.; Onderko, E. L.; Yosca, T. H.; Calixto, J. C.; Karp, R. F.; Livada, J.; Rittle, J.; Green, M. T. Reactive Intermediates in Cytochrome P450 Catalysis. *J. Biol. Chem.* **2013**, *288*, 17074–17081.
- (17) Green, M. T.; Dawson, J. H.; Gray, H. B. Oxoiron(IV) in Chloroperoxidase Compound II Is Basic: Implications for P450 Chemistry. *Science* **2004**, *304*, 1653–1656.
- (18) Yosca, T. H.; Rittle, J.; Krest, C. M.; Onderko, E. L.; Silakov, A.; Calixto, J. C.; Behan, R. K.; Green, M. T. Iron(IV)hydroxide pKa and the Role of Thiolate Ligation in C-H Bond Activation by Cytochrome P450. *Science* **2013**, *15*, 825–829.
- (19) Behan, R. K.; Green, M. T. On the Status of Ferryl Protonation. *J. Inorg. Biochem.* **2006**, *100*, 448–459.
- (20) Sutin, N.; Creutz, C. Properties and Reactivities of the Luminescent Excited States of Polypyridine Complexes of Ruthenium(II) and Osmium(II). In *Inorganic and Organometallic Photochemistry; Advances in Chemistry; American Chemical Society: Washington, DC, 1978; Vol. 1.*
- (21) Creutz, C.; Chou, M.; Netzel, T. L.; Okumura, M.; Sutin, N. Lifetimes, Spectra, and Quenching of the Excited States of Polypyridine Complexes of Iron(II), Ruthenium(II), and Osmium(II). *J. Am. Chem. Soc.* **1980**, *102*, 1309–1319.
- (22) Winkler, J.; Gray, H. Electron Transfer in Ruthenium-Modified Proteins. *Chem. Rev.* **1992**, *92*, 369–379.
- (23) Gray, H. B.; Winkler, J. R. Electron Transfer in Proteins. *Annu. Rev. Biochem.* **1996**, *65*, 537–561.
- (24) Gray, H. B.; Winkler, J. R. Long-Range Electron Transfer. *Proc. Natl. Acad. Sci.* **2005**, *102*, 3534–3539.
- (25) Shih, C.; Museth, A. K.; Abrahamsson, M.; Blanco-Rodríguez, A. M.; Di Bilio, A. J.; Sudhamsu, J.; Crane, B. R.; Ronayne, K. L.; Towrie, M.; Vlček, Jr., A.; Richards, J. H.; Winkler, J. R.; Gray, H. B. Tryptophan-Accelerated Electron Flow Through Proteins. *Science* **2008**, *320*, 1760–1762.
- (26) Ener, M. E.; Lee, Y.-T.; Winkler, J. R.; Gray, H. B.; Cheruzel, L. Photooxidation of Cytochrome P450-BM3. *Proc. Natl. Acad. Sci.* **2010**, *107*, 18783–18786.
- (27) Warren, J. J.; Herrera, N.; Hill, M. G.; Winkler, J. R.; Gray, H. B. Electron Flow through Nitrotyrosinate in *Pseudomonas Aeruginosa* Azurin. *J. Am. Chem. Soc.* **2013**, *135*, 11151–11158.

- (28) Blanco-Rodríguez, A. M.; Busby, M.; Gradinaru, C.; Crane, B. R.; Di Bilio, A. J.; Matousek, P.; Towrie, M.; Leigh, B. S.; Richards, J. H.; Vlček, Jr., A.; Gray, H. B. Excited-State Dynamics of Structurally Characterized [Re(I)(CO)₃(phen)(HisX)]⁺ (X=83, 109) *Pseudomonas Aeruginosa* Azurins in Aqueous Solution. *J. Am. Chem. Soc.* **2006**, *128*, 4365–4370.
- (29) Mines, G. A.; Bjerrum, M. J.; Hill, M. G.; Casimiro, D. R.; Chang, I.-J.; Winkler, J. R.; Gray, H. B. Rates of Heme Oxidation and Reduction in Ru(His33)cytochrome c at Very High Driving Forces. *J. Am. Chem. Soc.* **1996**, *118*, 1961–1965.
- (30) Bard, A. J.; Faulkner, L. R. *Electrochemical Methods. Fundamentals and Applications*; 2nd ed.; John Wiley & Sons, Inc.: New York, 2001.
- (31) Michaelis, L.; Hill, E. S. The Viologen Indicators. *J. Gen Physiol.* **1933**, *16*, 859–873.
- (32) Wardman, P. Reduction Potentials of One-Electron Couples Involving Free-Radicals in Aqueous-Solution. *J. Phys. Chem. Ref. Data* **1989**, *18*, 1637–1755.
- (33) Yamada, A.; Yoshikuni, T.; Kato, Y.; Tanaka, N. A Polarographic Rate Study on the Acid Hydrolysis of Several Halogen Cobalt(III) Complexes. *Bull Chem Soc Jpn* **1980**, *53*, 942–946.
- (34) Dunn, A.; Dmochowski, I.; Winkler, J.; Gray, H. Nanosecond Photoreduction of Cytochrome P450cam by Channel-Specific Ru-Diimine Electron Tunneling Wires. *J. Am. Chem. Soc.* **2003**, *125*, 12450–12456.
- (35) Guengerich, F. P. Cytochrome p450 Enzymes in the Generation of Commercial Products. *Nat. Rev. Drug Discov.* **2002**, *1*, 359–366.
- (36) Meinhold, P.; Peters, M. W.; Chen, M. M. Y.; Takahashi, K.; Arnold, F. H. Direct Conversion of Ethane to Ethanol by Engineered Cytochrome P450 BM3. *ChemBioChem* **2005**, *6*, 1765–1768.
- (37) Xu, F.; Bell, S., G.; Lednik, J.; Insley, A.; Rao, Z.; Wong, L.-L. The Heme Monooxygenase Cytochrome P450cam Can Be Engineered to Oxidize Ethane to Ethanol. *Angew. Chem. Int. Ed.* **2005**, *44*, 4029–4032.
- (38) Kawakami, N.; Shoji, O.; Watanabe, Y. Direct Hydroxylation of Primary Carbons in Small Alkanes by Wild-Type Cytochrome P450BM3 Containing Perfluorocarboxylic Acids as Decoy Molecules. *Chem. Sci.* **2013**, *4*, 2344–2348.
- (39) Tran, N.-H.; Huynh, N.; Bui, T.; Nguyen, Y.; Huynh, P.; Cooper, M. E.; Cheruzel, L. Light-Initiated Hydroxylation of Lauric Acid Using Hybrid P450 BM3 Enzymes. *Chem. Commun.* **2011**, *47*, 11936–11938.
- (40) Tran, N.-H.; Huynh, N.; Chavez, G.; Nguyen, A.; Dwaraknath, S.; Nguyen, T.-A.; Nguyen, M.; Cheruzel, L. A Series of Hybrid P450 BM3 Enzymes with Different Catalytic Activity in the Light-Initiated Hydroxylation of Lauric Acid. *J. Inorg. Biochem.* **2012**, *115*, 50–56.

- (41) Lebel, H.; Marcoux, J.-F.; Molinaro, C.; Charette, A. B. Stereoselective Cyclopropanation Reactions. *Chem. Rev.* **2003**, *103*, 977–1050.
- (42) Chen, D. Y.-K.; Pouwer, R. H.; Richard, J.-A. Recent Advances in the Total Synthesis of Cyclopropane-Containing Natural Products. *Chem. Soc. Rev.* **2012**, *41*, 4631–4642.
- (43) Callot, H. J.; Piechocki, C. Cyclopropanation Using rhodium(III) Porphyrins: Large Cis vs Trans Selectivity. *Tetrahedron Lett.* **1980**, *21*, 3489–3492.
- (44) Callot, H. J.; Piechocki, C. Sterically Crowded Cyclopropanation Catalysts. Syn-Selectivity Using rhodium(III) Porphyrins. *Tetrahedron* **1982**, *38*, 2365–2369.
- (45) Li, Y.; Huang, J.-S.; Xu, G.-B.; Zhu, N.; Zhou, Z.-Y.; Che, C.-M.; Wong, K.-Y. Spectral, Structural, and Electrochemical Properties of Ruthenium Porphyrin Diaryl and Aryl(alkoxycarbonyl) Carbene Complexes: Influence of Carbene Substituents, Porphyrin Substituents, and Trans-Axial Ligands. *Chem. Eur. J.* **2004**, *10*, 3486–3502.
- (46) Smith, D. A.; Reynolds, D. N.; Woo, L. K. Cyclopropanation Catalyzed by Osmium Porphyrin Complexes. *J. Am. Chem. Soc.* **1993**, *115*, 2511–2513.
- (47) Maxwell, J. L.; Brown, K. C.; Bartley, D. W.; Kodadek, T. Mechanism of the Rhodium Porphyrin-Catalyzed Cyclopropanation of Alkenes. *Science* **1992**, *256*, 1544–1547.
- (48) Coelho, P. S.; Brustad, E. M.; Kannan, A.; Arnold, F. H. Olefin Cyclopropanation via Carbene Transfer Catalyzed by Engineered Cytochrome P450 Enzymes. *Science* **2013**, *339*, 307–310.
- (49) Sanders, J. K. M.; Bampos, N.; Clyde-Watson, Z.; Darling, S. L.; Hawley, J. C.; Kim, H.-J.; Mak, C. C.; Webb, S. J. Axial Coordination Chemistry of Metalloporphyrins. *Inorganic, Organometallic and Coordination Chemistry; The Porphyrin Handbook*; Academic Press: San Diego, CA, 2000; Vol. 3, pp. 1–48.

Chapter 2

**PHOTO-TRIGGERED OXIDATION OF
RU-MODIFIED CYTOCHROME P450 BM3**

Portions of this work are excerpted with permission from:

M. E. Ener, Y-T. Lee, J. R. Winkler, H. B. Gray, L. Cheruzel.
Proc. Nat. Acad. Sci. **2010**, *107*, 18783-18786.

Copyright 2010 National Academy of Sciences

2.1. Background: Toward high-valent P450 intermediates

Cytochromes P450 (P450s) catalyze a dazzling array of regio- and stereospecific oxidation reactions, including the hydroxylation of aliphatic and aromatic hydrocarbons and the epoxidation of alkenes.^{1,2} This activity requires the controlled formation of extremely reactive species within the protein framework. In the native catalytic cycle, P450s activate dioxygen with the aid of two electrons from reduced nicotinamide adenine dinucleotide (phosphate) (NAD(P)H); one oxygen atom is delivered to the organic substrate, and the other is released as water.

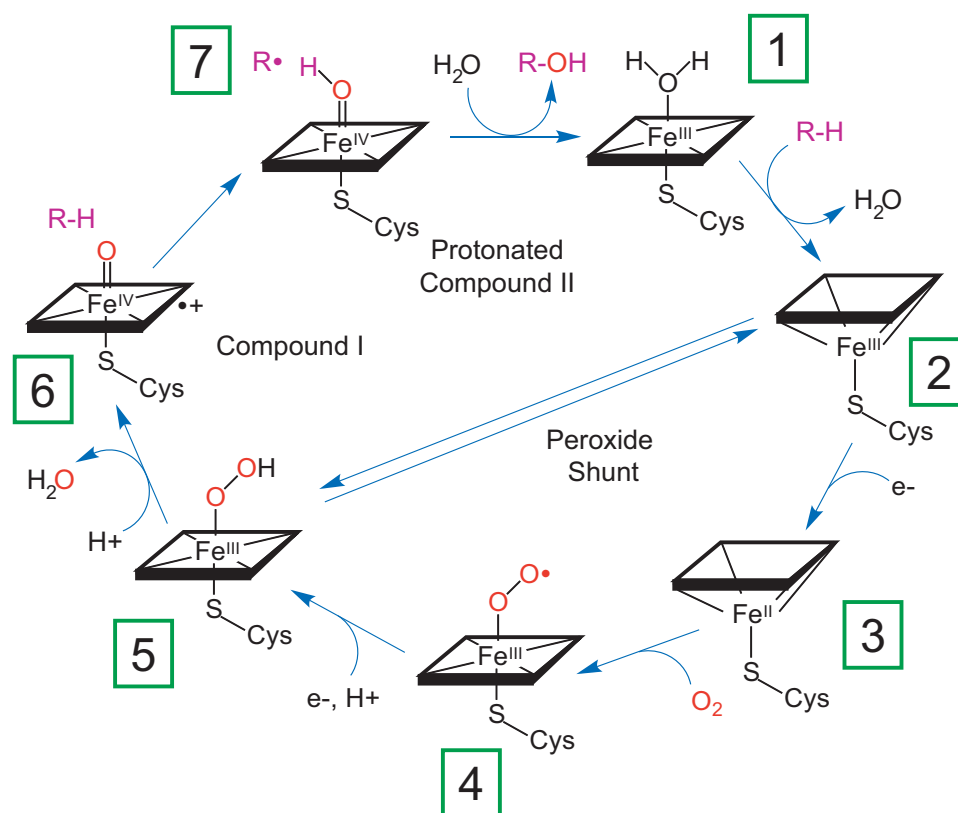


Figure 2.1. Catalytic cycle for P450-catalyzed hydroxylation reactions.

The consensus P450 catalytic cycle (**Figure 2.1**) implicates a ferryl porphyrin radical cation (compound I, **CI**, intermediate 7) as the active oxygenating agent.³ In the postulated mechanism, **CI** abstracts a hydrogen atom from the bound

substrate molecule to form a transient Fe^{IV}-hydroxide complex (compound II, **CII**, intermediate **6**), and radical recombination (or rebound) with the substrate produces oxygenated product.^{4,5} Substrate release from the active site and re-binding of a water molecule regenerates the ferric resting state of the enzyme.

As described in Chapter 1, the elusive high-valent species, **CI** and **CII**, have been the target of decades of time-resolved spectroscopic studies. One intrinsic challenge in their pursuit is that the native electron transfer (ET) events that activate dioxygen are slow,^{6,7} and require the expensive redox cofactor, NADH. One method to circumvent these rate limiting reactions involves direct heme oxidation by oxygen atom donors such as peroxyacids (e.g., *meta*-chloroperoxybenzoic acid, *mCPBA*) or hydrogen peroxide. In 2010, rapid mixing with *mCPBA* was used to generate and trap **CI** in highly purified samples of the thermophilic P450 CYP119 from *Sulfolobus acidocaldarius*.¹⁰ This reactive species was characterized by UV-visible absorption, electron paramagnetic resonance (EPR), and Mössbauer spectroscopies, and was found to be active for hydroxylation of model substrates such as lauric acid. Single-turnover hydroxylation studies yielded an observed second order rate constant of $k_{\text{obs}} = 1.1 \times 10^7 \text{ M}^{-1} \text{ s}^{-1}$.¹⁰

The events of H• abstraction to form **CII**, and subsequent radical-rebound to produce hydroxylated product, have yet to be directly observed. Mechanistic studies of P450 catalysis in cryogenic matrices suggest that the barrier to formation of compound I (**Figure 2.1**, 5→6) is higher than that for its reaction with substrate (6→7→1).¹¹ In order to gain insights into these rapid, reactive processes, new methods must be developed to generate high-valent P450 species on a timescale that is comparable to the rate of reaction with substrate. Experiments in which enzyme oxidation is initiated by rapid mixing of enzyme with a chemical oxidant

or substrate have a dead time of 0.25 ms - 10 ms (e.g., for a Bio-Logic® SFM-400 stopped-flow). This timescale may be too slow to observe the fundamental bond-breaking and bond-making events of interest.

Photo-triggered methods provide a faster way to initiate reactions, with extremely high temporal resolution. Electronic transitions (including photo-induced excitation) are essentially instantaneous on the timescale of molecular motions. The dead time for monitoring a laser-triggered photochemical event is only limited by the temporal length of a laser pulse or the instrument response (~20 ns for the setup described herein, see Appendix B). The Gray laboratory has a long history of photo-initiating ET in proteins using inorganic photosensitizers, including ruthenium diimines and rhenium tricarbonyl complexes. Curious readers are directed toward a number of excellent reviews for further details.¹²⁻¹⁴

A flash-quench cycle elicits ET with protein redox cofactors. In this method, a laser pulse generates a reactive, electronic excited state (**Figure 2.2**). Interaction of excited state with exogenous small molecule quenchers results in electron transfer quenching to generate a more oxidized photosensitizer species. The charge separation accomplished by the bimolecular ET increases the lifetime of the reactive photosensitizer, and provides additional driving force. For example, ~500 mV of potential is gained by reversible, oxidative quenching of $[\text{Ru}(\text{bpy})_3]^{2+}$ (E° vs. NHE in water: $\text{Ru}^{\text{III/II}} = 1.3 \text{ V}$; $\text{Ru}^{*\text{II/I}} = 0.8 \text{ V}$), and the lifetime is increased from ~600 ns to nearly 100 μs .^{17,18}

In earlier work, $[\text{Ru}(\text{bpy})_3]^{2+}$ (bpy = 2,2'-bipyridine) was employed in a bimolecular flash-quench photochemical oxidation procedure to generate **CII** and **CI** in the heme enzyme horseradish peroxidase (HRP) and in the “minienzyme” microperoxidase-8 (MP8), a heme-containing, 8-amino acid fragment from

cytochrome *c*.^{15,16} By oxidizing the active site directly, this route avoids the use of dioxygen or reactive oxygen species entirely. Instead, the high-valent ferryl species, which can incorporate an oxygen atom into substrate, is generated by oxidation of a water molecule that ligates the heme in the Fe^{III} resting state.

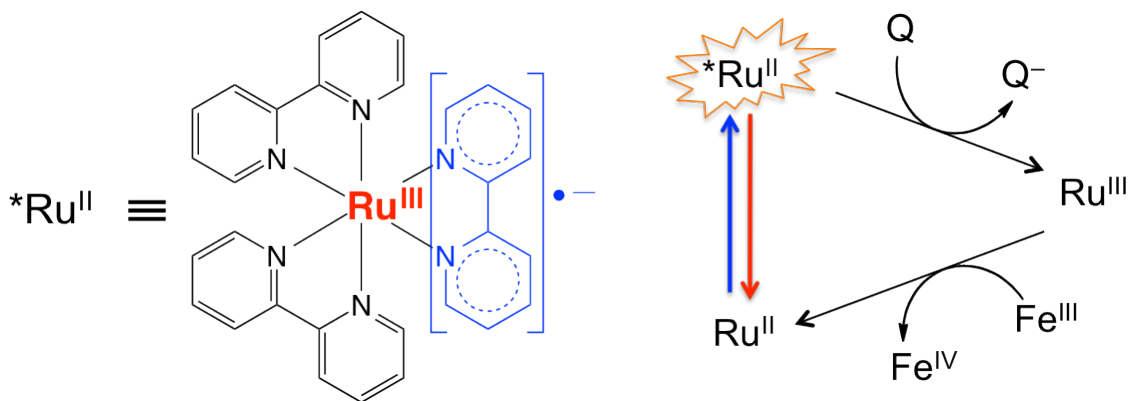


Figure 2.2. $[Ru^{II}(bpy)_3]^{2+}$ flash-quench and oxidation of the a heme protein active site.

The approach of employing $[Ru(bpy)_3]^{2+}$ in solution was unsuccessful with P450, however, owing to the deep burial of the heme active site inside the polypeptide matrix of the enzyme. We circumvented this problem by covalently attaching the photosensitizer to the P450 surface. This has allowed us to successfully laser-trigger photochemical heme oxidation in a Ru-P450 system, monitor the kinetics of electron transfer using transient absorption (TA) spectroscopy, and extract kinetics parameters for the rate of heme oxidation. The details of photosensitizer-attachment, crystallographic characterization, laser-triggered heme oxidation, and kinetics modeling are discussed in this Chapter.

2.2. Motivation and selection of the photochemical system

Photosensitizer

As described in Chapter 1, the Gray laboratory has used a variety of photosensitizers for triggering ET in proteins, and selective tethering at histidine or cysteine can be achieved. The heme domain of P450 BM3 contains 13 native histidines, but only three native cysteines, one of which provides proximal ligation for the heme. We have selected cysteine-labeling, using a ruthenium(II) bis-bipyridine iodoacetamidophenanthroline $[\text{Ru}(\text{bpy})_2(\text{IAphen})]^{2+}$ complex (**Figure 2.3**) that can be readily synthesized by published procedures.¹⁹ This photosensitizer is excited in the blue-green region of the visible spectrum, has a long excited state lifetime in deoxygenated water (900 ns),¹⁹ and, when oxidized to Ru^{III} by flash-quench, has a sufficiently high reduction potential to oxidize the enzymatic active site (~ 1.3 V vs. NHE).¹⁷

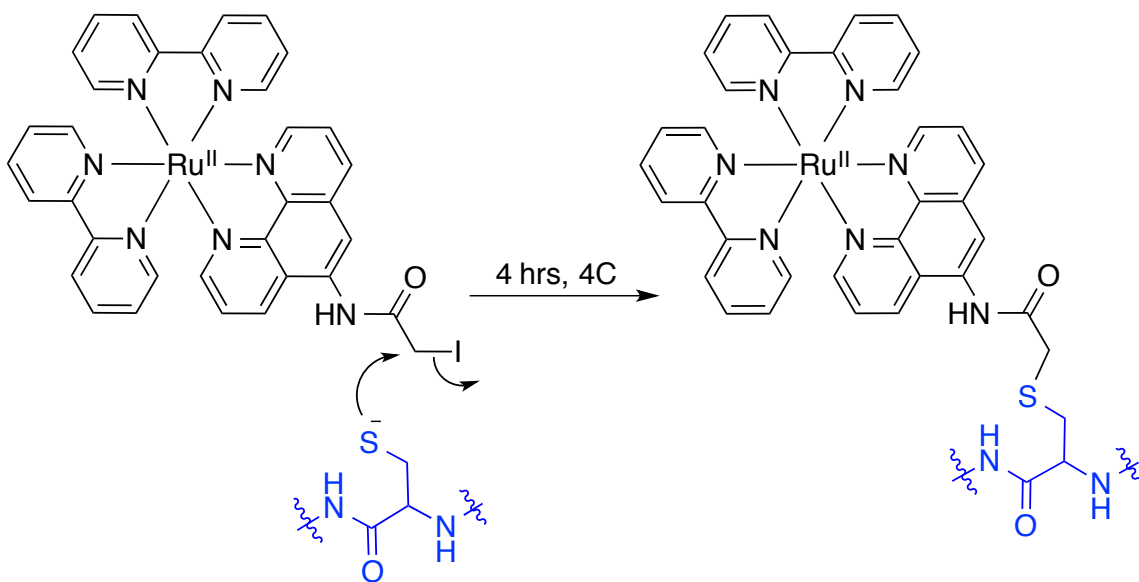


Figure 2.3. $[\text{Ru}(\text{bpy})_2(\text{IAphen})]^{2+}$ tethering to cysteine, to form the conjugate Cys- $\text{Ru}(\text{bpy})_2(\text{Aphen})$.

Exogenous Oxidative Quencher

We have selected ruthenium(III) hexaamine trichloride as a reversible, exogenous oxidative quencher. This complex is water soluble (> 50 mM, $\text{pH} \leq 8$), has little or no absorbance in the regions of interest (390-500 nm), and undergoes rapid electron transfer with ruthenium diimine photosensitizers (vide infra). Some care must be taken to avoid decomposition: at high pH (> 8) and/or temperature (> 50 °C), $[\text{Ru}(\text{NH}_3)_6]^{3+}$ decomposes and turns deep purple/black. In solutions of low ionic strength, this complex may also cause protein precipitation (observed for P450 and Nitric Oxide Synthase); this can be avoided by using protein solutions that contain 100-200 mM NaCl.

We also attempted use of methyl viologen (dichloride salt) and chlorocobalt(III)pentaamine (dichloride salt). Upon irradiation (e.g., laser flash-quench transient absorption studies), both of these quenchers caused Ru-P450 sample degradation as observed by permanent bleaching of the P450 Soret (see Appendix C). Therefore, all of the studies described in this Chapter use $[\text{Ru}(\text{NH}_3)_6]\text{Cl}_3$ as the oxidative quencher.

P450 Mutants

To achieve selective surface modification with the photosensitizer, we used site directed mutagenesis to remove two native cysteine residues (C62A, C156S) from the P450 BM3 heme domain. These two mutations had been made previously in order to achieve specific attachment at a non-native cysteine for photochemical and electrochemical methods.^{20,21} The resulting double-mutants are stable and active toward oxidation of fatty acids (e.g., palmitate and laurate) in the presence of oxygen donors (e.g., hydrogen peroxide or mCPBA). For our purposes, a single cysteine was introduced at residue 97 (K97C). This position was chosen by former

Gray group postdoctoral fellow, Lionel Cheruzel, for surface-exposure and proximity to the heme. The cysteine C α to heme iron distance is 16.8 Å (**Figure 2.4**). Additionally, residue 97 is directly adjacent to Trp96, which lies within hydrogen-bonding contact of one of the heme propionates. The role of this intervening residue will be further explored in Chapters 3 and 4.

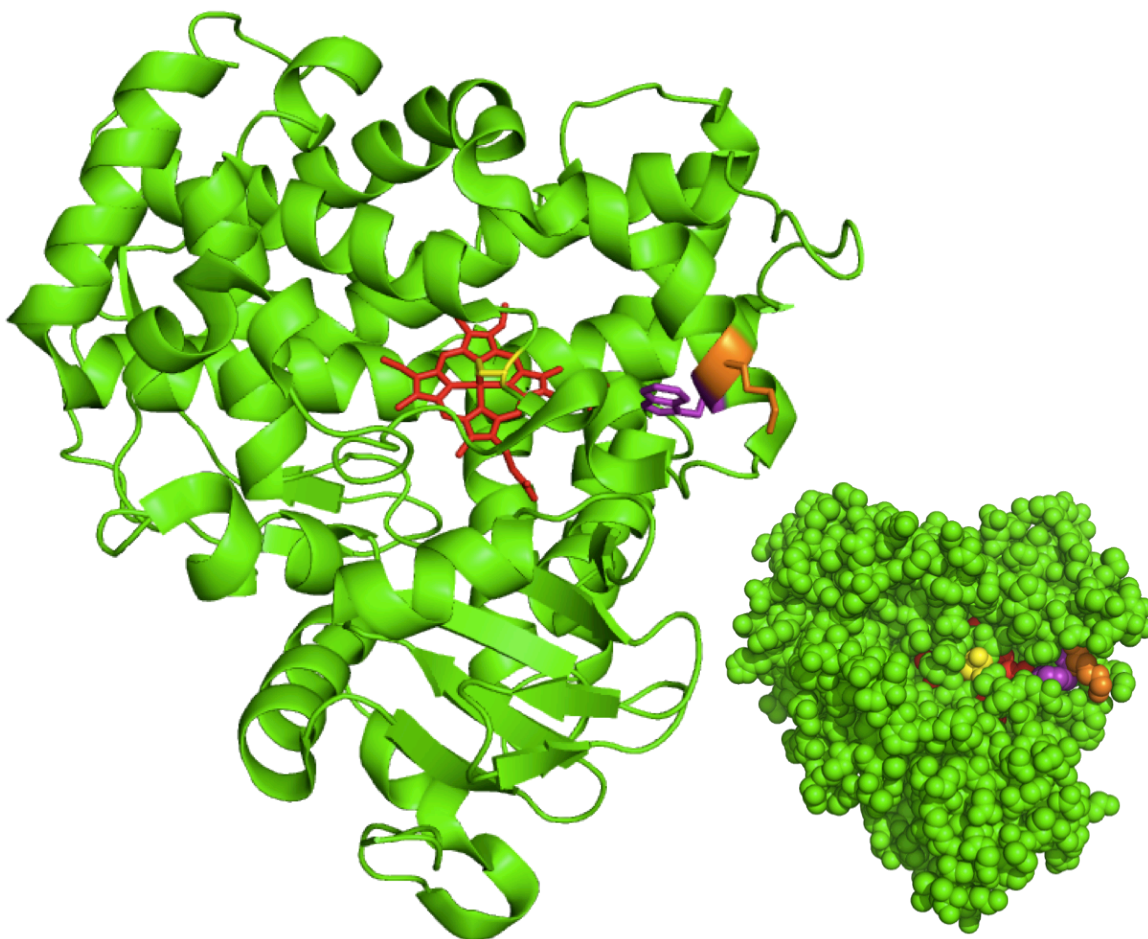


Figure 2.4. K97 labeling site. **Left:** Structure of the P450 BM3 heme domain from the proximal face (pdb 2IJ2) highlighting the heme (red), axial ligand C400 (yellow), W96 (purple), and K97 (orange). **Right:** Space-filling model illustrating surface exposure of K97 (orange). (Figures made with PyMol, 2009)

2.3. Results

2.3.1. Characterization

The Ru^{II}(bpy)₂(Aphen)-P450(BM3)C62A/C156S/K97C conjugate (abbreviated Ru^{II}_{K97C}-P450_{BM3}) has been characterized by ultraviolet-visible absorbance (UV-vis), X-ray diffraction, and steady state and time-resolved fluorometry. The mass of the conjugate (54,200 Da) corresponds to that of the apo (heme-free) unlabeled protein (53,520 Da) plus the ruthenium photosensitizer (777 Da), minus the mass of iodide.

UV-visible absorbance

The triple-mutant P450 BM3 C62A/C156S/K97C has characteristic absorption features that are almost identical to wild-type: a Soret band at 418 nm, a near UV band at 360 nm, and Q-bands at 536 and 569 nm. The Ru_{K97C}-P450_{BM3} conjugate has an additional shoulder at 450 nm, due to the characteristic ruthenium diimine MLCT absorbance (**Figure 2.5**).

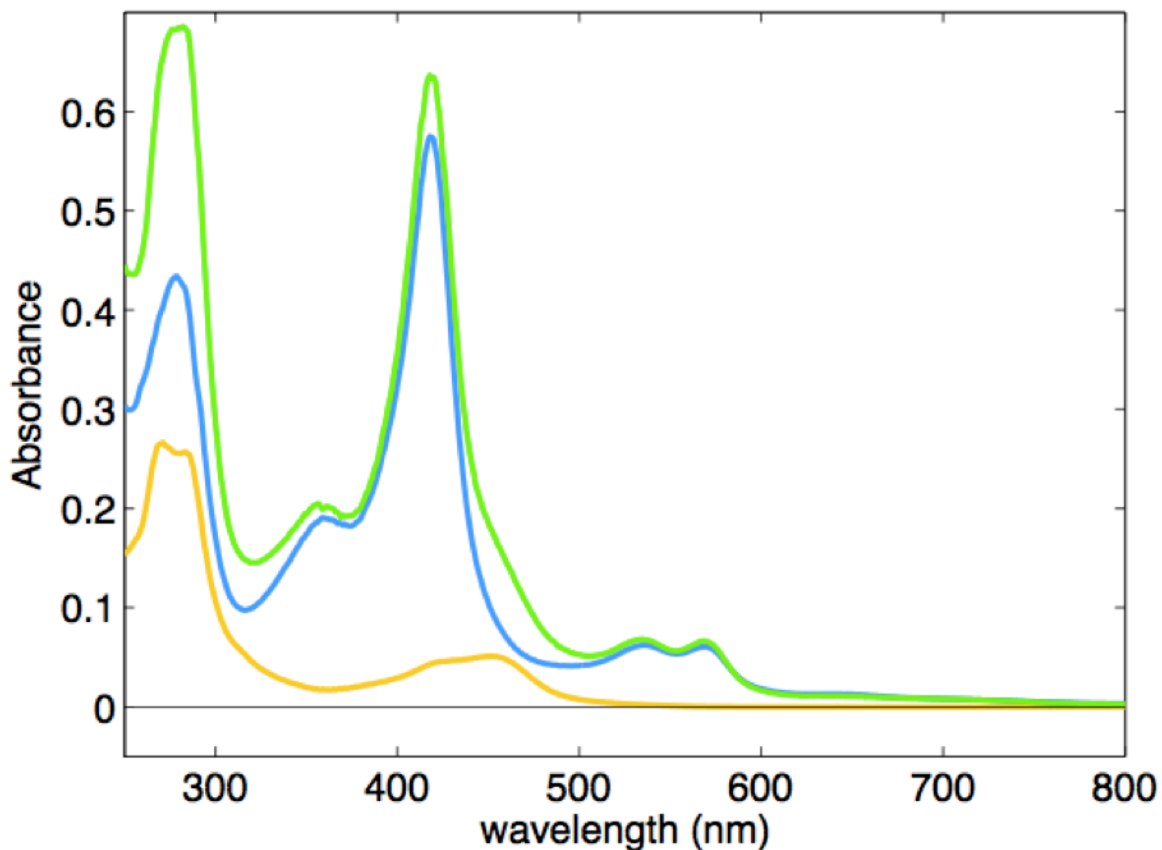


Figure 2.5. Absorption spectra of $[\text{Ru}(\text{bpy})_2(\text{IAphen})]^{2+}$ (yellow), P450-BM3 C62A/C156S/K97C (blue), $\text{Ru}_{\text{K97C}}\text{-P450}_{\text{BM3}}$ (green), at approximately equal concentrations.

Steady-state Luminescence

The free photosensitizer $[\text{Ru}(\text{bpy})_2(\text{Aphen})]^{2+}$ and $\text{Ru}_{\text{K97C}}^{\text{II}}\text{-Fe}_{\text{P450}}^{\text{III}}$ conjugate have been examined by steady-state luminescence spectroscopy. When excited with blue light (e.g., 480 nm), both samples show a broad luminescence band in the red region of the visible spectrum, with $\lambda_{\text{max}} = 620$ nm. The steady-state spectra of $[\text{Ru}(\text{bpy})_2(\text{Aphen})]^{2+}$ and $\text{Ru}_{\text{K97C}}^{\text{II}}\text{-Fe}_{\text{P450}}^{\text{III}}$ are nearly superimposable, and very closely resemble that of $[\text{Ru}(\text{bpy})_3]^{2+}$ ($\lambda_{\text{max}} = 626$ nm) (**Figure 2.6**). Un-labeled P450 is not luminescent in the visible region.

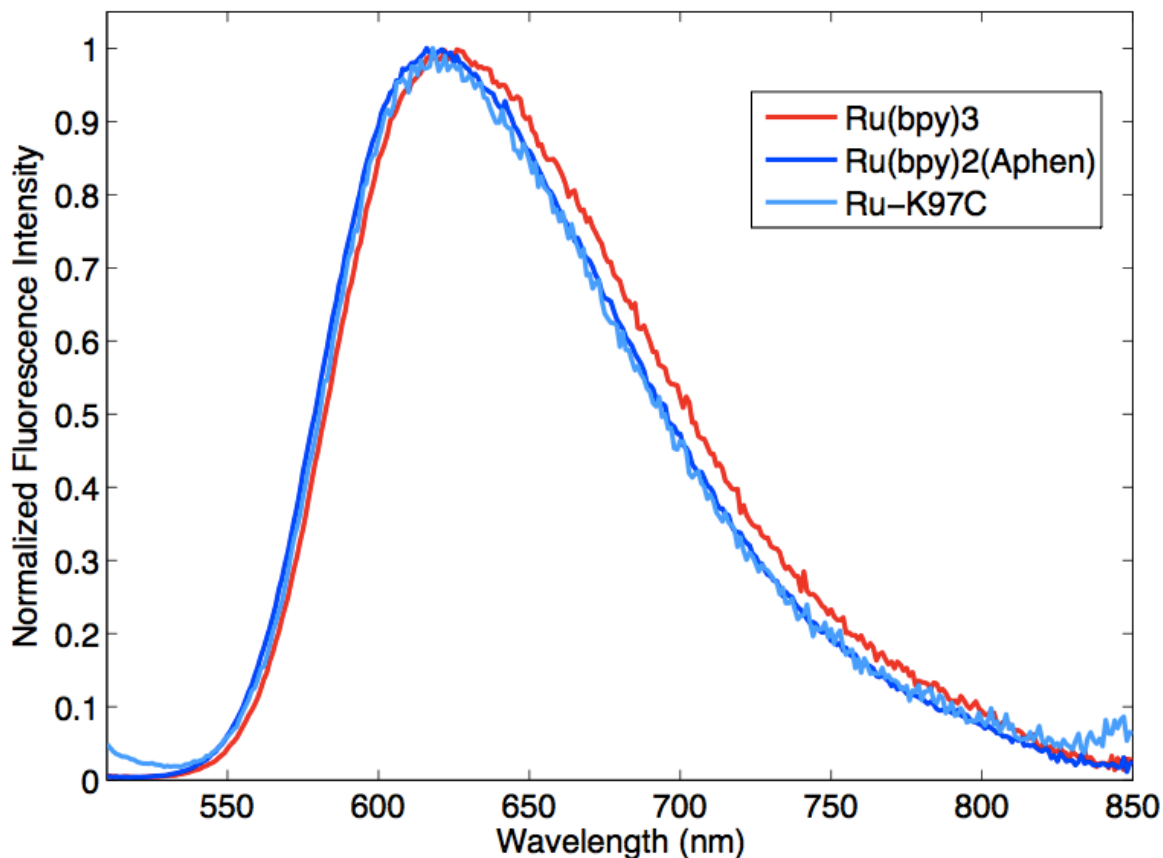


Figure 2.6. Steady-state luminescence spectra of Ru photosensitizers in deoxygenated water. $[\text{Ru}^{\text{II}}(\text{bpy})_3]^{2+}$ (red), free photosensitizer $[\text{Ru}^{\text{II}}(\text{bpy})_2(\text{Aphen})]^{2+}$ (dark blue), and conjugate $\text{Ru}^{\text{II}}_{\text{K97C}}\text{-Fe}^{\text{III}}_{\text{P450}}$ (light blue).

X-ray Crystal Structure Analysis

We have determined the X-ray crystal structure of $\text{Ru}^{\text{II}}_{\text{K97C}}\text{-Fe}^{\text{III}}_{\text{P450}}$ to 2.4-Å resolution (**Figure 2.7**). Two monomers were found in the asymmetric unit; the root-mean-squared deviation (rmsd) between the $\text{C}\alpha$ atom positions in the two monomers is 0.34 Å, confirming that the two polypeptides have nearly identical conformations. Interestingly, the substrate channel is occupied by two unidentified electron density peaks. Additionally, the structure of $\text{Ru}^{\text{II}}_{\text{K97C}}\text{-Fe}^{\text{III}}_{\text{P450}}$ more closely resembles that of the substrate-bound (closed) P450-BM3 enzyme (rmsd of 0.44 Å for $\text{C}\alpha$ with the structure 2UWH²²), in which the F and G helices (known as the

“lid domain”) contract inward toward the heme.²³ In contrast, the substrate-free (open) form overlays with an rmsd of 0.66 Å (for the structure 2IJ2²⁴) (**Figure 2.7**).

Table 2.1. X-ray crystallographic data collection, refinement statistics, and validation.

Data collection	
Wavelength, Å	0.979
Unit cell, Å	117.08, 117.08, 273.85
Space group	P41212
Resolution range, Å	45.52–2.40 (2.53–2.40)*
No. of total reflections	793,591
No. of unique reflections	74,965
Completeness, %	99.7 (99.6)
R_{merge} , %	12.6 (82.7)
$\langle I/\sigma(I) \rangle$	15.4 (4.2)
Wilson B-value, Å ²	45.6
Refinement statistics	
Resolution range, Å	10–2.4
No. of reflections used	69,343
Free R reflections, %	5.0
R/R_{free}	0.200/0.237
rmsd bond length, Å	0.0113
rmsd bond angle, deg	1.374
Ramachandran analysis, %	
No. of residues in	
Favored regions	97.4
Allowed regions	2.6
Outlier regions	0.0
PDB entry	3NPL

*Data for the outermost shell are given in parentheses.

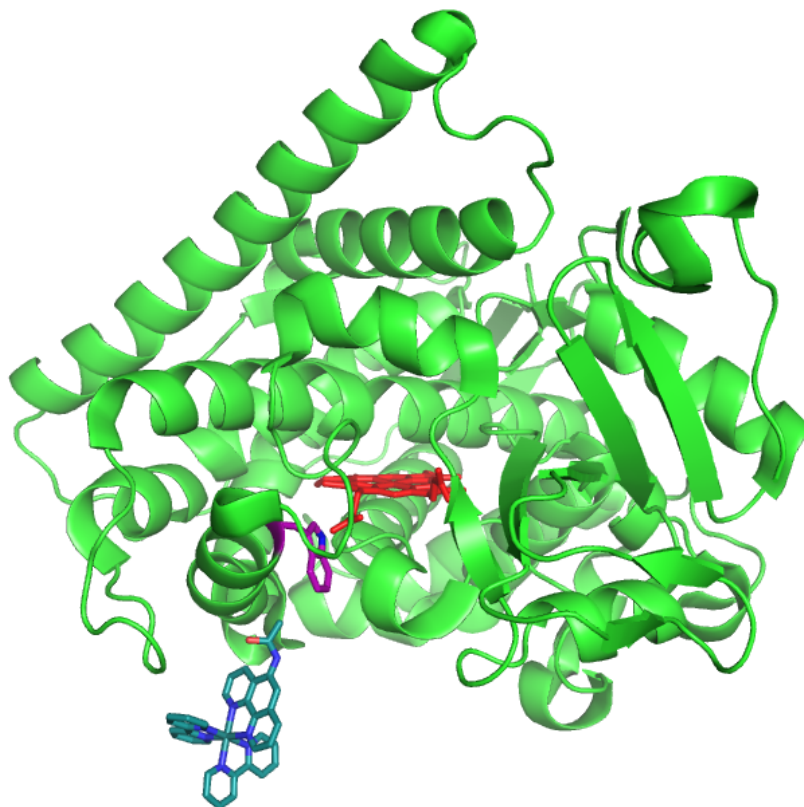


Figure 2.7. The $\text{Ru}_{\text{K97C}}\text{-P450}_{\text{BM3}}$ structure. (PDB: 3NPL) $\text{Ru}^{\text{II}}(\text{bpy})_2(\text{Aphen})$ photosensitizer is colored blue, the heme is colored red and tryptophan96 is colored purple.

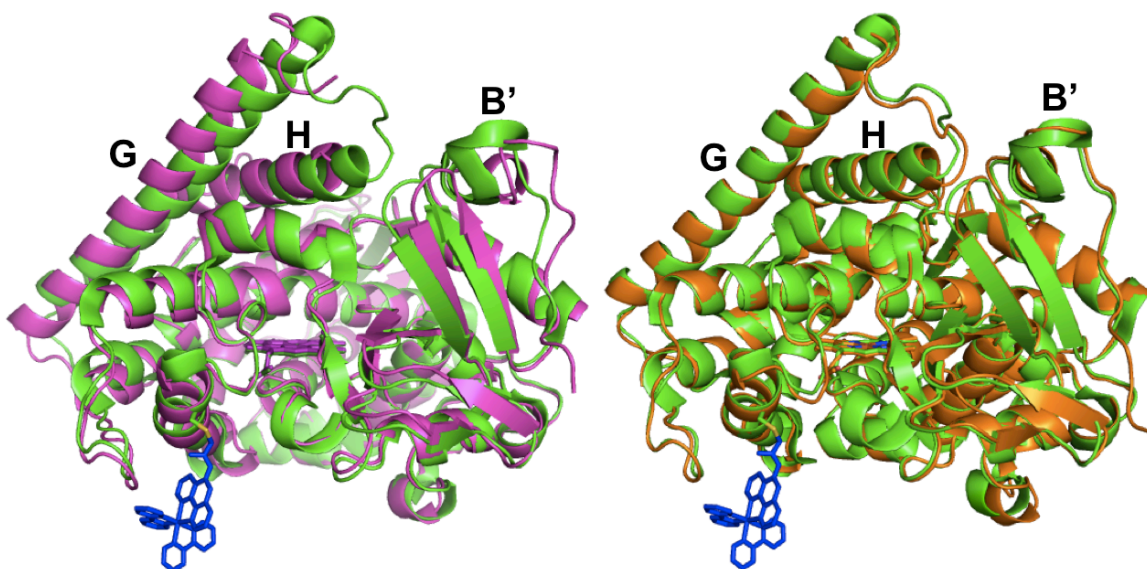


Figure 2.8. Overlay of $\text{Ru}_{\text{K97C}}\text{-P450}_{\text{BM3}}$ with wild type substrate-free and substrate-bound forms. **Left:** Substrate-free (open) form (pink, PDB: 2IJ2), RMS 0.662. **Right:** Substrate-bound (closed) form (orange, PDB: 2UWH) RMS 0.440.

The Ru-photosensitizer is well defined in only one monomer of the crystal structure, owing to π -stacking of the bipyridine ligands with aromatic residues on adjacent crystal units (**Figure 2.9**). The distance between the Fe-heme and Ru-photosensitizer is 24 Å.

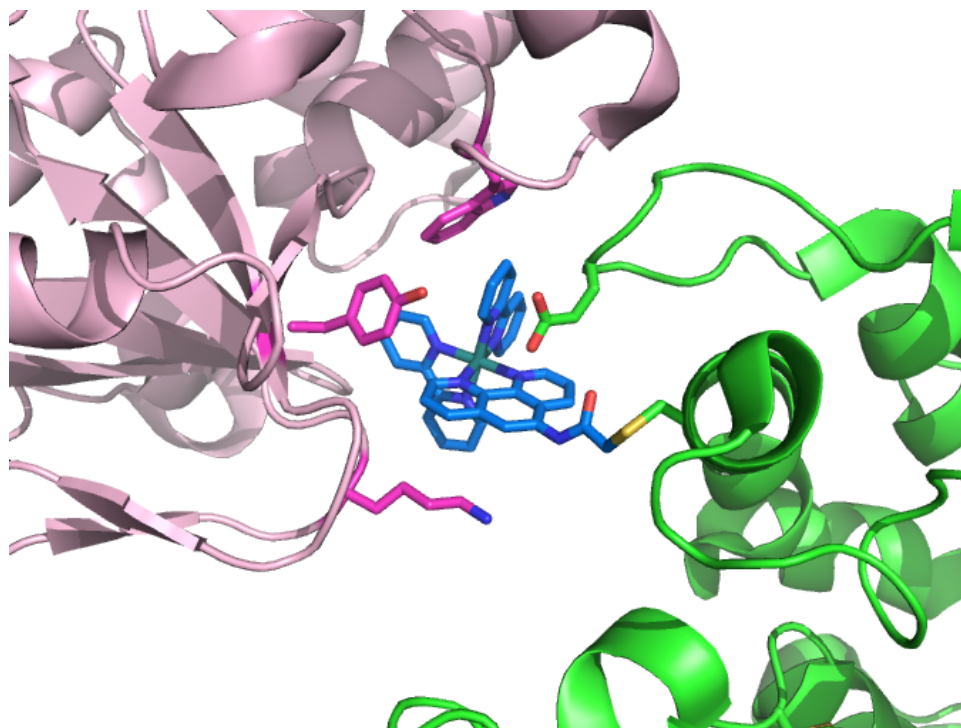


Figure 2.9. Stacking of Ru_{K97C}-P450_{BM3} with an adjacent crystal unit. P450: green, photosensitizer: blue. Adjacent crystal unit: pink. Trp90 and Tyr344 edge-to-edge distances of 3.5-4.5 Å with the two bipyridine ligands. Glu 244 stacks beneath one of the bipyridine ligands, within 3.5 Å of the plane of the phenanthroline ligand.

The Ru-photosensitizer in the second monomer, which lacks the π -stacking interactions with neighboring protein molecules, is highly disordered. This is probably due to flexibility of the cysteine-acetamide linkage. These observations suggest conformational freedom for the Ru-photosensitizer. The 24-Å Ru-Fe distance is likely near the maximum separation in the distribution of conformations sampled by the Ru complex in dilute Ru^{II}_{K97C}-Fe^{III}_{P450} solutions

since the ligands of the photosensitizer may form favorable hydrophobic with amino acid residues on the protein surface, decreasing the Fe-Ru separation.

2.3.2. Laser flash-quench experiments

In order to examine photo-triggered ET in a time-resolved manner, laser samples were prepared under inert atmosphere with either the Ru^{II}_{K97C}-Fe^{III}_{P450} conjugate or the free photosensitizer ([Ru(bpy)₂(Aphen)]²⁺) in the presence or absence of exogenous quencher. Formation of the ferryl species from the ferric aquo resting state requires loss of protons, and we anticipated that the photo-triggered ET reaction would be pH dependent. Samples were prepared in buffers: 20 mM sodium acetate (pH 6, 7), 50 mM tris or 50 mM sodium borate (pH 8).

Time-resolved luminescence

The excited state luminescence decays of both [Ru(bpy)₃]²⁺ and the free photosensitizer [Ru(bpy)₂(IAphen)]²⁺ are monoexponential; $\tau(*[Ru(bpy)_2(IAphen)]^{2+})$ is 720 ns. Somewhat unexpectedly, the time-resolved luminescence decay of Ru^{II}_{K97C}-Fe^{III}_{P450} ($\lambda_{obsd} = 630$ nm) is biexponential, with components of $\tau_1(*Ru^{II}_{K97C}-Fe^{III}_{P450}) = 670$ ns, $\tau_2(*Ru^{II}_{K97C}-Fe^{III}_{P450}) = 140$ ns (**Figure 2.10**). This biexponential nature of the Ru^{II}_{K97C}-Fe^{III}_{P450} decay does not appear to be affected by protein concentration over a range of 1-20 μ M (see Appendix C). This suggests that a monomer-dimer equilibrium is not the cause of this biexponential behavior. We attribute these two exponential components to two separate conformations of the tethered photosensitizer conformations that do not exchange on the timescale of the luminescence measurement. The disorder present in the crystal structure supports the possibility of multiple conformations, but we do not have sufficient information to speculate on their exact identities.

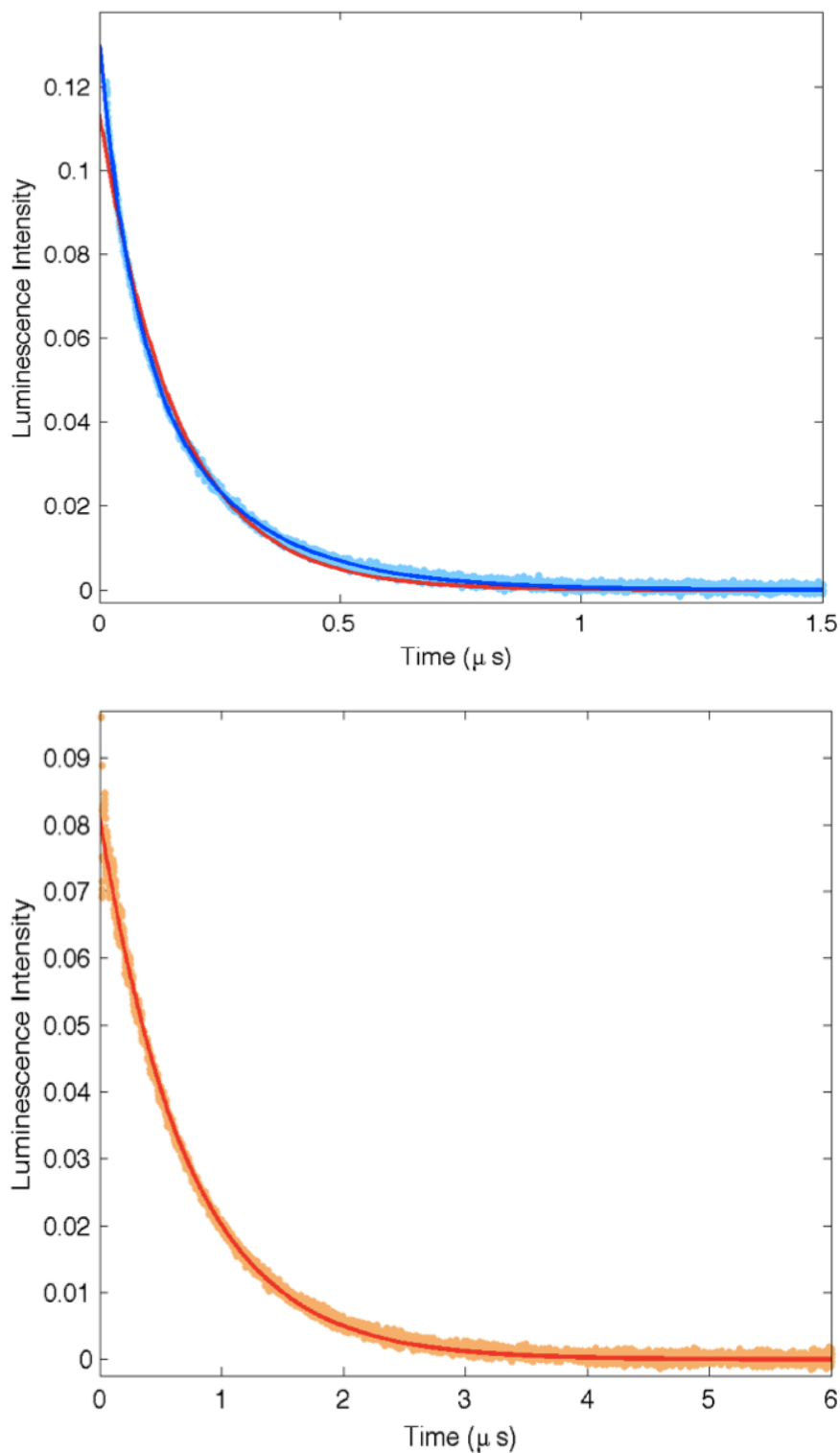


Figure 2.10. Time resolved 630 nm luminescence decays in the absence of quencher. **Top:** Ru^{II}_{K97C}-Fe^{III}_{P450} (cyan), and **Bottom:** [Ru^{II}(bpy)₂(IAphen)]²⁺ (orange). Monoexponential fits are in red, biexponential fit (Ru^{II}_{K97C}-Fe^{III}_{P450} only) is in blue.

In the presence of the exogenous electron transfer quencher, $[\text{Ru}(\text{NH}_3)_6]\text{Cl}_3$, luminescence lifetimes decrease. The lifetimes in the presence of quencher appear to be more monoexponential, and approximate rate constants are extracted using a monoexponential fit. Stern-Volmer analysis of $^*\text{Ru}^{\text{II}}_{\text{K97C}}\text{-Fe}^{\text{III}}_{\text{P450}}$ luminescence decay in the presence of various $[\text{Ru}(\text{NH}_3)_6]^{3+}$ concentrations (**Figure 2.11**) produces a bimolecular quenching rate constant (k_q) of $1.4 \times 10^9 \text{ M}^{-1} \text{ s}^{-1}$ (pH 8); this is close to diffusion limited (**Figure 2.12**).

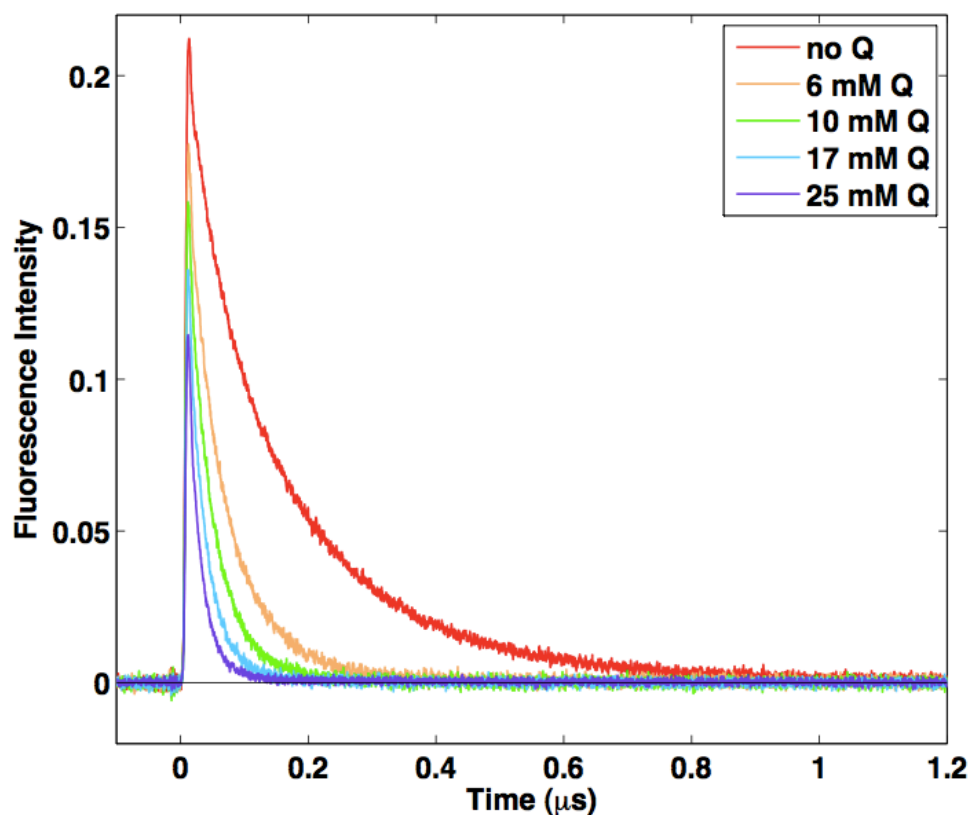


Figure 2.11. Luminescence decays of $\text{Ru}_{\text{K97C}}\text{-P450}_{\text{BM3}}$ (pH 8) at various concentrations of $[\text{Ru}(\text{NH}_3)_6]^{3+}$ quencher.

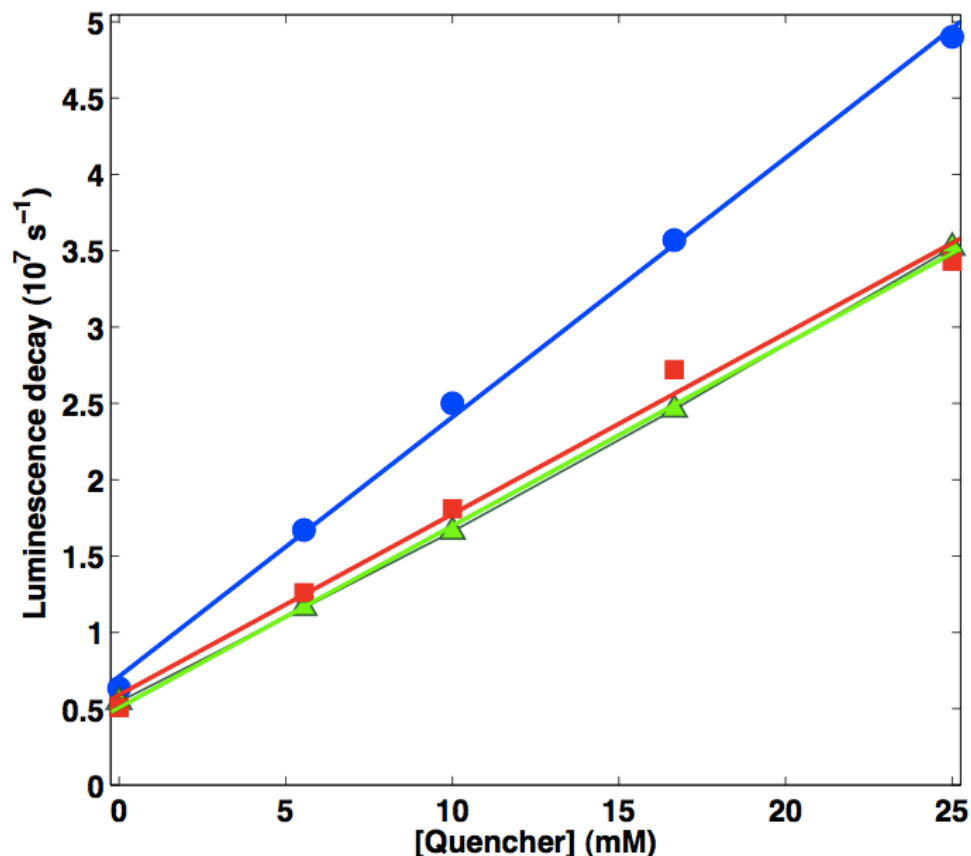


Figure 2.12. Stern-Volmer quenching of Ru_{K97C}-P450_{BM3} with [Ru(NH₃)₆]³⁺ at three pH values. Luminescence decay rates are determined from monoexponential fits. pH 8 borate buffer (blue circles), pH 7 sodium acetate buffer (green triangles), pH 6 sodium acetate buffer (red squares).

Transient absorption

Both the Ru photosensitizer and P450 heme have strong electronic absorbance in the 390-440 nm region: P450 Soret $\epsilon(\lambda_{\text{max}}: 418 \text{ nm}) = 95,000 \text{ M}^{-1}\text{cm}^{-1}$; ⁷ [Ru(bpy)₂(Aphen)]²⁺ $\epsilon(\lambda_{\text{max}}: 450 \text{ nm}) = 16,600 \text{ M}^{-1}\text{cm}^{-1}$.¹⁹ The shapes and positions of these electronic transitions are sensitive to metal oxidation state and environment; each species has a distinct absorption profile. By monitoring multiple wavelengths (390-440 nm) over time, we can identify the formation and decay of ET intermediates following laser excitation. This process is greatly

facilitated by control studies (e.g., the absence of quencher, or the free photosensitizer), as well as comparison to absorption profiles in the literature.

In the absence of exogenous quencher, TA traces of $[\text{Ru}(\text{bpy})_2(\text{Aphen})]^{2+}$ and $\text{Ru}^{\text{II}}_{\text{K97C}}\text{-Fe}^{\text{III}}_{\text{P450}}$ following excitation ($\lambda_{\text{ex}} = 480 \text{ nm}$) are essentially identical. Data at all wavelengths reveal bleaching ($\Delta Abs < 0$) from 390-440 nm, consistent with the well-characterized behavior of metal-to-ligand charge-transfer (MLCT) excited Ru-diimine complexes.¹⁷ The transient signals returns to baseline at the same rate as luminescence decays, and we find no evidence for the formation of additional transient species (**Figure 2.13**).

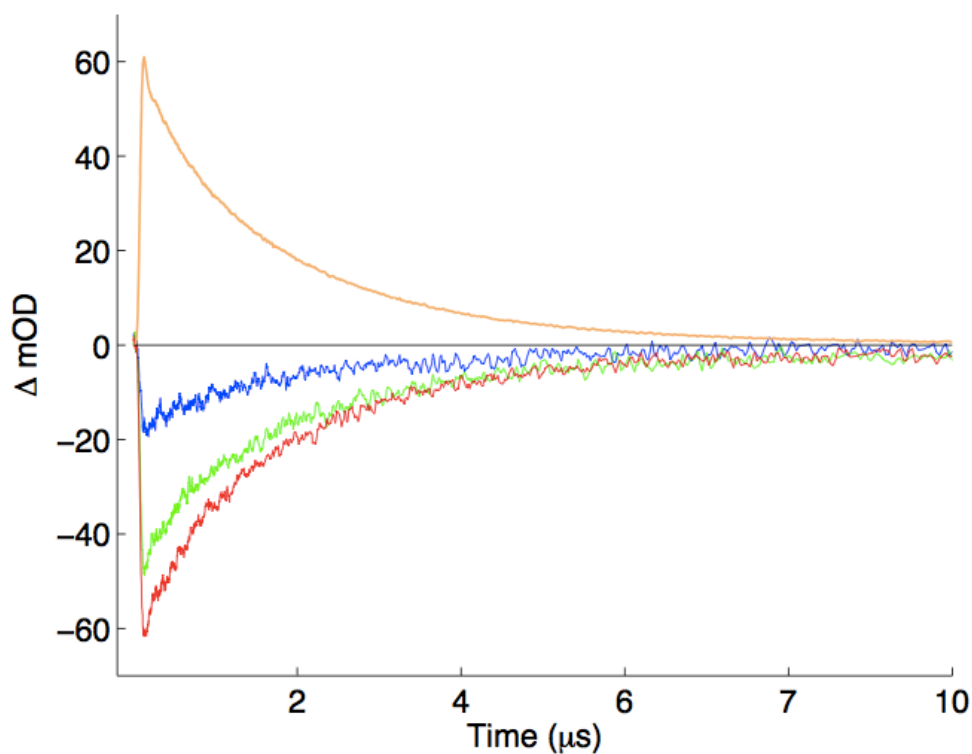


Figure 2.13. Single-wavelength transient absorption of $\text{Ru}^{\text{II}}_{\text{K97C}}\text{-Fe}^{\text{III}}_{\text{P450}}$ in the absence of quencher. 400 nm: blue; 420 nm: green; 440 nm: red, and a scaled overlay of the luminescence decay at 630 nm. The sample is in 50 mM borate buffer, pH 8. Laser excitation is $\lambda_{\text{ex}} = 480 \text{ nm}$.

TA analysis of the free photosensitizer $[\text{Ru}(\text{bpy})_2(\text{Aphen})]^{2+}$ in the presence of quencher allows us to identify transient features associated with Ru^{III} -photosensitizer species. TA data at all wavelengths examined are characterized by bleaches with biphasic recovery; the first kinetics phase is attributed to $^*\text{Ru}^{\text{II}} \rightarrow \text{Ru}^{\text{III}}$ ET quenching, and agrees with the luminescence decay rate (**Figure 2.14**). $[\text{Ru}^{\text{III}}(\text{bpy})_2(\text{IAphen})]^{3+}$ is characterized by a bleach at all wavelengths examined (390-440 nm); this feature decays to baseline within 100 μs , presumably through back-ET with reduced quencher ($[\text{Ru}^{\text{II}}(\text{NH}_3)_6]^{2+}$) (see Appendix C for additional comments on this recombination rate).

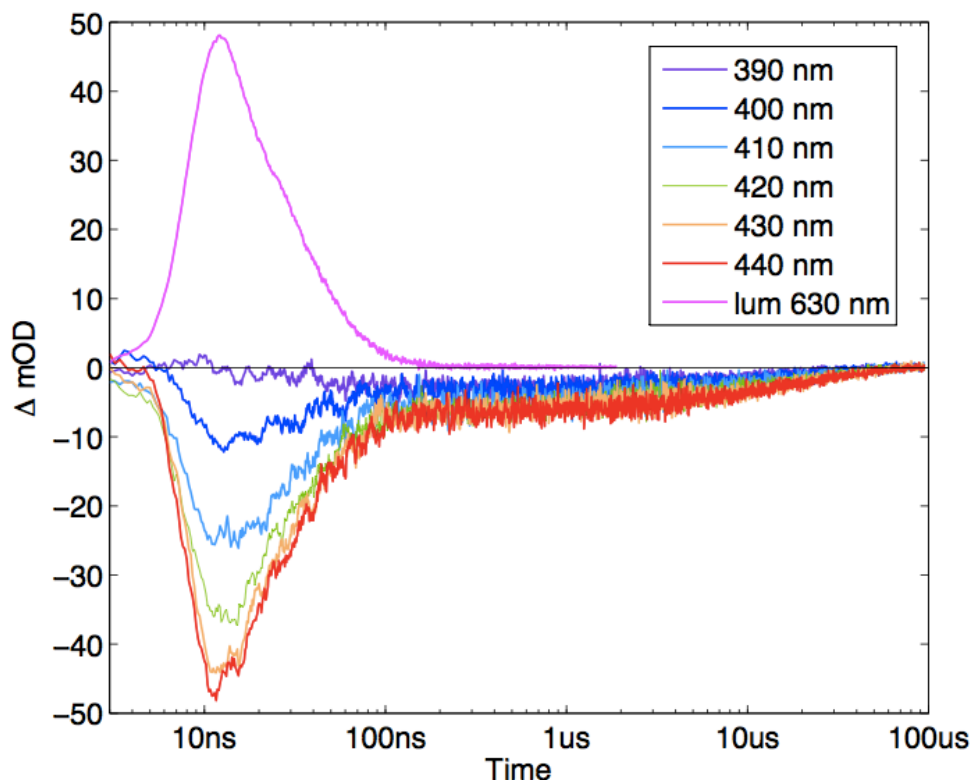


Figure 2.14. Transient Absorption data for flash-quench of $[\text{Ru}(\text{bpy})_2(\text{IAphen})]^{2+}$ with 17 mM $[\text{Ru}(\text{NH}_3)_6]^{3+}$. The scaled luminescence decay (630 nm) is overlaid (top, pink) for comparison.

Flash-quench of $\text{Ru}^{\text{II}}_{\text{K97C}}\text{-Fe}^{\text{III}}_{\text{P450}}$ in the presence of quencher reveals substantially more complex kinetic behavior, indicating the presence of multiple intermediates

that form and disappear over the microsecond to second time range (**Figure 2.15**). The most prominent features are: a persistent bleach at 420 nm (which coincides with λ_{max} of the ground state Fe^{III} heme Soret), an increase in absorption at 390 nm on the microsecond timescale, and an increase in absorbance at 440 nm on the 10 ms – 1 s timescale. These features are distinct from $[\text{Ru}^{\text{II}}(\text{bpy})_2(\text{IAphen})]^{3+}$ data in both timescale and wavelength profile, and suggest oxidation of the heme active site. The last TA feature is significantly affected by buffer pH, over the pH range of 6-8; the amplitude of the 440 nm feature is greatest at high pH (**Figure 2.16**).

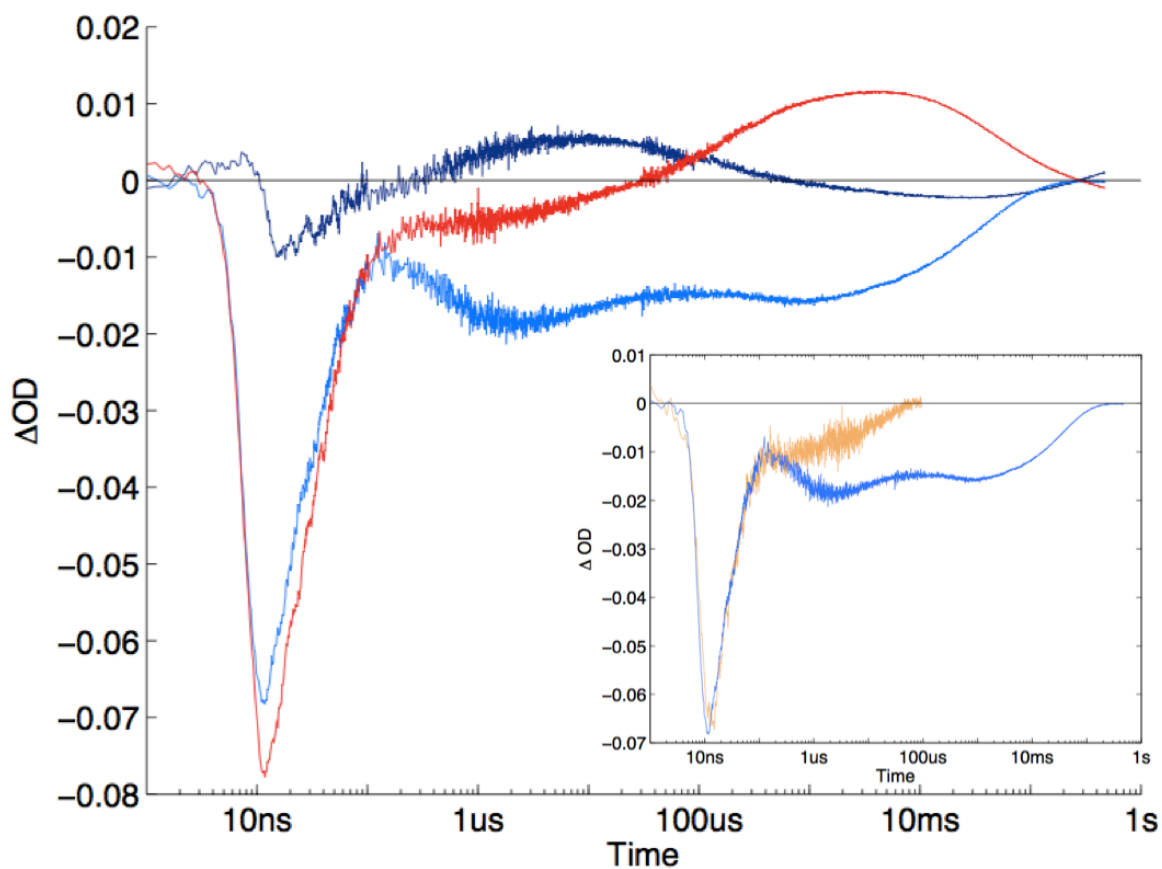


Figure 2.15. Single-wavelength transient absorption following flash-quench ($\lambda_{\text{ex}}=480$ nm) of $\text{Ru}^{\text{II}}_{\text{K97C}}\text{-Fe}^{\text{III}}_{\text{P450}}$ at pH 8. 420 nm (blue), 390 nm (dark blue), 440 nm (red). **Inset:** TA at 420 nm for $\text{Ru}^{\text{II}}_{\text{K97C}}\text{-Fe}^{\text{III}}_{\text{P450}}$ (blue) and $[\text{Ru}^{\text{II}}(\text{bpy})_2(\text{Aphen})]^{2+}$ (orange).

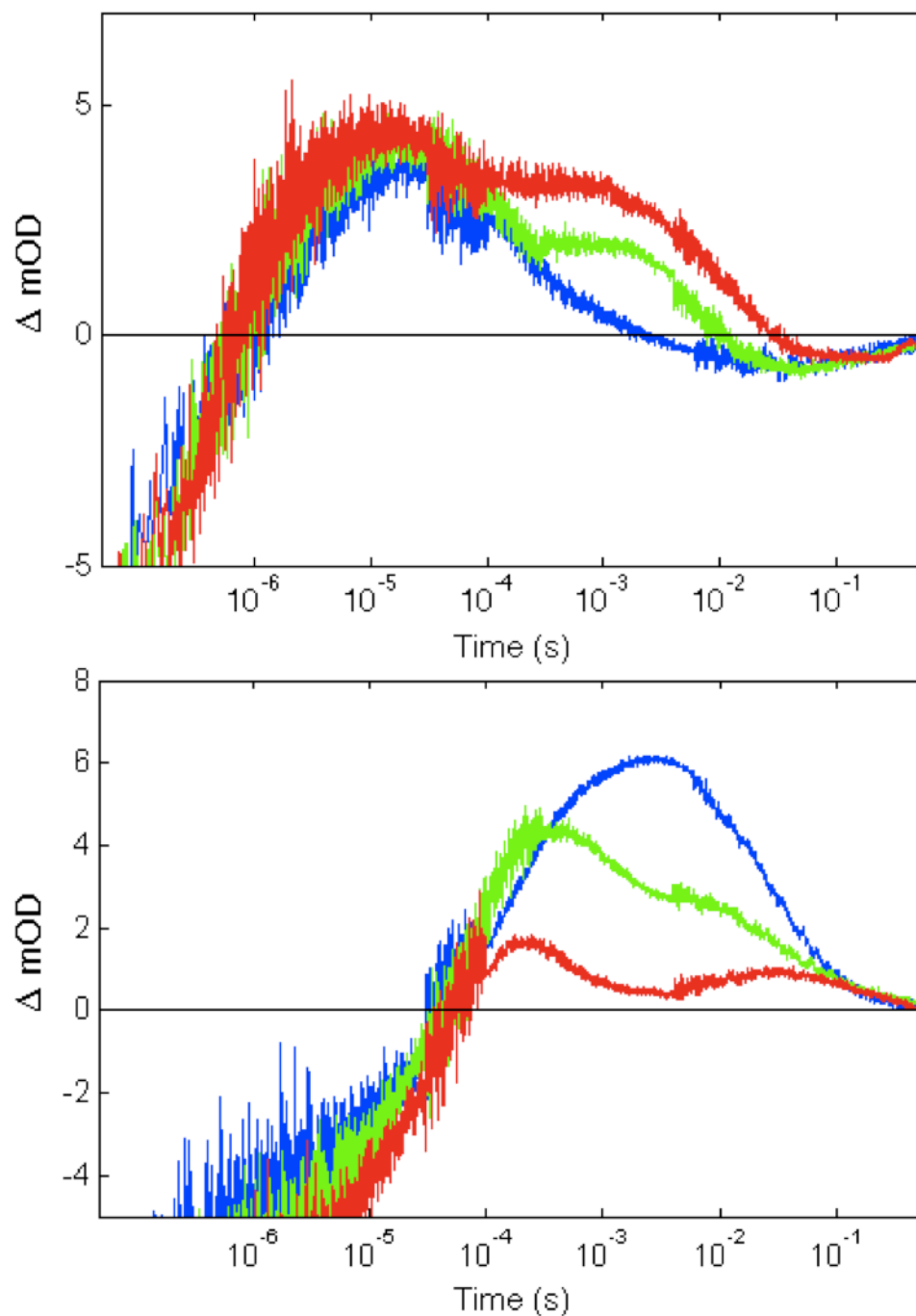


Figure 2.16. pH dependence of Ru_{K97C}-P450_{BM3} transient absorption features. pH 6 (red), pH 7 (green), pH 8 (blue). **Top:** 390 nm. **Bottom:** 440 nm.

Kinetics Analysis of TA Data

In order to determine the number of kinetics phases, and therefore the number of potential intermediates formed by flash-quench, we performed a truncated generalized singular value decomposition analysis (tgSVD) of the TA data (Regularization Tools, Per Christian Hansen,²⁵ see sample script in Appendix D) (**Figure 2.17**). The plot of the tgSVD shows the magnitude (y-axis) of the contribution of each rate constant k (x-axis) to the overall fitting of the transient absorption data. Grouping of the rate constants into five clusters indicates that as many as five distinct kinetic phases contribute to the recovery of TA signals to baseline.

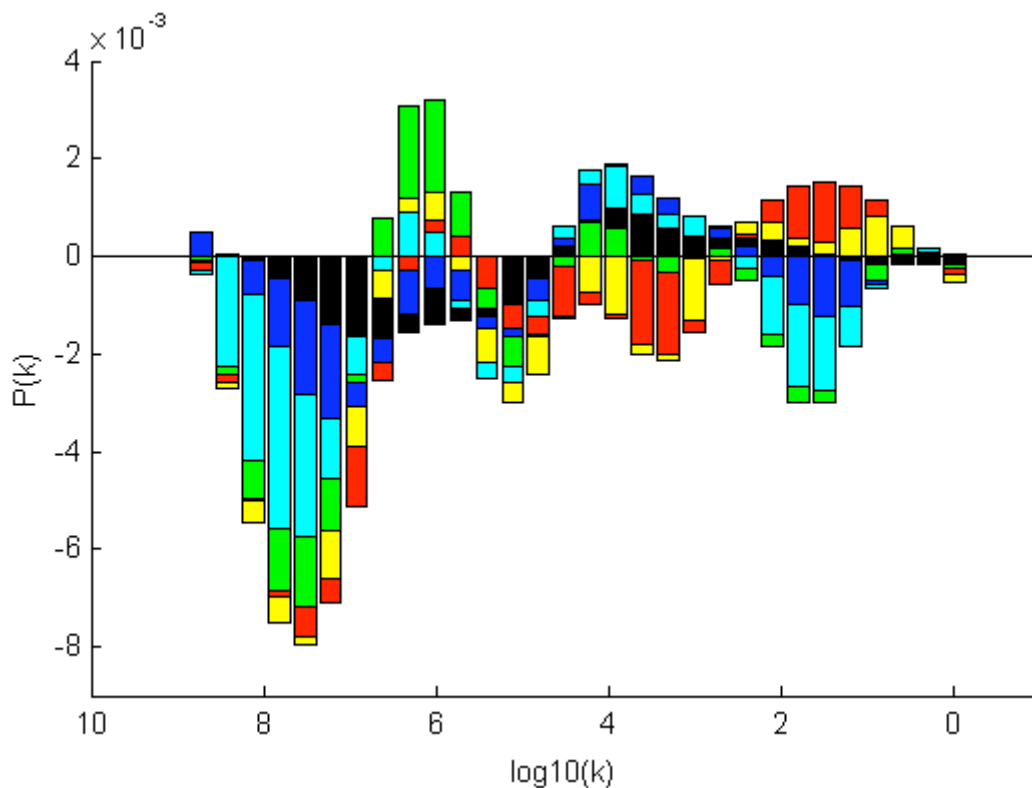


Figure 2.17. tgSVD of TA data for $\text{Ru}^{\text{II}}_{\text{K97C}}\text{-Fe}^{\text{III}}_{\text{P450}}$ with $[\text{Ru}(\text{NH}_3)_6]^{3+}$ at six wavelengths. black: 390 nm; blue: 400 nm; cyan: 410 nm; green: 420 nm; yellow: 430 nm; red: 440 nm, in 50 mM borate buffer, pH 8.

The position of each of the clusters also gives a first-order estimate of the rate constant for each kinetics phase. These estimates greatly facilitate the success of multiexponential fitting procedures. Starting with these rate constants, we have performed a global least-squares fitting of the TA data recorded at six wavelengths (390, 400, 410, 420, 430, 440 nm), to a sum of five exponentials with amplitude coefficients ρ_{1-5} and observed rate constants γ_{1-5} (Equation 1.1) (see a sample fitting script in Appendix D).

Equation 1.1:

$$TA(\lambda_n) = \rho_{n1} \exp(-\gamma_1 t) + \rho_{n2} \exp(-\gamma_2 t) + \rho_{n3} \exp(-\gamma_3 t) + \rho_{n4} \exp(-\gamma_4 t) + \rho_{n5} \exp(-\gamma_5 t)$$

Based on our interpretation of the nature and decay rate of the first transient absorption signal (*vide infra*), we can fix the first observed rate constant as that for the luminescence quenching (obtained from monoexponential fitting of the luminescence decay at 630 nm). The remaining four rate constants are extracted from the global fitting (**Figure 2.18**), and are listed in **Table 2.2**. We find analogous trends in the data from pH 6 to 8.

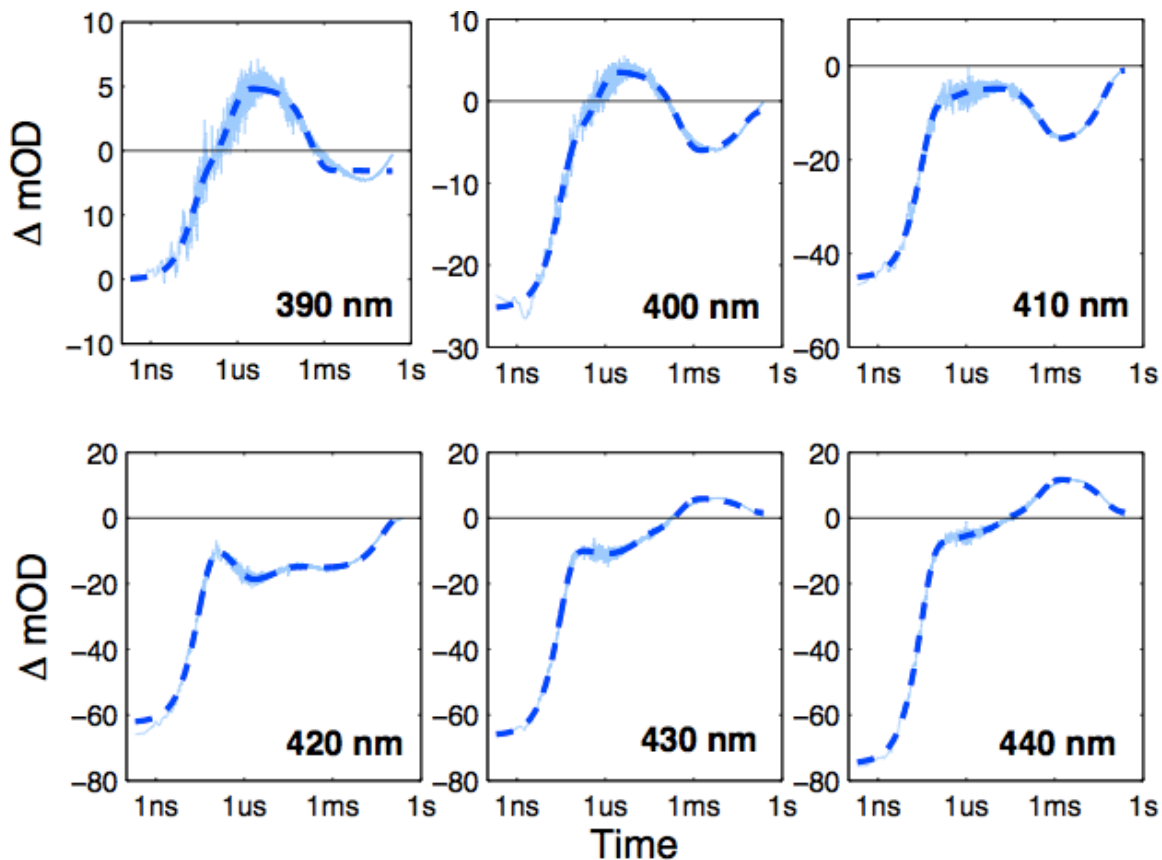


Figure 2.18. Global fitting of $\text{Ru}^{\text{II}}_{\text{K97C}}\text{-Fe}^{\text{III}}_{\text{P450}}$ TA data at pH 8. Light blue: data. Dark blue dashed: global fit.

Table 2.2. Observed rate constants (γ_{1-5} , s^{-1}) extracted from global fitting of single-wavelength TA at six wavelengths (390-440 nm).

pH	γ_1	γ_2	γ_3	γ_4	γ_5
6	$2.5(3)\times 10^7$	$1.5(5)\times 10^6$	$2.0(3)\times 10^5$	$2(1)\times 10^4$	$6(1)\times 10^1$
7	$2.4(3)\times 10^7$	$1.5(6)\times 10^6$	$1.5(3)\times 10^5$	$1.2(3)\times 10^4$	$7(2)\times 10^1$
8	$3.0(4)\times 10^7$	$2(5)\times 10^6$	$1.0(3)\times 10^5$	$4(1)\times 10^3$	$3(1)\times 10^1$

2.4. Discussion

The five distinct kinetics phases suggest that six distinct species are formed following excitation of the Ru photosensitizer. The first transient species is easily identified as excited $^*\text{Ru}^{\text{II}}_{\text{K97C}}\text{-Fe}^{\text{III}}_{\text{P450}}$, by comparison to TA signals of the un-

quenched Ru-P450 conjugate and of the free, quenched photosensitizer. The second species is formed in the quenching reaction with $[\text{Ru}(\text{NH}_3)_6]^{3+}$, and can be identified as $\text{Ru}^{\text{III}}_{\text{K97C}}\text{-Fe}^{\text{III}}_{\text{P450}}$ using similar logic. The final species formed is $\text{Ru}^{\text{II}}_{\text{K97C}}\text{-Fe}^{\text{III}}_{\text{P450}}$, since all TA signals return to baseline; this, along with sample stability over thousands of flash-quench cycles, suggests full reversibility of the photo-triggered reaction. Three transient species remain to be identified; these are most likely associated with oxidation of the P450 heme center, as they are distinct from any TA signals observed for the free photosensitizer. We refer to these species as $\text{P450}(\text{OX}_{1-3})$ in the discussion below.

2.4.1. Kinetics Model

We have developed a sequential kinetics model for the $\text{Ru}^{\text{II}}_{\text{K97C}}\text{-Fe}^{\text{III}}_{\text{P450}}$ TA data (Figure 2.19).

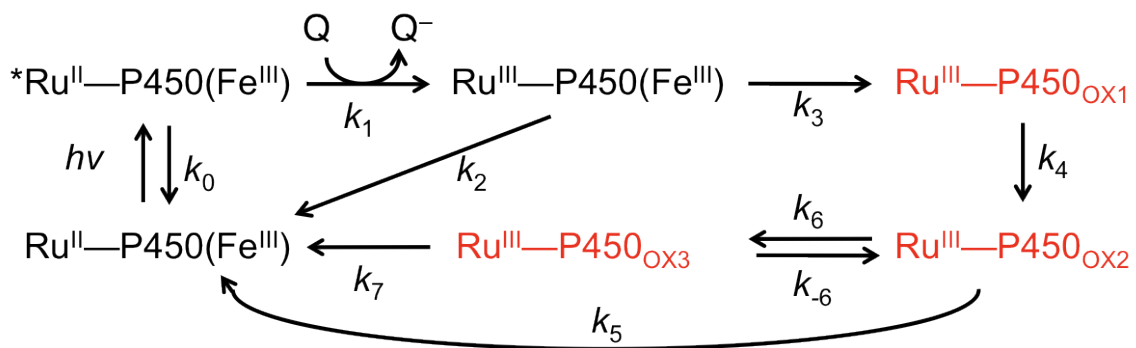


Figure 2.19. Scheme for photochemical oxidation of cytochrome P450. Elementary rate constants k_0 - k_7 are shown for the proposed reactions. Unidentified oxidized P450 species ($\text{P450}(\text{OX}_{1-3})$) are highlighted in red.

We have solved the rate law for this model, allowing us to express the observed rate constants (γ_{1-5}) and amplitude coefficients (ρ_{1-5}) in terms of nine elementary rate constants ($k_0, k_1, k_2, k_3, k_4, k_5, k_6, k_6, k_7$) and the initial $\text{*Ru}^{\text{II}}_{\text{K97C}}\text{-Fe}^{\text{III}}_{\text{P450}}$ concentration. This method is used to extract unscaled difference spectra for each transient species (Figure 2.20, see Appendix C for details).

This system is underdetermined; there are nine elementary rate constants in the kinetics model, but only five observed rate constants can be determined from exponential fitting. Therefore, the parameters in the kinetics model cannot be determined by the TA data alone. Values for k_1 , k_3 , k_5 , and $K_{\text{eq}} = k_6/k_{-6}$ must be supplied in order to determine molar difference spectra for the six intermediate species. The known spectra of $^*\text{Ru}^{\text{II}}$ - and Ru^{III} -diimine species constrain the possible values of k_1 and k_3 . The balance between k_5 and k_7 has no effect on the relative difference spectra extracted from the data, so k_5 was set equal to k_7 . The equilibrium constant K_{eq} was optimized to provide the best agreement between the transient difference spectra recorded at the three different pH values (**Figure 2.20**).

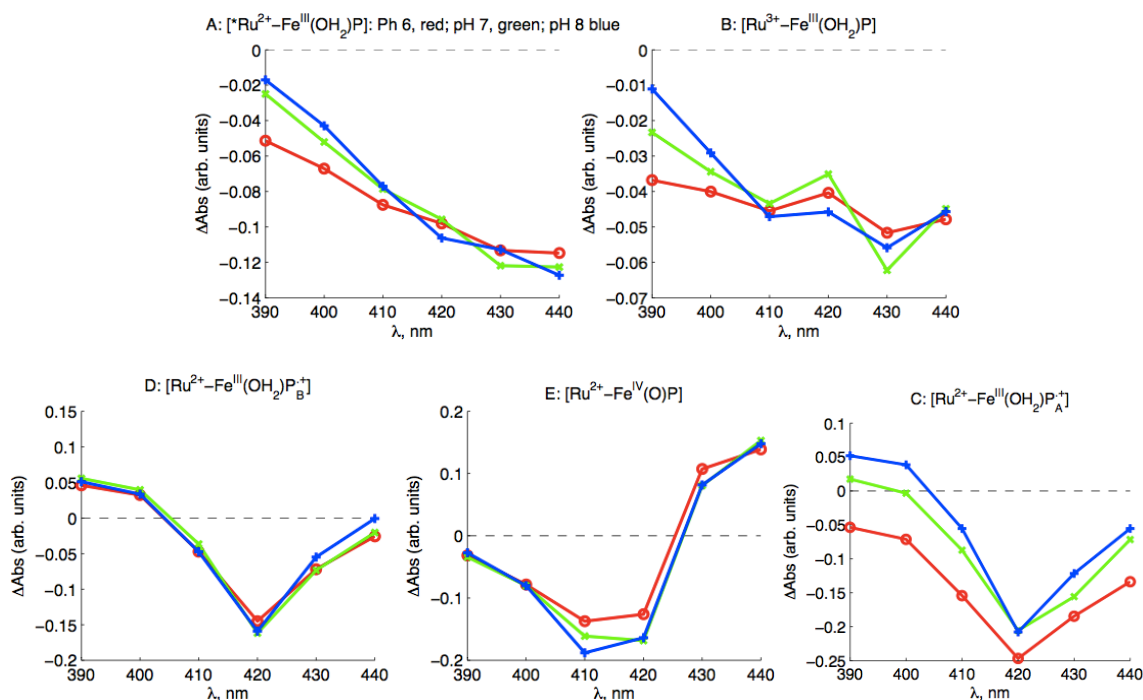


Figure 2.20. Extracted difference spectra of intermediate species. **Top:** Ru-based intermediates. **Bottom:** Oxidized P450 intermediates ($\text{P450}_{\text{OX1-3}}$).

Table 2.3. Extracted kinetics parameters. **Top:** Rate constants k (s^{-1}) for the kinetics model of flash-quench. **Bottom:** $K_{eq}=k_6/k_{-6}$; $^*\phi_{ET}$ and ϕ_{ET} are the yields for formation of $^*Ru^{II}$ and Ru^{III} , respectively.

pH	k_0	k_1	k_2	k_3	k_4	k_5	k_6	k_{-6}	k_7
6	5×10^6 (0.3×10^6)	2×10^7 (0.3×10^7)	1×10^6 (0.4×10^6)	4×10^5 (0.8×10^5)	2×10^5 (0.2×10^5)	7×10^1 (1.6×10^1)	1×10^4 (0.5×10^4)	1.5×10^4 (0.7×10^4)	7×10^1 (1.6×10^1)
7	5.5×10^6 (0.3×10^6)	1.5×10^7 (0.3×10^7)	1×10^6 (0.6×10^6)	5.5×10^5 (0.3×10^5)	1.5×10^5 (0.1×10^5)	8×10^1 (0.3×10^1)	7×10^3 (3×10^3)	4.5×10^3 (1×10^3)	8×10^1 (0.3×10^1)
8	6×10^6 (0.3×10^6)	1.5×10^7 (0.6×10^7)	1×10^6 (0.6×10^6)	8.5×10^5 (2×10^5)	1×10^5 (0.2×10^5)	4×10^1 (0.3×10^1)	3.5×10^3 (0.7×10^3)	3.5×10^2 (0.8×10^2)	4×10^1 (0.3×10^1)

pH	K_{eq}	$^*\phi_{ET}$	ϕ_{ET}
6	0.7	0.8 (0.05)	0.5 (0.25)
7	1.5	0.7 (0.15)	0.5 (0.2)
8	10	0.5 (0.25)	0.5 (0.05)

The difference spectra of $^*Ru^{II}_{K97C}-Fe^{III}_{P450}$ and $Ru^{III}_{K97C}-Fe^{III}_{P450}$ extracted from the kinetics analysis exhibit bleaching at 430 nm of the Ru^{2+} MLCT absorption band. Of primary interest are the difference spectra corresponding to intermediates labeled $P450_{OX1-3}$.

As discussed in Chapter 1, flash-quench oxidation of horseradish peroxidase (HRP) and microperoxidase-8 (MP-8) first proceed by transient oxidation of the porphyrin ring ($Fe^{III}-OH_2(P^{*+})$); subsequent internal rearrangement and deprotonation led to the ferryl, $Fe^{IV}=O(P)$, product (**CII**). The initial porphyrin radical in HRP and MP-8 are also characterized by a bleach of the heme Soret.^{15,16} The blue shift in absorption for these porphyrin radical intermediates is also consistent with synthetic models of Fe(III)-porphyrin cation radicals.²⁶

The spectra of $P450_{OX1}$ and $P450_{OX2}$ are quite similar, and are also characterized by a bleach of the Soret absorption band (centered at 420 nm). The spectrum of $P450_{OX2}$ displays somewhat more absorbance at 390 nm than that of $P450_{OX1}$, but

otherwise closely resembles that of P450_{OX1}. Reasoning by analogy to our results on the oxidation of HRP and MP8, and the similarity of their difference spectra, we suggest that P450_{OX1} and P450_{OX2} correspond to six-coordinate porphyrin radical cations: Ru^{II}_{K97C}-Fe^{III}(OH₂)P^{•+}_{(A)P450} and Ru^{II}_{K97C}-Fe^{III}(OH₂)P^{•+}_{(B)P450}.

The apparent equilibrium constant between P450_{OX2} and P450_{OX3} varies with pH (K_{eq} : 0.8, pH 6; 2.9, pH 7; 10, pH 8), suggesting that a proton is lost in the formation of P450_{OX3}. Moreover, the difference spectrum for this species indicates a red-shifted Soret absorption band analogous to that reported for the Fe^{IV}(OH)P center in CPO CII,²⁷ as well as photochemically-generated CII in HRP and MP-8.

Hence, we suggest that P450_{OX3} is Ru^{II}_{K97C}-Fe^{IV}(OH)P_{P450}. Internal charge transfer in Fe^{III}(OH₂)P^{•+}_{(B)P450} is accompanied by rapid loss of a proton (possibly to water), producing Fe^{IV}(OH)P_{P450}. The formation of flash-quench generated CII in HRP was slower (k_{obs} of 4.1 s⁻¹) due to rate-limiting water ligation. CII formation in P450 proceeds on the millisecond timescale because a water molecule already occupies the sixth coordination site of the ferric heme.

The specific rate of Fe^{III}(OH₂)P^{•+}_{(A)P450} formation in our conjugate is comparable to that found for reconstituted myoglobin containing a heme tethered directly to Ru(diimine)₃²⁺.²⁸ This observation suggests that a favorable pathway couples the P450 porphyrin to Ru^{III}, possibly involving the Trp96-heme propionate hydrogen bond.²⁹ The conversion of Ru^{II}_{K97C}-Fe^{III}(OH₂)P^{•+}_{(A)P450} to Ru^{II}_{K97C}-Fe^{III}(OH₂)P^{•+}_{(B)P450} may be a consequence of changes in polypeptide or solvent conformation in the P450 heme pocket.³⁰

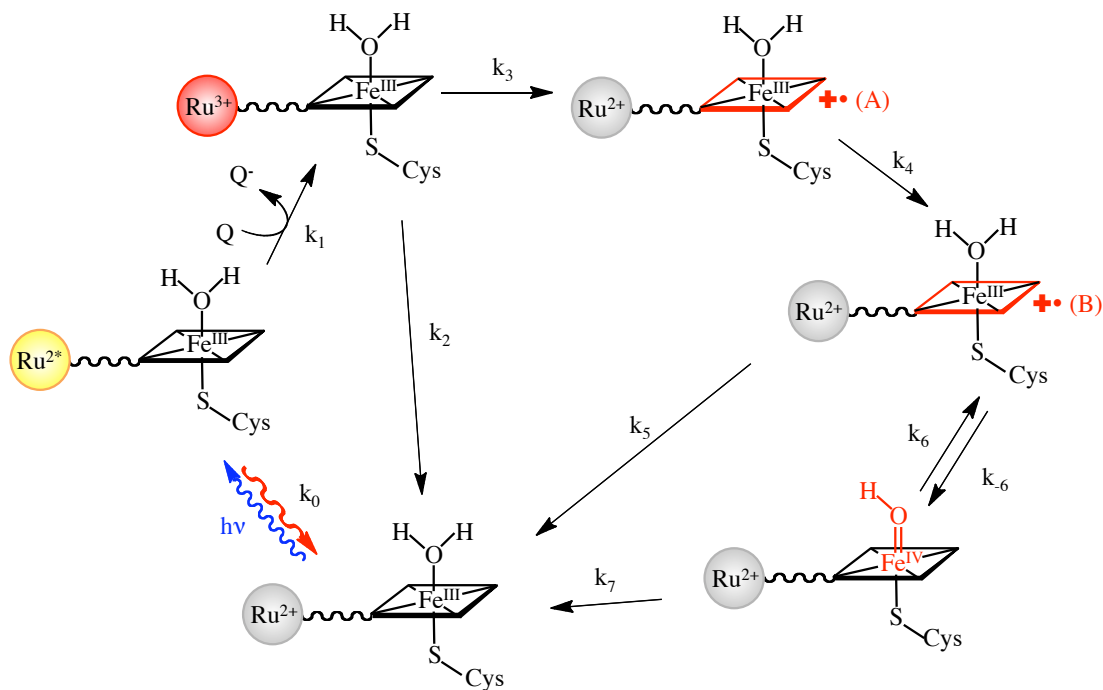


Figure 2.21. Photo-triggered cycle for flash-quench oxidation of $\text{Ru}^{\text{III}}_{\text{K97C}}\text{-Fe}^{\text{III}}_{\text{P450}}$.

All of these intermediates are short-lived; transient absorbance features return to baseline within 500 ms, indicating recovery of resting state $\text{Ru}^{\text{II}}_{\text{K97C}}\text{-Fe}^{\text{III}}(\text{OH}_2)\text{P}_{450}$. We have modeled this process as recovery from both the ferryl species (k_7 , $\text{Ru}^{\text{II}}_{\text{K97C}}\text{-Fe}^{\text{IV}}(\text{OH})\text{P}_{450}$) and its porphyrin radical cation precursor (k_5 , $\text{Ru}^{\text{II}}_{\text{K97C}}\text{-Fe}^{\text{III}}(\text{OH}_2)\text{P}^{\bullet+}_{(\text{B})\text{P450}}$) (Fig. 4), but it is not possible to determine the two rate constants since equilibration between $\text{Ru}^{\text{II}}_{\text{K97C}}\text{-Fe}^{\text{III}}(\text{OH}_2)\text{P}^{\bullet+}_{(\text{B})\text{P450}}$ and $\text{Ru}^{\text{II}}_{\text{K97C}}\text{-Fe}^{\text{IV}}(\text{OH})\text{P}_{450}$ is faster than the ground-state recovery process. The precise nature of the resting state recovery process remains unclear. It should be described by second-order reaction kinetics, but the experimental data are better modeled by a simple exponential process. Nevertheless, $[\text{Ru}(\text{NH}_3)_6]^{2+}$ seems to be involved in the recovery reaction because in the presence of $[\text{Ru}(\text{NH}_3)_6]^{3+}$ as quencher, transient absorption data are consistent over the course of multiple hours, and the Soret absorption band appears relatively unaffected after many rounds of flash-quench excitation. However, similar measurements with an irreversible quencher

([Co(NH₃)₅Cl]³⁺) induce bleaching of the Soret band and rapid sample degradation.

2.5. Concluding Remarks

We have developed a flash-quench method to oxidize the buried resting ferric aquo state of the P450-BM3 heme domain to **CII** without the use of reactive oxygen species (O₂, H₂O₂). The catalytic cycle runs in reverse by photochemically splitting water at the heme site. It is likely that the observed ferryl species is protonated over the pH range of 6-8, as consistent with the current view of chloroperoxidase and P450 **CII**. The finding that internal oxidation of the iron center is rate limiting has allowed us to observe porphyrin radical cation intermediates. As porphyrin oxidation occurs on the microsecond timescale, we can reasonably expect a second round of flash-quench on photochemically generated **CII** to produce **CI**.

Efforts toward this second oxidation step will be greatly facilitated by a better understanding of the coupling pathway between the photosensitizer and heme, and development of a system in which **CII** is stable on the order of seconds-to-minutes. Examination of the role of W96 and implementation of the photochemical system in the thermophilic P450 CYP119 are described in Chapter 3.

2.6. Acknowledgments

This effort would not have been possible without the ground work laid by Lionel Cheruzel, including design of the mutant, development of labeling protocols, crystallization the Ru-P450 conjugate, and patient training of graduate students (myself). Jay Winkler's guidance and insights were critical for navigating the

intricate details of data analysis, fitting, and kinetics modeling. The synthesis of photosensitizer model compounds (iodo-free $[\text{Ru}(\text{bpy})_2(\text{Aphen})]^{2+}$), and acquisition of steady state fluorimetry data, was done by Katja Luxem.

2.7. Materials and Methods

Chemicals

Buffer salts were obtained from J.T. Baker. Dicyclohexylcarbodiimide (DCC), iodoacetic acid, and 5-amino-1,10-phenanthroline were obtained from Sigma Aldrich. $\text{Ru}(2,2'\text{-bipyridine})_2\text{Cl}_2$ and $[\text{Ru}(\text{NH}_3)_6]\text{Cl}_3$ were obtained from Strem Chemicals; these were used without further purification. Mutagenesis primers were obtained from Operon. Solutions were prepared using 18 M Ω cm water unless otherwise noted.

Procedures

A detailed description of experimental protocols can be found in Appendix B. A brief description of the procedures is given below, highlighting any deviations from the general protocol. All images of protein crystal structures in this Chapter were made using PyMol graphics software for Mac.

2.7.1. Ru photosensitizer

Synthesis

This photosensitizer was synthesized according to published procedures. Briefly, iodoacetic anhydride was formed by addition of N,N'-Dicyclohexylcarbodiimide (DCC) to a solution of iodoacetic acid in ethyl acetate. Following removal of urea by filtration and evaporation to dryness, the iodoacetic anhydride in acetonitrile

was added to a solution of 5-amino-1,10-phenanthroline in acetonitrile and stirred overnight at room temperature. Solid product (5-iodoacetamido-1,10-phenanthroline, (IAphen)) was refluxed with Ru(bpy)₂Cl₂ in methanol for 3 hours; a color change from purple to red is observed. After cooling and filtration, product can be precipitated by addition of concentrated aqueous NH₄PF₆. Alternatively, the compound can be concentrated and redissolved in water without further purification. The starting material impurities do not interact with P450, and do not appear to impact the labeling process.

Characterization

The photosensitizer was characterized by nuclear magnetic resonance (NMR), steady-state luminescence, and transient luminescence and absorption.

2.7.2. Mutagenesis and expression of P450-BM3 mutants

Plasmid

The recombinant P450-BM3 heme domain, consisting of the first 463 residues with an N-terminal 6-histidine tag, was obtained courtesy of Andrew Udit (Occidental College, Los Angeles California), within the pCWori⁺ vector, which also contains genes for ampicillin resistance and IPTG induction.

Mutagenesis

The triple mutant C62A/C156S/K97C was made using Qiagen QuikChange site-directed mutagenesis using the following primers:
CTAATTAAAGAAGCAGCCGATGAATCACG (C62A),
CGATTGGTCTTAGCGGCTTTAAC (C156S),

GCTGGACGCATCAAAAAAATTGGTGCAAAGCGC (K97C). The P450 gene was sequenced (Laragen) to verify successful mutagenesis.

Expression

P450 enzymes were overexpressed in *E. coli*. Briefly, overnight Luria Bertani medium cultures were used to inoculate 1x Terrific Broth induction cultures with added mineral supplements, shaken at 37 °C. At an OD(600 nm) ~1, the temperature was lowered to 30 °C, expression was induced with isopropyl β -D-thiogalactopyranoside (IPTG), and α -aminolevulinic acid was added. After expression for 24 or 40 hours (for P450 BM3 and CYP119, respectively), cells were harvested by centrifugation and stored at -80 °C.

Extraction and purification

P450 enzymes were extracted by sonication in the presence of protease inhibitors (benzamidine hydrochloride and Pefabloc SC hydrochloride). After centrifugation, the supernatant was purified by nickel immobilized metal affinity chromatography on a batch column. Samples were further purified by FPLC anion exchange chromatography and gel filtration.

Purity was determined by UV-vis absorption (A_{418}/A_{280}), SDS-PAGE, and mass spectrometry. Dithiothreitol (DTT) was added to protein not intended for immediate use, and samples were flash-frozen in liquid nitrogen and stored at -80°C.

2.7.3. Ru-P450 conjugation

The complex $[\text{Ru}(\text{bpy})_2(\text{IAphen})]^{2+}$ (IAphen = 5-iodoacetamido-1,10-phenanthroline) was covalently coupled to triple mutant C62A/C156S/K97C (abbreviated as tK97C) at Cys97 to give the conjugate $\text{Ru}^{\text{II}}_{\text{K97C}}\text{-Fe}^{\text{III}}_{\text{P450}}$.

Briefly, approximately three-fold excess of $[\text{Ru}^{\text{II}}(\text{bpy})_2(\text{IAphen})]^{2+}$ was added to a $\sim 10 \mu\text{M}$ P450 solution in 20 mM Tris buffer, pH 8. The reaction solution shaken gently for ~ 4 hours at 4 °C in the dark, followed by desalting to remove excess photosensitizer and purification of Ru-labeled and unlabeled enzymes by anion exchange chromatography on an MonoQ or HiPrepQ FPLC column.

This conjugate was characterized by mass spectrometry, UV-Vis and luminescence spectroscopies (steady state, time-resolved), and X-ray crystallography. The conjugate $\text{Ru}^{\text{II}}_{\text{K97C}}\text{-Fe}^{\text{III}}_{\text{P450}}$ demonstrates activity in the hydroxylation of lauric acid via the peroxide shunt.³¹

2.7.4. Crystallization and structure determination

Crystals of $\text{Ru}^{\text{II}}_{\text{K97C}}\text{-Fe}^{\text{III}}_{\text{P450}}$ were obtained by the sitting-drop vapor diffusion method: 27 mg/ml $\text{Ru}^{\text{II}}_{\text{K97C}}\text{-Fe}^{\text{III}}_{\text{P450}}$ in 10 mM potassium phosphate, pH 8.4 was mixed with a crystallization well solution of 2 M $(\text{NH}_4)_2\text{SO}_4$ (w/v) in a 1:1 ratio (v/v). Crystals formed over a period of 2 days at 4 °C, and were flash frozen directly from the crystallization solution. X-ray diffraction data were collected at 100 K using beamline 7-1 at the Stanford Synchrotron Radiation Laboratory. Diffraction data were processed with Mosflm and Scala. Initial model for the $\text{Ru}^{\text{II}}_{\text{K97C}}\text{-Fe}^{\text{III}}_{\text{P450}}$ structure was derived from the palmitic acid-bound P450-BM3 structure (pdb ID 2UWH) by molecular replacement using Molrep. Coot and Refmac5 were used for model fitting and refinement. The final models were

validated using the programs Procheck, Sfcheck and Molprobity. Most of the above processes were done with the graphical interface to the CCP4 program suite. All structural graphics were generated using the Pymol Graphics System.

Statistics for data collection and refinement are shown in the Table S1. Atomic coordinates and structure factors were deposited in the Protein Data Bank under the entry 3NPL.

2.7.5. Preparation of laser samples

Laser samples were composed of either Ru^{II}_{K97C}-Fe^{III}_{P450} or the model complex [Ru(bpy)₂(IAphen)]²⁺ (~10 μM), with and without oxidative quencher (17 mM [Ru(NH₃)₆]Cl₃) in buffered solution (pH 6: 20 mM sodium acetate; pH 7: 20 mM sodium acetate; pH 8: 50 mM sodium borate or 50 mM Tris; additionally, each buffer contained sodium chloride). Samples were placed in a high-vacuum four-sided quartz cuvette, equipped with a small stir bar. Deoxygenation was achieved via gentle pump-backfill cycles with argon.

For acquisition of time-resolved fluorescence and transient absorption data, samples were excited with 8 ns laser pulses at 480 nm. Luminescence decays were monitored at 630 nm. Single wavelength transient absorption (TA) kinetics were monitored every 10 nm from 390-440 nm, averaging ~500 shots per wavelength. Data from five separate timescales (2 μs, 40 μs, 400 μs, 10 ms, and 500 ms) were collected, log-compressed, and spliced together to produce full kinetics traces. See Appendix D for log-compression and splicing scripts in Matlab.

2.8. References

- (1) Guengerich, F. P. Common and Uncommon Cytochrome P450 Reactions Related to Metabolism and Chemical Toxicity. *Chem. Res. Toxicol.* **2001**, *14*, 611–650.
- (2) Ortiz de Montellano, P. *Cytochrome P450: Structure, Mechanism and Biochemistry*; 3rd ed.; Kluwer Academic/Plenum Publishers: New York, 2005.
- (3) Denisov, I. G.; Makris, T. M.; Sligar, S. G.; Schlichting, I. Structure and Chemistry of Cytochrome P450. *Chem. Rev.* **2005**, *105*, 2253–2278.
- (4) Groves, J. T. The Bioinorganic Chemistry of Iron in Oxygenases and Supramolecular Assemblies. *Proc. Natl. Acad. Sci.* **2003**, *100*, 3569–3574.
- (5) Green, M. T. C-H Bond Activation in Heme Proteins: The Role of Thiolate Ligation in Cytochrome P450. *Curr. Opin. Chem. Biol.* **2009**, *13*, 84–88.
- (6) Munro, A. W.; Daff, S.; Coggins, J. R.; Lindsay, J. G.; Chapman, S. K. Probing Electron Transfer in Flavocytochrome P-450 BM3 and Its Component Domains. *Eur. J. Biochem.* **1996**, *239*, 403–409.
- (7) Noble, M. A.; Miles, C. S.; Chapman, S. K.; Lysek, D. A.; Mackay, A. C.; Reid, G. A.; Hanzlik, R. P.; Munro, A. W. Roles of Key Active-Site Residues in Flavocytochrome P450 BM3. *Biochem. J.* **1999**, *339*, 371–379.
- (8) Rittle, J.; Green, M. T. Cytochrome P450 Compound I: Capture, Characterization, and C-H Bond Activation Kinetics. *Science* **2010**, *330*, 933–937.
- (9) Davydov, R.; Makris, T. M.; Kofman, V.; Werst, D. E.; Sligar, S. G.; Hoffman, B. M. Hydroxylation of Camphor by Reduced Oxy-Cytochrome P450cam: Mechanistic Implications of EPR and ENDOR Studies of Catalytic Intermediates in Native and Mutant Enzymes. *J. Am. Chem. Soc.* **2001**, *123*, 1403–1415.
- (10) Winkler, J.; Gray, H. Electron Transfer in Ruthenium-Modified Proteins. *Chem. Rev.* **1992**, *92*, 369–379.
- (11) Gray, H. B.; Winkler, J. R. Electron Transfer in Proteins. *Annu. Rev. Biochem.* **1996**, *65*, 537–561.
- (12) Gray, H. B.; Winkler, J. R. Long-Range Electron Transfer. *Proc. Natl. Acad. Sci.* **2005**, *102*, 3534–3539.
- (13) Creutz, C.; Chou, M.; Netzel, T. L.; Okumura, M.; Sutin, N. Lifetimes, Spectra, and Quenching of the Excited States of Polypyridine Complexes of Iron(II), Ruthenium(II), and Osmium(II). *J. Am. Chem. Soc.* **1980**, *102*, 1309–1319.
- (14) Sutin, N.; Creutz, C. Properties and Reactivities of the Luminescent Excited States of Polypyridine Complexes of Ruthenium(II) and Osmium(II).

- Inorganic and Organometallic Photochemistry*; Advances in Chemistry; American Chemical Society: Washington, DC, 1978; Vol. 1.
- (15) Berglund, J.; Pascher, T.; Winkler, J. R.; Gray, H. B. Photoinduced Oxidation of Horseradish Peroxidase. *J. Am. Chem. Soc.* **1997**, *119*, 2464–2469.
 - (16) Low, D.; Winkler, J.; Gray, H. Photoinduced Oxidation of Microperoxidase-8: Generation of Ferryl and Cation-Radical Porphyrins. *J. Am. Chem. Soc.* **1996**, *118*, 117–120.
 - (17) Castellano, F. N.; Dattelbaum, J. D.; Lakowicz, J. R. Long-Lifetime Ru(II) Complexes as Labeling Reagents for Sulfhydryl Groups. *Anal. Biochem.* **1998**, *255*, 165–170.
 - (18) Sevrioukova, I. F.; Immoos, C. E.; Poulos, T. L.; Farmer, P. J. Electron Transfer in the Ruthenated Heme Domain of Cytochrome P450BM-3. *Isr. J. Chem.* **2000**, *40*, 47–53.
 - (19) Udit, A. K.; Hill, M. G.; Bittner, V. G.; Arnold, F. H.; Gray, H. B. Reduction of Dioxygen Catalyzed by Pyrene-Wired Heme Domain Cytochrome P450 BM3 Electrodes. *J. Am. Chem. Soc.* **2004**, *126*, 10218–10219.
 - (20) Huang, W.-C.; Westlake, A. C. G.; Marechal, J.-D.; Joyce, M. G.; Moody, P. C. E.; Roberts, G. C. K. Filling a Hole in Cytochrome P450 BM3 Improves Substrate Binding and Catalytic Efficiency. *J. Mol. Biol.* **2007**, *373*, 633–651.
 - (21) Haines, D. C.; Tomchick, D. R.; Machius, M.; Peterson, J. A. Pivotal Role of Water in the Mechanism of P450BM-3. *Biochemistry* **2001**, *40*, 13456–13465.
 - (22) Li, H.; Poulos, T. L. Modeling Protein-Substrate Interactions in the Heme Domain of Cytochrome P450(BM-3). *Acta Crystallogr. Sect D* **1995**, *51*, 21–32.
 - (23) Hansen, P. C. Regularization Tools: A Matlab Package for Analysis and Solution of Discrete Ill-Posed Problems. *Numer. Algorithms* **1994**, *6*, 1–35.
 - (24) Ikezaki, A.; Tukada, H.; Nakamura, M. Control of Electronic Structure of a Six-Coordinate Iron (III) Porphyrin Radical by Means of Axial Ligands. *Chem. Commun.* **2008**, *19*, 2257–2259.
 - (25) Green, M. T.; Dawson, J. H.; Gray, H. B. Oxoiron(IV) in Chloroperoxidase Compound II Is Basic: Implications for P450 Chemistry. *Science* **2004**, *304*, 1653–1656.
 - (26) Hamachi, I.; Tsukiji, S.; Shinkai, S.; Oishi, S. Direct Observation of the Ferric-Porphyrin Cation Radical as an Intermediate in the Phototriggered Oxidation of Ferric- to Ferryl-Heme Tethered to Ru(bpy)₃ in Reconstituted Materials. *J. Am. Chem. Soc.* **1999**, *121*, 5500–5506.
 - (27) Shih, C.; Museth, A. K.; Abrahamsson, M.; Blanco-Rodríguez, A. M.; Di Bilio, A. J.; Sudhamsu, J.; Crane, B. R.; Ronayne, K. L.; Towrie, M.; Vlček Jr., A.; Richards, J. H.; Winkler, J. R.; Gray, H. B. Tryptophan-Accelerated Electron Flow Through Proteins. *Science* **2008**, *320*, 1760–1762.

- (28) Fishelovitch, D.; Shaik, S.; Wolfson, H. J.; Nussinov, R. How Does the Reductase Help to Regulate the Catalytic Cycle of Cytochrome P450 3A4 Using the Conserved Water Channel. *J. Phys. Chem. B* **2010**, *114*, 5964–5970.
- (29) Cirino, P. C.; Arnold, F. H. Regioselectivity and Activity of Cytochrome P450 BM-3 and Mutant F87A in Reactions Driven by Hydrogen Peroxide. *Adv. Synth. Catal.* **2002**, *344*, 932–937.

Chapter 3

**PHOTO-TRIGGERED ELECTRON TRANSFER
THROUGH TRYPTOPHAN
IN RU-P450 SYSTEMS**

3.1. Background: Light to ET

To accomplish metabolic processes that drive biological function, cells must deliver electrons and holes over many-angstrom distances, and generate highly reactive species in a very controlled manner. The photosynthetic reaction center in plants is a paradigm in its ability to harness the energy in sunlight to produce high-energy states that can rapidly and efficiently separate charges (electrons and holes) over greater than 20 Å. This allows use of the reactive electrons to generate reduced nicotinamide adenine dinucleotide (phosphate) (NAD(P)H) and adenosine triphosphate (ATP) (the energy currency of the cell), and sequestration of the reactive holes to oxidize water and generate molecular oxygen.

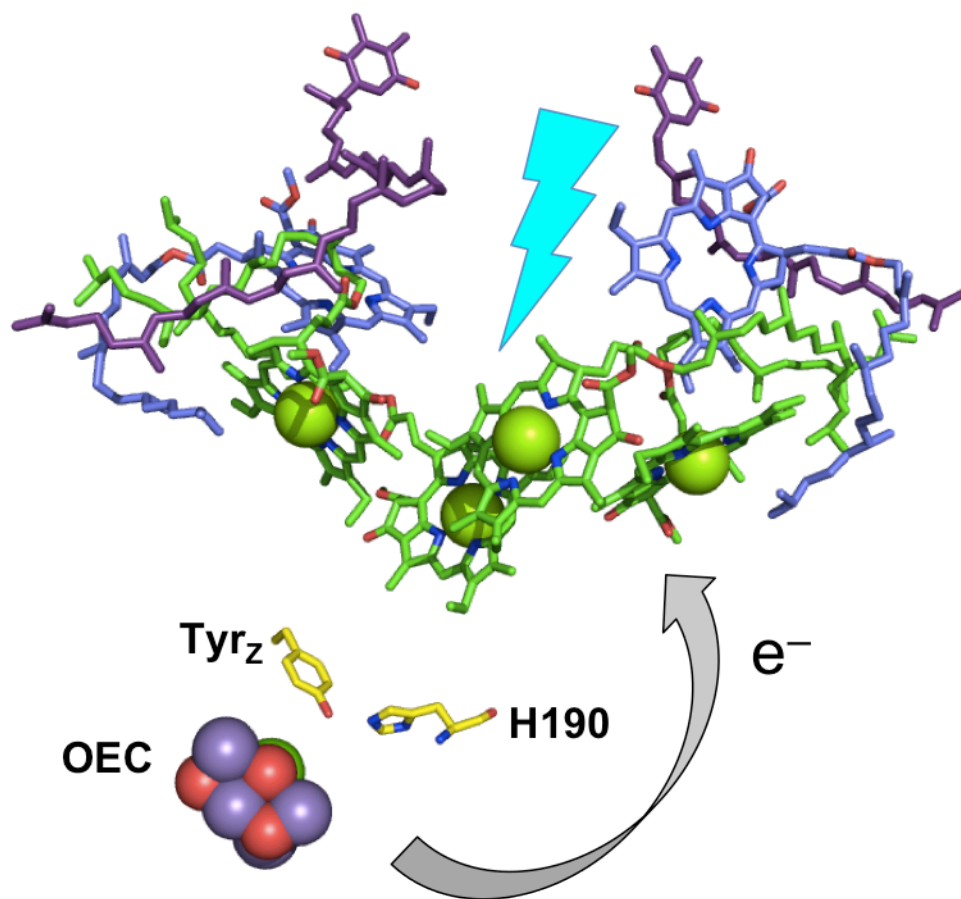


Figure 3.1. Photo-excitation of P680 chromophores in Photosystem II triggers oxidation of the oxygen evolving complex (OEC).

As described in Chapter 2, we have developed a ruthenium photosensitizer/cytochrome P450 BM3 conjugate system (**Figure 3.2**) that similarly harnesses light energy (a laser pulse) to photochemically oxidize the P450 active site by one electron.¹ We have generated the high-valent heme-hydroxo species known as compound II (CII) by oxidizing an axially-bound water molecule (**Figure 3.3**). This is the first step in running cytochrome P450 backwards to access the highly-reactive, iron-oxo ligand radical intermediate known as compound I (CI).

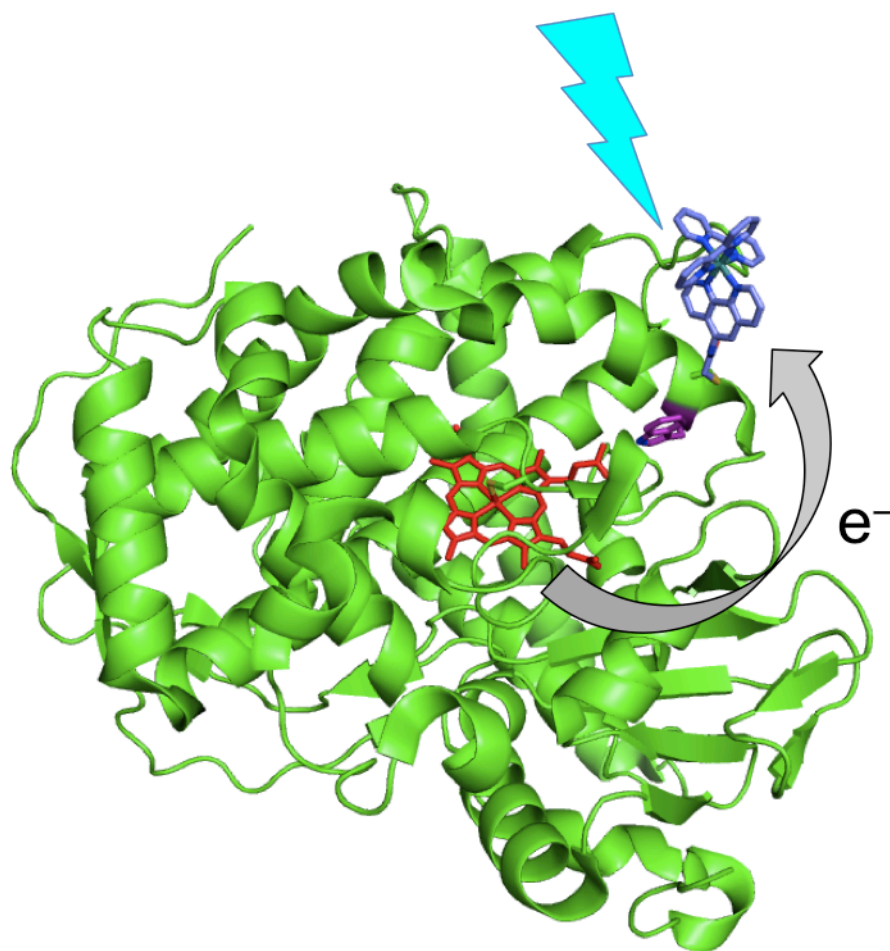


Figure 3.2. Photo-excitation of the tethered ruthenium complex triggers oxidation of the P450 heme active site. The photosensitizer ($\text{Ru}^{\text{II}}(2,2'$ -bipyridine) $_2(5$ -acetamido-1,10-phenanthroline)) is highlighted in blue, the heme is red, and intervening tryptophan 96 is colored purple.

CI is capable of hydroxylating unactivated alkane C–H bonds, a critical transformation in the biosynthesis of steroids, among many other cellular processes. This reactive species has been chemically generated by rapid mixing of *m*CPBA (*meta*-chloroperoxybenzoic acid with the thermophilic P450 CYP119.² However, the processes of hydrogen atom abstraction from substrate to form CII, and subsequent radical rebound to generate hydroxylated product and regenerate the resting state, have yet to be observed directly. The rate of formation of CI is often slower than that for its reaction with substrate.³ Photochemical oxidation of the active site provides a rapid means of generating these oxidized species, with very high temporal resolution.

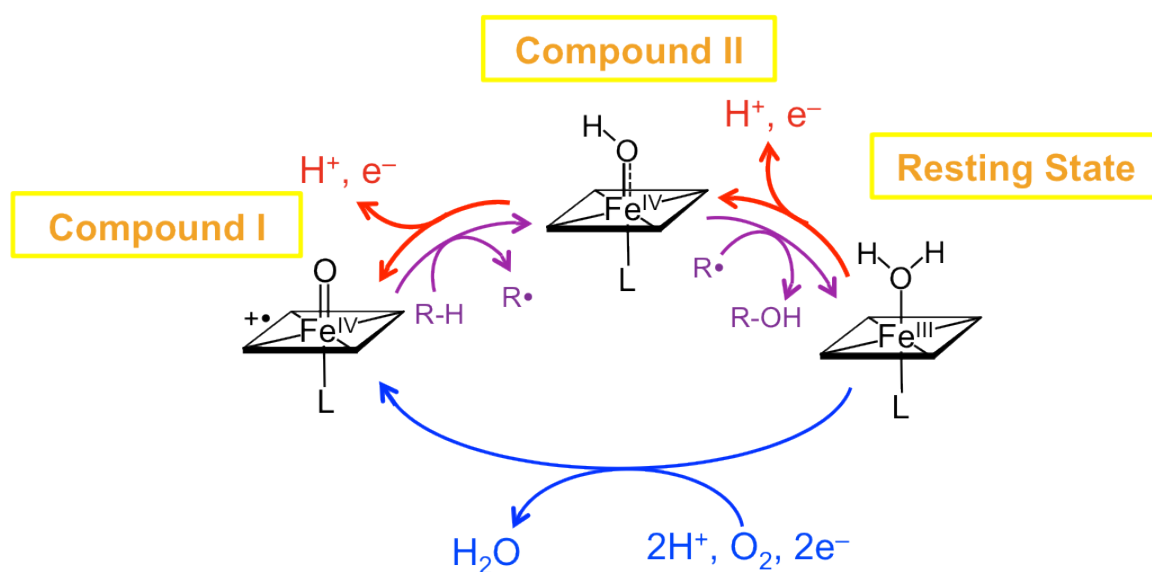


Figure 3.3. Formation of high-valent CI and CII. Blue arrows: reductive activation of dioxygen (native catalytic cycle). Red arrows: oxidative activation of water. Purple arrows: hydroxylation of substrate (RH).

Generation of CI requires two-electron oxidation of the heme (**Figure 3.3**, red arrows). If we wish to achieve, observe, and characterize this second electron transfer by photochemical oxidation (flash-quench), we need to first obtain a stable pool of the precursor CII. Photochemically generated CII decays within a

few hundred milliseconds. Additionally, the yield of this species low; rough estimates place this yield at less than 20%, based on the observed transient absorption features (Chapter 2), and reported absorption profile of CII species in chloroperoxidase (a related, thiolate-ligated heme enzyme) and P450.^{4,5} Thus, it would be extremely challenging to observe photochemical generation of CI via two sequential rounds of flash-quench, much less characterize the reaction of this active hydroxylating species with substrate.

Instead, if we can generate CII by chemical means with sufficient yield and purity, we may be able to photo-trigger the second oxidation step. The rigorous purification that can be achieved for thermo-stable CYP119 has been cited as the most critical aspect for chemical oxidation to CI in high yield.⁶ If we can extend our photochemical system to CYP119, we anticipate that one-electron *chemical* oxidation followed by one-electron *photochemical* oxidation will form CI.

If we wish to use flash-quench to generate observable yields of CI, we also must gain a better understanding of the factors affecting the rate and yield of photochemical heme oxidation. The rate constant for heme oxidation to the porphyrin radical ($\text{Fe}^{\text{III}}(\text{OH}_2)\text{P}^{\bullet+}$) is $k = 8 \times 10^5 \text{ s}^{-1}$ at pH 8.¹ This rate is similar to that observed for heme systems containing a direct, covalent linkage between the photosensitizer and the porphyrin framework,⁷ suggesting that a favorable coupling pathway connects the photosensitizer and heme in our Ru-P450 conjugate.

The intervening protein medium between electron donor and acceptor influence the efficiency of ET over long distances; this is discussed in more detail in Chapter 4. In particular, aromatic amino acid residues can participate as redox intermediates in multi-step ET, or electron “hopping.”⁸⁻¹⁰ Tryptophan is a redox

intermediate in photo-triggered electron hopping in a rhenium-modified blue copper protein, *Pseudomonas aeruginosa* azurin (**Figure 3.5**). The electronically excited rhenium carbonyl complex transiently oxidizes a nearby tryptophan, which in turn oxidizes the copper center.⁸ This multistep reaction accelerated the overall copper oxidation event by two orders of magnitude compared to single step ET tunneling over the same distance.

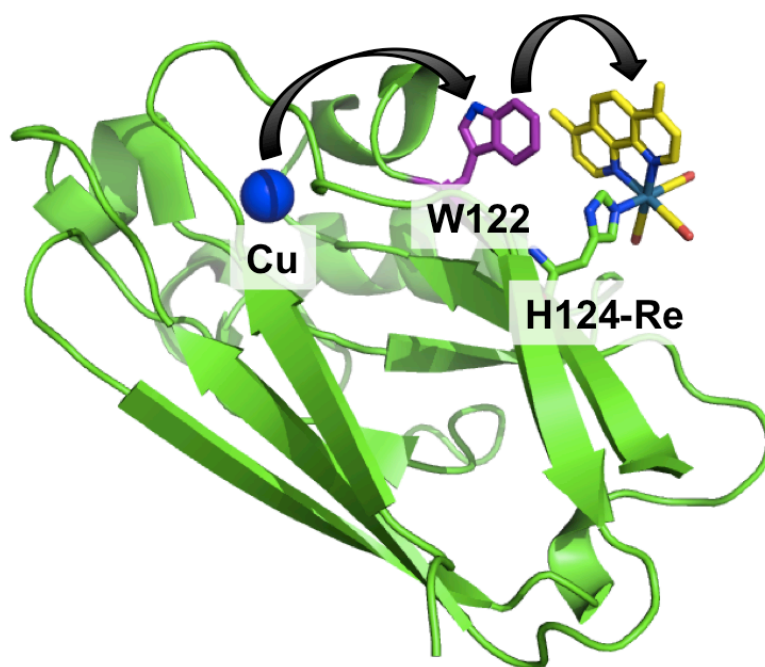


Figure 3.4. Multistep ET in rhenium-labeled azurin. Black arrows indicate the two ET steps that oxidize the protein metal center.

We noted that the photosensitizer tethering position in our Ru-P450_{BM3} conjugate is directly adjacent to tryptophan 96, which forms hydrogen bonds with a heme propionate. We have hypothesized that this intervening tryptophan facilitates hole transfer to the heme (**Figure 3.5**), in analogy to work on azurin.

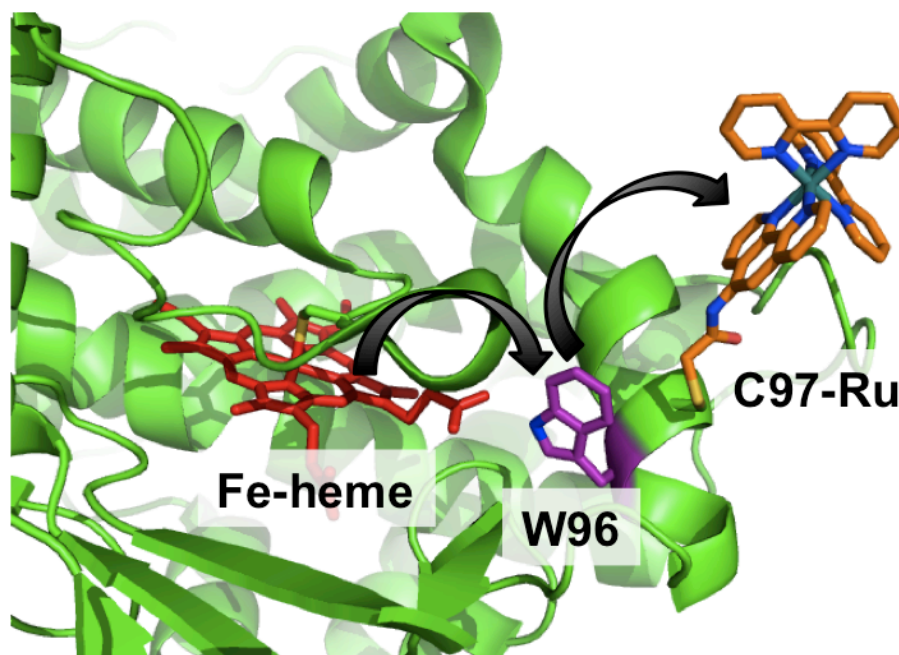


Figure 3.5. Multistep ET in ruthenium-labeled cytochrome P450. Black arrows indicate the two ET steps that oxidize the protein metal center.

This Chapter describes our efforts to probe the role of W96 in the photochemical heme oxidation of Ru_{C97}-P450 BM3, and to engineer a similar system that will allow photo-triggered oxidation of the CYP119 active site, with the aim of photochemical production of compound I in this thermostable enzyme.

3.1.1. P450 systems: Motivation and selection

The functional photochemical system in P450 BM3 (Chapter 2) involves a triple mutant of the heme domain, which will be abbreviated as C97-BM3(W). Two native surface-exposed cysteines were removed (C62A/C156S) and a single cysteine added (K97C) to achieve selective, covalent conjugation of the photosensitizer [Ru(2,2'-bipyridine)₂(5-iodoacetamido-1,10-phenanthroline)]²⁺ (Ru^{II}(bpy)₂(Iaphen)) directly adjacent to W96 (**Figure 3.6**).

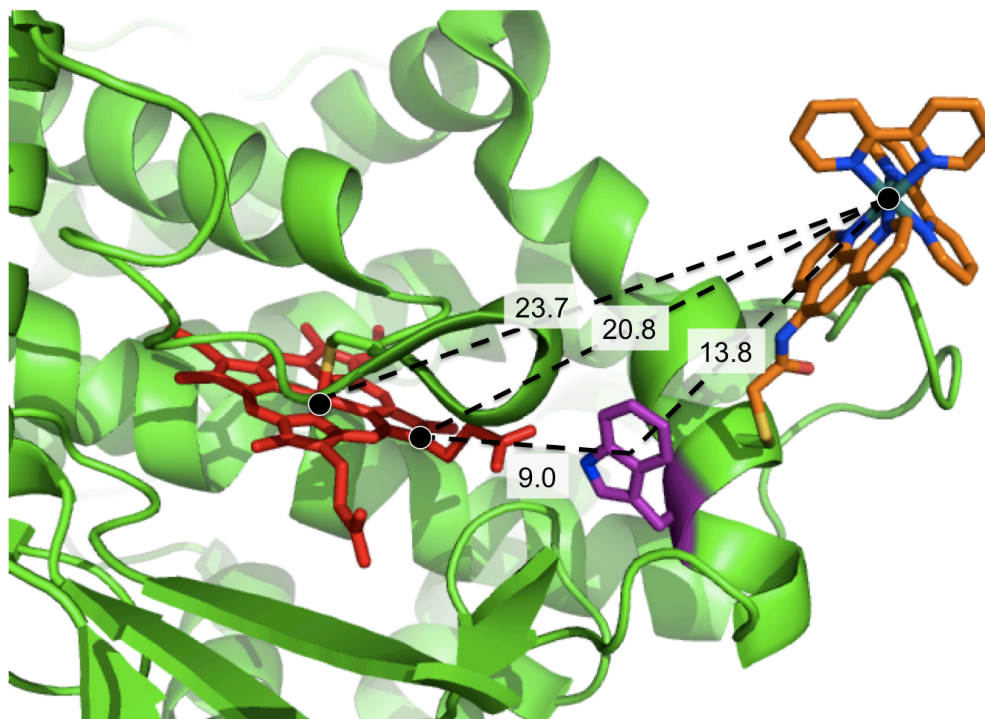


Figure 3.6. Putative multistep ET pathway in Ru_{C97}-BM3(W). Residue W96 forms hydrogen-bond contacts with the heme propionates (2.7, 3.5 Å). Highlighted distances are: Ru-Fe (23.7 Å), Ru-porphyrin edge (20.8 Å), Ru-W(centroid) (13.8 Å), W(centroid)-Fe (12.9 Å), W(centroid)-edge of pyrrole (9.0 Å).

To probe the role of this intervening tryptophan, we have generated the quadruple “W-negative” mutant: C62A/C156S/K97C/W96H, abbreviated C97-BM3(wH). Note that the subscript refers to the native residue, in this case, tryptophan. This mutation is expected to preserve hydrogen-bonding with the heme propionates, an aspect that is thought to provide structural stability to the heme.¹¹ More importantly, this mutation will act as a control in which multistep electron transfer is not expected to occur. The His^{•+}/His reduction potential ($E^\circ = 1.5$ V vs. NHE, phosphate buffer pH 8) is much higher than the analogous Trp^{•+}/Trp potential ($E^\circ = 0.98$ V vs. NHE, phosphate buffer pH 8).¹² The Ru^{III/II} reduction potential is approximately 1.3 V vs. NHE.^{13,14} Oxidation of histidine would be thermodynamically *uphill* by 200 mV, whereas oxidation of tryptophan has a

driving force of approximately 300 mV. If this W96 is indeed involved in multistep electron transfer, we would expect the W96H mutation to drastically impair photochemical heme oxidation by Ru^{III} oxidants.

Alternatively, this tryptophan could act as a sink for electron holes, sequestering the oxidizing equivalents away from the heme and lowering the yield of compound II formation. Chemical oxidation of P450-cam from *Pseudomonas putida* and P450-BM3 by oxygen donors (hydrogen peroxide, peroxyacids) has been shown to result in formation of a so-called “compound ES”, a ferryl species in which one oxidizing equivalent had been transferred to an amino-acid side chain near the heme – either tryptophan or tyrosine.^{15,16} If this is the case for our photochemical system, we would anticipate that the W96H mutation would actually *increase* the observed rate and yield of heme oxidation.

To develop a photochemical system in CYP119, we chose to mimic Ru-P450-BM3 as closely as possible. In the slightly smaller, more compact CYP119 (**Figure 3.7**), the only native cysteine residue is C317; this residue is buried within the protein active site, and provides critical thiolate ligation to the heme. Therefore, a single mutation is sufficient to achieve selective photosensitizer conjugation. In the native structure of CYP119, H76 forms hydrogen bonds to the CYP119 heme propionates, analogous to W96 in P450 BM3. The adjacent residue is D77 (analogous to K97), and we have mutated this to cysteine to allow photosensitizer conjugation (**Figure 3.8**). This mutant will be abbreviated C77-CYP119(H).

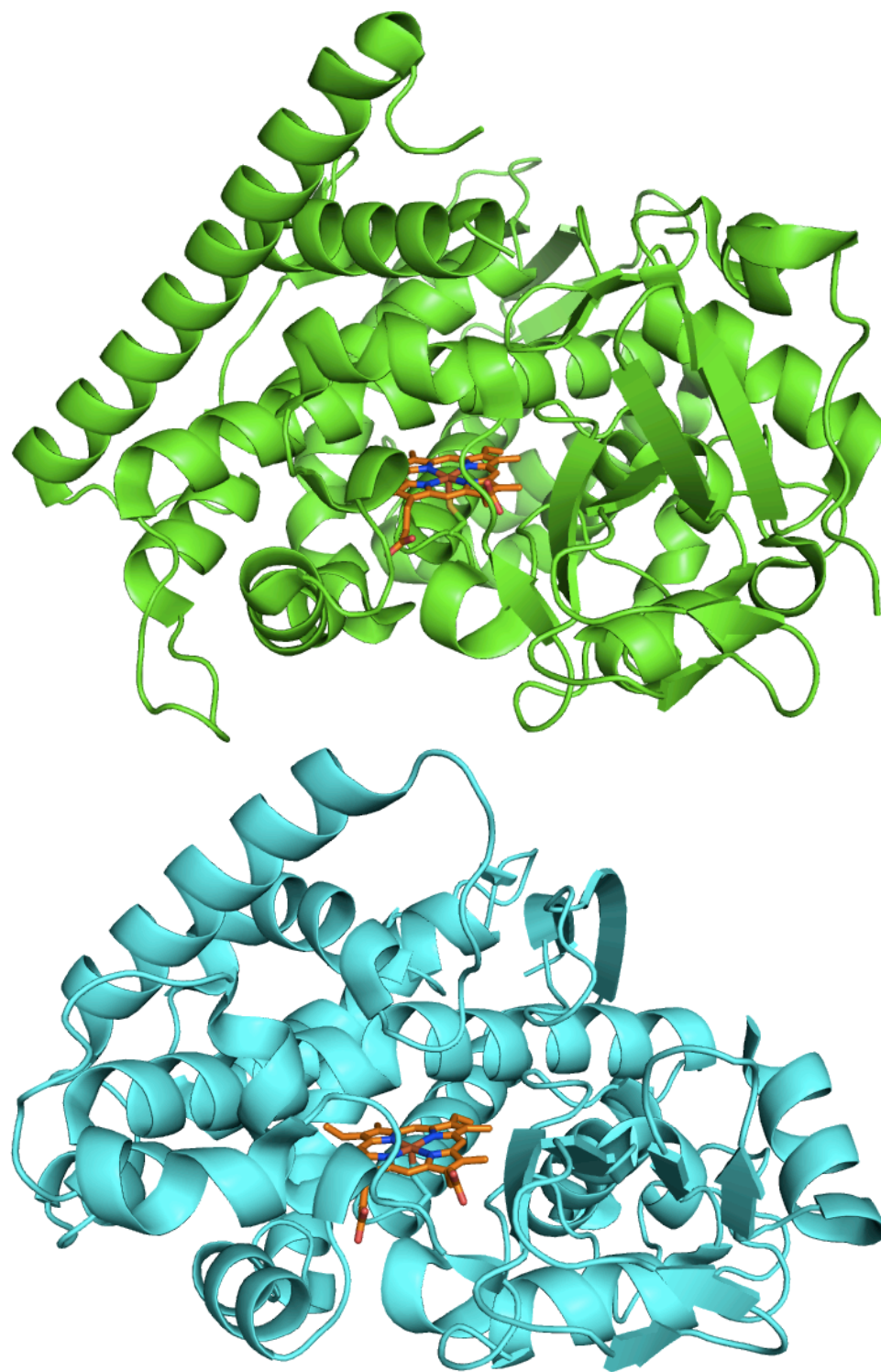


Figure 3.7. Structures of P450 BM3 (top, green. PDB: 2IJ2) and CYP119 (bottom, cyan. PDB 1IO7).

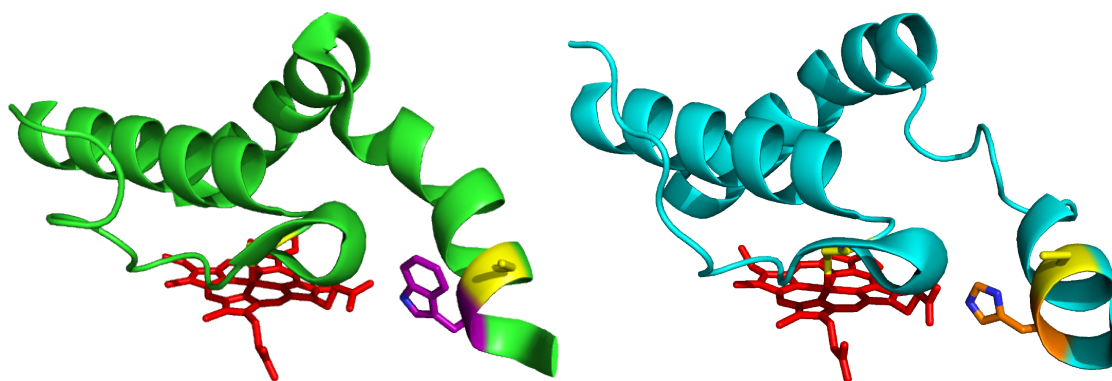


Figure 3.8. Photosensitizer conjugation sites in P450-BM3 (left, green) and CYP119 (right, cyan) are highlighted in yellow.

As discussed for the P450-BM3 systems, we wish to probe the role of tryptophan in assisting or impeding electron transfer. With this goal in mind, we will also generate a tryptophan-containing CYP119 double mutant D77C/H76W. This mutant is abbreviated as C77-CYP119_(HW); note, again, that the subscript denotes the native residue.

3.2. Results and Analysis

3.2.1. Characterization of mutants

It is possible that a seemingly-insignificant mutation can have large effects on protein stability and structure. It is critical to verify that there are no observable changes in structure or stability of the mutants. The three mutants have been characterized by UV-visible absorption, and mass spectrometry. Crystals were obtained for the C97-BM3_(WH) mutant, and the crystal structure was determined.

UV-visible absorbance

All of the P450 mutants have strong Soret absorbances near 420 nm, and Q-band features in the 500-600 nm range. The P450-BM3 mutants have a Soret maximum at 418 nm, while both CYP119 mutants have a Soret maximum at 416 nm (**Figure**

3.9). The Soret maximum is very sensitive to environment, including changes in buffer composition and protein purity. Therefore, small changes in absorbance must be assessed with care. The origin of the discrepancy in absorbance between C97-BM3_(wH) and the other three mutants has not been determined.

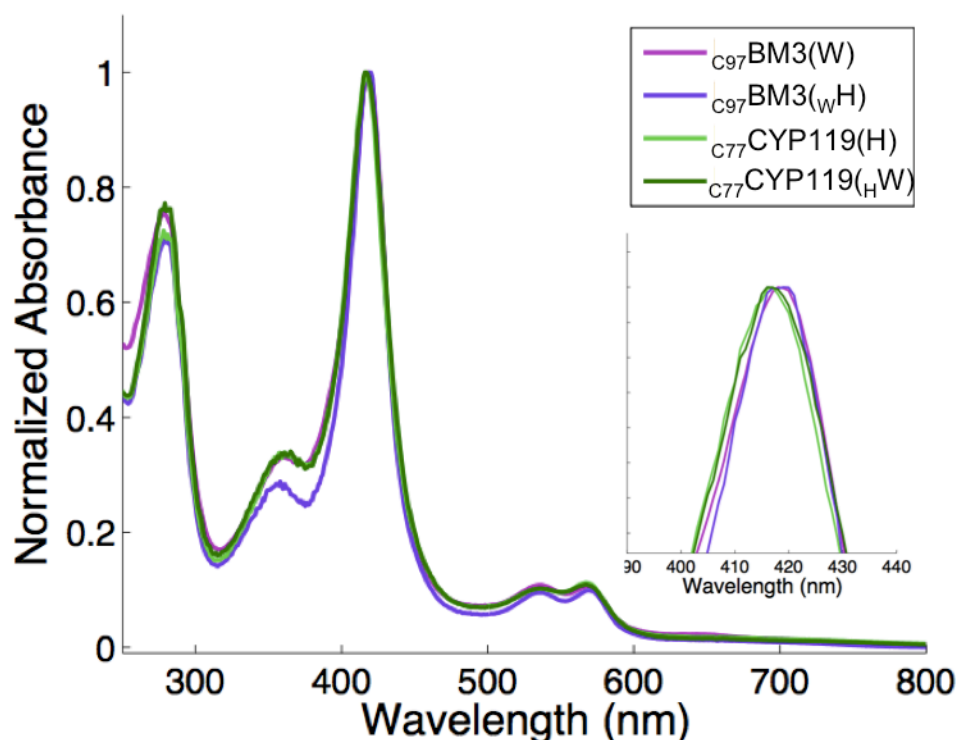


Figure 3.9. UV-visible absorbance spectra of P450 mutants. C97-BM3(W) (magenta), C97-BM3_(wH) (purple), C77-CYP119(H) (light green), C77-CYP119_(HW) (dark green).

X-ray crystal structure analysis of C97-BM3_(wH)

The crystal structure of C97-BM3_(wH) has been determined with 2.2 Å resolution. Two monomers were found in the asymmetric unit. The C97-BM3_(wH) structure overlays very well with WT P450 BM3 in the open, substrate-free form (pdb: 2IJ2, RMSD = 0.277). C97-BM3_(wH) overlays significantly less well with the closed, substrate-bound form (2UWH, RMSD = 0.666) (**Figure 3.10**). This is in contrast

to the crystal structure of Ru_{C97}-BM3(W), which crystallized in the open form, with an unidentified substrate in the pocket.

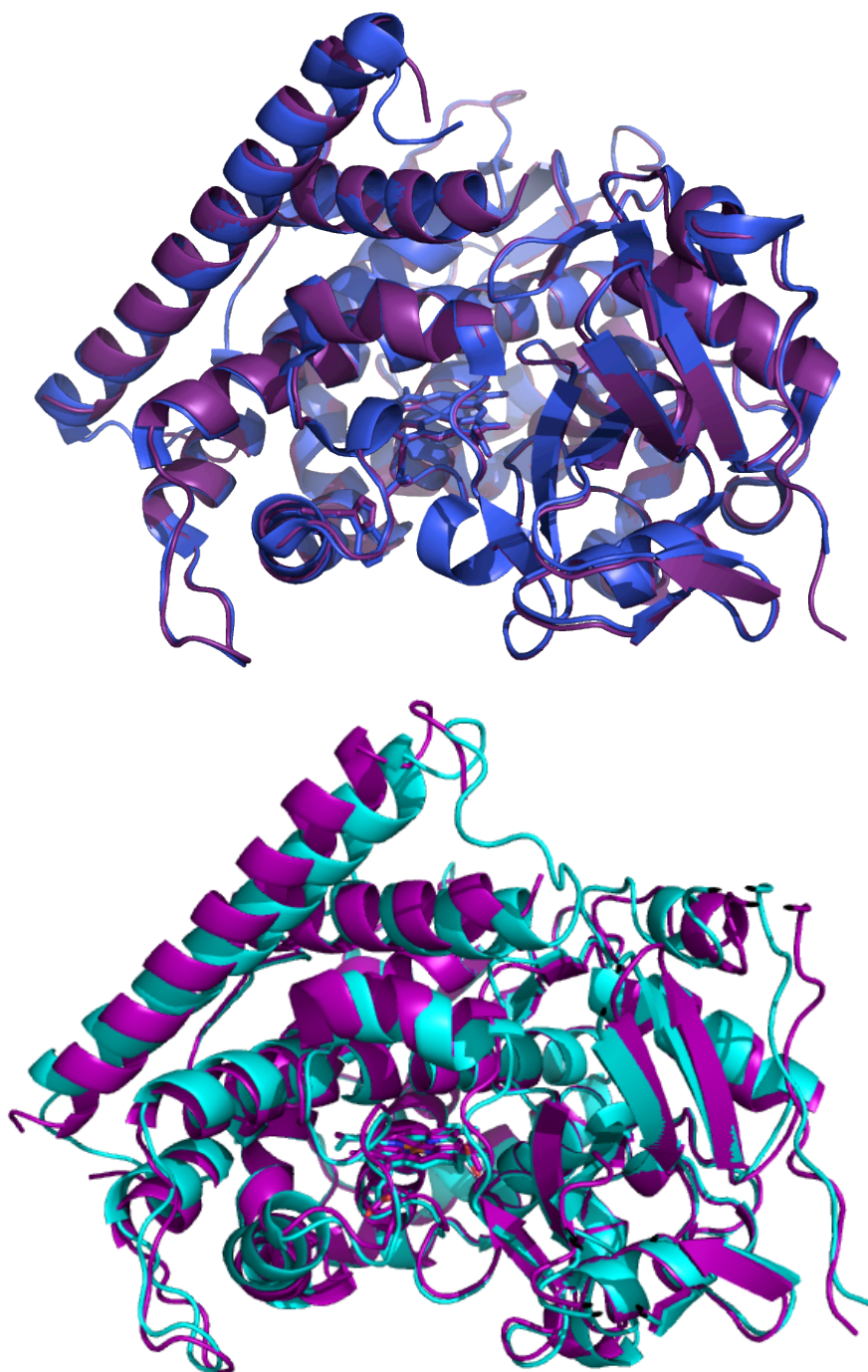


Figure 3.10. Overlay of C97-BM3_(wH) (purple) with open and closed WT BM3 structures. **Top:** Open form (blue). **Bottom:** Closed form (cyan).

Electron density clearly shows the W96H mutation (**Figure 3.11**). H96 is within hydrogen-bond distance of the heme propionate (2.8 and 4.4 Å between His96 Ne and the two propionate oxygen atoms, respectively). The position of this residue overlays almost exactly with the indole moiety of W96 in the wild-type structure.

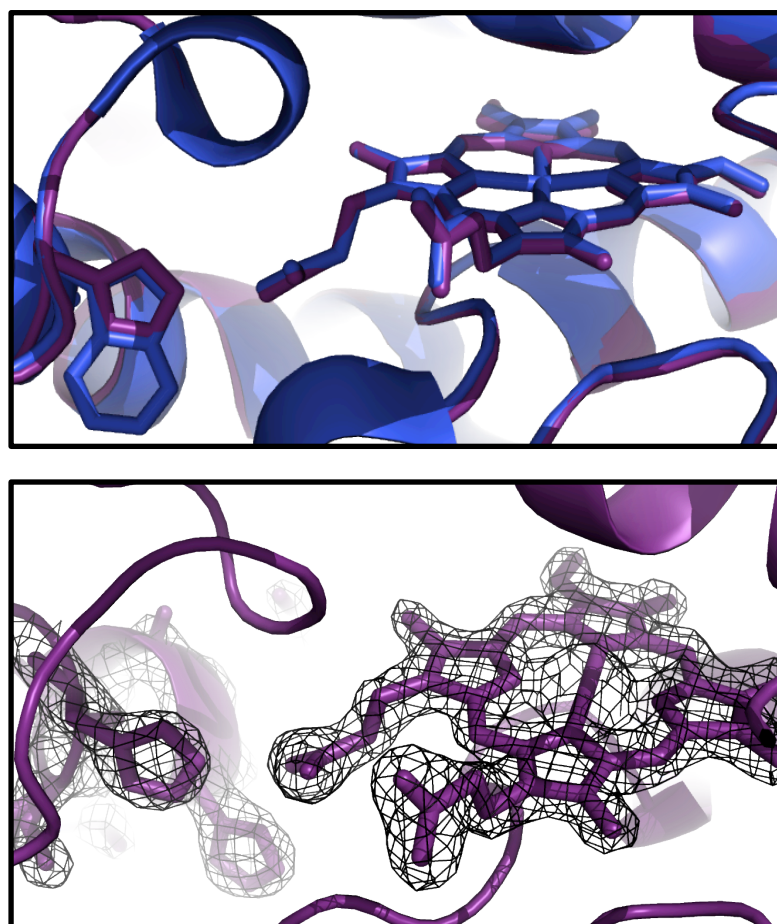


Figure 3.11. C97-BM3_(wH) active site. **Top:** Overlay of C97-BM3_(wH) (purple) with WT P450 BM3 (PDB: 2IJ2, blue), highlighting the overlay of W96 and H96 residues. **Bottom:** Electron density map showing H96 within hydrogen bond contact of the heme propionates.

Based on comparison of the C97-BM3_(wH) structure to that of WT P450 BM3, it appears that this single mutation has no significant effect on the structure. We anticipate that possible changes in rate or yield of heme oxidation are a direct

result of the tryptophan-to-histidine substitution, and not to other structural perturbations.

3.2.2. Ru-P450 Luminescence

Steady state and transient luminescence spectroscopies were used to probe the nature of the photosensitizer conjugated to the P450 surface. When excited with blue light (e.g., 480 nm), the steady-state spectrum of all Ru-P450 conjugates closely resembles those of the free photosensitizer $[\text{Ru}^{\text{II}}(2,2'\text{-bipyridine})_2(5\text{-acetamido-1,10-phenanthroline})]^{2+}$ ($[\text{Ru}(\text{bpy})_2(\text{A-phen})]^{2+}$) and $[\text{Ru}(\text{bpy})_3]^{2+}$ (see Chapter 2 for an example). None of the unlabeled P450 mutants show detectable luminescence.

Luminescence decays and exponential fits of all four Ru-P450 conjugates are shown in **Figure 3.13**. Lifetimes for all four mutants are reported in **Table 3.1**. As discussed in Chapter 2, the $\text{Ru}^{\text{II}}_{\text{C97-BM3(W)}}$ excited state decay is biexponential, with approximately 65% of a 200 ns decay component, and 35% of a 50 ns decay component. We interpreted this observation as two different conformations of the photosensitizer that do not exchange on the timescale of this measurement. In the presence of quencher, the luminescence lifetime is dramatically reduced, and can be approximated by a monoexponential decay with lifetime of 30 ns.

The other mutants show similar luminescence decays, with minor differences. The histidine-containing mutants ($\text{Ru}^{\text{II}}_{\text{C97-BM3(WH)}}$ and $\text{Ru}^{\text{II}}_{\text{C77-CYP119(H)}}$) are nearly monoexponential. As is evident from the overlays (**Figure 3.14**), there is a strong similarity in the luminescence decay of the two histidine-containing mutants (green, blue), as well as similarity between the tryptophan containing mutants (red, purple). Curiously, the excited state of $\text{Ru}^{\text{II}}_{\text{C77-CYP119(H)}}$ is not as effectively quenched by 17 mM $[\text{Ru}(\text{NH}_3)_6]^{3+}$, in comparison to the other conjugates.

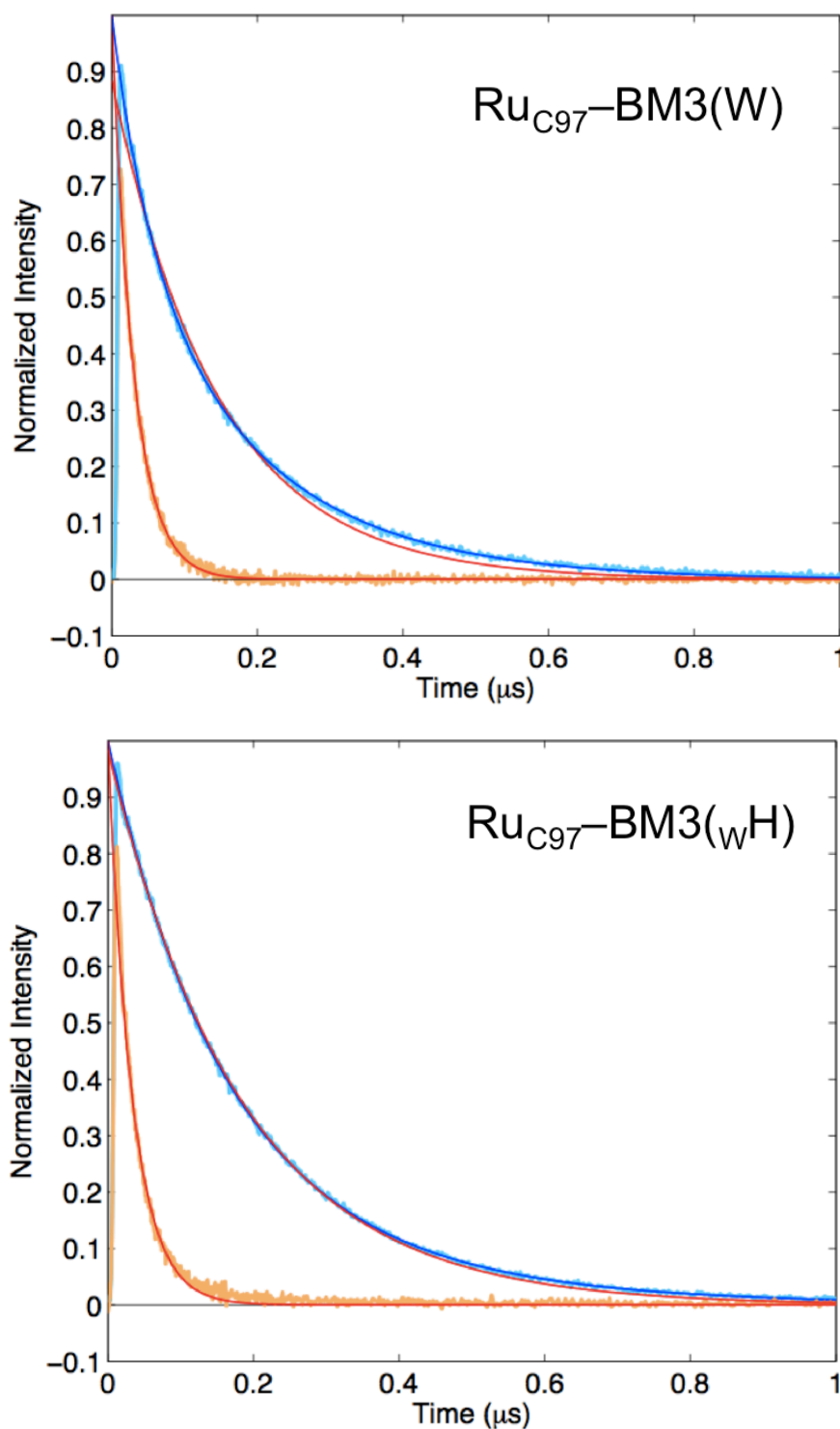


Figure 3.12. Time-resolved luminescence decays of Ru-BM3 conjugates in the presence (blue) and absence (orange) of 17 mM $[\text{Ru}(\text{NH}_3)_6]^{3+}$ quencher. Monoexponential fits are shown in red, biexponential fits are shown in dark blue. Samples were excited at 480 nm, and luminescence was detected at 630 nm.

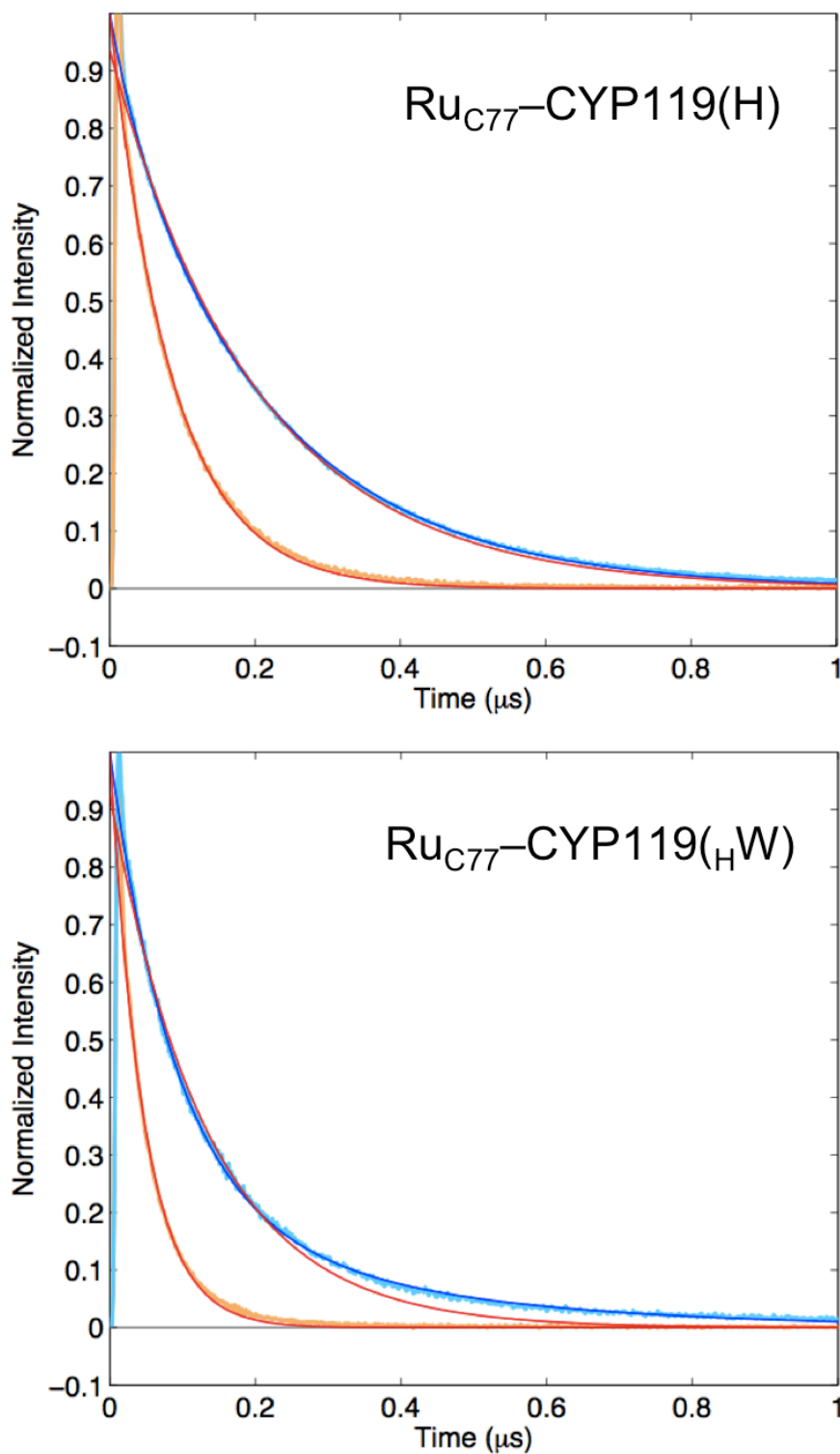


Figure 3.13. Time-resolved luminescence decays of Ru-CYP119 conjugates in the presence (blue) and absence (orange) of 17 mM $[\text{Ru}(\text{NH}_3)_6]^{3+}$ quencher. Monoexponential fits are shown in red, biexponential fits are shown in dark blue. Samples were excited at 480 nm, and luminescence was detected at 630 nm.

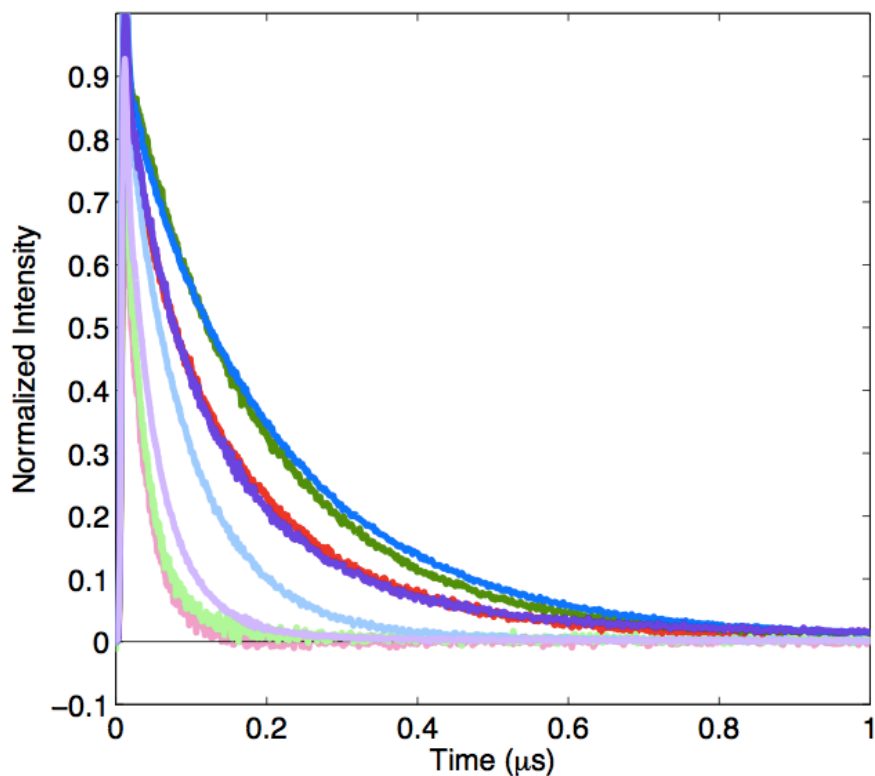


Figure 3.14. Overlay of luminescence decays for four Ru-P450 conjugates. 630 nm, in the absence (bold colors) and presence (pastels) of 17 mM $[\text{Ru}(\text{NH}_3)_6]^{3+}$ quencher. $\text{Ru}^{\text{II}}_{\text{C97}}\text{-BM3(W)}$ (red, pink); $\text{Ru}^{\text{II}}_{\text{C97}}\text{-BM3}_{(\text{WH})}$ (green); $\text{Ru}^{\text{II}}_{\text{C77}}\text{-CYP119(H)}$ (blue); $\text{Ru}^{\text{II}}_{\text{C77}}\text{-CYP119}_{(\text{HW})}$ (purple).

Table 3.1. Excited state lifetimes of four Ru-P450 conjugates in the absence and presence of 17 mM $[\text{Ru}(\text{NH}_3)_6]^{3+}$ quencher. Both major (a) and minor (b) components are listed for the biexponential fit. Samples were excited at 480 nm, and luminescence was detected at 630 nm.

Enzyme	conditions	$\tau_{\text{mono}}(\text{ns})$	$\tau_{\text{a}}(\text{ns})$	$\tau_{\text{b}}(\text{ns})$	%a	%b
$\text{Ru}_{\text{C97}}\text{-BM3(W)}$	unquenched	140	190	52	65	35
	$[\text{Ru}(\text{NH}_3)_6]^{3+}$	30				
$\text{Ru}_{\text{C97}}\text{-BM3}_{(\text{WH})}$	unquenched	180	160	310	80	20
	$[\text{Ru}(\text{NH}_3)_6]^{3+}$	33				
$\text{Ru}_{\text{C77}}\text{-CYP119(H)}$	unquenched	200	220	45	85	15
	$[\text{Ru}(\text{NH}_3)_6]^{3+}$	91				
$\text{Ru}_{\text{C77}}\text{-CYP119}_{(\text{HW})}$	unquenched	130	91	320	75	25
	$[\text{Ru}(\text{NH}_3)_6]^{3+}$	48				

3.2.3. Ru-P450 transient absorption

We have probed ET in the Ru-P450 systems using single-wavelength transient absorption (TA) spectroscopy. As described in Chapter 2 and illustrated in **Figure 3.9**, both the photosensitizer and P450 heme have strong electronic absorbance in the 390-440 nm region, and the shapes and positions of these electronic transitions are sensitive to metal oxidation state and environment.

As found for Ru^{II}C97-BM3(W), TA traces of the other three mutants in the absence of exogenous quencher reveal bleaching in the 390-440 nm region, consistent with formation and decay of the *Ru(II) excited state; there is no observed formation of electron transfer intermediates. None of the unlabeled proteins show detectable transient absorption features following excitation at 480 nm (data not shown).

P450-BM3 mutants: effect of tryptophan 96

We first compare the tryptophan- and histidine-containing P450-BM3 photochemical systems. As described in Chapter 2, transient absorption features for RuC97-BM3(W) displays complex, multiexponential kinetics in the presence of ET quencher, [Ru(NH₃)₆]³⁺ (**Figure 3.15**, left). In particular, we observed a bleach at 420 nm (the peak of the heme Soret) which persisted for nearly 200 ms; this was indicative of heme oxidation. Additionally, we observed an increase in absorption at 440 nm, which was attributed to the formation of high-valent CII on the millisecond timescale. If heme oxidation occurs in the other mutants, we expect to see similar TA features.

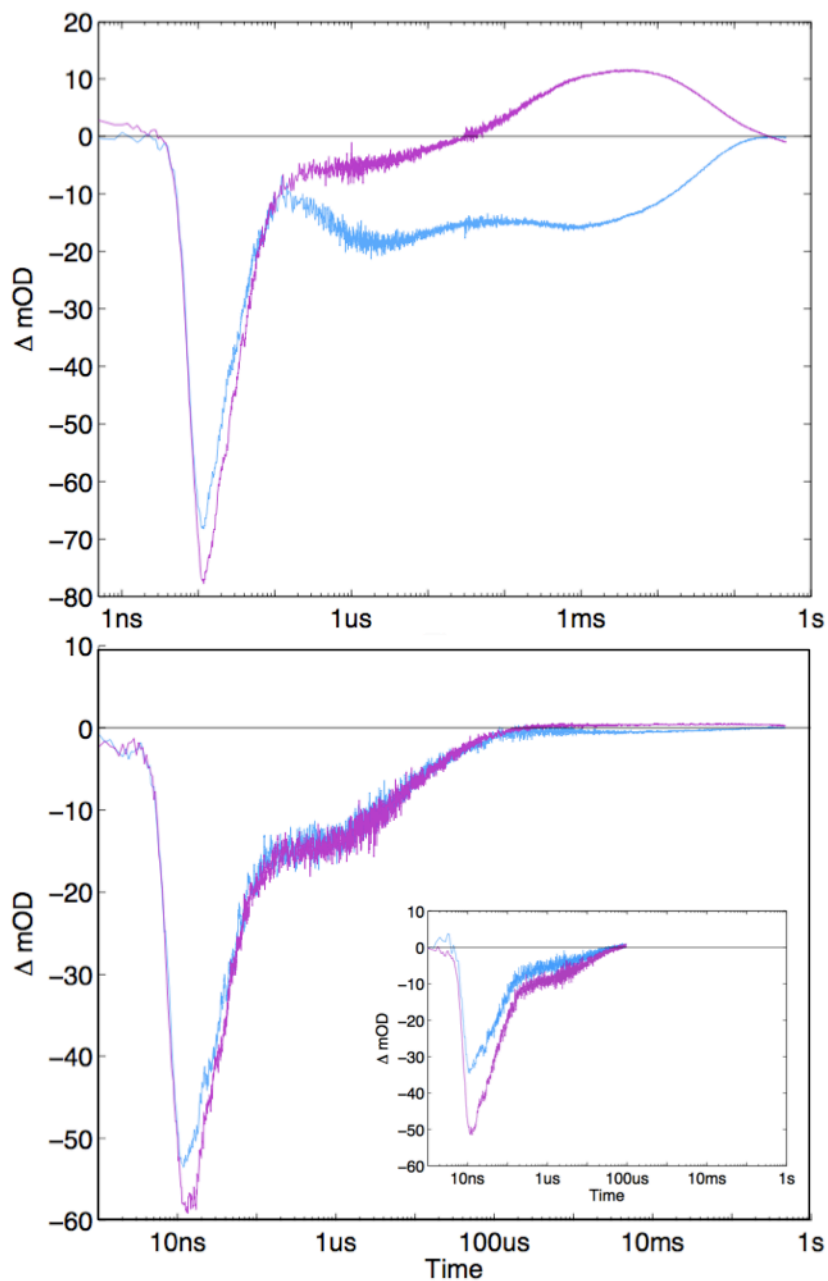


Figure 3.15. Single wavelength TA traces of Ru_{K97C} - $P450_{BM3}$ conjugates in the presence of $[Ru(NH_3)_6]^{3+}$, following excitation at 480 nm. Blue: 420 nm; Purple: 440 nm. **Top:** $RuC97$ - $BM3(W)$. **Bottom:** $RuC97$ - $BM3(WH)$. **Inset:** Model complex $[Ru(bpy)_2(Aphen)]^{2+}$ with $[Ru(NH_3)_6]^{3+}$, for comparison.

For the histidine-containing mutant, RuC97-BM3(wH), TA traces in the presence of $[\text{Ru}(\text{NH}_3)_6]^{3+}$ are significantly simpler (**Figure 3.15**, right). TA features at all wavelengths examined (390-440 nm) show biphasic decays that return to baseline within 200 μs . There is no persistent bleach at 420 nm past 100 μs , nor is there an increase in absorption at 440 nm at any point in time. The observed features can be explained by a simple reaction scheme involving only the photosensitizer, with no heme oxidation (**Figure 3.16**). Indeed, the TA traces for RuC97-BM3(wH) are nearly identical to those seen for the free photosensitizer $[\text{Ru}(\text{bpy})_2(\text{Aphen})]^{2+}$ with $[\text{Ru}(\text{NH}_3)_6]^{3+}$ (**Figure 3.15**, inset).

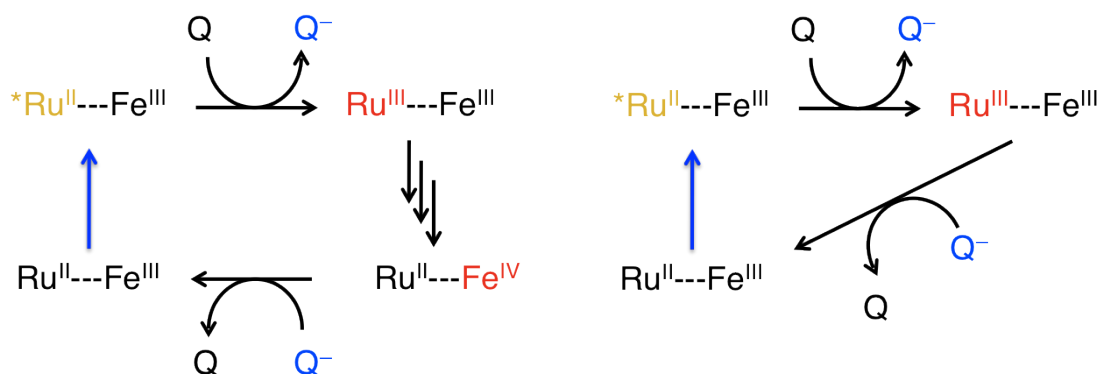


Figure 3.16. Flash-quench schemes. **Left:** Photochemically-generated $\text{Ru}^{\text{III}}_{\text{C97-BM3(W)}}$ oxidizes the BM3(W) heme. Multiple arrows indicate that several processes are required to form the Fe(IV) product. **Right:** Photochemically-generated $\text{Ru}^{\text{III}}_{\text{C97-BM3(wH)}}$ nonproductively recombines with reduced quencher.

ET reactivity of CYP119 mutants

We have also examined flash-quench of $\text{Ru}_{\text{C77-CYP119(H)}}$ and $\text{Ru}_{\text{C77-CYP119(H)W}}$ in the presence of $[\text{Ru}(\text{NH}_3)_6]^{3+}$. For $\text{Ru}_{\text{D77C-CYP119(H)}}$, biphasic kinetics are observed in the 390-440 nm region (**Figure 3.17**). These are nearly identical to those observed for $\text{Ru}_{\text{C97-BM3(wH)}}$, and can be explained in a similar $^*\text{Ru}^{\text{II}} \rightarrow \text{Ru}^{\text{III}} \rightarrow \text{Ru}^{\text{II}}$ reaction scheme, with no involvement of the heme center.

TA traces for Ru_{C77}-CYP119_(HW) are distinct from its histidine-containing counterpart, and can be compared to the tryptophan-containing BM3 mutant. As seen for the functional system Ru_{C97}-BM3(W), there is a small but persistent bleach at 420 nm, and another (even smaller) increase in absorbance at 440 nm on the millisecond timescale. These transient signals are much smaller than for Ru_{C97}-BM3(W) (< 5 mOD), but they have similar wavelength profiles, and occur on similar timescales (**Figure 3.17**, inset).

Unfortunately, the small signal amplitudes and poor signal-to-noise ratio make it difficult to extract rate constants for the formation and decay of intermediates in the Ru_{C77}-CYP119_(HW) system. The ET event of interest is oxidation of the porphyrin to form Fe^{III}(OH₂)(porphyrin)^{+•} species. In Ru_{C97}-BM3(W), this is observed as a pronounced, re-bleaching at 420 nm that reaches completion at ~ 2 μs (see **Figure 3.17**, inset). Additionally, two Fe^{III}(OH₂)(porphyrin)^{+•} species were identified, in addition to the formation of CII. In Ru_{C97}-BM3_(WH), however, this second bleach not apparent, and cannot be readily distinguished from Ru^{III} formation. The low signal-to-noise ratio at all wavelengths examined also makes it difficult to characterize intermediates (such as multiple Fe^{III}(OH₂)(porphyrin)^{+•} species). Guided by the transient at 440 nm, it may be possible to determine a rate for CII formation. However, without knowing the identity of the preceding species, it is difficult to draw conclusions as to the molecular nature of that event.

From the current TA data, we cannot quantitatively determine if the small amplitudes are primarily a result of decreased heme oxidation rate, or a decrease in yield by competition with nonproductive ET processes. It appears that the maximum signal amplitude at 440 nm occurs at 4 ms for Ru_{C97}-BM3(W) (**Figure 3.17** inset, red trace), while the maximum signal for Ru_{C77}-CYP119_(HW) is seen at

30 ms; this suggests that a difference in rate of CII formation may account for some of the discrepancy.

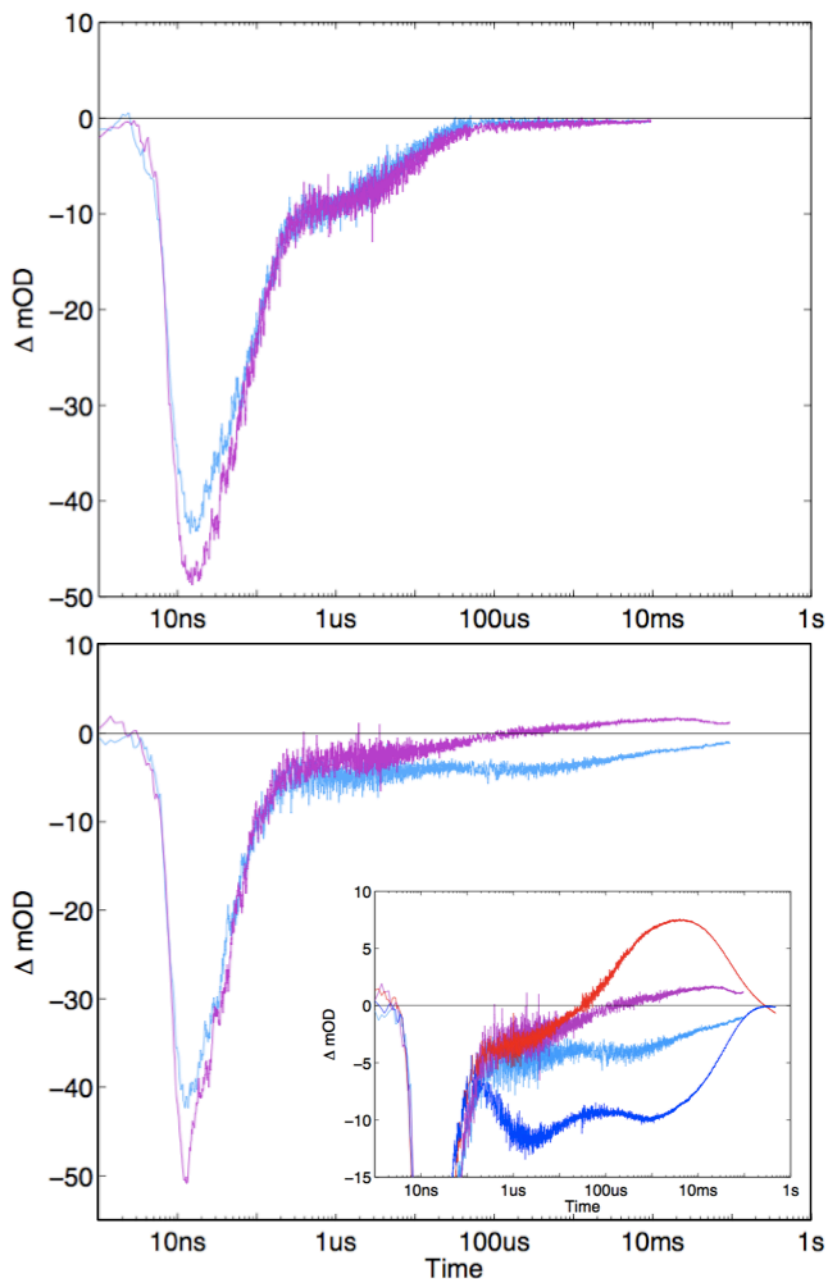


Figure 3.17. Single wavelength transient absorption traces of Ru-CYP119 conjugates in the presence of $[Ru(NH_3)_6]^{3+}$, following excitation at 480 nm. Light blue: 420 nm; purple: 440 nm. **Left:** Ru_{C77} -CYP119(H). **Right:** Ru_{C77} -CYP119(H)W). **Inset:** Overlay of TA from Ru_{C97} -BM3(W) scaled to the magnitude of the $*Ru^{II}$ bleach: 440 nm (red), 420 nm (dark blue).

Temperature dependence

The flash-quench transient absorption studies for Ru-CYP119 conjugates also were conducted at elevated temperature (40 °C).

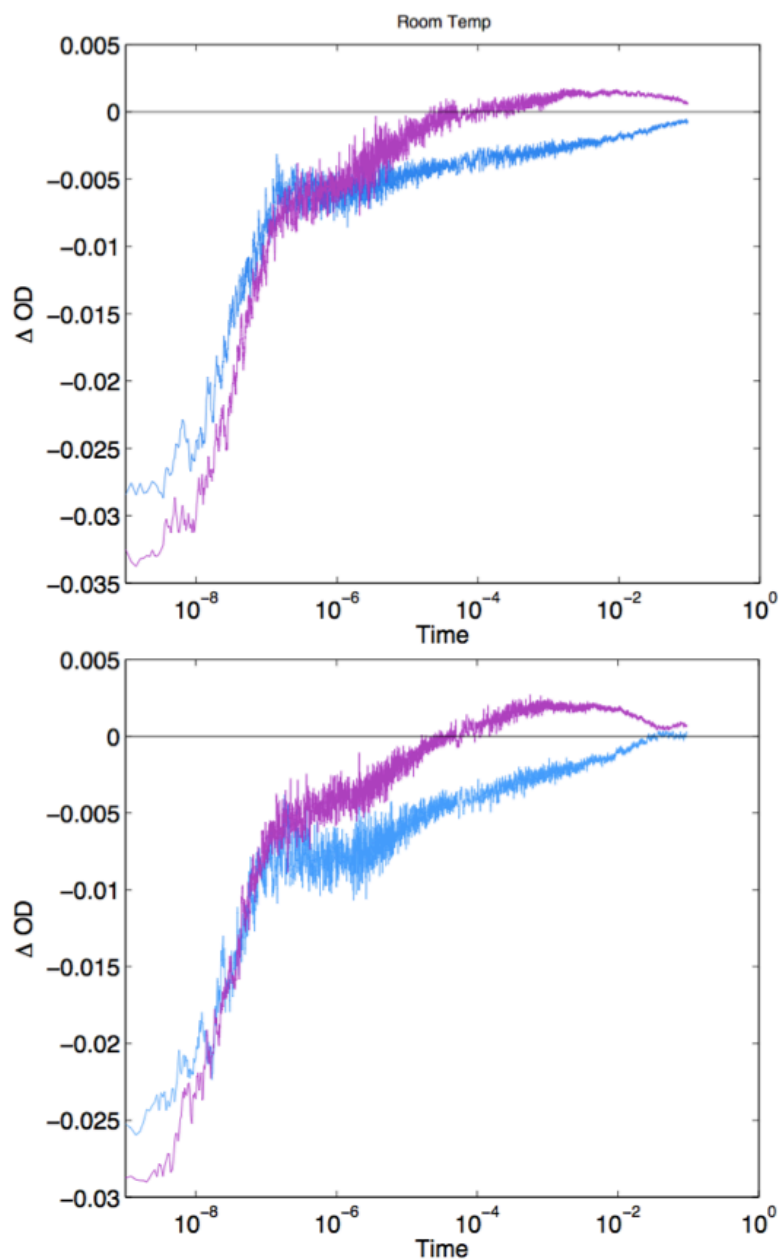


Figure 3.18. TA data of Ru_{C77}-CYP119_(HW) at variable temperature. 420 nm (blue) and 440 nm (purple). **Top:** Room temperature. **Bottom:** 40 °C.

The magnitudes of TA features are slightly larger at a temperature of 40 °C, however, the increase is not sufficient to distinguish ET quenching of the photosensitizer (Ru^{III} formation) from porphyrin oxidation. While the CYP119 enzyme is stable over temperatures of 80 °C, the $[\text{Ru}(\text{NH}_3)_6]^{3+}$ quencher noticeably decomposes at temperatures of 70 °C.

Search for the transient tryptophan radical

Direct observation of the oxidized tryptophan intermediate would provide more tangible support for a hopping mechanism. Tryptophan radical cation ($\text{W}^{\bullet+}$) and neutral radical (W^{\bullet}) species absorb in the visible region (**Figure 3.19**), with approximate extinction coefficients of $\epsilon(\lambda_{\text{max}}: 560 \text{ nm}) = 3000 \text{ M}^{-1} \text{ cm}^{-1}$ and $\epsilon(\lambda_{\text{max}}: 510 \text{ nm}) = 2300 \text{ M}^{-1} \text{ cm}^{-1}$, respectively.¹⁷ We examined TA in the 500-600 nm region to see if such an intermediate could be identified in the $\text{Ru}_{\text{C97}}\text{-BM3(W)}$ and $\text{Ru}_{\text{C77}}\text{-CYP119(HW)}$ systems (see Appendix C for more details). Unfortunately, we are unable to identify the formation of these species.

If the rate of tryptophan oxidation is slower than its reduction via ET from the porphyrin, we would not anticipate accumulation of $\text{W}^{\bullet+}/\text{W}^{\bullet}$ species. It is also possible that any tryptophan radical transients are obscured by changes in absorbance of the ruthenium photosensitizer ($^*\text{Ru}^{\text{II}}, \text{Ru}^{\text{III}}, < 30 \mu\text{s}$) and the P450 Q-bands. In particular, the latter fully overlap with the ($\text{W}^{\bullet+}$) and (W^{\bullet}) absorbances, but with much higher extinction coefficients: $\epsilon(\lambda_{\text{max}}: 536 \text{ nm}) = 9800 \text{ M}^{-1} \text{ cm}^{-1}$ and $\epsilon(\lambda_{\text{max}}: 568 \text{ nm}) = 9570 \text{ M}^{-1} \text{ cm}^{-1}$.

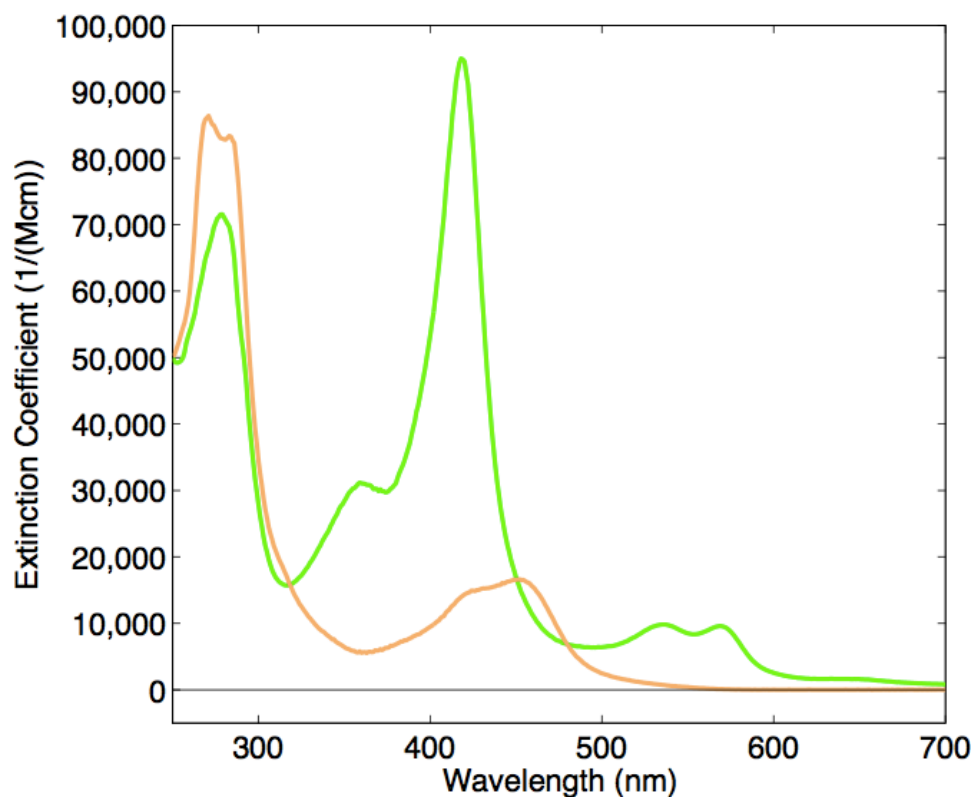


Figure 3.19. UV-visible absorbance spectra P450 and Ru photosensitizer. $[\text{Ru}(\text{bpy})_2(\text{IAphen})]^{2+}$ (orange) and $\text{Ru}_{\text{C97-BM3(W)}}$ (green), assuming $\epsilon(418 \text{ nm}, \text{P450 BM3})=95,000 \text{ M}^{-1} \text{ cm}^{-1}$,¹⁸ $\epsilon(450 \text{ nm}, [\text{Ru}(\text{bpy})_2(\text{Aphen})]^{2+})=15,000 \text{ M}^{-1} \text{ cm}^{-1}$.¹⁹

3.3. Discussion

We expressed and characterized a P450 BM3 mutant in which W96 has been replaced by histidine: C97-BM3(WH). This point mutation does not affect the structure of this enzyme, as examined by crystal structure analysis and comparison to wild-type P450 BM3. The $\text{Ru}_{\text{C97-BM3(WH)}}$ conjugate system supports flash-quench to form Ru^{III} oxidants, as observed by TA. There is no observable formation of oxidized P450 intermediates, such as porphyrin cation radicals and CII species. These results suggest that in our original construct, $\text{Ru}_{\text{C97-BM3(W)}}$, the W96 residue is transiently oxidized in a multi-step electron transfer reaction; this accelerates the ET event and allows accumulation of oxidized heme species. In the absence of W96, the rate of single-step heme oxidation may be unable to

compete with bimolecular recombination with reduced quencher ($\tau \sim 25 \mu\text{s}$). We cannot conclusively rule out the possibility that W96 acts as a sink for some portion of the photogenerated holes. However, our TA data suggest that the ET rate advantage conveyed by W96 is a more important pathway.

We also generated a thermostable CYP119 Ru-P450 conjugate in which the photosensitizer-tethering point mimics that of the Ru-BM3 system. Flash-quench of Ru_{C77}-CYP119(H) generates Ru^{III}; however, no heme oxidation is observed. TA data are nearly identical to those of the histidine-containing P450 BM3 system, Ru_{C97}-BM3(WH). The H76W mutation (Ru_{C77}-CYP119(HW)) is sufficient to allow observation of at least a small amount of oxidized heme species. This observation also supports involvement of tryptophan in photochemical oxidation. We suggest that this residue (BM3(W) or CYP119(HW)) provides a relay station for accelerated multistep ET.

Many challenges still face this analysis. The small signal amplitudes and poor signal-to-noise of Ru_{C77}-CYP119(HW) transient features make it difficult to extract rate constants for the formation and decay of ET intermediates, particularly the formation of the initial porphyrin radical. The tryptophan side chain is significantly bulkier than that of histidine, and it is possible that the H76W mutation has caused a larger structural change which makes ET more difficult. Crystallographic characterization of the CYP119 mutants would be helpful for identifying or ruling out structural disruptions; these efforts are ongoing.

Another possibility for the small observed yield of heme oxidation is that the W^{+•}/W or por^{+•}/por reduction potentials in CYP119 may be different from those in P450 BM3. Unfortunately, the reactivity of these oxidized intermediates precludes experimental determination of reduction potentials.

Final thoughts and avenues for future work

One of the main objectives of developing the photochemical system in CYP119 was to establish a more robust framework in which we could chemically generate CII, followed by flash-quench to generate the active species, CI. By identifying the importance of the tryptophan residue in accelerating ET and/or improving ET yield, we have been able to observe the first indication of photochemical ET in CYP119. However, if we wish to observe photochemical generation of CI, we must make significant improvements on two fronts.

First, we must improve the rate and yield of heme oxidation in CYP119. This can be facilitated by a better understanding of the complex factors affecting ET. Crystallization of CYP119 mutants can help elucidate whether other structural features affect the hopping pathway between photosensitizer and heme. The photosensitizer potential can be tuned and the linker-length shortened by synthetic modification, the conjugation-site can be changed, and other mutations may be made to the protein scaffold in order to optimize ET. This knowledge will be useful not only in developing these specific P450 systems, but in using the intramolecular flash-quench method to generate oxidized intermediates in other biological systems.

Second, we must investigate the generation of CII by *chemical* means. Compound ES (CII with an additional hole localized on an amino acid side chain) has been generated in high yield and characterized in CYP158 from *Streptomyces coelicolor*.⁵ Similar investigation must be accomplished for CYP119, focusing efforts on the generation of a *singly* oxidized CII species. Chemical oxidation of Ru-P450 conjugates will be further complicated by the redox nature of the photosensitizer

itself. All of these issues must be carefully examined and optimized for before we can expect to observe the second oxidative electron transfer.

3.4. Conclusions

The single W96H mutation in P450 BM3 completely eliminates photochemical heme oxidation in Ru-P450 conjugates. The P450 structure and stability appear unaffected by this mutation, suggesting that W96 is indeed involved in the electron transfer event. Flash-quench oxidation of the histidine-containing Ru_{C77}-CYP119(H) conjugate was unsuccessful, and the single H76W mutation was sufficient to restore a small amount of electron transfer with the heme active site. While we are unable to directly detect formation of a tryptophan radical species, the observation that heme oxidation occurs *only* in the presence of an intervening tryptophan for both P450-BM3 and CYP119 systems strongly implicates this residue as a redox intermediate in multistep electron transfer. We will analyze the kinetics of electron hopping in Chapter 4.

3.5. Acknowledgments

I would like to specifically acknowledge Eric Brustad for assistance in protein crystallization and structure determination. Jay Winkler and Jeff Warren provided helpful discussions.

3.6. Materials and Methods

Materials

Buffer salts were obtained from J.T. Baker. Dicyclohexylcarbodiimide (DCC), iodoacetic acid, and 5-amino-1,10-phenanthroline were obtained from Sigma Aldrich. [Ru(2,2'-bipyridine)₂]Cl₂ and [Ru(NH₃)₆]Cl₃ were obtained from Strem

Chemicals. All chemicals were used as received with no further purification. Solutions were prepared using 18 MΩcm water unless otherwise noted. Mutagenesis primers were obtained from Operon.

Procedures

A detailed description of experimental protocols can be found in Appendix B. A brief description of the procedures is given below, highlighting any deviations from the general protocol. All figures of protein structures were made in PyMol graphics software for Mac.

3.6.1. Photosensitizer Synthesis

Synthesis

This photosensitizer was synthesized according to published procedures. Briefly, iodoacetic anhydride was formed by addition of N,N'-Dicyclohexylcarbodiimide (DCC) to a solution of iodoacetic acid in ethyl acetate. Following removal of urea by filtration and evaporation to dryness, the iodoacetic anhydride in acetonitrile was added to a solution of 5-amino-1,10-phenanthroline in acetonitrile and stirred overnight at room temperature. Solid product (5-iodoacetamido-1,10-phenanthroline (IAphen)) was refluxed with Ru(bpy)₂Cl₂ in methanol for 3 hours; a color change from purple to red is observed. After cooling and filtration, product can be precipitated by addition of concentrated aqueous NH₄PF₆. Alternatively, the compound can be concentrated and redissolved in water without further purification. The starting material impurities do not interact with P450, and do not appear to impact the labeling process.

Characterization

The photosensitizer was characterized by nuclear magnetic resonance (NMR), steady-state luminescence, and transient luminescence and absorption.

3.6.2. Protein mutagenesis, expression, and purification

Plasmid

The recombinant P450-BM3 heme domain, consisting of the first 463 residues with an N-terminal 6-histidine tag, was obtained courtesy of Professor Andrew Udit (Occidental College, Los Angeles California), within the pCWori⁺ vector (also containing genes for ampicillin resistance and IPTG induction). Recombinant CYP119 with an N-terminal 6-histidine tag was obtained courtesy of Professor Paul Ortiz de Montellano (University of California, San Francisco), also within the pCWori⁺ vector.

Mutagenesis

Qiagen Quik-Change site-directed mutagenesis was used to generate the desired P450 mutants. The mutagenesis primers (forward, 5'-3') were: BM3-W96H: GGACGCATGAAAAAATCATTGCAAAGCGCATAATATC; CYP119-D77C: GATCCCCCTCTCCATTGTGAGTTAAGATCAATGTCAGC and CYP119-(D77C)H76W: CCTCAGATCCCCCTCTCTGGTGTGAGTTAAGATCAATGTC

Overexpression in E. coli.

The P450 mutants BM3-C62A/C156S/K97C/W96H (_{C97}BM3_(WH)), CYP119-D77C (_{C77}CYP119_(H)), and CYP119-D77C/H76W (_{C77}CYP119_(HW)) were overexpressed in the BL21-DE3 strain of *E. coli*. Briefly, overnight LB cultures were used to inoculate 1x TB (for P450 BM3) or 2x TB (for CYP 119) induction cultures. After

approximately three hours at 37 °C ($OD_{600} \sim 1$) the temperature was lowered to 30 °C, expression was induced with IPTG and α -aminolevulinic acid was added. After expression for 24 or 40 hours (for P450 BM3 and CYP119, respectively), cells were harvested by centrifugation and stored at -80 °C.

P450 enzymes were extracted by sonication, centrifuged to pellet cellular debris, and purified by Ni immobilized metal affinity chromatography (IMAC) . Enzymes were further purified by anion-exchange FPLC and gel filtration. Dithiothreitol (DTT) was added to reduce intermolecular disulfide bonds for samples not intended for immediate use. 40% glycerol was added to these samples, which were flash-frozen in liquid nitrogen and stored at -80 °C.

P450 mutants were characterized by UV-vis spectroscopy and mass spectrometry.

3.6.3. Conjugation to Ru-photosensitizer

Briefly, approximately three-fold excess of $Ru^{II}(bpy)_2(IAphen)$ was added to a $\sim 10 \mu M$ P450 solution in 20 mM Tris buffer, pH 8 (buffer-exchanged to remove DTT). The reaction solution shaken gently for ~ 4 hours at 4 °C in the dark, followed by desalting to remove excess photosensitizer, and purification of Ru-labeled and unlabeled enzymes by anion exchange chromatography on a MonoQ or HiPrepQ FPLC column.

Successful conjugation and separation of Ru-P450 was verified by UV-vis, mass spectrometry, and fluorometry.

3.6.4. Crystallization and structure determination

Crystals of C_{97} -BM3_(WH) were obtained by the sitting-drop vapor diffusion method: 10 mg/mL C_{97} -BM3_(WH) in 10 mM Tris, 10 mM sodium chloride, pH 7.4

was mixed with a crystallization well solution of 0.1 M sodium cacodylate pH 6.0, 0.14 M MgCl₂, 18% PEG 3350 in a 1:1 ratio (v/v). Crystal formation could be observed within a period of 30 minutes, but were allowed to form over 24 hours at 20 °C, and were flash-frozen directly from solution. X-ray diffraction data were collected at Stanford Synchrotron Radiation Laboratory Beamline 12-2.

3.6.5. Preparation of laser samples

Laser samples were composed of ~10 μM Ru-P450 conjugate, with and without oxidative quencher (17 mM [Ru(NH₃)₆]Cl₃) in buffered solution (pH 8: 50 mM sodium borate or 50 mM Tris); additionally, each buffer contained sodium chloride to prevent precipitation. Samples were placed in a high-vacuum four-sided quartz cuvette with high-vacuum Teflon valve, equipped with a small stir bar. Deoxygenation was achieved via gentle pump-backfill cycles with argon.

For acquisition of time-resolved fluorescence and transient absorption data, samples were excited with 10 ns laser pulses at 480 nm. Luminescence decays were monitored at 630 nm. Single wavelength transient absorption (TA) kinetics were monitored every 10 nm from 390-440 nm, averaging ~500 shots per wavelength. Data from five separate timescales (2 μs, 40 μs, 400 μs, 10 ms, and 500 ms) were collected, log-compressed, and spliced together to produce full kinetics traces. See Appendix D for log-compression and splicing scripts in Matlab.

3.7. References

- (1) Ener, M. E.; Lee, Y.-T.; Winkler, J. R.; Gray, H. B.; Cheruzel, L. Photooxidation of Cytochrome P450-BM3. *Proc. Natl. Acad. Sci.* **2010**, *107*, 18783–18786.
- (2) Rittle, J.; Green, M. T. Cytochrome P450 Compound I: Capture, Characterization, and C-H Bond Activation Kinetics. *Science* **2010**, *330*, 933–937.
- (3) Davydov, R.; Makris, T. M.; Kofman, V.; Werst, D. E.; Sligar, S. G.; Hoffman, B. M. Hydroxylation of Camphor by Reduced Oxy-Cytochrome P450cam: Mechanistic Implications of EPR and ENDOR Studies of Catalytic Intermediates in Native and Mutant Enzymes. *J. Am. Chem. Soc.* **2001**, *123*, 1403–1415.
- (4) Green, M. T.; Dawson, J. H.; Gray, H. B. Oxoiron(IV) in Chloroperoxidase Compound II Is Basic: Implications for P450 Chemistry. *Science* **2004**, *304*, 1653–1656.
- (5) Yosca, T. H.; Rittle, J.; Krest, C. M.; Onderko, E. L.; Silakov, A.; Calixto, J. C.; Behan, R. K.; Green, M. T. Iron(IV)hydroxide pKa and the Role of Thiolate Ligation in C-H Bond Activation by Cytochrome P450. *Science* **2013**, *15*, 825–829.
- (6) Krest, C. M.; Onderko, E. L.; Yosca, T. H.; Calixto, J. C.; Karp, R. F.; Livada, J.; Rittle, J.; Green, M. T. Reactive Intermediates in Cytochrome P450 Catalysis. *J. Biol. Chem.* **2013**, *288*, 17074–17081.
- (7) Hamachi, I.; Tsukiji, S.; Shinkai, S.; Oishi, S. Direct Observation of the Ferric-Porphyrin Cation Radical as an Intermediate in the Phototriggered Oxidation of Ferric- to Ferryl-Heme Tethered to Ru(bpy)₃ in Reconstituted Materials. *J. Am. Chem. Soc.* **1999**, *121*, 5500–5506.
- (8) Shih, C.; Museth, A. K.; Abrahamsson, M.; Blanco-Rodríguez, A. M.; Di Bilio, A. J.; Sudhamsu, J.; Crane, B. R.; Ronayne, K. L.; Towrie, M.; Vlček, Jr., A.; Richards, J. H.; Winkler, J. R.; Gray, H. B. Tryptophan-Accelerated Electron Flow Through Proteins. *Science* **2008**, *320*, 1760–1762.
- (9) Warren, J. J.; Ener, M. E.; Vlček Jr., A.; Winkler, J. R.; Gray, H. B. Electron Hopping through Proteins. *Coord. Chem. Rev.* **2012**, *256*, 2478–2487.
- (10) Warren, J. J.; Herrera, N.; Hill, M. G.; Winkler, J. R.; Gray, H. B. Electron Flow through Nitrotyrosinate in Pseudomonas Aeruginosa Azurin. *J. Am. Chem. Soc.* **2013**, *135*, 11151–11158.
- (11) Munro, A. W.; Malarkey, K.; McKnight, J.; Thomson, A. J.; Kelly, S. M.; Price, N. C.; Lindsay, J. G.; Coggins, J. R.; Miles, J. S. The Role of Tryptophan 97 of Cytochrome P450 BM3 from Bacillus Megaterium in Catalytic Function. Evidence against the “Covalent Switching” Hypothesis of P-450 Electron Transfer. *Biochem. J.* **1994**, *303*, 423–428.

- (12) Huvaere, K.; Skibsted, L. H. Light-Induced Oxidation of Tryptophan and Histidine. Reactivity of Aromatic N-Heterocycles toward Triplet-Excited Flavins. *J. Am. Chem. Soc.* **2009**, *131*, 8049–8060.
- (13) Creutz, C.; Chou, M.; Netzel, T. L.; Okumura, M.; Sutin, N. Lifetimes, Spectra, and Quenching of the Excited States of Polypyridine Complexes of Iron(II), Ruthenium(II), and Osmium(II). *J. Am. Chem. Soc.* **1980**, *102*, 1309–1319.
- (14) Sutin, N.; Creutz, C. Properties and Reactivities of the Luminescent Excited States of Polypyridine Complexes of Ruthenium(II) and Osmium(II). In *Inorganic and Organometallic Photochemistry; Advances in Chemistry*; American Chemical Society: Washington, DC, 1978; Vol. 1.
- (15) Raner, G.; Thompson, J.; Haddy, A.; Tangham, V.; Bynum, N.; Reddy, R.; Ballou, D.; Dawson, J. Spectroscopic Investigations of Cytochrome P450(BM3)-F87G of Intermediates in the Reaction with Surrogate Oxygen Atom Donors. *J. Inorg. Biochem.* **2006**, *100*, 2045–2053.
- (16) Spolitak, T.; Dawson, J.; Ballou, D. Rapid Kinetic Investigations of Peracid Oxidation of Ferric Cytochrome P450cam: Nature and Possible Function of Compound ES. *J. Inorg. Biochem.* **2006**, *100*, 2034–2044.
- (17) Solar, S.; Getoff, N.; Surdhar, P. S.; Armstrong, D. A.; Singh, A. Oxidation of Tryptophan and N-Methylindole by N_3^* , Br_2^{*-} , and $(SCN)_2^{*-}$ Radicals in Light- and Heavy-Water Solutions: A Pulse Radiolysis Study. *J. Phys. Chem.* **1991**, *95*, 3639–3643.
- (18) Quaroni, L. G.; Seward, H. E.; McLean, K. J.; Girvan, H. M.; Ost, T. W. B.; Noble, M. A.; Kelly, S. M.; Price, N. C.; Cheesman, M. R.; Smith, W. E.; Munro, A. W. Interaction of Nitric Oxide with Cytochrome P450BM3. *Biochemistry* **2004**, *43*, 16416–16431.
- (19) Castellano, F. N.; Dattelbaum, J. D.; Lakowicz, J. R. Long-Lifetime Ru(II) Complexes as Labeling Reagents for Sulfhydryl Groups. *Anal. Biochem.* **1998**, *255*, 165–170.

Chapter 4

**MULTISTEP ELECTRON TRANSFER:
“HOPPING MAPS” TUTORIAL
AND APPLICATION**

Portions of this work are excerpted with permission from:

J. J. Warren, M. E. Ener, A. Vlček Jr., J. R. Winkler, H. B. Gray.
Coord. Chem. Rev. **2012**, 256, 2478-2487.

Copyright 2012 Elsevier B. V.

4.1. Electron transfer through proteins

Biological energy conversions are critical for cellular function. Photosynthesis harnesses the energy from sunlight to generate reactive chemical bonds in adenosine triphosphate (ATP) and reduced nicotinamide adenine dinucleotide (NADH).^{1,2} Cellular respiration generates those same species using energy stored in the chemical bonds of sugars (glucose).^{3,4} These complex reactions are carried out by an intricate network of membrane-bound multi-protein systems (**Figure 4.1**). More than 10 individual electron transfer (ET) steps take place during the catalysis that couples ATP and NADH synthesis to the oxidation of water (photosynthesis) or the reduction of O₂ (respiration).

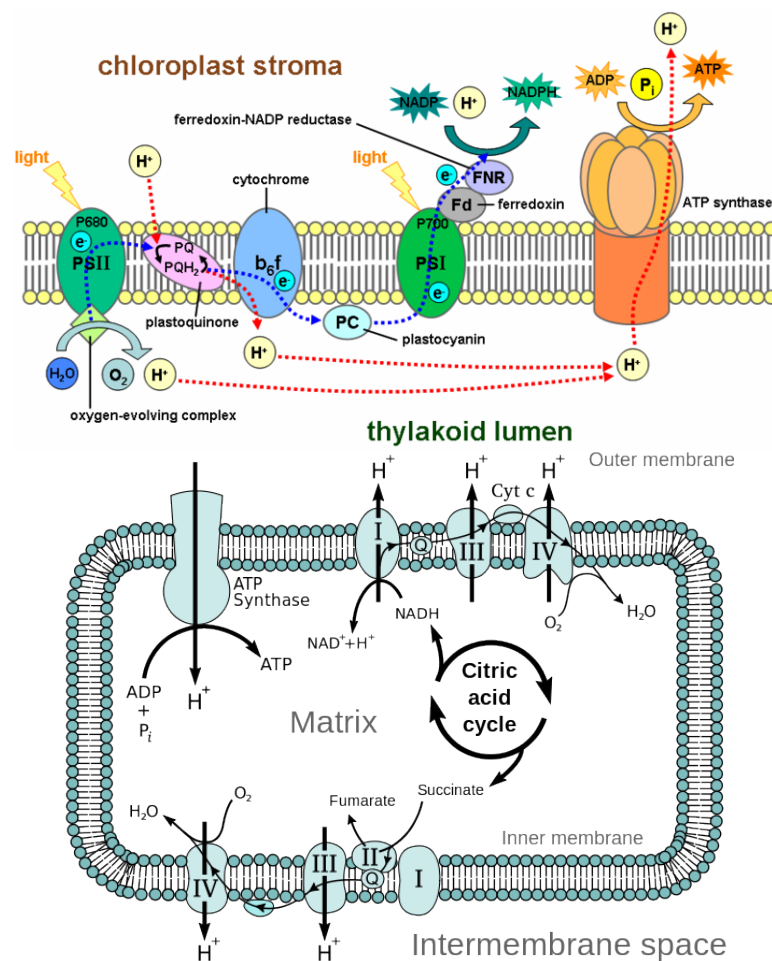


Figure 4.1. Multistep ET in biological energy conversion systems. **Top:** Photosynthetic reaction scheme. **Bottom:** Aerobic respiration in mitochondria.

A simpler energy conversion system was discussed in Chapters 2 and 3; light energy (a laser pulse) was used to generate the high-valent compound II (CII) in Ru photosensitizer–cytochrome P450 conjugates by oxidizing a water molecule bound to the heme. Even within this artificial system, as many as four individual ET events maybe contribute to CII formation (**Figure 4.2**): ET quenching of the $^*Ru^{II}$ excited state to form Ru^{III} , transient oxidation of tryptophan⁹⁶, hole transfer to the porphyrin ring, and hole transfer to the iron center.

In all of these systems, native and artificial, electrons and holes must be rapidly and efficiently separated, and transported across many-angstrom distances. Recombination of these electron-hole pairs would result in nonproductive loss of energy as heat, without accomplishing the desired reactions. For examples of scale, the width of a membrane lipid bilayer can span be 30 Å or more,⁵ and the Ru-Fe distance in Ru-P450 conjugates is 24 Å.

In order to address these complex, multi-ET processes, we must first understand the factors that govern single-step ET within simple systems (e.g., small, model proteins). We then can asses how enzymes use multiple, short ET steps (electron “hopping”) to rapidly transport charges over biologically-relevant distances.

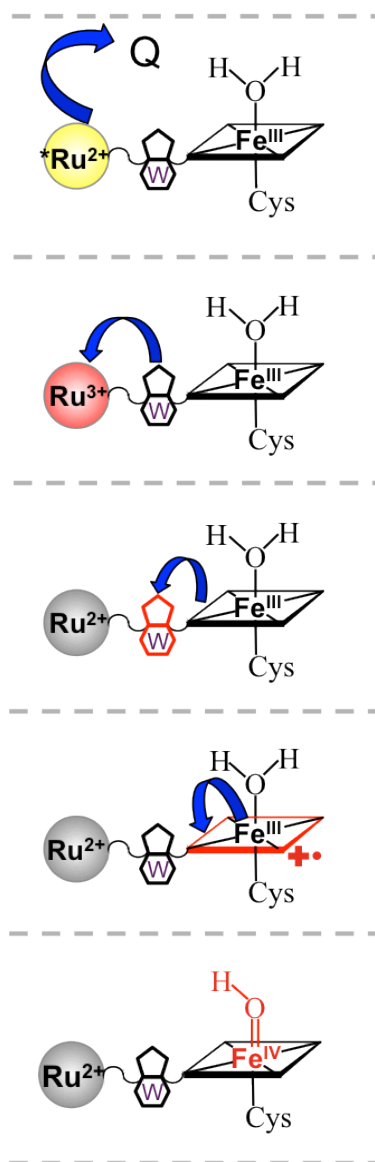


Figure 4.2. Sequential ET steps in the photo-triggered oxidation of Ru-P450 conjugates. Blue arrows represent individual ETs. Oxidized species are colored red. Q is an exogenous quencher.

Method for examining ET in proteins: photochemical triggering

The Gray group and others have spent decades studying fundamental aspects of ET within proteins by tethering inorganic photosensitizers to protein surfaces (Figure 4.3). As mentioned for Ru-P450 conjugates, laser pulses trigger ET between the photosensitizer excited (or quenched) state, and a redox active center

within the protein. Redox active centers include copper in *Pseudomonas aeruginosa* azurin,⁶⁻⁹ heme iron in cytochrome *c*,¹⁰⁻¹³ and also amino acid side chains within complex enzymes such as ribonucleotide reductase (the enzyme that deoxygenates nucleotides, necessary for DNA, **Figure 4.4**).¹⁴ By varying the nature and location of the tethered photosensitizer, as well as the composition of the intervening protein, the effects of distance, driving force, and biological medium can be examined.^{6,13} These studies and others have shown that ET events through biological media can be analyzed using semiclassical ET theory.

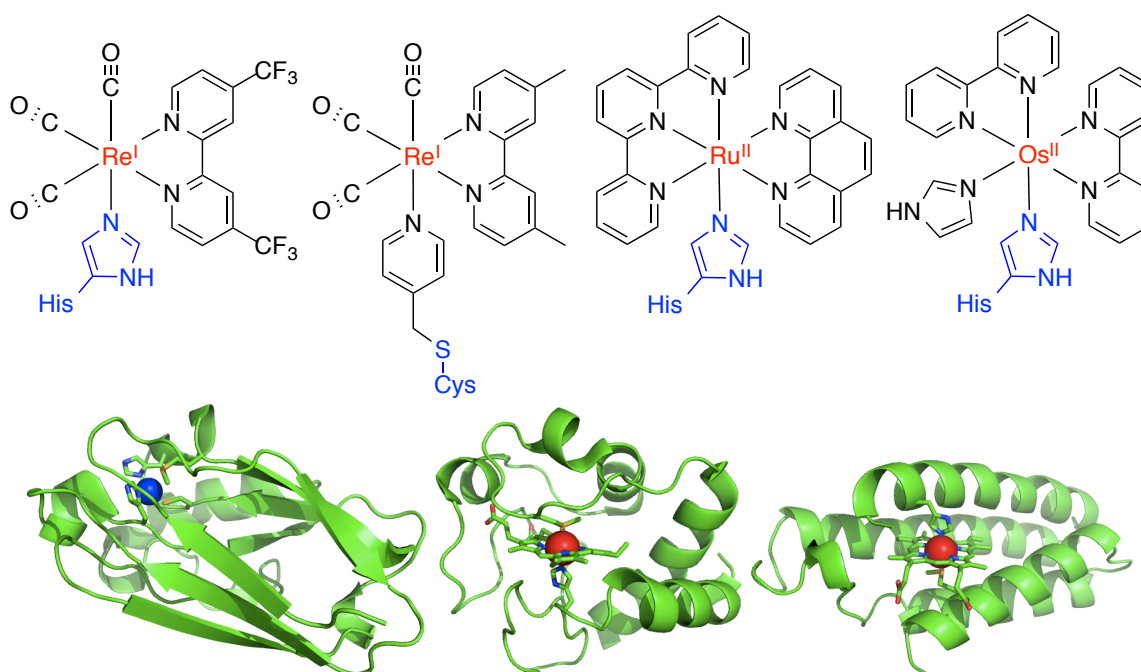


Figure 4.3. Photosensitizers and metallo-proteins. **Top:** A variety of photosensitizers tethered to amino acids. **Bottom:** redox active model proteins. Left to right: *P. aeruginosa* azurin (PDB: 1JZG, Cu in blue), horse heart cytochrome *c* (PDB: 1HRC, heme Fe in red), cytochrome b562 (PDB: 256B, heme Fe in red). All images of protein crystal structures in this Chapter were made using PyMol graphics software for Mac.

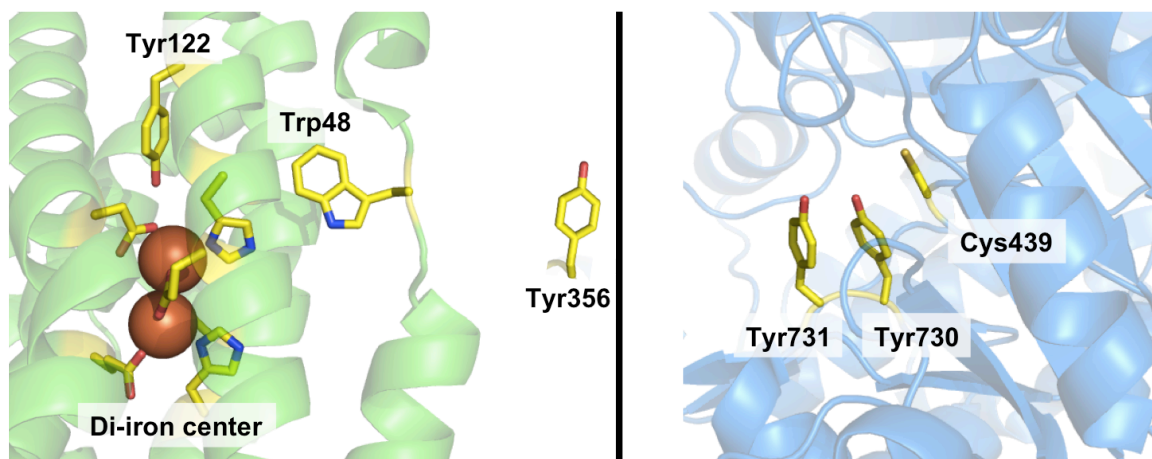


Figure 4.4. Ribonucleotide reductase from *E. coli*. Amino acid side chains along an ET path between Tyr122 radical-initiation and Cys439 active site (alpha, R1 subunit: blue, PDB 1RLR; beta, R2 subunit: green, PDB 1MRX).

This Chapter first offers a basic description of the theoretical underpinnings required for analyzing single-step ET, and some of the conclusions that have come out of single-step analysis in biological systems. This is followed by extension of electron tunneling to describe electron hopping, with a discussion of biochemical systems that employ this mechanism. We describe the step-by-step generation of a “hopping map,” a plot of multistep ET rate dependence on driving force for the first and overall reaction steps. We examine the utility of the hopping map for analyzing photo-triggered two-step hopping in rhenium-labeled azurin, and draw some general conclusions from this reactivity. We address some of the challenges and limitations of this type of analysis, and discuss the applicability to native ET systems. Finally, we address the utility of this hopping analysis for multistep ET in ruthenium-labeled cytochrome P450 (Chapters 2 and 3).

4.2. Single-step electron tunneling: semiclassical theory

We will begin examining ET reactions using semiclassical theory. ET between an electron/hole donor (D) and an acceptor (A) can be described using two harmonic

potential energy surfaces (**Figure 4.5**), where the positions along the horizontal axis describe nuclear configurations and geometries, and the vertical axis describes the system's free energy. The parabolic surface on the left (red) describes the reactant state in which the electron or hole (denoted as a dot) resides on the donor moiety: ($D^{\bullet}|A$). The right surface (blue) describes the product state, in which the electron/hole has been transferred to the acceptor ($D|A^{\bullet}$).

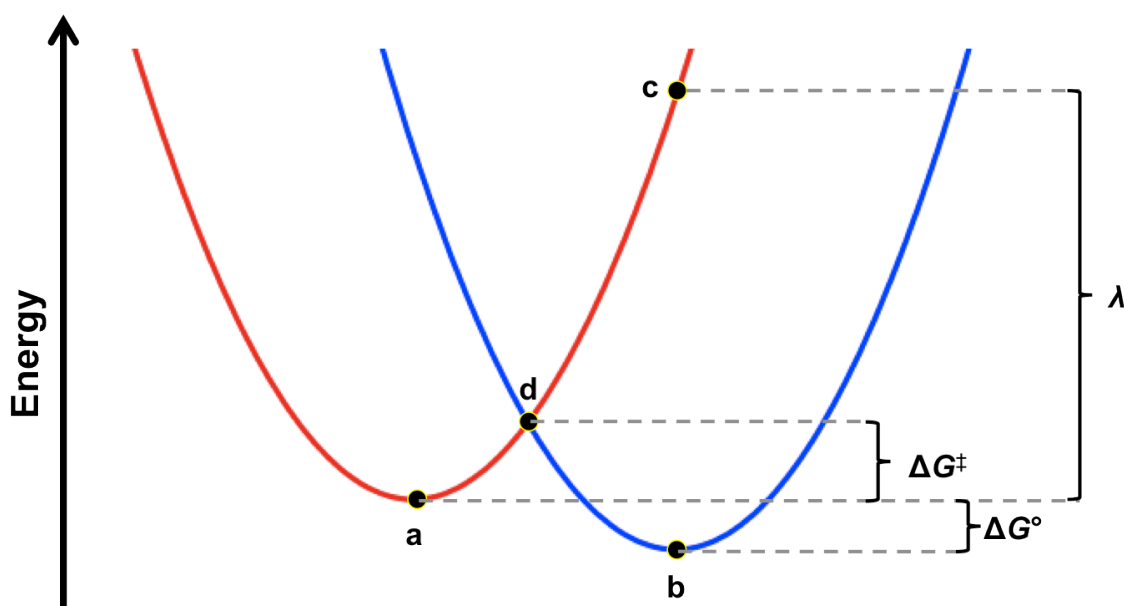


Figure 4.5. Energy diagram illustrating thermodynamic parameters for an ET reaction. The vertical axis is increasing energy; the horizontal axis describes the nuclear coordinate. Reactant state ($D^{\bullet}|A$): red; product state ($D|A^{\bullet}$): blue.

The thermodynamic driving force for the reaction ($-\Delta G^{\circ}$) is given by the difference in energy between the minima of the reactant and product state surfaces (points a and b, respectively). Different nuclear and solvent configurations stabilize the reactant and product states (the energy minima are at different positions along the horizontal axis); thus, both inner sphere (nuclear) and outer sphere (solvent) rearrangements must accompany the ET reaction. This reorganization energy, λ , is a sum of nuclear (λ_{inner}) and solvent (λ_{outer})

components. In **Figure 4.5**, λ is defined as the difference in energy of the reactant (or product) state in the reactant (a) and product configurations (c).

The Franck-Condon principle states that the movement of electrons is much faster than the movement of nuclei. For thermal ET to occur with conservation of energy, the reactant and product geometries (and energies) must be equal. This is the point at which the reactant and product state surfaces intersect (d). The energy difference between the reactant state minimum (a) and this intersection (d) is the activation energy (ΔG^\ddagger) required in order for the reaction to proceed.

For ET to occur, the two diabatic states must mix to form two adiabatic states (**Figure 4.6**, dashed lines). The electronic coupling matrix element which mixes the reactant and product states is known as H_{AB} ; the energy difference at the point of intersection between the upper and lower adiabatic curves is equal to $2H_{AB}$. From this diagram, it should be evident that enhanced electronic communication between the reactant and product states (larger H_{AB} , and more mixing between the states) lowers the activation barrier for thermal ET.

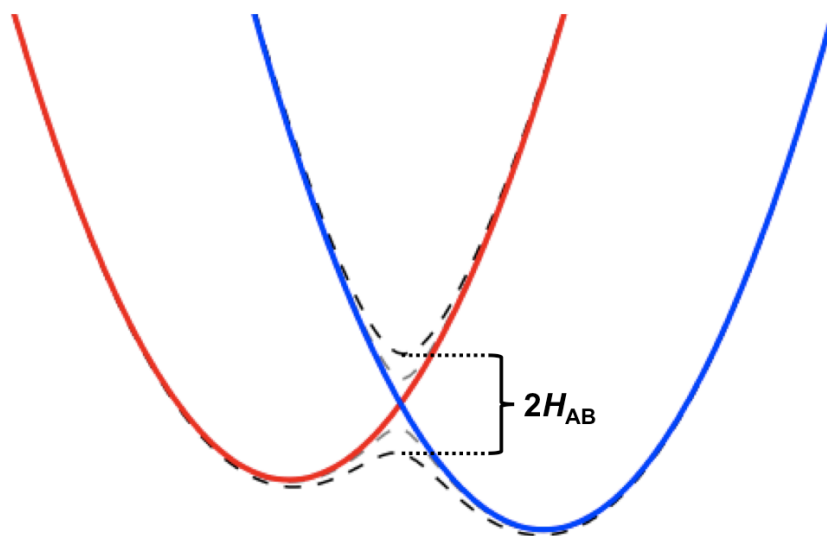


Figure 4.6. Energy diagram illustrating diabatic (solid lines) and adiabatic (dashed lines) states, and the coupling parameter H_{AB} .

The specific rate of ET (k_{ET}) between donor and acceptor can be described by Equations 4.1 and 4.2. (For more details on the origin and development of this equation, the curious reader is directed to papers by R. A. Marcus¹⁵⁻¹⁸).

$$k_{ET} = \sqrt{\frac{4\pi^3}{h^2 \lambda k_B T}} H_{AB}^2 \exp\left(\frac{-(\Delta G^\circ + \lambda)^2}{4\lambda k_B T}\right) \quad (4.1)$$

$$H_{AB} = H_{AB}(r_0) \exp\left(-\frac{1}{2}\beta(r - r_0)\right) \quad (4.2)$$

Here, k_B and h are the Boltzmann and Planck constants, respectively. The ET rate is dependent on reaction driving force ($-\Delta G^\circ$), reorganization energy (λ), and distance between electron/hole donor and acceptor (r). H_{AB} is related to the D-A distance by Equation 4.2, where β is the decay constant for tunneling, r_0 is the limit of contact (taken as the sum of van der Waals radii), and r is as given above. In general, ΔG° and λ depend on D and A molecular composition and local environment, while H_{AB} is a function of D-A distance and the structure of the intervening medium (described by β).

If all other parameters are held constant, increased driving force (more negative ΔG° values) results in increased ET rate – but only up to a point. The maximum ET rate occurs when $-\Delta G^\circ$ is equal to λ ; this is known as a “driving force optimized” reaction. Further increases in driving force result in decreased ET rates; this is known as the “inverted region.”

For reactions that are driving force optimized, the exponential term in Equation 4.1 becomes unity, and the ET rate depends primarily on donor-acceptor distance and the intervening medium. Assuming that λ is constant across a series, it can be seen from Equation 4.2 that a plot of $\log(k_{ET})$ is linearly proportional to the D-A separation ($r-r_0$), with a slope that is proportional to β .

Experimental Measurements

Investigations by the Gray group and others have probed this driving force optimized regime in abiological model systems (small molecules, frozen organic glasses) and proteins. By analyzing aggregate data from myriad experiments, a tunneling timetable can be constructed to describe the distance dependence of ET through different media, including proteins (**Figure 4.7**). As described by semiclassical theory, $\log(k_{\text{ET}})$ is linearly related to the D-A separation ($r-r_0$), with a slope that is proportional to β .

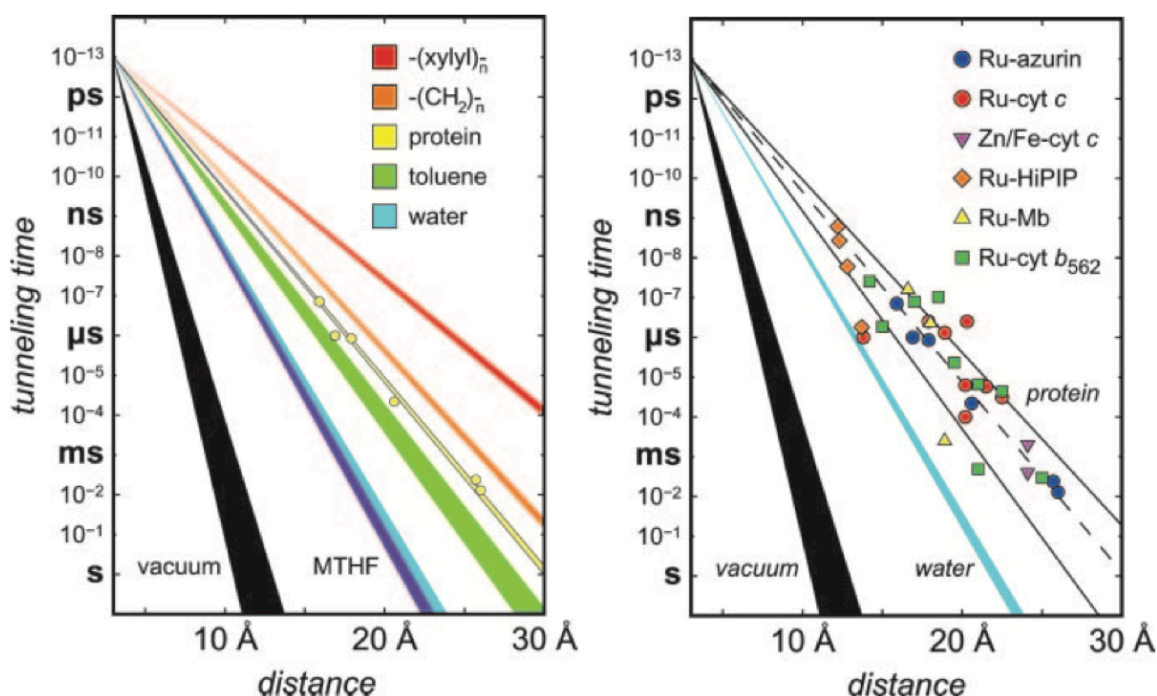


Figure 4.7. Tunneling timetables for driving force-optimized ET reactions.¹⁹ The “tunneling time” on the y-axis is the inverse of the ET rate constant. **Left:** comparison of ET through different media. **Right:** comparison of ET rates for different protein systems.

One of the most important messages in **Figure 4.7** is that as D-A distances increase linearly, the ET time increases exponentially. Single-step ET processes over large distances (> 30 Å, such as the width of a membrane bilayer), could take

minutes or days, even for reactions that are driving force optimized. Another mechanism is needed to accomplish such long-distance ET events rapidly enough to support cellular processes. As will be demonstrated, breaking the overall ET event into multiple shorter (and therefore faster) hopping steps can allow the net ET reaction to proceed on a relevant timescale.

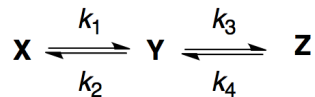
4.3. Multistep electron transfer

If there is an additional redox site between D and A that can accommodate an electron/hole, the overall transfer from D to A can occur in two shorter-distance (and potentially faster) tunneling steps; D to I, then I to A. In order to understand natural and model biological systems, and other multistep ET reactions, we would like to compare these hopping pathways to those of single-step ET. Since each of the hopping steps obeys the ET rate dependence based on its individual values of ΔG° , λ , and r , we can calculate the overall hopping reaction rate and compare it to that for single-step tunneling, to see if there is a “hopping advantage.”

Two-step hopping requires three sites: the initial electron (hole) donor (D), a relay station to which this electron (hole) is temporarily transferred (I), and the final electron (hole) acceptor (A). Oxidized or reduced I is a real intermediate that, in principle, can be detected spectroscopically. It is helpful to think of these three sites together as a single system that can be described by the location of the electron/hole, as shown in Equations 4.3a-c.



We write the hopping reactions as follows:



The corresponding rate equations are given in Equations 4.4a-c:

$$\frac{d[X]}{dt} = -k_1[X] + k_2[Y] \quad (4.4a)$$

$$\frac{d[Y]}{dt} = k_1[X] - k_2[Y] - k_3[Y] + k_4[Z] \quad (4.4b)$$

$$\frac{d[Z]}{dt} = k_3[Y] - k_4[Z] \quad (4.4c)$$

By solving this set of differential equations, we obtain expressions for each of the concentrations as functions with respect to time (i.e., $[X](t)$, $[Y](t)$, $[Z](t)$). We assume that the initial concentrations of Y and Z are zero; the resulting equations are more complicated without this assumption. Mathematica software (Wolfram Research) can be used to solve these equations analytically. We are interested in the overall electron transfer rate constant from the initial donor to the acceptor, therefore, the function $[Z](t)$ is particularly useful. The very lengthy output from Mathematica for $[Z](t)$ can be simplified to the following form (Equation 4.5):

$$[Z](t)_{\text{hopping}} = \frac{[X]_0 k_1 k_3}{2bc} \left[2c - (c - a\sqrt{c}) \exp\left(\frac{1}{2}(-a - \sqrt{c})t\right) - (c + a\sqrt{c}) \exp\left(\frac{1}{2}(-a + \sqrt{c})t\right) \right] \quad (4.5)$$

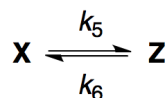
where a , b , and c are defined as:

$$a = k_1 + k_2 + k_3 + k_4 \quad (4.6a)$$

$$b = k_1k_3 + k_1k_4 + k_2k_4 \quad (4.6b)$$

$$c = a^2 - 4b \quad (4.6c)$$

Eventually we will want to compare the overall rates of single-step ET and two-step hopping, therefore, an analogous expression for $[Z](t)$ using the single-step mechanism must be defined.



$$X = D^{+/-} \cdots A \quad (4.7a)$$

$$Z = D \cdots A^{+/-} \quad (4.7b)$$

Solving the differential equations in the same manner as described above, the single-step expression is given in Equation 4.8, again assuming that $[Z]_0$ is 0.

$$[Z](t)_{tunneling} = \frac{[X]_0 k_5 [1 - \exp(-(k_5 + k_6)t)]}{k_5 + k_6} \quad (4.8)$$

Comparison of the $[Z](t)$ functions for both mechanisms (Equations 4.5 and 4.8, respectively) shows that hopping is a biexponential process, while single-step tunneling is monoexponential. In order to compare these two mechanisms directly (and determine the rate advantage for hopping), we need to determine an average ET time (τ). The “survival probability” function, $F(t)$ (Equation 4.9) gives the probability (from zero to one) that an electron at any point in time will have *not yet* undergone the complete ET to generate product (Z).

$$F(t) = \frac{[Z](t) - [Z](\infty)}{[Z](0) - [Z](\infty)} \quad (4.9)$$

Integration of this function ($F(t)$) gives the desired average ET time (Equation 4.10).

$$\tau = \int_0^{\infty} F(t) dt \quad (4.10)$$

Substitution with the $[Z](t)_{\text{hopping}}$ and $[Z](t)_{\text{tunneling}}$ functions from Equations 4.5 and 4.8 gives:

$$\tau_{\text{hopping}} = \frac{k_1 + k_2 + k_3 + k_4}{k_1 k_3 + k_1 k_4 + k_2 k_4} \quad (4.11)$$

$$\tau_{\text{tunneling}} = \frac{1}{k_5 + k_6} \quad (4.12)$$

For construction of the hopping map, we are interested in average ET time with respect to ΔG° of the first hopping step, which is the branching point between the two mechanisms, as well as the driving force of the overall reaction. Accordingly, the expressions for τ in terms of rate constants (k_1 through k_6) must now be converted to expressions in terms of ΔG° and the other ET parameters (β , λ , H_{AB} , r). Substitution of Equation 4.2 into Equation 4.1 and collection of constants yield a general equation for a single-step tunneling:

$$k_{ET} = C_0 \exp\left(-\beta(r - r_0) - \frac{(\Delta G^\circ + \lambda)^2}{4\lambda k_B T}\right) \quad (4.13)$$

$$C_0 = \sqrt{\frac{4\pi^3}{h^2 \lambda k_B T}} (H_{AB}(r_0))^2 \quad (4.14)$$

We also define expressions for the reverse rate constants (k_2 , k_4) in terms of forward rate constants (k_1 , k_3) by using the definition of ΔG° :

$$k_2 = k_1 \exp\left(\frac{\Delta G^\circ_{DI}}{k_B T}\right) \quad (4.15)$$

$$k_4 = k_3 \exp\left(\frac{\Delta G^\circ_{IA}}{k_B T}\right) \quad (4.16)$$

$$\Delta G^\circ_{DA} = \Delta G^\circ_{DI} + \Delta G^\circ_{IA} \quad (4.17)$$

where ΔG°_{DI} and ΔG°_{IA} are the standard free energy changes for the first and second hopping steps, respectively, and ΔG°_{DA} is the overall reaction free energy change. Note that this notation assumes that the reaction starts from a donor, D. Depending on the particular system, this can be either an electron donor or a hole donor. Substitution of Equations 4.13-4.16 into Equations 4.11 and 4.12 and subsequent simplification yields τ in terms of the ET parameters (Equations 4.18 and 4.19). These expressions have been simplified by assuming that a single β and λ apply for all ET reactions in the system, but this is not necessary (as will be seen for hopping maps, *vide infra*).

$$\tau_{hop} = \frac{\exp\left(\beta(r_2 - r_0) + \frac{(\Delta G^\circ_{IA} + \lambda)^2}{4\lambda RT}\right) \left(1 + \exp\left(\frac{\Delta G^\circ_{DI}}{RT}\right)\right) + \exp\left(\beta(r_1 - r_0) + \frac{(\Delta G^\circ_{DI} + \lambda)^2}{4\lambda RT}\right) \left(1 + \exp\left(\frac{\Delta G^\circ_{IA}}{RT}\right)\right)}{C_0 \left(1 + \exp\left(\frac{\Delta G^\circ_{IA}}{RT}\right) + \exp\left(\frac{\Delta G^\circ_{DA}}{RT}\right)\right)} \quad (4.18)$$

$$\tau_{tunneling} = \frac{1}{C_0 \exp(-\beta(r_T - r_0)) \left(\exp\left(\frac{-(\Delta G^\circ_{DA} + \lambda)^2}{4\lambda RT}\right) + \exp\left(\frac{-(\Delta G^\circ_{DA} - \lambda)^2}{4\lambda RT}\right) \right)} \quad (4.19)$$

The values r_1 , r_2 , and r_T correspond to the D-I, I-A, and D-A distances, respectively. Note that these are straight-line distances, so r_T need not be the sum of r_1 and r_2 .

Substitution of Equation 4.18, using Equation 4.17, gives τ_{hopping} in terms of $\Delta G^{\circ}_{\text{DI}}$ and $\Delta G^{\circ}_{\text{DA}}$. The dependence of τ_{hopping} on $\Delta G^{\circ}_{\text{DA}}$ and $\Delta G^{\circ}_{\text{IA}}$ can be represented graphically on a hopping map. The values of τ_{hopping} span many orders of magnitude, so we construct contour plots of $-\log_{10}(\tau_{\text{hopping}})$ (represented by the color gradient), with $-\Delta G^{\circ}_{\text{DA}}$ as the x-axis, and $-\Delta G^{\circ}_{\text{DI}}$ as the y-axis.

A computer program for the construction of hopping maps is available for download at <http://www.bilrc.caltech.edu>. The Matlab scripts used to generate this program also can be found in Appendix D.

4.4. Construction of Hopping Maps: an example for Re-Azurin

We will first examine use of the hopping map program to construct a hopping map for a known rhenium-labeled azurin system in which tryptophan acts as the redox intermediate.²⁰

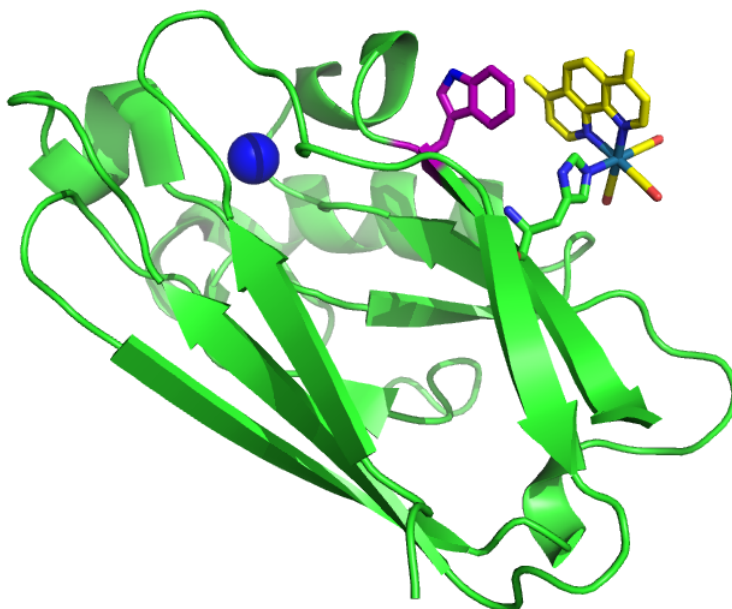


Figure 4.8. The $\text{Re}_{\text{H124}}\text{-W}_{\text{122}}$ -Azurin hopping system. The Re photosensitizer is highlighted in yellow, W122 in purple, and the Cu center in blue. PDB 2I70.

Inputs in two prompts are required to generate each map. The first prompt requests the ET parameters for the system of interest, namely temperature T (K), donor-intermediate-acceptor distances r (Å), and the parameters β (Å⁻¹), and λ (eV) (**Figure 4.9**).

The image shows a dialog box titled "ET Parameters" with the following fields and values:

Parameter	Value
temperature (K)	298
A-I distance (Å)	8.1
β step 1 (1/Å)	1.1
λ step 1 (eV)	0.8
I-B distance (Å)	12.8
β step 2 (1/Å)	1.1
λ step 2 (eV)	0.8
A-B distance (Å)	19.4
β single step (1/Å)	1.1
λ single step (eV)	0.8

Figure 4.9. Prompt #1: ET parameters. In this notation, “A” is the donor, or starting point, “I” is the intermediate, and “B” is the acceptor, or end point of the ET reaction.

In all cases, the van der Waals contact (r_0) is assumed to be 3 Å, and $H_{AB}(r_0)$ is 0.0231 eV. These parameters affect the rates and contours associated with each map. For demonstration purposes, the default variables in this prompt are those used for the Re_{H124}-W_{I22}-Azurin system. Note that the hopping map program

allows variation of β and λ values for each individual ET. For all analyses in this Chapter, we will use constant β and λ values within a system. The effect of variability/uncertainty in each ET parameter is discussed in Section 4.5.

Pressing “OK” in the first prompt brings up a second one (**Figure 4.10**). This prompt accepts parameters that define hopping map visualization: the range of driving forces to be examined (ΔG_{DI}° and ΔG_{DA}° , eV), resolution, and contour intervals. Note that these parameters do not affect the fundamental hopping rates associated with a given system. Maps with larger range and higher resolution take more time to generate; this prompt gives the user control over the speed and quality with which each map is generated.

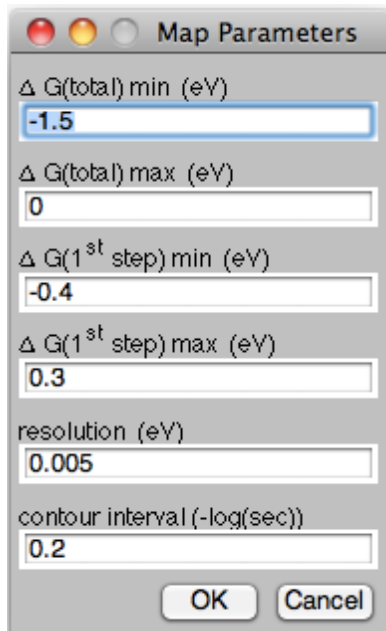


Figure 4.10. Prompt #2: Hopping Map parameters

Pressing “OK” in the second prompt will generate the hopping map. Once the map has been generated, the prompts will re-appear, to allow construction of another map. This time, the default parameters are the previously input values. When no more maps are desired, pressing “Cancel” on both prompts exits the program.

A sample hopping map for $\text{Re}_{\text{H124}}\text{-W}_{122}\text{-Azurin}$ has been generated using the values shown above **Figure 4.11**. The program output includes the hopping map with labeled axes, a record of the ET parameters used in the generation of this map, and a color bar indicating the hopping time associated with each color.

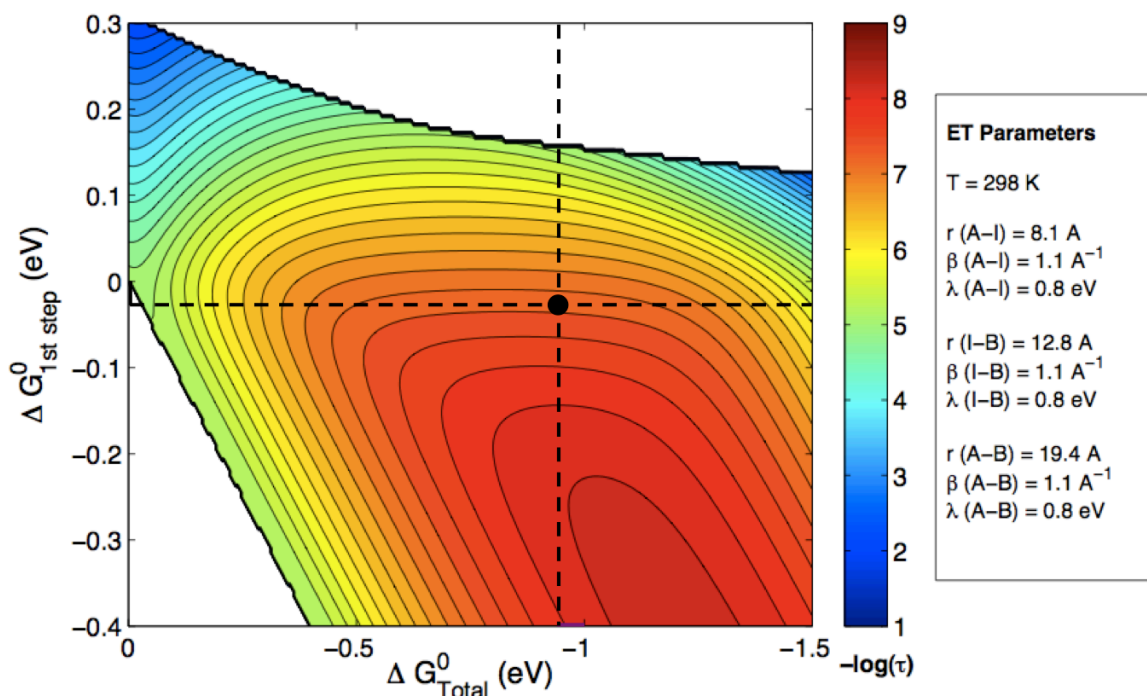


Figure 4.11. Sample hopping map for $\text{Re}_{\text{H124}}\text{-W}_{122}\text{-Azurin}$. ET parameters are displayed in the side bar. A black dot has been placed at $\Delta G_{\text{total}}^{\circ} = -0.94 \text{ eV}$, $\Delta G_{1\text{st step}}^{\circ} = -0.028 \text{ eV}$.

The color contours represent the predicted hopping time, for any given $\Delta G_{\text{DI}}^{\circ}$ for intermediate formation, and $\Delta G_{\text{DA}}^{\circ}$ for the complete reaction. Redder, or “hotter” regions indicate faster hopping and smaller time constants τ . For example, the reddest, most inner region of this map ($\Delta G_{\text{DI}}^{\circ} \sim -0.3 \text{ eV}$, $\Delta G_{\text{DA}}^{\circ} \sim -1.2 \text{ eV}$) corresponds to a $-\log(\tau)$ value of 8.2-8.3, or a hopping time of 5-6 ns; the bluest edge (upper left corner) corresponds to a $-\log(\tau)$ value of 2.2-2.4, or a hopping time of 4-6 ms.

Two portions of the map are shown in white; these are regions in which we would not predict to observe hopping. The region in the upper right is one in which $\tau_{\text{hopping}}/\tau_{\text{tunneling}} < 1$; in other words, where hopping is predicted to be equal to or slower than single-step ET. As will be seen, the position and shape of this perimeter vary based on the assumed ET parameters. The bottom left hand corner, to the left of the solid black line, is the region in which the second hopping step is endergonic. In this case, the intermediate acts as an electron/hole sink, instead of promoting the second ET step. This black line corresponds to $\Delta G_{\text{DI}}^{\circ} = \Delta G_{\text{DA}}^{\circ}$, and is the same for all maps.

By examining the driving forces at work in $\text{Re}_{\text{H124}}\text{-W}_{122}\text{-Azurin}$, we can place this system on the map and compare predicted and experimental ET rates. The driving force for the first ET step (tryptophan oxidation) was determined to be -28 meV, based on kinetics analysis of the forward and reverse ETs between W_{122} and $^*\text{Re}$.^{20,21} On the map, this regime is indicated by a horizontal dashed line. Photo-induced metal-to-ligand charge transfer (MLCT) generates a highly oxidizing triplet excited state ($^*\text{Re}^{\text{II}}\text{dmp}^{\bullet-}$); this excited state potential ($E^{\circ} (^*\text{Re}^{\text{II}}\text{dmp}^{\bullet-}) / (\text{Re}^{\text{I}}\text{dmp}^{\bullet-})$) is taken to be 1.25 V vs. NHE; all reduction potentials are vs. NHE, unless otherwise noted.^{22,23} The azurin $\text{Cu}^{\text{II/I}}$ potential was determined at 0.31 V (pH 7).²⁴ Thus, the overall driving force is 0.94 eV. The black dot in **Figure 4.11** represents this location, with a predicted time constant of 44 ns. This within a factor of 2 of the experimentally determined time constant (31 ns).²⁰

A number of important features are evident in the hopping map. In cases where the first hop occurs with little driving force ($\Delta G_{\text{DI}}^{\circ} \sim 0$, on the vertical axis), the horizontal nature of the map contours indicates that overall ET rate is much more sensitive to changes tryptophan oxidation ($\Delta G_{\text{DI}}^{\circ}$) than in the overall driving force ($\Delta G_{\text{DA}}^{\circ}$). As an example, let's again examine the black dot on the map. Increasing

or decreasing the driving force for tryptophan oxidation by 50 mV (without affecting the overall driving force) results in a range of time constants of 54-570 ns, variation by an order of magnitude. Similar variation in total driving force (without affecting the driving force for tryptophan oxidation) only results in a range of 145-160 ns, roughly 10% variability. Conversely, for systems in which ΔG_{DI}° is very negative (bottom rows of the map), the contours are more vertical, and total ET time (τ) is much more dependent on the overall driving force.

Another key feature is the border along the upper right hand corner. This indicates that the multistep advantage is lost for systems in which the first ET event is endergonic by more than ~ 200 mV. Such systems may still undergo ET, but it is more likely to proceed via single step tunneling.

A final observation is that the hopping map displays the inverted region with respect to overall driving force; ET times associated with $\Delta G_{DA}^{\circ} = -1.5$ V are slower than those at $\Delta G_{DA}^{\circ} = -1.2$ V across the entire range of ΔG_{DI}° .

4.5. ET parameters: selection process, effects, and limitations

For the $\text{Re}_{\text{H124}}\text{-W}_{122}\text{-Azurin}$ system, many of the ET parameters can be measured directly, and all of the fundamental rate constants have been determined experimentally by transient luminescence and absorption spectroscopies.²⁰ However, the values of β , λ , r_1 and r_3 are still subject to interpretation, even for this well-characterized protein system. Additionally, there is debate over the precise reduction potentials (and therefore, driving forces) associated with donor, intermediate, and acceptor. For more complex biochemical systems, the process of selecting parameters and analyzing the hopping map becomes even more complicated.

In this section we use the Re-Azurin system to illustrate the effect that these ET parameters (and uncertainty in their values) have on the rates and shapes associated with the hopping map, and discuss various approaches for determining or estimating these parameters. To facilitate comparison, all hopping maps in this section are scaled to the same ET time (τ) axis: 100 ms (dark blue) to 1 ns (dark red).

Temperature

The first variable requested by the Hopping Map program is temperature. This is often the easiest parameter to determine for an experimental system, and will be ambient temperature (298 K) for a large number of biological systems.

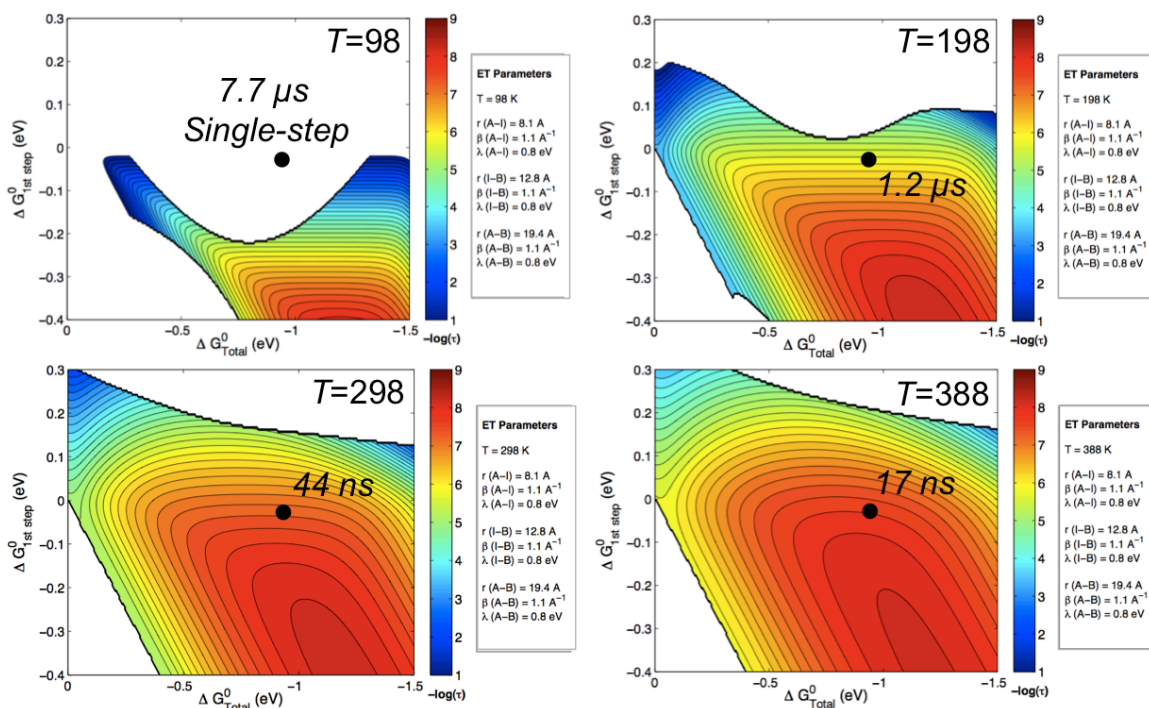


Figure 4.12. Temperature dependence of the Re_{H124}-W₁₂₂-Azurin hopping map. $r_1=8.1 \text{ \AA}$, $r_2=12.8 \text{ \AA}$, $r_T=19.4 \text{ \AA}$; $\beta=1.1 \text{ \AA}^{-1}$; $\lambda=0.8 \text{ eV}$. The black dot is located at $\Delta G_{\text{Total}}^{\circ} = 0.94 \text{ eV}$, $\Delta G_{\text{1st step}}^{\circ} = -0.028 \text{ eV}$.

These maps highlight the fact that the region of hopping advantage shrinks at lower temperature. This indicates that for this system, hopping is more sensitive to temperature than single-step tunneling; it slows down more at low temperatures, and speeds up more at high temperatures. By $T = 98$ K, we do not expect to observe hopping for $\text{Re}_{\text{H124}}\text{-W}_{122}\text{-Azurin}$.

Another observation from these maps is that the optimal total driving force ($\Delta G_{\text{DA}}^{\circ} = -1.2$ V) is constant across a nearly 300 K range of temperatures. In other words (and, as is expected from Equation 4.1), the inverted region does not shift with temperature. As will be seen, the only parameter that affects the point of inversion is λ .

Distance

In a case such as Re-Azurin, where the ET system has been crystallographically characterized, it seems straightforward to determine values for r . However, these straight line distances do not account for specific ET pathways.²⁵⁻²⁷ As a first approximation, the total ET distance (Cu to Re) is measured as the straight line between the metal centers: 19.4 Å. However, the intermediate ET steps which transiently oxidize W122 in are not as well defined.

The original, published hopping analysis used distances to and from the tryptophan C2 carbon: ($r_1 = 8.9$ Å, $r_2 = 11.1$ Å, $r_T = 19.4$ Å).²⁰ However, for a delocalized, aromatic π system, the electron does not necessarily originate from a single atom. One could, alternatively, use the average distance between the 9 atoms in the Trp indole and the Re or Cu center ($r_1 = 8.1$ Å, $r_2 = 12.8$ Å, $r_T = 19.4$ Å); these are the distances we have used in the example hopping maps thus far. One could also use the closest edge-to-edge distances ($r_1 = 6.3$ Å, $r_2 = 10.8$ Å, $r_T = 19.4$ Å). As yet another alternative, one could take into account calculated descriptions of the

highest occupied molecular orbital (HOMO) of indole as the source of the electron for the first ET step, and calculated and experimental formulations of the spin density on Trp radical cation as the source of the hole for the second step.²⁸ As a simplification of this formulation, we use the average distance of the six benzyl atoms to Re as r_1 (7.4 Å), the average distance of the five pyrrole atoms to Cu as r_2 (11.8 Å) and the Re-Cu distance as r_T (19.4 Å).

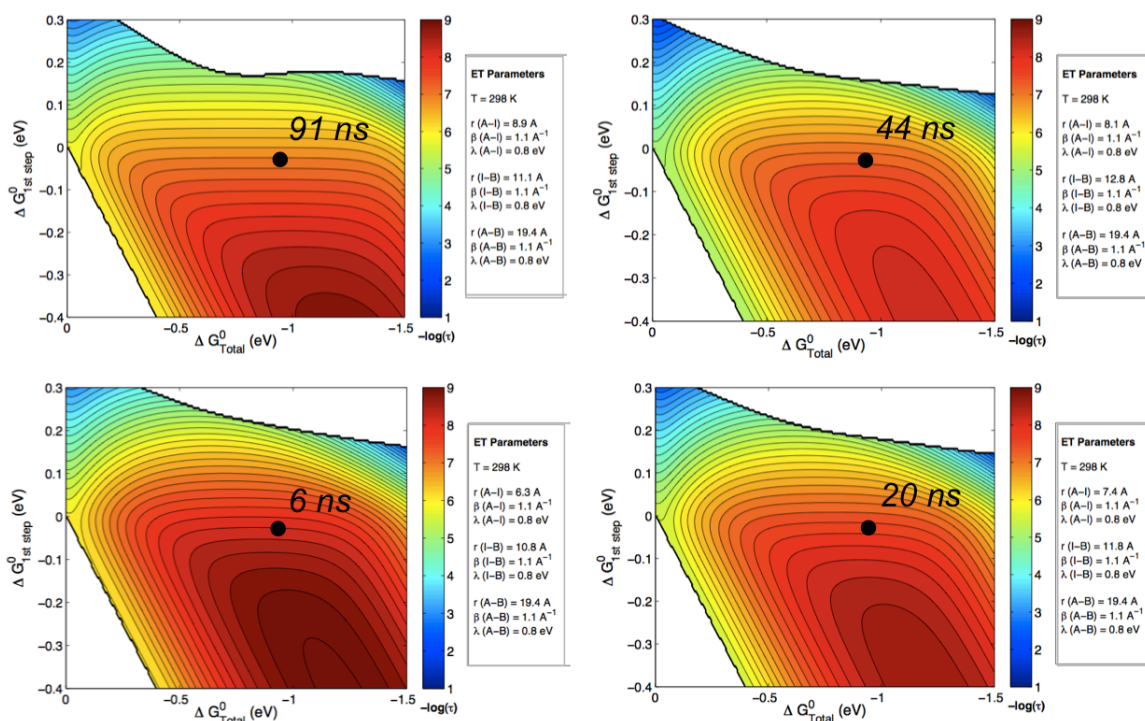


Figure 4.13. Hopping maps for ReH₁₂₄-W₁₂₂-Azurin with differing distance formulations. $\beta=1.1$ Å⁻¹; $\lambda=0.8$ eV. The black dot is located at $\Delta G_{\text{Total}}^{\circ} = -0.94$ eV, $\Delta G_{\text{1st step}}^{\circ} = -0.028$ eV.

These different distance formulations change the rate by just over an order of magnitude (at the black dot), but do not greatly affect the perimeter (area of hopping advantage) or map contours, particularly in the region of interest. We conclude that changes of less than ± 1 Å usually affect the hopping times by less than a factor of 10.

Tunneling decay constant, β

Based on experimental data, the average tunneling decay constant (β) for proteins is 1.1 \AA^{-1} (shown in the tunneling timetable (**Figure 4.7**)). The original hopping analysis used this value. However, there is significant scatter in the tunneling timetable, and different protein systems may have different decay constants. A superexchange coupling model that takes into account structural complexity can be used to explain this scatter.^{26,27,29–33} Experimental determination of β for each individual system is impractical, and so approximations must be made. Knowledge of specific ET pathways facilitates estimation of β . The hopping maps allow us to easily investigate how variation in β results in discrepancies in τ_{hopping} .

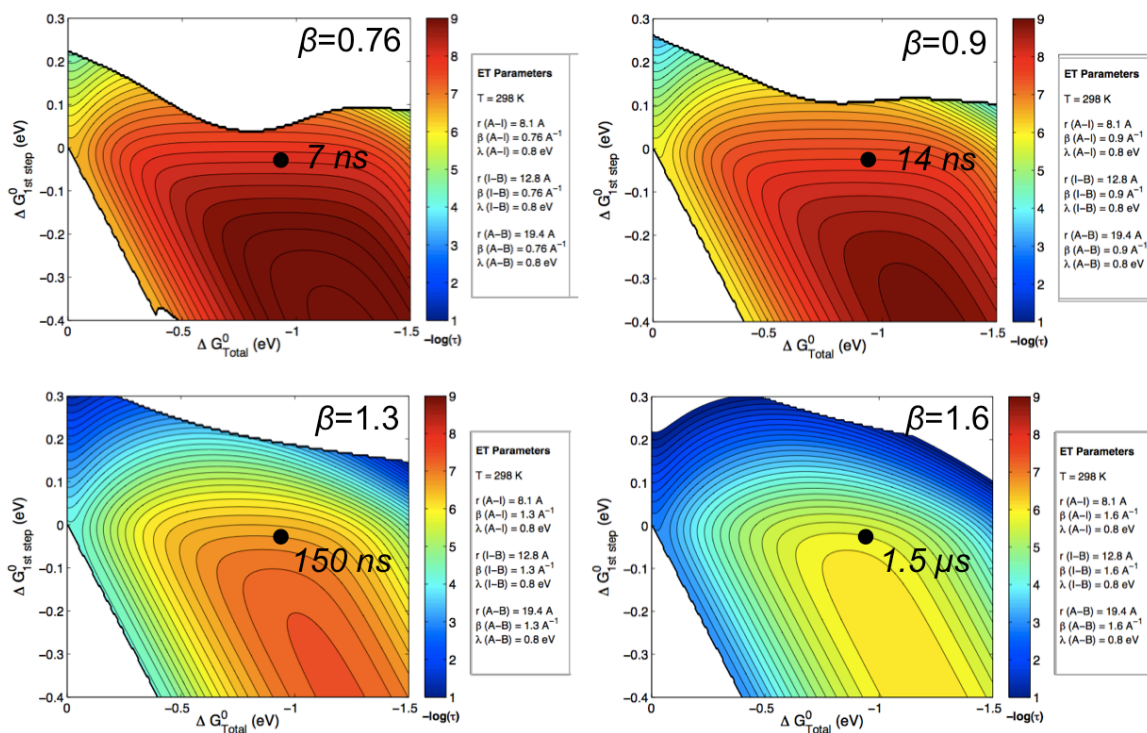


Figure 4.14. Hopping maps for Re_{H124}-W₁₂₂-Azurin with differing values of β . $\lambda = 0.8 \text{ eV}$, $r_1 = 8.1 \text{ \AA}$, $r_2 = 12.8 \text{ \AA}$, $r_T = 19.4 \text{ \AA}$. The black dot is at $\Delta G_{\text{Total}}^0 = -0.94 \text{ eV}$, $\Delta G_{\text{1st step}}^0 = -0.028 \text{ eV}$.

Larger values of β result in increased hopping total ET times, just as in single-step tunneling. In this case, single-step tunneling is more sensitive to β than is hopping; as β (and ET times) decrease, the region of hopping advantage also shrinks. This is opposite what was observed for temperature, where a decrease in ET times was accompanied by an increase in the region of hopping advantage.

Within the context of a protein, the parameter β is essentially bound by the limiting values of tunneling through aqueous glasses ($\beta = 1.6$)^{34,35} and conjugated xylyl chain ($\beta = 0.76$).³⁶ In practice, the lower bound can be raised further, to that for an alkane chain ($\beta = 1.0$).³⁷ Of the 32 data points for electron-tunneling through the protein medium, (**Figure 4.7**), only two fall above the line of $\beta = 1.0$; hopping has been implicated in both cases. In the case of Re_{H124}-W₁₂₂-Azurin, variation of β by $\pm 0.2 \text{ \AA}^{-1}$ (from the starting value of 1.1 \AA^{-1}) results in increase or decrease in ET time by less than a factor of four.

Reorganization energy, λ

As discussed previously, the reorganization required for a given reaction is composed of both inner- (nuclear) and outer-sphere (solvent) rearrangements. Electron transfer events are charged, by nature. Thus, a polar environment (such as solvation by water molecules) reorganizes more in response to ET. By sequestering redox cofactors within a hydrophobic protein environment, enzymes reduce reorganization and the energy of activation for ET. The inner-sphere reorganization energy of many metalloproteins also is small, particularly when there is no change in spin state, and/or when the ligand geometry is constrained.³⁸ Experimental reorganization energies have been determined by varying the driving force for single-step ET (**Table 4.1**). The reorganization energy used in the original hopping was 0.8 eV, based on these types of experimental investigations.^{9,19}

However, different systems, particularly those not evolved for rapid ET, may have alternate values of λ .

Table 4.1. Reorganization energies for various proteins. Table is adapted from Ref 38.^{13,38–45} a: Ref. 39, b: Ref. 13, c: Ref. 40, d: Ref. 41, e: Ref. 42, f: Ref. 43, g: Ref. 44, h: Ref. 45.

	Protein (method)	λ (eV)
Cytochromes	cytochrome c (calculation) ^a	0.69
	cytochrome b5 (calculation) ^a	1.06
	cytochrome c (Ru-cyt c, experimental) ^b	0.74
	cyt c/cyt b5 (experimental) ^c	0.7
Blue Copper	azurin (Ru/Os-Az, experimental) ^d	0.82
	azurin (Ru-Az, experimental) ^e	0.71
	plastocyanin (Ru-Pc, experimental) ^f	0.7 - 0.75
Iron Sulfur Proteins	high-potential Fe ₄ S ₄ (experimental) ^g	< 1
Bacterial Reaction Centers	BRCs (experimental, theoretical) ^h	0.7

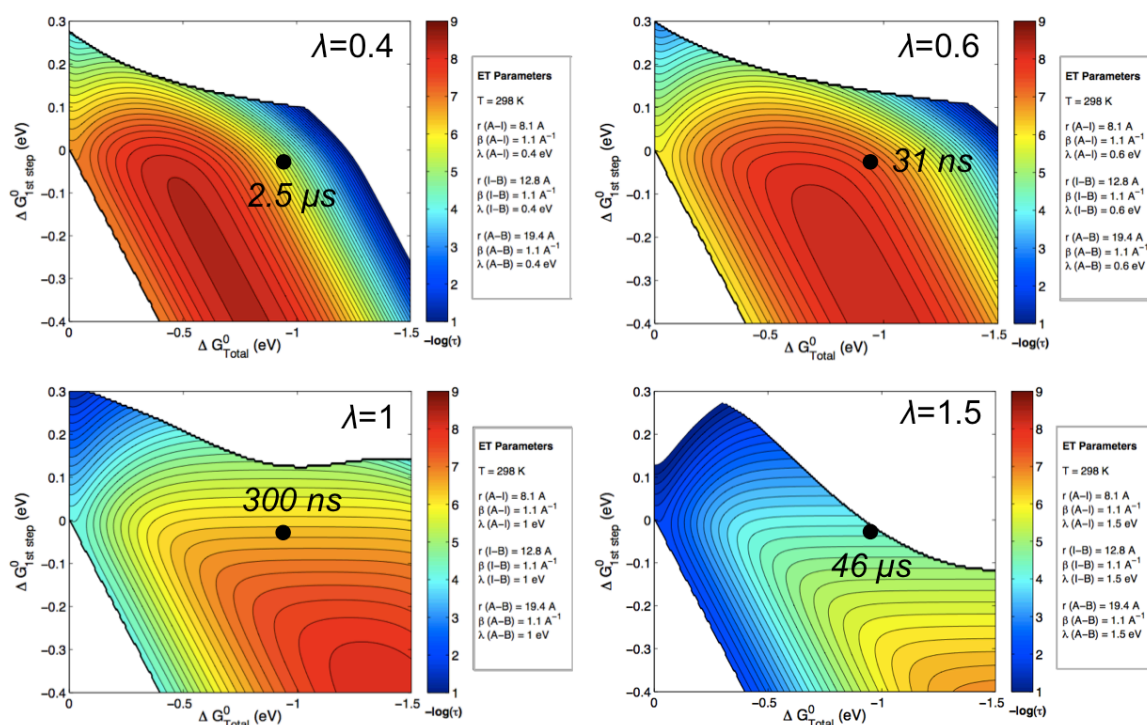


Figure 4.15. Hopping maps for ReH₁₂₄-W₁₂₂-Azurin with differing values of λ . $\beta=1.1 \text{ \AA}^{-1}$, $r_1=8.1 \text{ \AA}$, $r_2=12.8 \text{ \AA}$, $r_T=19.4 \text{ \AA}$. The black dot is at $\Delta G_{\text{total}}^{\circ} = -0.94 \text{ eV}$, $\Delta G_{\text{1st step}}^{\circ} = -0.028 \text{ eV}$.

Changes in λ affect both the rates and contours of the map. As λ increases, the “hottest” center widens and shifts to more negative values of both $\Delta G_{\text{DA}}^\circ$ and $\Delta G_{\text{DI}}^\circ$. At the driving forces of interest for the $\text{Re}_{\text{H124}}\text{-W}_{122}\text{-Azurin}$ system ($\Delta G_{\text{DA}}^\circ = -0.94$ eV, $\Delta G_{\text{DI}}^\circ = -0.028$ eV), there is inversion with respect to λ ; the maximum rate occurs at $\lambda = 0.6\text{-}0.8$, and decreases at both smaller and larger values.

$\text{Re}_{\text{H124}}\text{-W}_{122}\text{-Azurin}$ is nearly driving force optimized for λ . There is little variation between $\lambda = 0.6$ and 0.8 eV. However, outside of that optimal range, ET times change dramatically with variation in λ (as is expected). For driving force unoptimized systems in which λ is uncertain, hopping maps provide only a rough approximation of ET times, and must be assessed with care.

Driving forces

The parameters discussed above (T , β , λ , r) are needed for the construction of the map. However, complete hopping analysis requires placing the system of interest on the map, and determining the predicted τ values and rate advantage of hopping. In order to do this, one needs to have knowledge of the driving forces associated with the first and overall ET steps.

Unfortunately, the E° of relevant cofactors often are unknown. Due to the reactivity of many of the intermediates (such as amino acid radicals), there is significant variation in the reported values. Additionally, these potentials can be shifted from the solution values by the protein environment, and, if coupled with protonation/deprotonation, can be affected by pH and hydrogen-bonding.

For example, the solution $\text{W}^{\bullet+}/\text{W}$ potential has been estimated at $+1.15$ V (water),²² $+1.24$ V (water, pH 7),⁴⁶ or 0.98 V (water, pH 8).⁴⁷ Based on the experimentally measured rate for tryptophan oxidation in $\text{Re}_{\text{H124}}\text{-W}_{122}\text{-Azurin}$

(where W122 is relatively solvent exposed), ΔG_{DI}° was determined to be -0.028 V; assuming a ${}^*\text{Re}^{\text{II}}(\text{dmp}^{\bullet-})/\text{Re}^{\text{I}}(\text{dmp}^{\bullet-})$ potential of 1.25 V,²² this places the $W^{\bullet+}/W$ at 1.22 V. Driving forces for ET can be further complicated by changes in protonation state. Tryptophan radical cation is significantly more acidic than the neutral species ($pK_a=4.5$ vs. ~ 21).⁴⁸ Another redox active amino acid (and potential hopping intermediate), is tyrosine; this intermediate is much more sensitive to pH. The tyrosine neutral species has a pK_a of 10 , and a radical cation pK_a of -2 .⁴⁹ For both of these amino acids, the relevant driving forces are influenced by pH and hydrogen bonding (**Figure 4.16**).

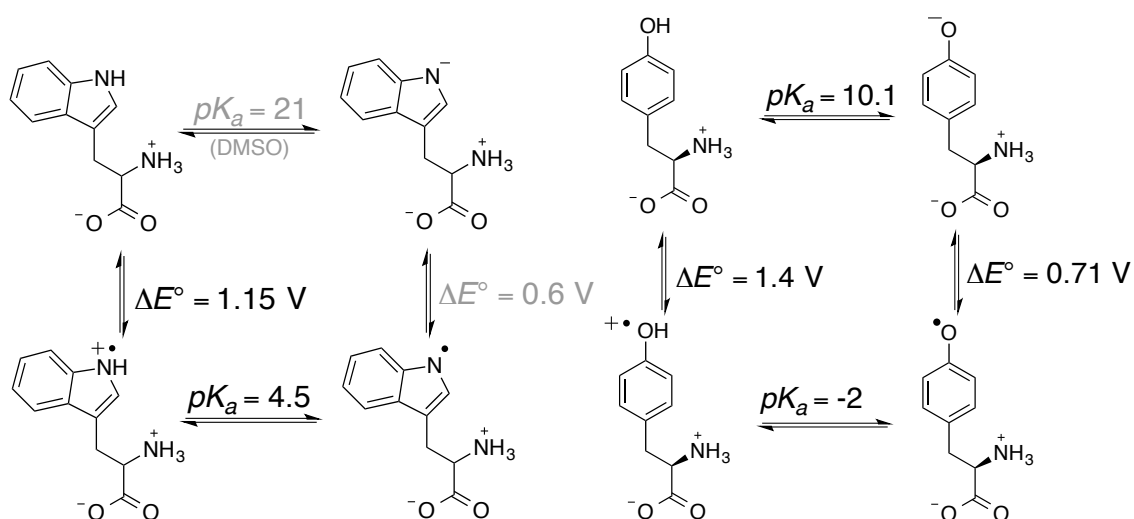


Figure 4.16. Square scheme for tryptophan (left) and tyrosine (right), including relevant reduction potentials and acid dissociation constants.^{48,49} Gray values indicate DMSO solutions.

4.6. Hopping Map Limitations

In the best cases, the hopping maps give insight into the advantage of hopping over single-step ET, and provide an estimate of hopping times within an order of magnitude. From the above analysis, small uncertainties in ET parameters ($r: \pm 1$ Å; $\beta \pm 0.2$ Å⁻¹, $\lambda \pm 0.1$ eV) can change the hopping times (τ) by less than a factor of

10. Additionally, the Hopping Maps program allows quick and facile analysis of the effect of these uncertainties for any given system.

However, these ET parameters can be greatly affected by the specific protein environment, and experimental measurement of many of these parameters is extremely difficult. Even once a hopping map has been constructed with confidence, accurate comparison between computed and experimental hopping rate constants requires accurate assessment of reaction driving forces. This is greatly complicated by the paucity of reliable reduction potential data for biological ET reactions that, for a given cofactor, strongly depend on the protein environment.

Even when exact comparison of experimental and predicted time constants is not possible, assessment of multiple maps can provide a range of expected values, and in some cases, may provide insight into the advantage of hopping over single-step tunneling. We will examine one of these highly underdetermined cases to assess the possibility of hopping in a ruthenium-cytochrome P450 system.

4.7. Application to the P450-W-Ru system

As described previously, we developed a system for phototriggered heme oxidation in a Ru-cytochrome P450 conjugate that requires the presence of a tryptophan situated between Ru and heme sites. We have experimentally determined the rate of porphyrin oxidation, which proceeds on the microsecond timescale with relatively little driving force. By examining a series of hopping maps, we aim to determine the feasibility of oxidative (hole) hopping in this system. Is hopping *possible*? And, based on our analyses, is hopping *probable*?

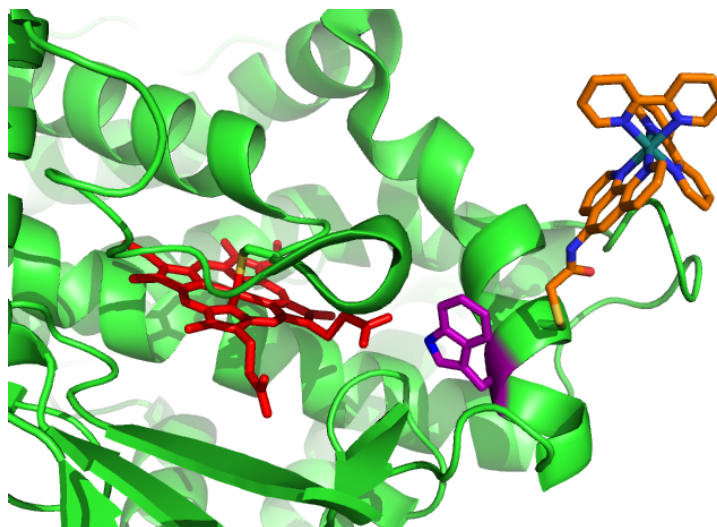


Figure 4.17. Hopping system in Ru_{K97C}-W₉₆-P450_{BM3} (PDB: 3NPL). The P450 heme is highlighted in red, W96 in purple, and the Ru photosensitizer in orange.

Estimates and Challenges

Hopping in the Ru-W-P450 system is underdetermined. Nevertheless, we can make estimates, and probe to what extent error in those estimates affects the hopping map. Temperature is the most certain parameter: 293 ± 2 K. We have no direct measurement of β and λ , but will begin by assuming the typical parameters of $\beta=1.1 \text{ \AA}^{-1}$; $\lambda=0.8$ eV, which apply to many systems (as discussed previously).

The Ru-W-P450 system has been crystallized, and we will use the crystallographic distances as our first estimates for r_1 , r_2 , and r_T . However, as described for Re_{H124}-W₁₂₂-Azurin, the ET origin associated with the aromatic tryptophan side chain is ill-defined. Additionally, the hole-acceptor in this case is not a metal center, but the large, conjugated porphyrin ring. Furthermore, the ruthenium photosensitizer is tethered to the protein surface via a flexible acetamido linker. Significant disorder in one unit of the crystal structure, and the biexponential luminescence decay support the existence of multiple conformations (and thus, multiple possible distances) in solution.

The crystallographic Ru-Fe distance is 23.7 Å. We are interested in oxidation of the porphyrin ligand; however, this center is approximately the average of the distances between the photosensitizer and conjugated porphyrin (23.9 Å). We will also examine the distance to the nearest pyrrole edge on the porphyrin: 20.8 Å. It is possible to bring the photosensitizer center even closer to the porphyrin by bending it into a depression in the surface (above the buried heme). Such an arrangement could decrease the through-space Ru-porphyrin distance by as much as 4 Å, and also bring Ru an estimated 2 Å closer to the tryptophan.

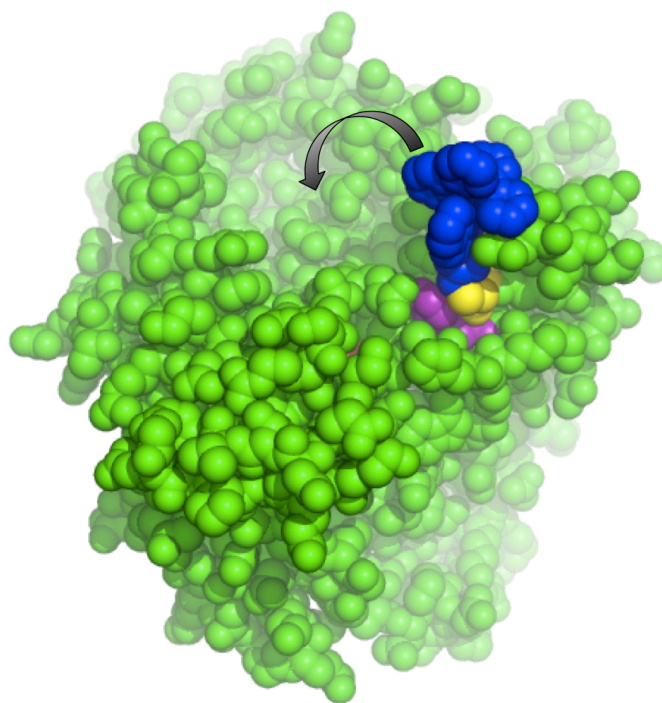


Figure 4.18. Model of the Ru-P450 surface. The photosensitizer is highlighted in blue, the cysteine linker in yellow, W96 in purple, and the buried heme in red.

Finally, we must make estimates for $\Delta G_{\text{total}}^{\circ}$ and $\Delta G_{\text{1st step}}^{\circ}$. Instead of placing a dot on the map, we will define a region in which we reasonably expect to find our Ru-P450 system. (As a reminder, all reduction potentials are referenced versus NHE.)

The oxidatively quenched photosensitizer has $E^\circ(\text{Ru}^{\text{III/II}}) \approx 1.3 \text{ V}$.^{50,51} The $E^\circ(\text{Fe}^{\text{IV/III}})$ in other heme enzymes (e.g., horseradish peroxidase) have been reported in a range of 0.72-1 V.⁵² A P450 relative, the heme-thiolate enzyme chloroperoxidase, has $E^\circ(\text{Fe}^{\text{IV/III}})$ estimated at 1.3 V.⁵³ We will assume that the P450 $E^\circ(\text{Fe}^{\text{IV/III}})$ is within the range of 0.9-1.3 V, and that the $E^\circ(\text{por}^{\bullet+}/\text{por})$ is at or above this value (so that the entire reaction is exergonic). For all analyses, we will use the driving force range: $-\Delta G^\circ_{\text{total}} = 0$ to 0.3 V. As discussed previously, a range of $W^{\bullet+}/W$ potentials have been reported (1-1.3 V), and these can be influenced significantly by hydrogen bonding and protein environment. Therefore, we will assume a range of driving force for first hop step ($-\Delta G^\circ_{\text{1st step}}$) of -0.10 to +0.3 V.

Single-step tunneling

To provide a comparison for the hopping rates, we will first examine the $\text{Ru}_{\text{K97C}}\text{-W}_{96}\text{-P450}_{\text{BM3}}$ system using single-step ET (Equations 4.1 and 4.2). Predicted ET times (τ) are listed in **Table 4.2**. Note that at low driving force, with a distance of $\sim 24 \text{ \AA}$, single-step ET takes nearly a second.

Table 4.2. Calculated single-step tunneling times for porphyrin oxidation, using a variety of ET parameters.

	$r_{\text{T}} (\text{\AA})$	$\beta (\text{\AA}^{-1})$	$\lambda (\text{eV})$	$\Delta G^\circ (\text{eV})$	$\tau (\mu \text{s})$
<i>Experimental</i>					1.3
	23.9	1.1	0.8	0	430,000
	23.9	1.1	0.8	-0.3	20,000
	23.9	0.8	0.5	-0.3	190
	20.8	1.1	0.8	0	77,000
	20.8	1.1	0.8	-0.3	670
	20.8	0.9	0.6	-0.3	3
	17	1.1	0.8	0	1,200
	17	1.1	0.8	-0.3	10
	17	0.9	0.6	-0.3	0.1

Hopping Analysis

By constructing a series of hopping maps, we aim to determine whether or not there is a *clear hopping advantage* within reasonable ET parameters. We will systematically vary ET parameters (r , β , λ) for the Ru-P450 system, and determine the effects on two-step hopping versus single-step tunneling. Each map is constructed with the same range of driving forces and same color scale as the Re-W-azurin system (to facilitate comparisons). The range of *expected* driving forces is bordered by dashed lines. Heme oxidation was observed experimentally, so we assume that $-\Delta G_{DA}^{\circ} > -\Delta G_{DI}^{\circ}$; in other words, the system does not fall in the white, bottom left corner of the maps.

Table 4.3. Minimum driving forces necessary to obtain the experimental ET time (within a factor of 3) for each hopping map.

	r_1 (Å)	r_2 (Å)	r_T (Å)	β (Å ⁻¹)	λ (eV)	ΔG_{DA}° (eV)	ΔG_{DI}° (eV)	τ (μ s)
<i>Experimental</i>								1.3
A	13.8	12.9	23.9	1.1	0.8	-0.300	-0.180	3
B	13.8	9	20.8	1.1	0.8	-0.140	-0.140	3
C	12.1	7.7	20.8	1.1	0.8	-0.025	-0.020	3
D	13.8	9	20.8	1	0.8	-0.075	-0.070	3
E	13.8	9	20.8	1.3	0.8	-0.300	-0.295	3
F	13.8	9	20.8	1.1	0.6	-0.005	0	3
G	13.8	9	20.8	1.1	1	-0.290	-0.285	3
H	12	9	17.0	1	0.8	-0.005	0.045	3
I	12	9	17.0	0.8	1.3	-0.250	-0.245	3

Within the context of each map, we can also determine minimum driving forces to give a time constant within a factor of three of the experimental value; these are given in **Table 4.3**. These values are mainly intended to orient the reader to the map, not to place the Ru-W-P450 system at a defined driving force.

Varying Distances

We first examine the longest distance for ET (**case A**), using the ruthenium center, the porphyrin centroid (average Ru-por distance = 23.9 Å), and the W centroid (average Ru-W, W-por distances). The other ET parameters are $\beta=1.1$, $\lambda=0.8$, as used previously for the original $\text{Re}_{\text{H124}}\text{-W}_{\text{122}}\text{-Az}$ system. In case A, hopping is clearly advantageous over the entire expected driving force range. The experimental time constant of 1.3 μs can be reproduced (within a factor of three) assuming reasonable driving forces of 300 meV and 180 meV (for $-\Delta G^{\circ}_{\text{DA}}$ and $-\Delta G^{\circ}_{\text{DB}}$, respectively). This is a rate advantage of *four orders of magnitude* compared to single-step ET.

Next, we set r_{T} as the distance to the nearest edge of the porphyrin: 20.8 Å (**case B**). The horizontal contours in this map (as well as all the others that follow) shows that hopping is limited entirely by the first step: tryptophan oxidation. The region of hopping advantage decreases. However, hopping still beats single-step tunneling within all of the expected driving forces, and the experimental time can be reproduced with milder overall driving forces (~ 150 meV).

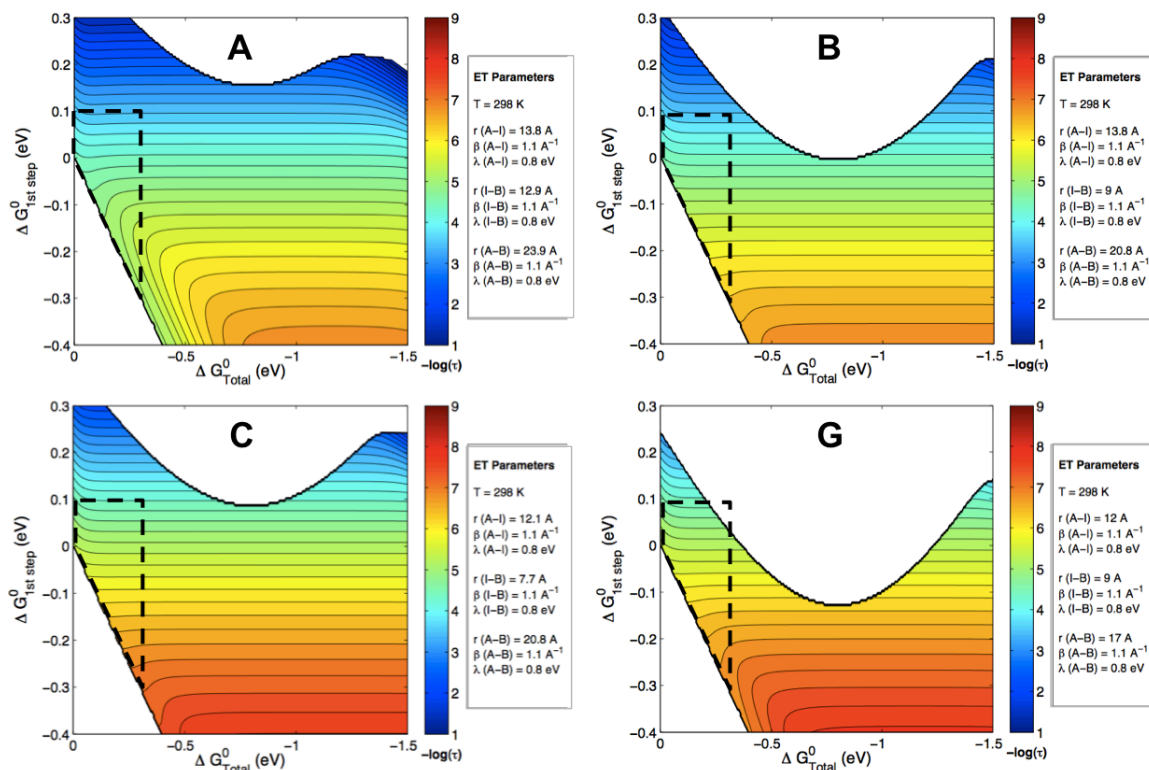


Figure 4.19. Hopping maps for RuC97-W96-P450_{BM3} heme oxidation: Distance formulations.

If we change the distance formulation to use the tryptophan edges (**case C**) instead of the centroid, we decrease the distance of the first hopping step. This decreases the overall hopping times, and increases the area of hopping advantage. Very little driving force ($\sim 0.02 \text{ eV}$) is required to reproduce the experimental time constant, using this formulation. Once again, hopping has a rate advantage of four orders of magnitude.

As discussed for the single-step analysis, a final possibility for distances is that the photosensitizer bends over, bringing it in closer proximity to the porphyrin (and also to the tryptophan). Comparison between cases B and G shows that rates increase by over an order of magnitude, and the region of hopping advantage significantly decreases. The hopping advantage is lost only in cases where the first hop is endergonic ($>0.05 \text{ eV}$), and the overall driving force is large.

Varying β and λ

We can also examine the effects of uncertainty in β and λ on the Ru_{K97C}-P450_{BM3} hopping map. A significant rate increase is seen by lowering β to 1.0 Å⁻¹ (**case D**), and a significant decrease is seen by raising β to 1.3 Å⁻¹ (**case E**). However, the region of hopping advantage does not change significantly. Since ET must proceed mainly through bonds, but with at least one through-space hop (between Trp96 and the porphyrin edge), we suspect that the original value of 1.1 Å⁻¹ is a reasonable approximation. Changes in λ significantly affect hopping times, and the region of hopping advantage (**cases F and G**). In each case, the experimental time constant can be reproduced, and hopping is advantageous at all expected driving forces.

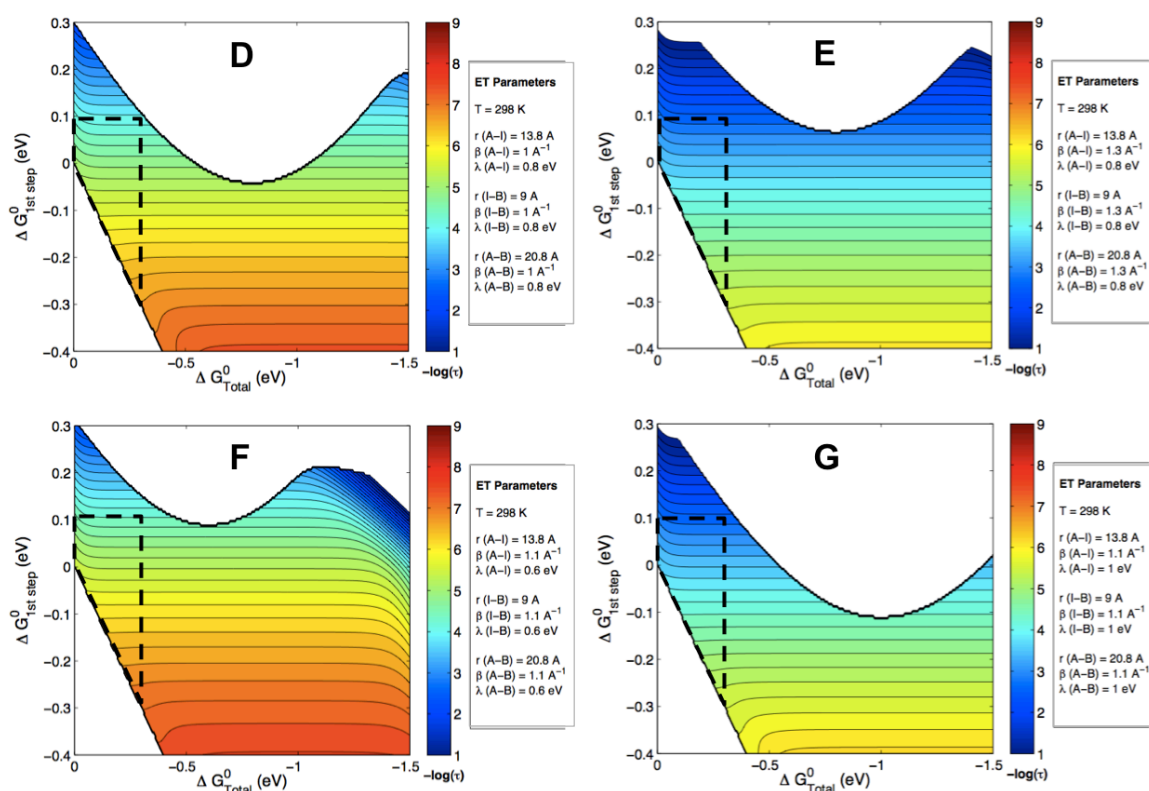


Figure 4.20. Hopping maps for Ru_{K97C}-P450_{BM3} photochemical heme oxidation: Altering β and λ .

All of these maps show a clear hopping advantage, even if single-step ET can reproduce the experimental rate constant within the expected driving forces. What would it take for single-step ET to out-compete hopping?

We present one final, “worst case” hopping scenario (**case I**). r_T is small in comparison to r_1 and r_2 (as the photosensitizer bends toward the P450 surface), β is small (tunneling through a conjugated chain), and λ is large. As shown in **Figure 4.21**, the Ru-W-P450 system is situated exactly where hopping is most advantageous: low overall driving force. Even if the first hop (e.g., tryptophan oxidation) is endergonic by 100 mV, the two-step process can be faster.

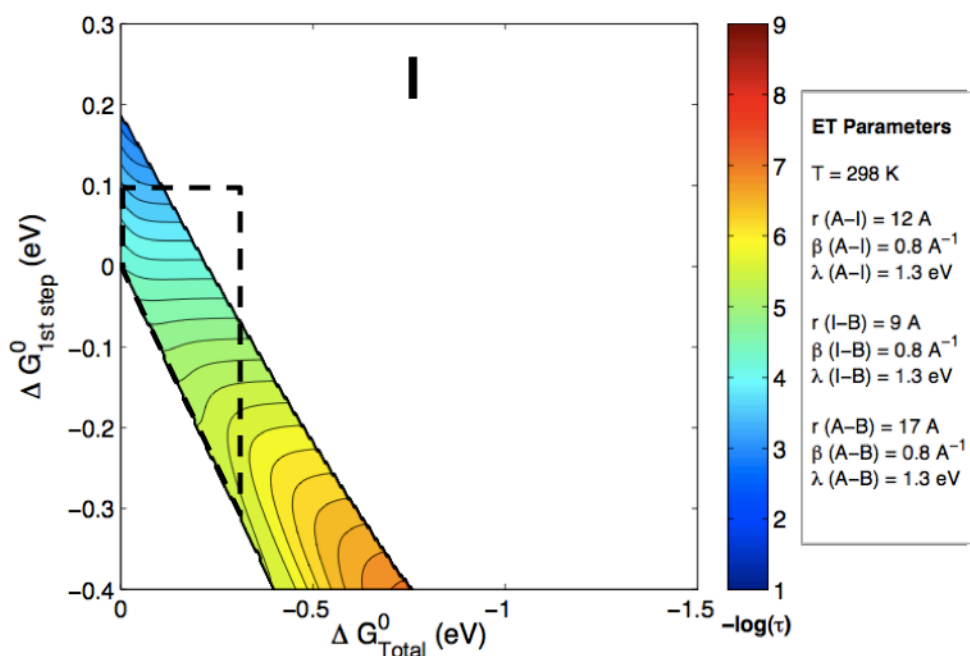


Figure 4.21. Hopping maps for Ru_{K97C}-P450_{BM3} photochemical heme oxidation: Worst case hopping scenario.

These hopping map analyses strongly support the idea of hopping in the Ru-P450 system. In every scenario examined, the experimental rate constant can be easily reproduced with reasonable ET parameters, and there is a rate advantage to hopping in the majority of driving forces.

4.8. Conclusions

This tutorial demonstrates the usage, utility, and limitations of Hopping Maps for the analysis of multistep ET events. We have used this analysis to examine the multistep photochemical heme oxidation in Ru_{K97C}-P450_{BM3}, and have shown that there is a clear hopping advantage at nearly all parameters explored. Creation of hopping maps is greatly facilitated by the availability of the hopping map program. However, construction and interpretation of hopping maps that have any relation to real chemical systems requires detailed knowledge of ET parameters.

4.9. Acknowledgments

The original hopping map analysis was conceived of and accomplished by Jay R. Winkler,²⁰ and his conversations have greatly facilitated construction of this hopping map program. Work for this Chapter was inspired by Harry B. Gray and Jeffrey J. Warren.

4.10. References

- (1) Moore, G. F.; Brudvig, G. W. Energy Conversion in Photosynthesis: A Paradigm for Solar Fuel Production. *Annu. Rev. Condens. Matter Phys.* **2011**, *2*, 303–327.
- (2) Nelson, N.; Yocum, C. F. Structure and Function of Photosystems I and II. *Annu. Rev. Plant Biol.* **2006**, *57*, 521–565.
- (3) Rich, P. R.; Marechal, A. The Mitochondrial Respiratory Chain. *Essays Biochem. Mitochondrial Funct.* **2010**, *47*, 1–23.
- (4) Kaila, V. R. I.; Verkhovskyy, M. I.; Wikstrom, M. Proton-Coupled Electron Transfer in Cytochrome Oxidase. *Chem. Rev.* **2010**, *110*, 7062–7081.
- (5) Lewis, B. A.; Engelman, D. M. Lipid Bilayer Thickness Varies Linearly with Acyl Chain Length in Fluid Phosphatidylcholine Vesicles. *J. Mol. Biol.* **1983**, *166*, 211–217.
- (6) Langen, R.; Chang, I.-J.; Germanas, J. P.; Richards, J. H.; Winkler, J. R.; Gray, H. B. Electron-Tunneling in Proteins - Coupling through a Beta-Strand. *Science* **1995**, *268*, 1733–1735.
- (7) Regan, J. J.; Di Bilio, A. J.; Langen, R.; Skov, L. K.; Winkler, J. R.; Gray, H. B.; Onuchic, J. N. Electron-Tunneling in Azurin - the Coupling across a Beta-Sheet. *Chem. Biol.* **1995**, *2*, 489–496.
- (8) Crane, B. R.; Di Bilio, A. J.; Winkler, J. R.; Gray, H. B. Electron Tunneling in Single Crystals of Pseudomonas Aeruginosa Azurins. *J. Am. Chem. Soc.* **2001**, *123*, 11623–11631.
- (9) Gray, H. B.; Winkler, J. R. Electron Tunneling through Proteins. *Q. Rev. Biophys.* **2003**, *36*, 341–372.
- (10) Winkler, J. R.; Nocera, D. G.; Yocom, K. M.; Bordignon, E.; Gray, H. B. Electron-Transfer Kinetics of pentaammineruthenium(III)(Histidine-33)-Ferricytochrome-c - Measurement of the Rate of Intramolecular Electron-Transfer between Redox Centes Separated by 15-A in a Protein. *J. Am. Chem. Soc.* **1982**, *104*, 5798–5800.
- (11) Casimiro, D.; Richards, J.; Winkler, J.; Gray, H. Electron Transfer in Ruthenium-Modified Cytochromes C. .sigma.-Tunneling Pathways through Aromatic Residues. *J. Phys. Chem.* **1993**, *97*, 13073–13077.
- (12) Meade, T. J.; Gray, H. B.; Winkler, J. R. Driving-Force Effects on the Rate of Long-Range Electron Transfer in Ruthenium-Modified Cytochrome c. *J. Am. Chem. Soc.* **1989**, *111*, 4353–4356.
- (13) Mines, G. A.; Bjerrum, M. J.; Hill, M. G.; Casimiro, D. R.; Chang, I.-J.; Winkler, J. R.; Gray, H. B. Rates of Heme Oxidation and Reduction in Ru(His33)cytochrome c at Very High Driving Forces. *J. Am. Chem. Soc.* **1996**, *118*, 1961–1965.
- (14) Pizano, A. A.; Lutterman, D. A.; Holder, P. G.; Teets, T. S.; Stubbe, J.; Nocera, D. G. Photo-Ribonucleotide Reductase Beta 2 by Selective Cysteine Labeling with a Radical Phototrigger. *Proc. Natl. Acad. Sci.* **2012**, *109*, 39–43.
- (15) Marcus, R. A. On the Theory of Oxidation-Reduction Reactions Involving Electron Transfer .1. *J. Chem. Phys.* **1956**, *24*, 966–978.
- (16) Marcus, R. A. Chemical + Electrochemical Electron-Transfer Theory. *Annu. Rev. Phys. Chem.* **1964**, *15*, 155.

- (17) Marcus, R. A. Electron-Transfer Reactions in Chemistry - Theory and Experiment. *Rev. Mod. Phys.* **1993**, *65*, 599–610.
- (18) Marcus, R. A. Electron Transfer Past and Future. In *Electron transfer - from isolated molecules to biomolecules, PT 2*; Advances in Chemical Physics; 1999; Vol. 106, pp. 1–6.
- (19) Gray, H. B.; Winkler, J. R. Long-Range Electron Transfer. *Proc. Natl. Acad. Sci.* **2005**, *102*, 3534–3539.
- (20) Shih, C.; Museth, A. K.; Abrahamsson, M.; Blanco-Rodríguez, A. M.; Di Bilio, A. J.; Sudhamsu, J.; Crane, B. R.; Ronayne, K. L.; Towrie, M.; Vlček, Jr., A.; Richards, J. H.; Winkler, J. R., Gray, H. B. Tryptophan-Accelerated Electron Flow Through Proteins. *Science* **2008**, *320*, 1760–1762.
- (21) Blanco-Rodríguez, A. M.; Busby, M.; Gradinaru, C.; Crane, B. R.; Di Bilio, A. J.; Matousek, P.; Towrie, M.; Leigh, B. S.; Richards, J. H.; Vlček Jr., A.; Gray, H. B. Excited-State Dynamics of Structurally Characterized [Re(I)(CO)₃(phen)(HisX)]⁺ (X=83, 109) *Pseudomonas Aeruginosa* Azurins in Aqueous Solution. *J. Am. Chem. Soc.* **2006**, *128*, 4365–4370.
- (22) Warren, J. J.; Ener, M. E.; Vlček Jr., A.; Winkler, J. R.; Gray, H. B. Electron Hopping through Proteins. *Coord. Chem. Rev.* **2012**, *256*, 2478–2487.
- (23) Takematsu, K.; Williamson, H.; Blanco-Rodríguez, A. M.; Sokolová, L.; Nikolovski, P.; Kaiser, J. T.; Towrie, M.; Clark, I. P.; Vlček, Jr., A.; Winkler, J. R.; Gray, H. B. Tryptophan-Accelerated Electron Flow Across a Protein-Protein Interface. *J. Am. Chem. Soc.* **2013**, *135*, 15515–15525.
- (24) Pascher, T.; Karlsson, B. G.; Nordling, M.; Malmström, B. G.; Vänngård, T. Reduction Potentials and Their pH Dependence in Site-Directed-Mutant Forms of Azurin from *Pseudomonas Aeruginosa*. *Eur. J. Biochem.* **1993**, *212*, 289–296.
- (25) Skourtis, S. S.; Waldeck, D. H.; Beratan, D. N. Fluctuations in Biological and Bioinspired Electron-Transfer Reactions. **2010**, *61*, 461–485.
- (26) Beratan, D. N.; Onuchic, J. N.; Winkler, J. R.; Gray, H. B. Electron-Tunneling Pathways in Proteins. *Science* **1992**, *258*, 1740–1741.
- (27) Onuchic, J. N.; Beratan, D. N.; Winkler, J. R.; Gray, H. B. Pathway Analysis of Protein Electron-Transfer Reactions. *Annu. Rev. Biophys. Biomol. Struct.* **1992**, *21*, 349–377.
- (28) Walden, S. E.; Wheeler, R. A. Distinguishing Features of Indolyl Radical and Radical Cation: Implications for Tryptophan Radical Studies. *J. Phys. Chem.* **1996**, *100*, 1530–1535.
- (29) Beratan, D. N.; Onuchic, J. N. Electron-Tunneling Pathways in Proteins - Influences on the Transfer Rate. *Photosynth. Res.* **1989**, *22*, 173–186.
- (30) Beratan, D. N.; Betts, J. N.; Onuchic, J. N. Protein Electron-Transfer Rates Set by the Bridging Secondary and Tertiary Structure. *Science* **1991**, *252*, 1285–1288.
- (31) Balabin, I. A.; Onuchic, J. N. A New Framework for Electron-Transfer Calculations - Beyond the Pathways-like Models. *J. Phys. Chem. B* **1998**, *102*, 7497–7505.

- (32) Regan, J. J.; Onuchic, J. N. Electron-Transfer Tubes. In *Electron transfer - from isolated molecules to biomolecules, PT 2*; Advances in Chemical Physics; 1999; Vol. 107, pp. 497–553.
- (33) Skourtis, S. S.; Beratan, D. N. High and Low Resolution Theories of Protein Electron Transfer. *J. Biol. Inorg. Chem.* **1997**, *2*, 378–386.
- (34) Ponce, A.; Gray, H. B.; Winkler, J. R. Electron Tunneling through Water: Oxidative Quenching of Electronically Excited Ru(tpy)₂(2+) (tpy=2,2':6,2"-Terpyridine) by Ferric Ions in Aqueous Glasses at 77K. *J. Am. Chem. Soc.* **2000**, *122*, 8187–8191.
- (35) Weidemaier, K.; Tavernier, H. L.; Swallen, S. F.; Fayer, M. D. Photoinduced Electron Transfer and Geminate Recombination in Liquids. *J. Phys. Chem. A* **1997**, *101*, 1887–1902.
- (36) Villahermosa, R. Thesis, California Institute of Technology: Pasadena, California, 2002.
- (37) Oevering, H.; Paddon-Row, M. N.; Heppener, M.; Oliver, A. M.; Cotsaris, E.; Verhoeven, J. W.; Hush, N. S. Long-Range Photoinduced through-Bond Electron-Transfer and Radiative Recombination via Rigid Nonconjugated Bridges - Distance and Solvent Dependence. *J. Am. Chem. Soc.* **1987**, *109*, 3258–3269.
- (38) Stubbe, J.; Nocera, D. G.; Yee, C. S.; Chang, M. C. Y. Radical Initiation in the Class I Ribonucleotide Reductase: Long-Range Proton-Coupled Electron Transfer? *Chem. Rev.* **2003**, *103*, 2167–2201.
- (39) Andrew, S. M.; Thomasson, K. A.; Northrup, S. H. Simulation of Electron-Transfer Self-Exchange in Cytochrome c and Cytochrome b5. *J. Am. Chem. Soc.* **1993**, *115*, 5516–5521.
- (40) McLendon, G.; Miller, J. R. The Dependence of Biological Electron Transfer Rates on Exothermicity. the Cytochrome C/cytochrome b5 Couple. *J. Am. Chem. Soc.* **1985**, *107*, 7811–7816.
- (41) Di Bilio, A. J.; Hill, M. G.; Bonander, N.; Karlsson, B. G.; Villahermosa, R. M.; Malmström, B. G.; Winkler, J. R.; Gray, H. B. Reorganization Energy of Blue Copper: Effects of Temperature and Driving Force on the Rates of Electron Transfer in Ruthenium- and Osmium-Modified Azurins. *J. Am. Chem. Soc.* **1997**, *119*, 9921–9922.
- (42) Skov, L. K.; Pascher, T.; Winkler, J. R.; Gray, H. B. Rates of Intramolecular Electron Transfer in Ru(bpy)₂(im)(His83)-Modified Azurin Increase below 220 K. *J. Am. Chem. Soc.* **1998**, *120*, 1102–1103.
- (43) Di Bilio, A. J.; Dennison, C.; Gray, H. B.; Ramirez, B. E.; Sykes, A. G.; Winkler, J. R. Electron Transfer in Ruthenium-Modified Plastocyanin. *J. Am. Chem. Soc.* **1998**, *120*, 7551–7556.
- (44) Babini, E.; Bertini, I.; Borsari, M.; Capozzi, F.; Luchinat, C.; Zhang, X.; Moura, G. L. C.; Kurnikov, I. V.; Beratan, D. N.; Ponce, A.; Di Bilio, A. J.; Winkler, J. R.; Gray, H. B. Bond-Mediated Electron Tunneling in Ruthenium-Modified High-Potential Iron-Sulfur Protein. *J. Am. Chem. Soc.* **2000**, *122*, 4532–4533.
- (45) Moser, C. C.; Keske, J. M.; Warncke, K.; Farid, R. S.; Dutton, P. L. Nature of Biological Electron Transfer. *Nature* **1992**, *355*, 796–802.

- (46) Merenyi, G.; Lind, J.; Shen, X. H. Electron-Transfer from Indoles, Phenol, and Sulfite (SO₃⁽⁻²⁾) to Chlorine Dioxide (ClO₂). *J. Phys. Chem.* **1988**, *92*, 134–137.
- (47) Huvaere, K.; Skibsted, L. H. Light-Induced Oxidation of Tryptophan and Histidine. Reactivity of Aromatic N-Heterocycles toward Triplet-Excited Flavins. *J. Am. Chem. Soc.* **2009**, *131*, 8049–8060.
- (48) Harriman, A. Further Comments on the Redox Potentials of Tryptophan and Tyrosine. *J. Phys. Chem.* **1987**, *91*, 6102–6104.
- (49) Warren, J. J.; Winkler, J. R.; Gray, H. B. Redox Properties of Tyrosine and Related Molecules. *FEBS Lett.* **2012**, *586*, 596–602.
- (50) Creutz, C.; Chou, M.; Netzel, T. L.; Okumura, M.; Sutin, N. Lifetimes, Spectra, and Quenching of the Excited States of Polypyridine Complexes of Iron(II), Ruthenium(II), and Osmium(II). *J. Am. Chem. Soc.* **1980**, *102*, 1309–1319.
- (51) Sutin, N.; Creutz, C. Properties and Reactivities of the Luminescent Excited States of Polypyridine Complexes of Ruthenium(II) and Osmium(II). In *Inorganic and Organometallic Photochemistry; Advances in Chemistry*; American Chemical Society: Washington, DC, 1978; Vol. 1.
- (52) Battistuzzi, G.; Bellei, M.; Bortolotti, C. A.; Sola, M. Redox Properties of Heme Peroxidases. *Arch. Biochem. Biophys.* **2010**, *500*, 21–36.
- (53) Green, M. T.; Dawson, J. H.; Gray, H. B. Oxoiron(IV) in Chloroperoxidase Compound II Is Basic: Implications for P450 Chemistry. *Science* **2004**, *304*, 1653–1656.

Chapter 5

**PHOTOCHEMICAL HEME REDUCTION AND
GAS BINDING IN CYTOCHROME P450**

5.1. Background: reductive activation of dioxygen

The cytochrome P450 superfamily of heme enzymes catalyzes a wide variety of biologically important transformations, including the metabolism of fatty acids and biosynthesis of signaling molecules. As described in Chapter 1, one-electron reduction of the ferric heme active site induces binding of dioxygen; a second reduction, followed by protonation and heterolysis of the O–O bond generates the catalytically active species, compound I (CI, **Figure 5.1**). Natively, the electrons originate from reduced nicotinamide adenine dinucleotide (phosphate), NAD(P)H, and are passed to the heme by a series electron transfer (ET) partner proteins. However, these native ET steps are much slower than the reaction of CI with substrate.^{1–3}

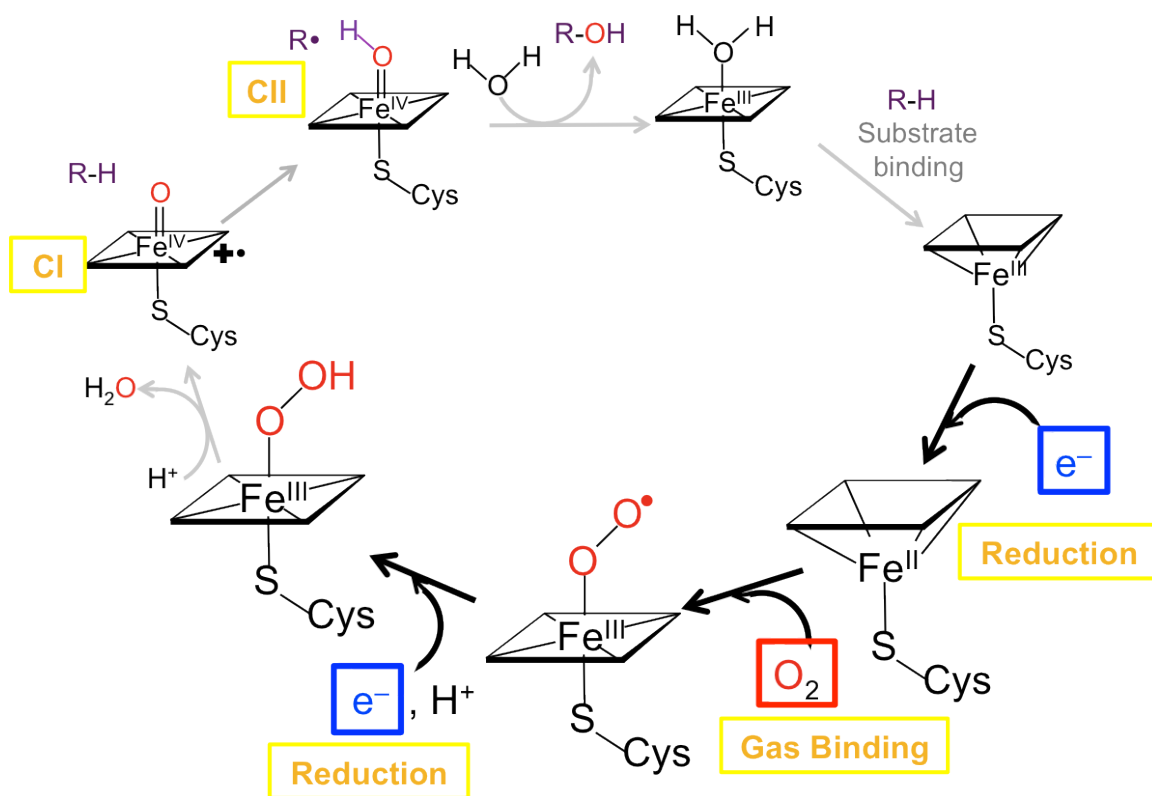


Figure 5.1. Canonical P450 catalytic scheme, highlighting the reductive ET events that activate dioxygen.

Many methods have been implemented in an effort to artificially generate and study this active species. Chemical oxidation by rapid mixing with peroxyacids such as *meta*-chloro-peroxybenzoic acid (*m*CPBA) was used to generate CI in highly purified samples of CYP119.² This method was successful for achieving spectroscopic characterization of the reactive intermediate, as well as single-turnover kinetics investigation of the reaction with substrate. However, the events of hydrogen abstraction to generate compound II (CII, **Figure 5.1**), and radical rebound to form hydroxylated substrate have yet to be observed directly. The dead-time of mixing experiments (e.g., 0.25-5 ms for Bio-Logic® SFM-400) preclude observation of reaction events that include hydrogen abstraction from substrate to form CII, and radical recombination which produces hydroxylated substrate.

In Chapter 2, we described how covalent tethering of a ruthenium photosensitizer to the P450 surface (**Figure 5.2**) can be used to photochemically generate the catalytically-relevant one-electron oxidized species, CII. The deadtime for monitoring these photo-triggered events is limited only by the laser pulse-width (~8 ns in the systems employed for these studies) and instrument response (< 30 ns). We were able to observe CII formation on the low millisecond timescale; this is at least two orders of magnitude faster than expected production by a chemical mixing reaction.

However, this photochemical method has significant limitations. The yields of oxidized products are low (estimated at < 20%). Additionally, each laser pulse can only initiate a single ET event; two oxidizing equivalents are needed to generate CI. Furthermore, photochemical heme oxidation proceeds at low driving force, and is sensitive to the intervening medium (see Chapters 3 and 4). Efforts to

reproduce this ET reactivity in the thermophilic CYP119 generated CII with even lower yield (< 5%).

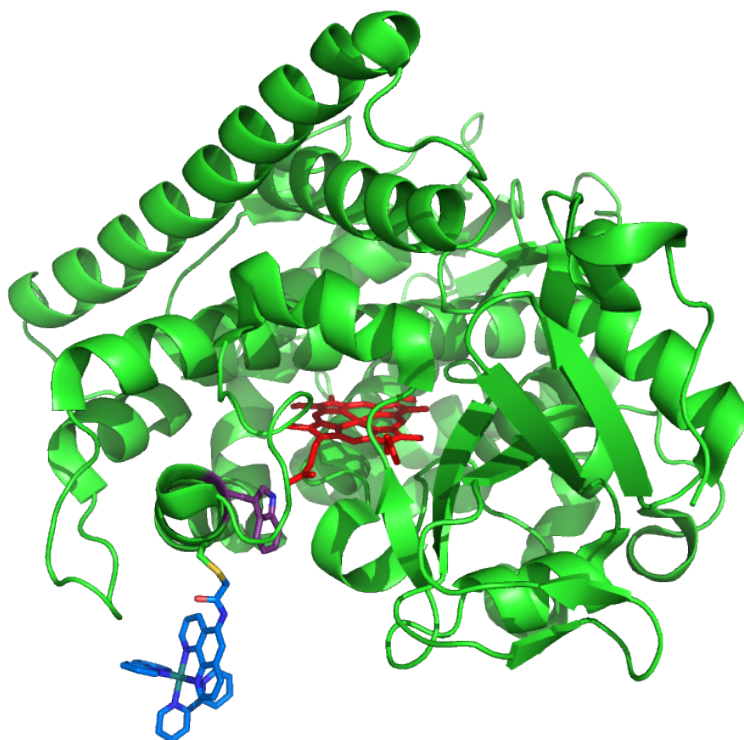


Figure 5.2. Structure of the Ru-P450_{BM3} conjugate. (PDB: 3NPL)

As described in Chapter 1, many features of the cytochrome P450 structure have evolved to facilitate enzyme reduction and the activation of dioxygen - not oxidative ET and activation of water. By using our tethered photosensitizer as a replacement for the native ET partners, we anticipated that *reductive* flash-quench (**Figure 5.3**) could be used to study other important aspects of the catalytic cycle, and may even be used to rapidly access CI.

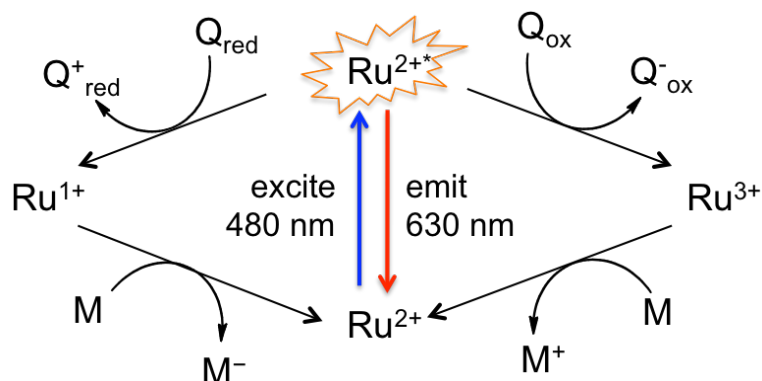


Figure 5.3. Flash-quench cycles for ET with the heme active site.

By supplying an appropriate small molecule quencher such as *para*-methoxydimethylaniline (*p*MeODMA), we can photochemically generate a reduced photosensitizer (Ru^{1+} , best characterized as $\text{Ru}^{\text{II}}\text{bpy}^{\bullet-}$). This species has almost 1 eV of driving force for reduction of the P450 heme: $E^\circ(\text{Ru}^{\text{II}}\text{bpy}/\text{Ru}^{\text{II}}\text{bpy}^{\bullet-}) = -1.3 \text{ V vs. NHE}$,^{4,5} $E^\circ(\text{P450 Fe}^{\text{III/II}}) = -0.43 \text{ V vs. NHE}$.⁶ These flash quench methods have been used to photochemically reduce Ru-labeled cytochrome *c*.⁷ They also were used to reduce Ru-labeled cytochrome P450-BM3 at residue 387, however, conjugation of the photosensitizer at residue 62 curiously showed no heme reduction.⁸

We set out to examine each successive step of P450 oxygen activation by photo-triggered methods, using tethered Ru photosensitizers as the source for reductive ET. We examine photochemical heme reduction, the first step in catalysis. We anticipated that this phototriggered method also could be used to initiate the second step in the native P450 catalytic cycle: binding of dioxygen to the active site. The binding of dioxygen to ferrous heme results in formation of a ferric-superoxo; this species is not thermally stable at room temperature, and decomposes to release superoxide (auto-oxidation).⁹ Carbon monoxide is often used as a more stable diatomic analogue. In some P450 variants, the $\text{Fe}^{\text{II}}\text{-CO}$ species undergoes protonation and/or dissociation of the proximal cysteine

thiolate ligand to generate an inactive species known as “P420.”¹⁰⁻¹² In our hands, the ferrous-CO complex of CYP119 is stable for up to seven months at 4 °C with no apparent change to the UV-visible absorbance spectrum. This approach of photo-triggering heme reduction and observing gas binding has been implemented by others, using organic photosensitizers; UV excitation of NADH was used to trigger P450 reduction via the NADH triplet excited state, and the authors observed binding of CO.¹³

The rate of CO binding to heme enzymes also can be examined by photolysis and rebinding. Excitation into the Fe^{II}-CO Soret or Q-bands causes nearly instantaneous photolysis and dissociation of CO. Some portion of the dissociated CO remains trapped within the protein pocket and rebinds rapidly to the five-coordinate ferrous heme – this is known as geminate recombination.¹⁴⁻¹⁶ Another portion of the dissociated CO has sufficient energy to escape into solution, and thus takes significantly longer to re-enter the protein cavity and rebind to the heme. Photolysis has been used to measure the rates of rebinding for both P450 BM3,^{15,16} and CYP119¹⁷. However, in the latter case of thermophilic CYP119, only room temperature rebinding has been reported, and sub-nanosecond kinetics have not been examined.

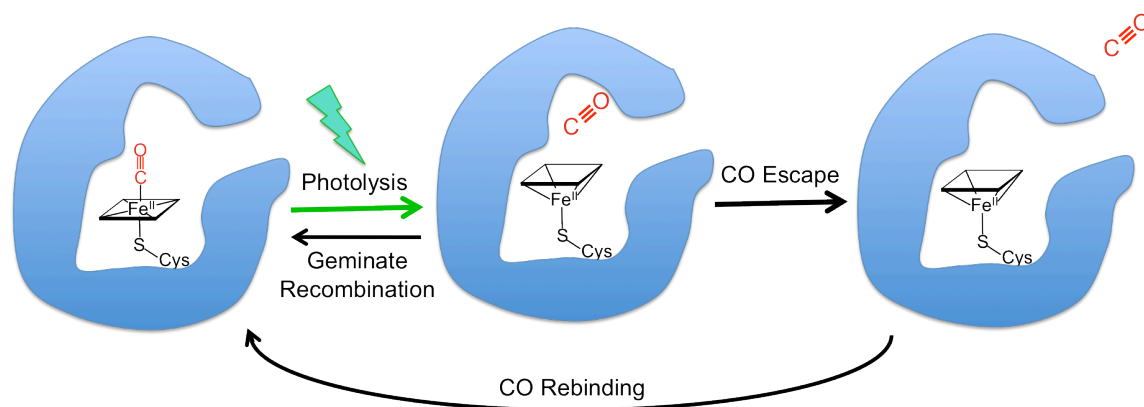


Figure 5.4. Cartoon of CO photolysis and rebinding. The blue shape represents the protein framework.

The third step in P450 catalysis involves a second ET event to produce the ferric superoxo; this final species converts directly to CI. This second electron also could be supplied by flash-quench. However, as addressed in Chapter 3, the yields and lifetimes of flash-quench generation of intermediates precludes the use of two sequential flash-quench cycles. It would be more effective to chemically generate a semi-stable pool of $\text{Fe}^{\text{III}}\text{-O}_2^{\bullet-}$. A stable ferric superoxo can be generated for the substrate bound P450 BM3 at low temperature (-60 °C) in Tris buffer.¹⁸ At these temperatures, the cryosolvent of 70:30 glycerol:Tris buffer behaves as a semi-solid glass, which would greatly inhibit bimolecular quenching reactions. There may be a higher temperature at which the $\text{Fe}^{\text{III}}\text{-O}_2^{\bullet-}$ lifetime is sufficiently long; one minute or more would allow flash-quench ET to generate $\text{Fe}^{\text{III}}\text{-O}_2^{2-}$, and observe the conversion to CI.

Another significant challenge facing flash-quench reduction of $\text{Fe}^{\text{III}}\text{-O}_2^{\bullet-}$ is that the ruthenium metal-to-ligand charge transfer (MLCT) bands overlap significantly with the P450 Soret and Q-bands; excitation into these protein absorptions can cause photodissociation of O_2 , analogous to $\text{Fe}^{\text{II}}\text{-CO}$. If the yields of photodissociation are competitive with yields of ruthenium excited state, it will be difficult or impossible to observe reduction of $\text{Fe}^{\text{III}}\text{-O}_2^{\bullet-}$ to $\text{Fe}^{\text{III}}\text{-O}_2^{2-}$ and subsequent formation of CI.

In this Chapter, we examine the kinetics of flash-quench heme reduction and assess the possibility for monitoring photochemical reduction-triggered gas binding. We then examine the kinetics of photo-triggered CO dissociation and re-binding to the heme for the thermophilic CYP119 under varying conditions of laser power, temperature, and the presence or absence of substrate. We identify unique aspects of CYP119 conformational dynamics, and assess thermodynamic activation parameters for the rebinding process.

5.2. Results and Analysis

5.2.1. Reductive flash-quench

We examined the photochemical reduction of four Ru-P450 conjugates that are described in Chapter 3: two are mutants of P450 BM3 from *Bacillus megaterium* (Ru_{C97}-BM3(W₉₆), Ru_{C97}-BM3(wH₉₆)) and two are mutants of CYP119, the thermophilic P450 from *Sulfolobus acidocaldarius* (Ru_{C77}-CYP119(H₇₆), Ru_{C77}-CYP119(HW₇₆)). Subscripts after Ru indicate the tethering location, i.e., non-native cysteine 97 or 77; subscripts in parentheses indicate the native residue. The presence of tryptophan directly adjacent to the tethering point (W96 or W76, for P450 BM3 and CYP119, respectively) was found to facilitate photochemical heme oxidation by acting as a redox intermediate for multistep hole transfer. However, we did not anticipate that these residues can participate in multistep *reductive* ET.

Luminescence

As described in Chapters 2 and 3, excitation at 480 nm results in luminescence ($\lambda_{\text{max}} = 630 \text{ nm}$) of both the free photosensitizer ([Ru(2,2'-bipyridine)₂(5-acetamido-1,10-phenanthroline)]²⁺, abbreviated [Ru(bpy)₂(Aphen)]²⁺) and the Ru-P450 conjugates. The photosensitizer has a monoexponential luminescence decay rate of 720 ns in deoxygenated buffer (50 mM sodium borate, pH 8). All of the Ru-P450 conjugates display biexponential luminescence decays; we attribute this observation to multiple conformations of the photosensitizer, which do not exchange on the timescale of this measurement. In the presence of 10 mM *p*MeODMA, luminescence lifetimes are significantly quenched (**Figure 5.5**), and can be fit to a monoexponential decay. Unlike what was observed for oxidative quenching with [Ru(NH₃)₆]³⁺ in Chapter 3, there is very little difference in the quenched lifetimes among the different Ru-P450 conjugates (**Table 5.1**).

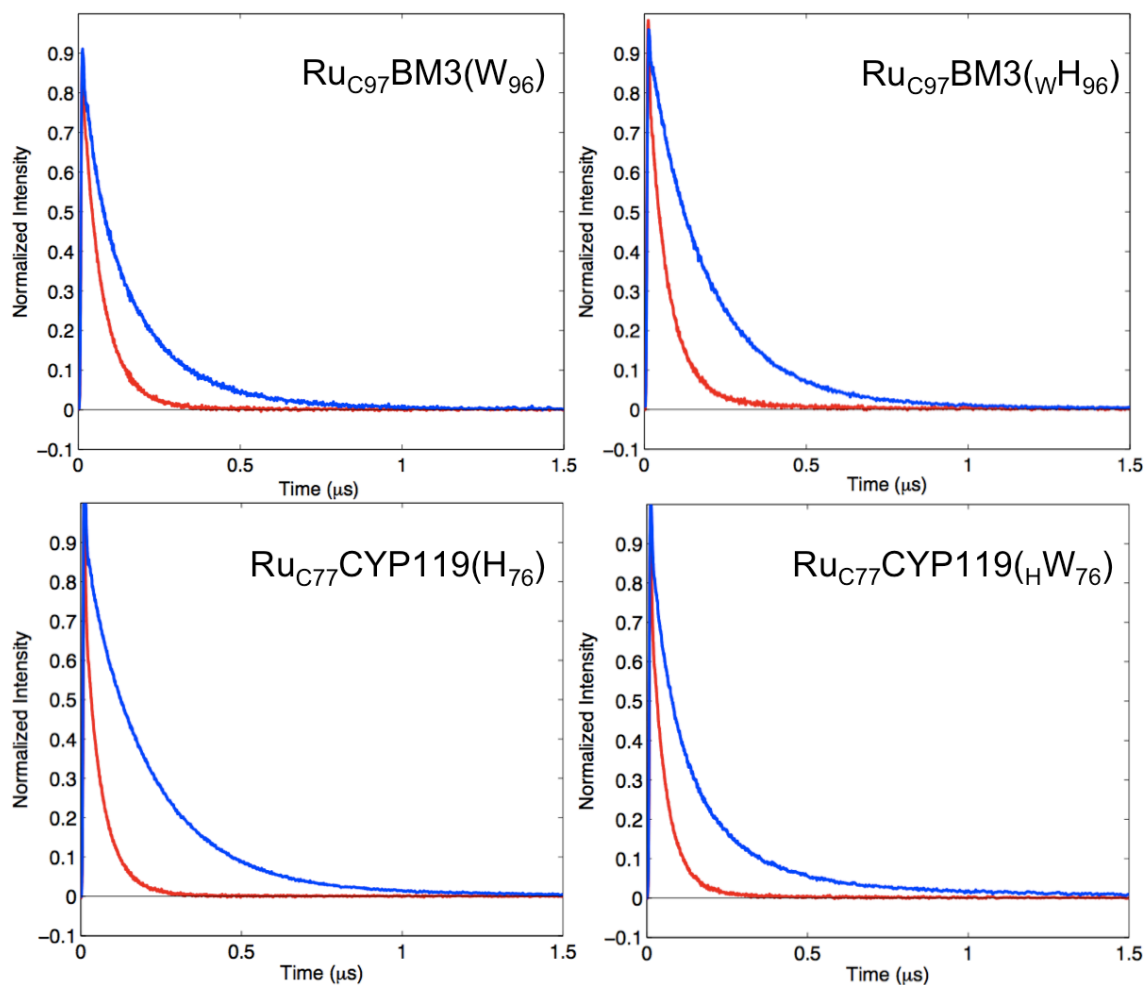


Figure 5.5. Luminescence decay at 630 nm of four Ru-P450 conjugates in the presence and absence of *p*MeODMA. $\lambda(\text{excitation}) = 480 \text{ nm}$.

Table 5.1. Luminescence lifetimes, taken from biexponential (unquenched) and monoexponential (quenched) fits.

Enzyme	conditions	$\tau_{\text{mono}}(\text{ns})$	$\tau_{\text{a}}(\text{ns})$	$\tau_{\text{b}}(\text{ns})$	%a	%b
Ru _{C97} -BM3(W ₉₆)	unquenched		190	52	65	35
	<i>p</i> MeODMA	62				
Ru _{C97} -BM3(W _H 96)	unquenched		160	310	80	20
	<i>p</i> MeODMA	65				
Ru _{C77} -CYP119(H ₇₆)	unquenched		220	45	85	15
	<i>p</i> MeODMA	54				
Ru _{C77} -CYP119(H _W 76)	unquenched		91	320	75	25
	<i>p</i> MeODMA	50				

Single-wavelength transient absorption

We have used single-wavelength transient absorption spectroscopy to monitor the flash-quench heme reduction in Ru-P450 systems. As described in Chapters 2 and 3, both the Ru photosensitizer and P450 heme have strong electronic absorbance in the 390-440 nm region (P450 Soret $\epsilon(\lambda_{\text{max}}: 418 \text{ nm}) = 95,000 \text{ M}^{-1}\text{cm}^{-1}$; $[\text{Ru}(\text{bpy})_2(\text{Aphen})]^{2+}$ $\epsilon(\lambda_{\text{max}}: 450 \text{ nm}) = 16,600 \text{ M}^{-1}\text{cm}^{-1}$ ¹⁹). The shapes and positions of these electronic transitions are sensitive to metal oxidation state and environment; and each species has a distinct absorption profile. By monitoring multiple wavelengths over time, we can identify the formation and decay of ET intermediates following laser excitation. This process is greatly facilitated by control studies (e.g., the absence of quencher), as well as comparison to absorption profiles in the literature.

In the absence of *p*MeODMA quencher, we observe transient bleaching ($\Delta\text{OD} < 0$) in the 400-440 nm visible region that is due to bleaching of the Ru photosensitizer MLCT band (see Chapters 2 and 3 for experimental data). The wavelength profiles of these transients are essentially identical for the free photosensitizer and the Ru-P450 conjugates, and the features return to baseline with the same decay constant as the luminescence lifetimes.

The Ru-P450 conjugates display multiphasic TA kinetics in the presence of *p*MeODMA (**Figure 5.6**).

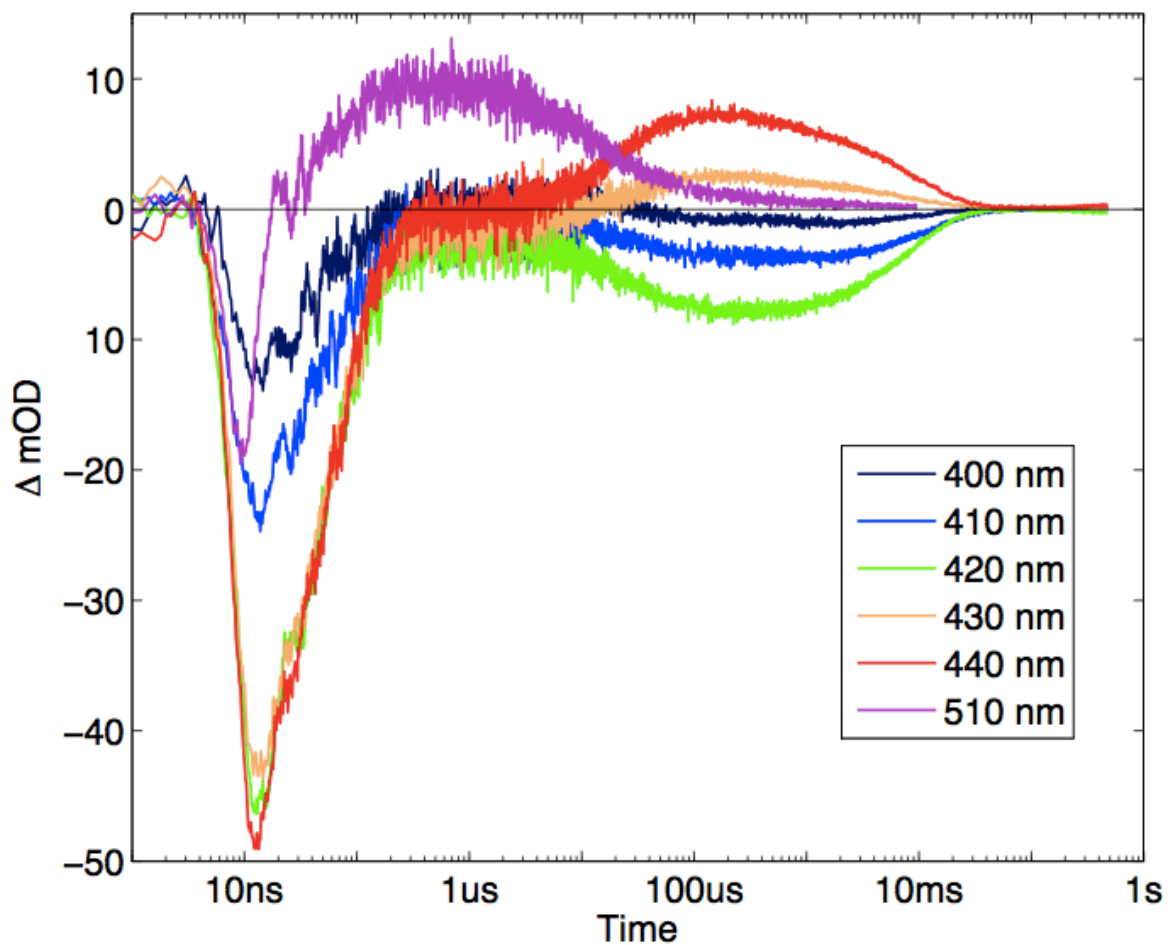


Figure 5.6. Single-wavelength transient absorption data of Ru-P450 at various wavelengths. Sample composition: 10 μM Ru_{C97}-BM3(W₉₆), 10 mM *p*MeODMA, 50 mM sodium borate, pH 8.

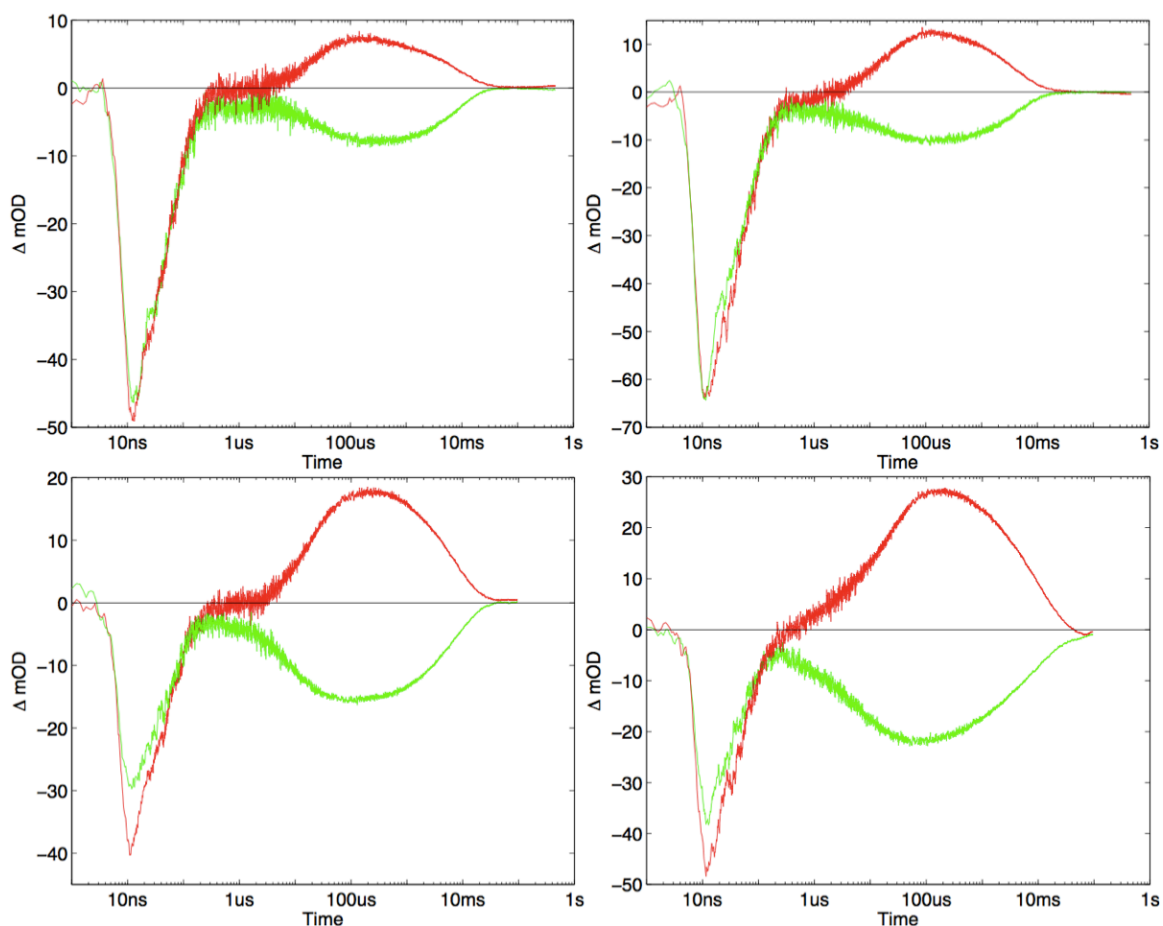


Figure 5.7. Single wavelength transient absorption data for flash-quench of four Ru-P450 mutants. $\lambda_{\text{excitation}} = 480 \text{ nm}$, $\lambda_{\text{probe}} = 420 \text{ nm}$ (green), 440 nm (red). Samples consisted of $10 \mu\text{M}$ Ru-P450, 10 mM *p*MeODMA, 50 mM sodium borate, pH 8. **Top left:** Ru_{C97}-BM3(W₉₆). **Top right:** Ru_{C97}-BM3(W_{H96}). **Bottom Left:** Ru_{C77}-CYP119(H₇₆). **Bottom Right:** Ru_{C77}-CYP119(H_{W76})

Assignment of Intermediates

This first transient is assigned as the $^*\text{Ru}^{\text{II}}$ excited state, in analogy to control studies; this feature decays rapidly, with the same decay constant as the quenched luminescence lifetime. A transient absorption feature at 510 nm appears at this same rate, and decays on the microsecond-to-millisecond timescale. Quenching of the Ru excited state results in formation of a *p*MeODMA radical cation; this species has been characterized by transient absorption, with an absorbance maximum of 484 nm ($\epsilon(484)=7200 \text{ M}^{-1}\text{cm}^{-1}$).^{20,21} This wavelength is too close to

the excitation wavelength to reliably probe, but there is still significant $p\text{MeODMA}^{\bullet+}$ absorbance at 510 nm, and we attribute our transient feature to this species.

Additionally, a new transient absorption feature appears on the microsecond timescale that is characterized by a bleach centered at 420 nm and a concomitant increase in absorption centered at 440 nm. TA at all wavelengths decay to baseline within the course of one second, indicating that the ET reaction is reversible.

It is of note that the red-shift associated with the observed transient species is different from the blue-shift and broadening associated with dithionite-induced heme reduction (**Figure 5.8**). The ferrous-ferric difference spectrum of WT P450 BM3 has maxima at 390, 460, and 550 nm, and a minimum at 420 nm; the transiently reduced spectrum has a maximum at 440 nm and minimum at 420 nm. This discrepancy also was observed for photochemical reduction of inducible nitric oxide synthase using non-covalently bound ruthenium wires.²² The spectral differences were attributed to a difference in spin state and coordination; chemically-reduced P450 and NOS are five-coordinate and high-spin. However, the rate of photochemical reduction may exceed ligand-loss and spin-conversion, resulting in a transient, low-spin ferrous species. The TA features of photochemically-reduced Ru-P450 conjugates are consistent with that observed upon flash-quench reduction of cytochrome P450_{cam} using imidazole-terminated Ru-photosensitizer wires that bind in the P450 substrate channel and ligate the heme iron (**Figure 5.8**, inset).²³ Cryoreduction of P450_{cam} at 77 K similarly resulted in a low-spin six-coordinate ferrous species with absorption around 440 nm, which converted to five-coordinate, high-spin upon annealing at higher temperatures.²⁴ Thus, we assign the feature at $\sim 100 \mu\text{s}$ to low-spin ferrous P450.

This reversibly reoxidizes to ferric on the millisecond timescale, and we observe no additional intermediates.

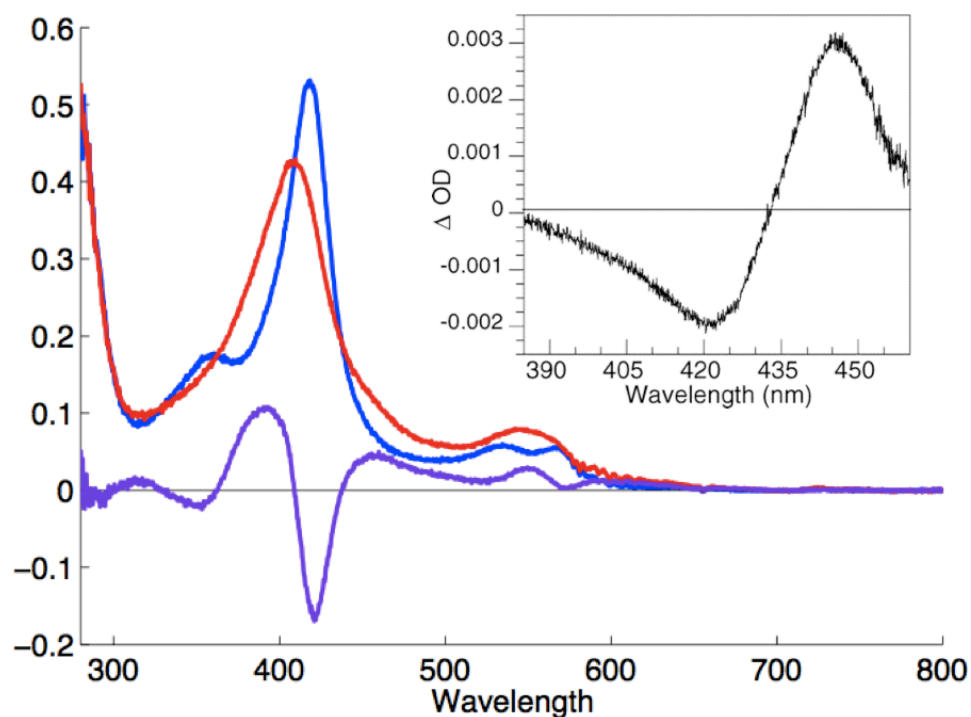


Figure 5.8. Spectra of ferric (blue) and ferrous (red) wild-type P450-BM3, and the ferrous – ferric difference spectrum (purple). **Inset:** Transient difference spectrum of photochemically reduced cytochrome P450_{cam} by noncovalent Ru-wires.²³

Fitting

Three kinetics phases are evident in the TA data. Thus, we performed a global least-squares fitting of the TA data recorded at 420 and 440 nm (and, for select mutants, 400, 410, 430 nm). Data were fit to a sum of three exponentials with amplitude coefficients ρ_{1-3} and observed rate constants γ_{1-3} (Equation 5.1). For fitting, see sample script in Appendix D. Similar to our analysis for photochemical heme *oxidation* described in Chapter 2, we fix the first observed rate constant as the quenched luminescence decay rate, as obtained from monoexponential fitting

of the luminescence decay at 630 nm. The remaining two rate constants are extracted from the global fitting, and are listed in **Table 5.2**.

$$y(n,t) = \rho_{n1} \exp(-\gamma_1 t) + \rho_{n2} \exp(-\gamma_2 t) + \rho_{n3} \exp(-\gamma_3 t) \quad (5.1)$$

Table 5.2. Rates of heme reduction extracted from global fitting of transient absorption data.

Enzyme	γ_1	γ_2	γ_3
Ru-K97C(W ₉₆)	1.6e7	3.6e4	1.1e2
Ru-K97C(W ₉₆ H ₉₆)	1.6e7	6e4	1.9e2
Ru-D77C(H ₇₆)	1.9e7	5.7e4	1.4e2
Ru-D77C(H ₇₆ W ₇₆)	1.9e7	8.1e4	1.3e2

The transient bleach at 420 nm and transient absorption at 440 nm observed on the microsecond timescale were assigned²³ as photochemical heme reduction (**Figure 5.8**, inset). Therefore, we assign the second rate constant as that of heme reduction. All four mutants exhibit very similar reduction rates, with maximum heme reduction complete at approximately 100 μ s.

Interestingly, after normalizing by the magnitude of the $^*Ru^{II}$ excited state bleach (440 nm), the magnitudes of the transient features associated with heme reduction (e.g., absorption at 440 nm) differ greatly among the different mutants. In particular, both of the CYP119 mutants exhibit signals which are greater by a factor of 2-3 (**Figure 5.9**). Since we do not have extinction coefficients for the transiently reduced species, we cannot tell how much of this difference in signal is attributable to a difference in yield. However, it would be surprising if a difference in extinction coefficients could account for the entirety of this discrepancy.

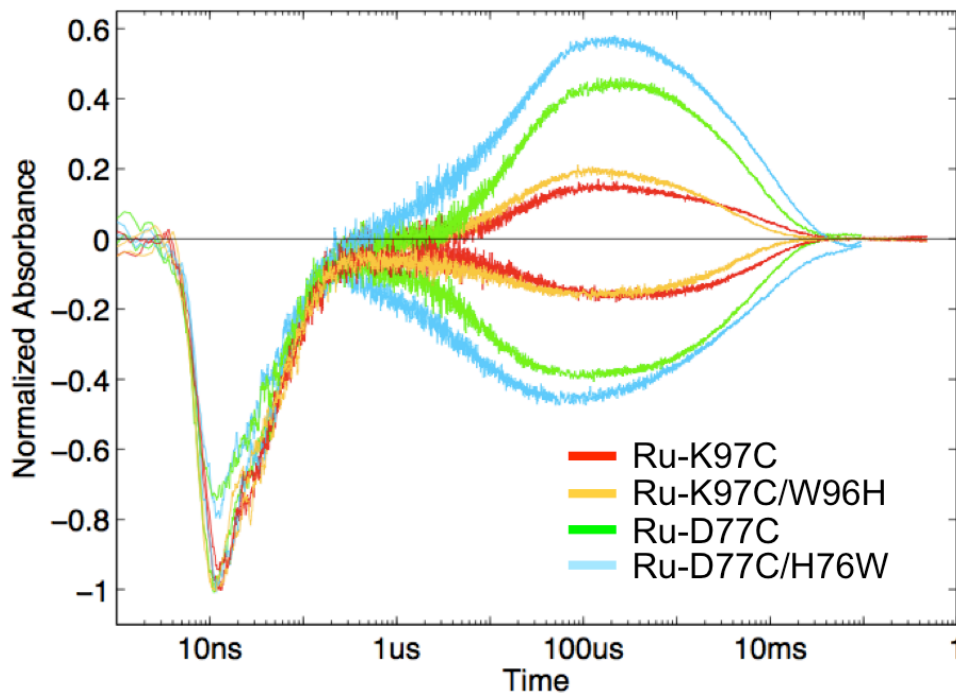


Figure 5.9. Normalized overlay of TA for the four Ru-P450 systems. 420 nm ($\Delta OD < 0$ at 100 μs) and 440 nm ($\Delta OD > 0$ at 100 μs), normalized to the intensity of the initial $^*Ru^{II}$ bleach (~ 10 ns) at 440 nm. Ru_{C97} -BM3(W_{96}) (red); Ru_{C97} -BM3(wH_{96}) (yellow), Ru_{C77} -CYP119(H_{76}) (green), Ru_{C77} -CYP119(HW_{76}) (blue).

All transient features decay to baseline within 100 ms; this return rate is extremely sensitive to small amounts of oxygen. In our proposed flash-quench scheme (**Figure 5.10**), re-oxidation of the ferrous center occurs via bimolecular recombination with oxidized *p*MeODMA. This recombination is expected to be a second order process; however, the disappearance of the transient features can be modeled as a first order process.

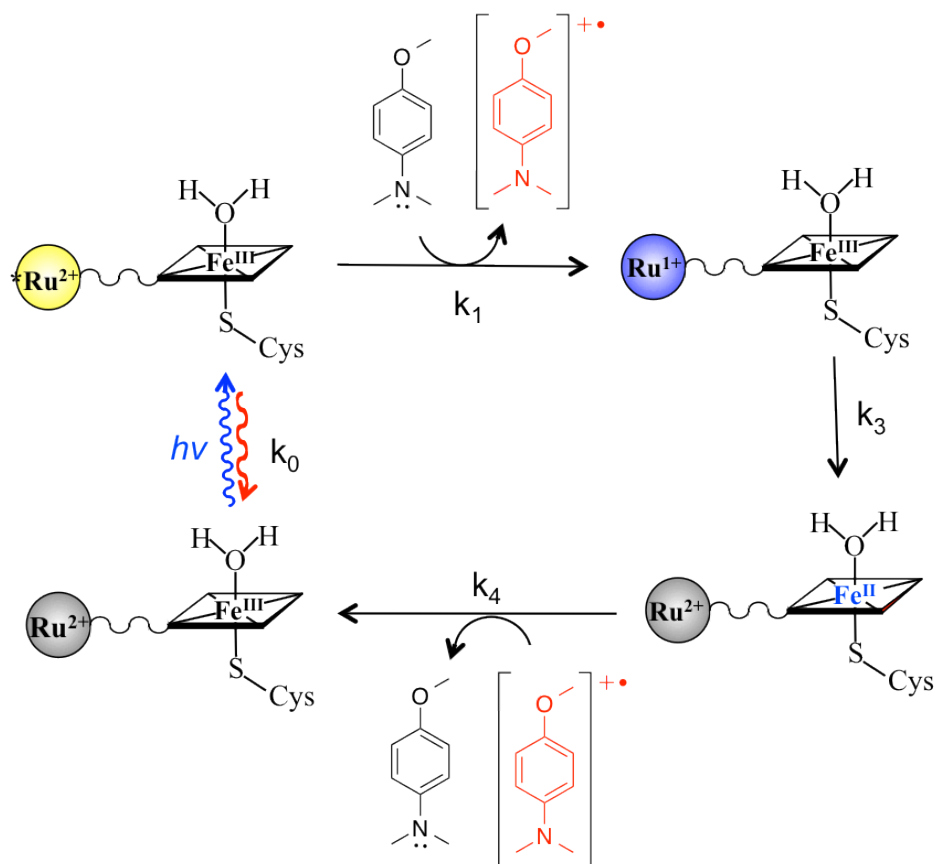


Figure 5.10. Flash-quench scheme for heme reduction.

Curiously, the transient absorbance at 510 nm, attributed to the oxidized *p*MeODMA radical, disappears much more quickly than reoxidation of the heme center (**Figure 5.6**). Accelerated quencher recovery was also observed upon oxidative quenching of Ru-P450 with methyl viologen (see Appendix C). This may be due to reaction of quencher radicals with trace amounts of oxygen. However, if this is the case, it remains unclear what reaction regenerates the resting state enzyme.

5.2.2. Reductive ET in the presence of CO

We anticipated that gas binding could be induced upon photochemical heme reduction. To that end, reductive flash-quench experiments were conducted under

an atmosphere of CO. However, the observed kinetics were irreproducible, and varied depending on the number of laser shots. Additionally, we observed the appearance of a shoulder at 450 nm in the sample absorbance spectrum, suggesting accumulation of Fe^{II}-CO. While we expected heme reduction and CO binding to be reversible, this observation suggests that newly generated Fe^{II}-CO persists on the order of minutes to hours. Somewhat unexpectedly, we also observed appearance of this shoulder at 450 nm even for pure protein samples in the *absence* of both photosensitizer and quencher (**Figure 5.11**).

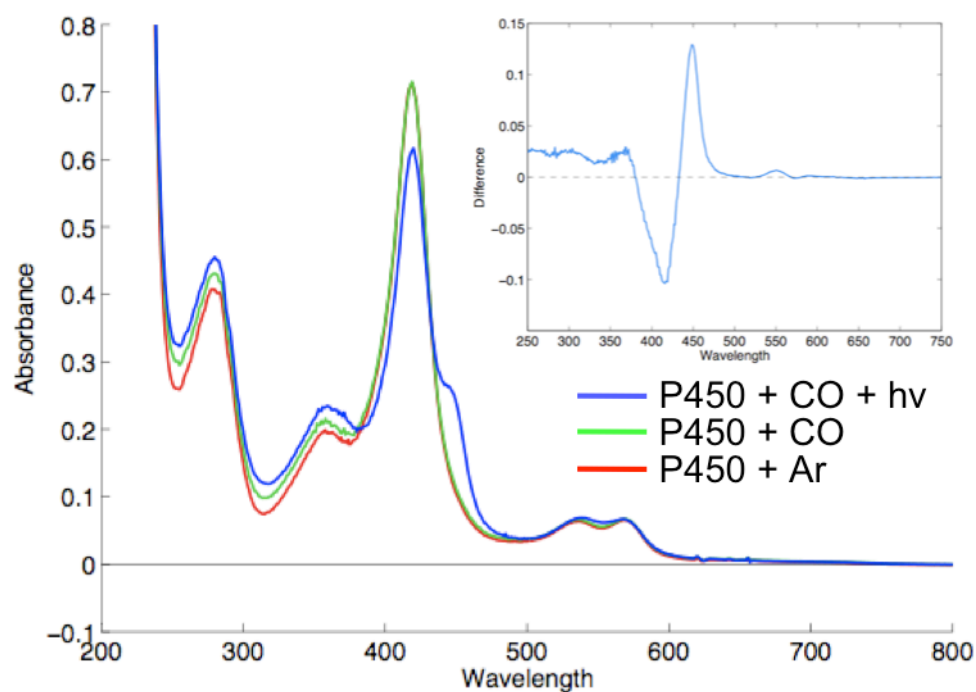


Figure 5.11. UV-visible absorbance spectra of Fe^{III}-P450 BM3 (double mutant: C62A/C156S, which contains no surface-exposed cysteines) under an atmosphere of argon (red) or an atmosphere of CO: before (green) and after (blue) excitation at 480 nm.

Samples that are not as rigorously deoxygenated do not show build-up of Fe^{II}-CO. This spontaneous reduction under irradiation of UV and visible light was observed for heme proteins, including P450.²⁵⁻²⁷ It is possible that transient photo-reduced species are trapped by the CO. This process severely complicates the analysis of

transient data, as the Fe^{II}-CO concentration is in flux; and we cannot conclusively measure a rate for CO binding using this method of photo-triggered reduction.

This observation, along with other cited sources, brings into question the effectiveness of methods to photo-trigger heme reduction by excitation of NAD(P)H.¹³ The organic reductant absorbs in the near UV, and overlaps extensively with the P450 absorption band at 360 nm. If P450 photo reduction and CO binding can be observed with excitation at 4 mJ/pulse of 480 nm, in the absence of any obvious chemical reductant, it is almost certain that 200 mJ/pulse radiation into the near-UV region of the P450 spectrum also would result in P450 reduction, albeit by a different mechanism than what was suggested by the authors.^{12,13}

5.2.3. CO photolysis and rebinding

The rate of CO *re*binding can be measured following photolysis the Fe^{II}-CO bond of chemically-reduced ferrous-CO. In particular, we set out to examine the kinetics of CO rebinding for thermophilic CYP119 over a range of temperatures, in the presence and absence of substrate, and with a variety of laser pulse powers.

Samples for photolysis consist of WT CYP119 reduced with dithionite under an atmosphere of CO, in specialized, high-vacuum quartz cuvettes (see Appendix B). The P450 ferrous-CO species is characterized by a split-Soret spectrum with a Soret absorbance maximum at 448 nm. Photolysis of the Fe-CO bond produces a five-coordinate ferrous species, for which the Soret band is broader and significantly blue-shifted (**Figure 5.12**).

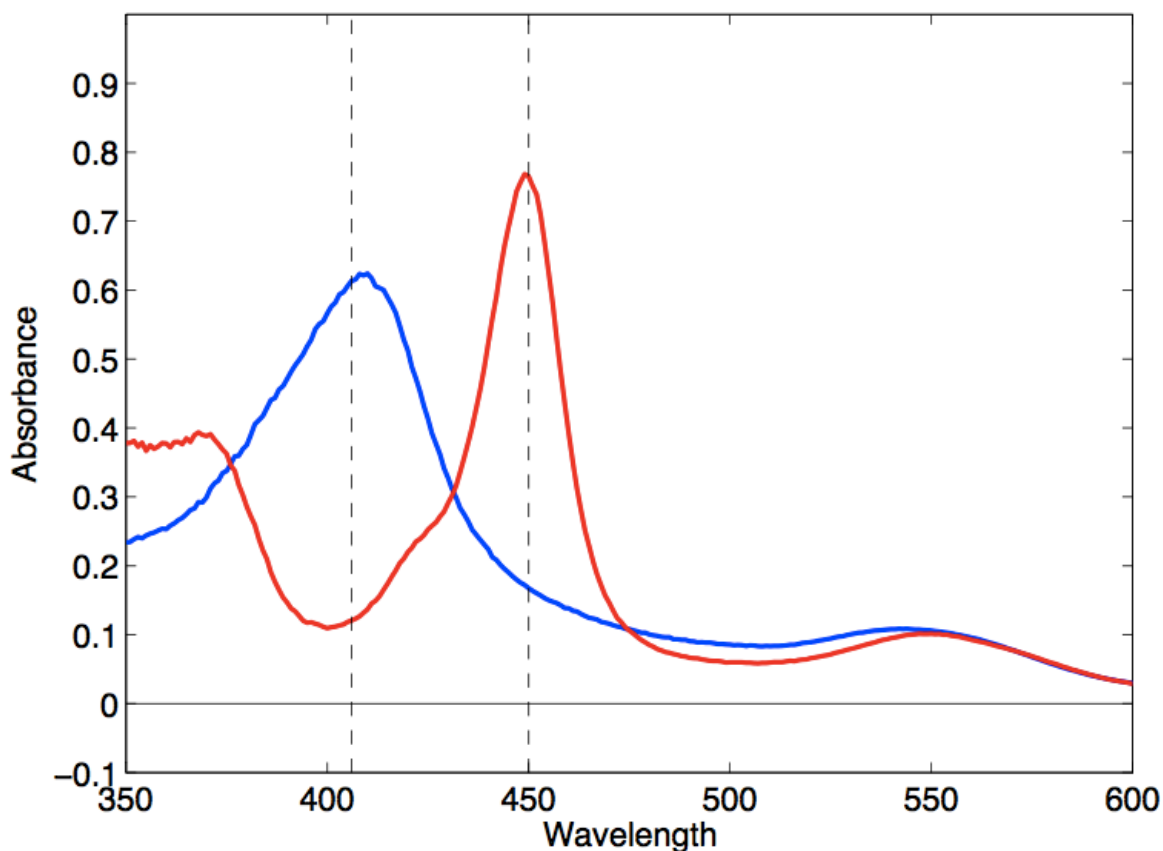


Figure 5.12. UV-visible absorbance spectra of five-coordinate, dithionite-reduced WT CYP119 (blue) and the corresponding six-coordinate ferrous CO species (red).

The multi-wavelength transient absorption spectra following excitation at 486 nm clearly show loss of the $\text{Fe}^{\text{II}}\text{-CO}$ band at ~ 450 nm, and increase in absorption at ~ 400 nm (**Figure 5.13**). This transient spectrum is in excellent agreement with the $\text{Fe}^{\text{II}}/\text{Fe}^{\text{II}}\text{-CO}$ difference spectrum (**Figure 5.13**, inset). By 4 ms, absorption has entirely returned to baseline, indicating full recovery of the starting, CO-bound ferrous species.

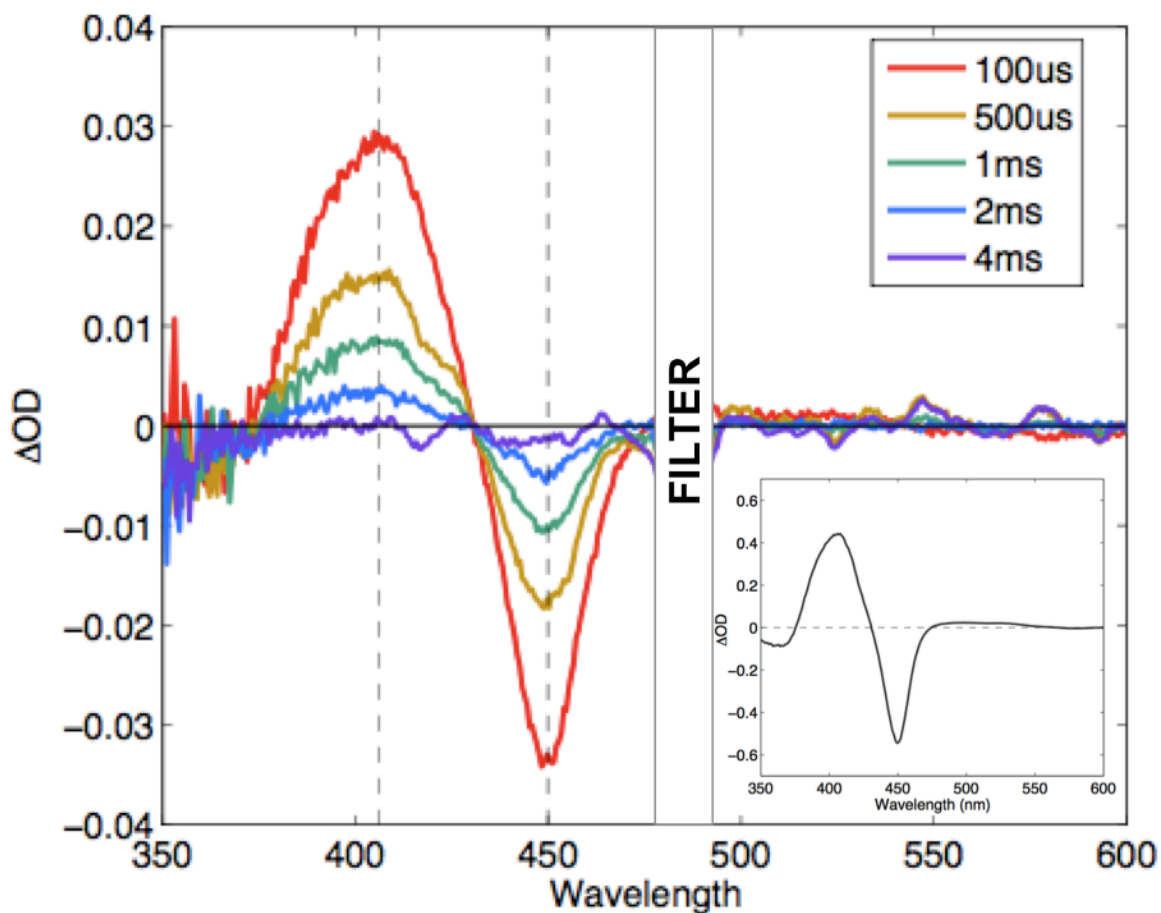


Figure 5.13. Transient difference spectra following flash-photolysis of WT CYP119 Fe^{II}-CO in 100 mM potassium phosphate buffer, pH 7.4, 20 °C. Excitation: 486 nm. A narrow notch filter blocks scattered laser light (and the probe light) 475-495 nm. Inset: Fe^{II}-Fe^{II}-CO difference spectrum.

As observed by single-wavelength transient absorption (**Figure 5.14**), two major kinetics components contribute to the recovery of the Fe^{II}-CO species. This behavior is commonly observed for CO rebinding in heme enzymes, including P450.¹⁴⁻¹⁶ The fast rebinding phase is associated with geminate recombination, and typically occurs on the picosecond-to-nanosecond timescale. The slow rebinding phase is associated with CO that has escaped into solution and must diffuse back into the active site; this typically occurs on the millisecond timescale.

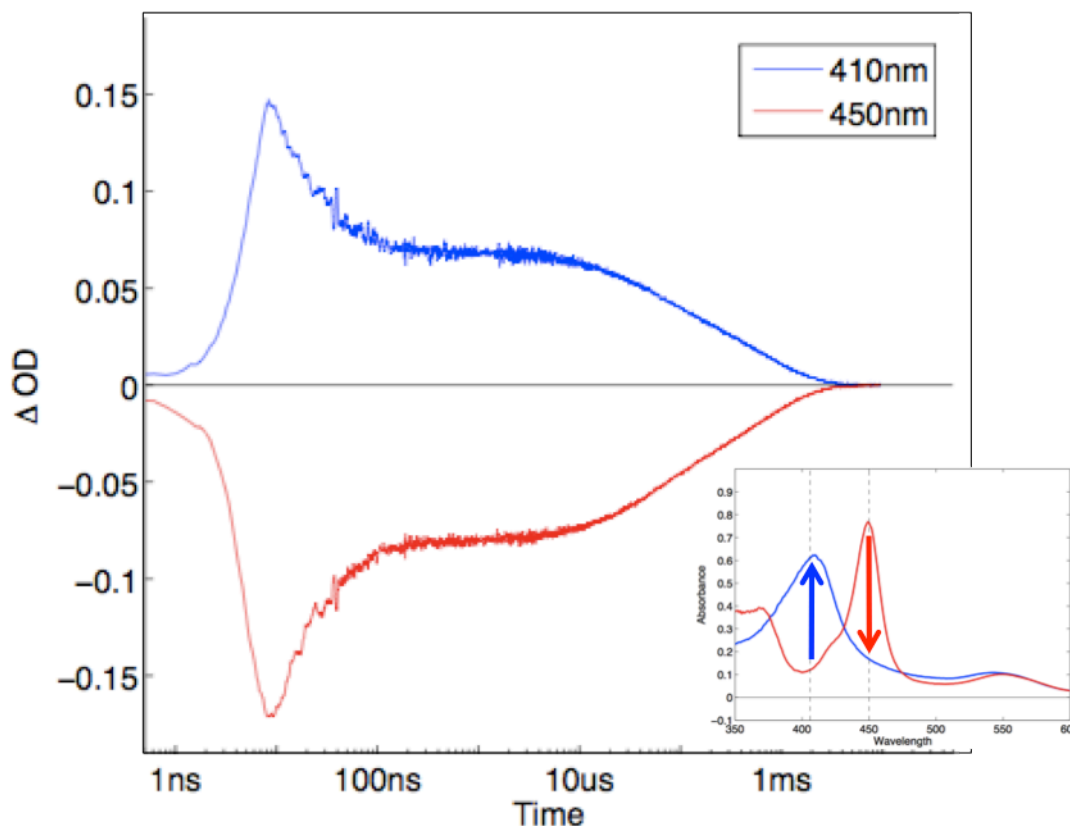


Figure 5.14. Single-wavelength TA following flash-photolysis of WT CYP119 Fe^{II}-CO in 100 mM potassium phosphate buffer, pH 7.4 buffer, 20 °C. Excitation: 460 nm. Single-wavelength transient absorption traces at 450 nm (red) and 410 nm (blue). **Inset:** Fe^{II}-P450_{CYP119} (blue) and Fe^{II}-CO-P450_{CYP119} (red).

In the presence of excess CO, one expects both geminate recombination and rebinding of escaped CO to obey first order and pseudo-first order kinetics (respectively). However, the single-wavelength TA data display complex kinetics behavior that cannot be fit to a sum of two exponentials. This also has been observed in flash photolysis of Fe^{II}-CO P450 BM3, and was attributed to multiple protein conformations with slow interconversion.¹⁵ There is also evidence for multiple solution conformations of substrate-free CYP119, as examined by NMR spectroscopy and dynamics simulations.²⁸ Interestingly, these studies both suggest that P450 BM3 and CYP119 lock down into a dominant conformation in the presence of tightly binding substrates.

Power dependence and yield of CO escape

There is a nonlinear power dependence on the yield of CO escape, which appears to saturate around 10 mJ/pulse (**Figure 5.15**). If we assume that this saturation corresponds to 100% photolysis of the Fe–CO bond, then we can determine the yield of CO escape following photolysis.

Using the initial absorption spectrum of the Fe^{II}-CO sample ($A_{450}=0.42$), and the steady-state and transient difference spectra (**Figure 5.13**), we can determine the expected absorption at 100% conversion to five-coordinate Fe^{II}. The corresponding $\Delta OD(406)_{\max} = 0.27$; our maximum signal at power saturation is 0.13, just under 50% of the maximum signal. This is significantly lower than the previously reported CO escape yield of 64%.¹⁷

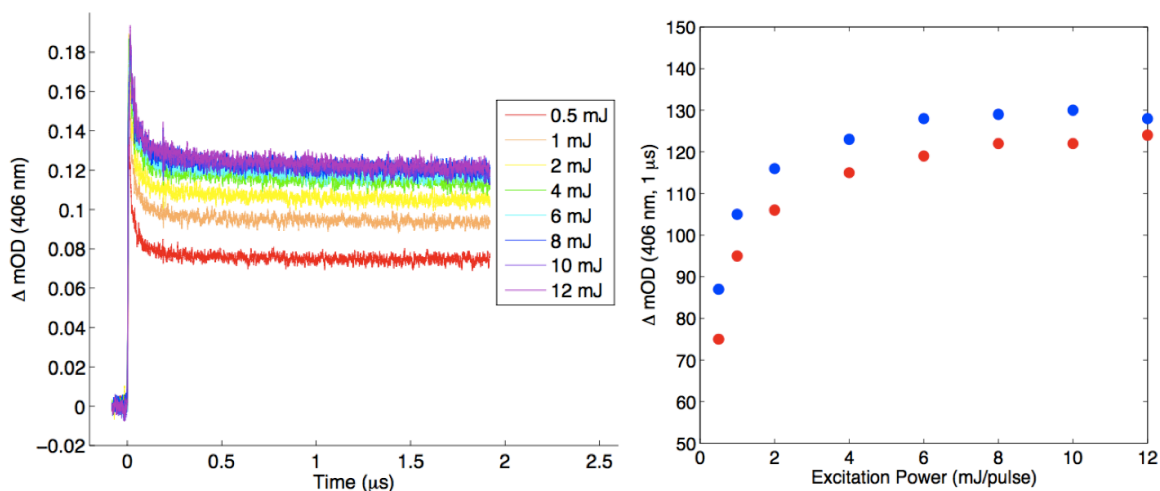


Figure 5.15. Power dependence of CO escape, 460 nm excitation, $A_{450}=0.42$. **Left:** Single-wavelength transient absorption at 406 nm. **Right:** Magnitude of CO escape for two samples, extracted from single wavelength TA data at 1 μs (red and blue dots; red corresponds to the figure on the right).

Temperature dependence (substrate-free)

CYP119 is an extremely thermostable protein, tolerating conditions of up to 90 °C or more. Therefore, we can examine a wide range of temperatures and determine its effect on the yields of CO escape and rates of rebinding. This temperature dependence is important for understanding the function of CYP119 under conditions that approximate those within its thermophilic parent organism, *Sulfolobus acidocaldarius*.

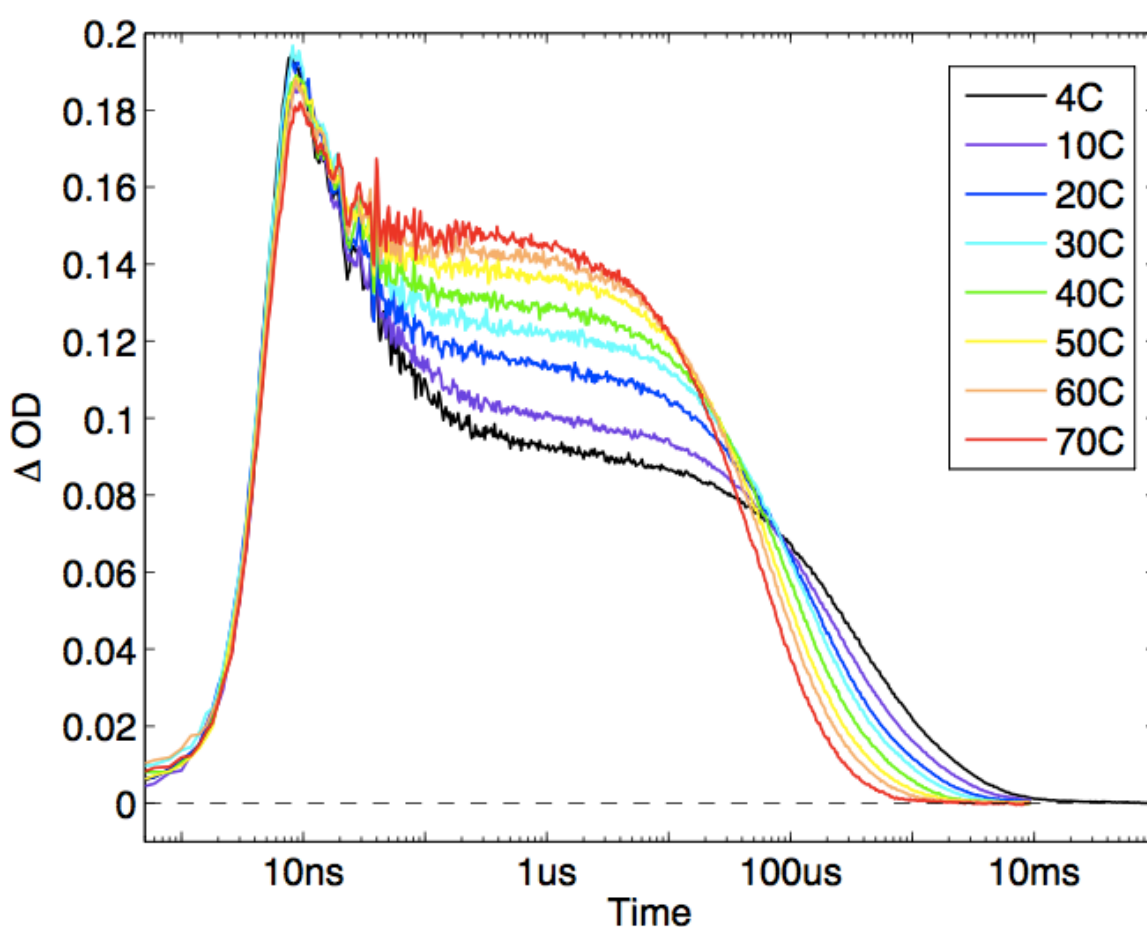


Figure 5.16. Temperature dependence of CO rebinding (no substrate). $\text{Abs}(\lambda_{\text{max}} : 449 \text{ nm}) = 0.41$, $\lambda(\text{excitation}) = 460 \text{ nm}$, 2 mJ/pulse.

Reassuringly, temperature appears to have had little effect on the magnitude of the initial TA signal, and we assume that the total photolysis yield is constant. As

temperature increases, there is an increase in the yield of CO escape, as evidenced by the increased signal magnitude at $\sim 1 \mu\text{s}$. Additionally, the rate of CO rebinding increases with increased temperature.

Temperature dependence in the presence of laurate

We have examined the effect of bound fatty acid substrate on the rates of CO rebinding following photolysis. The native substrate of CYP119 is yet unknown, but this variant does tightly bind and hydroxylate various fatty acids *in vitro*.²⁹ Lauric acid (dodecanoic acid) is used here as a model substrate; the binding constant is reported to be $1.2 \mu\text{M}$ in CYP119.²⁹ Upon binding, the fatty acid partially displaces the axial water molecule, causing a shift to high-spin. This results in blue-shifting of the Soret band for laurate-bound CYP119 (**Figure 5.17**).

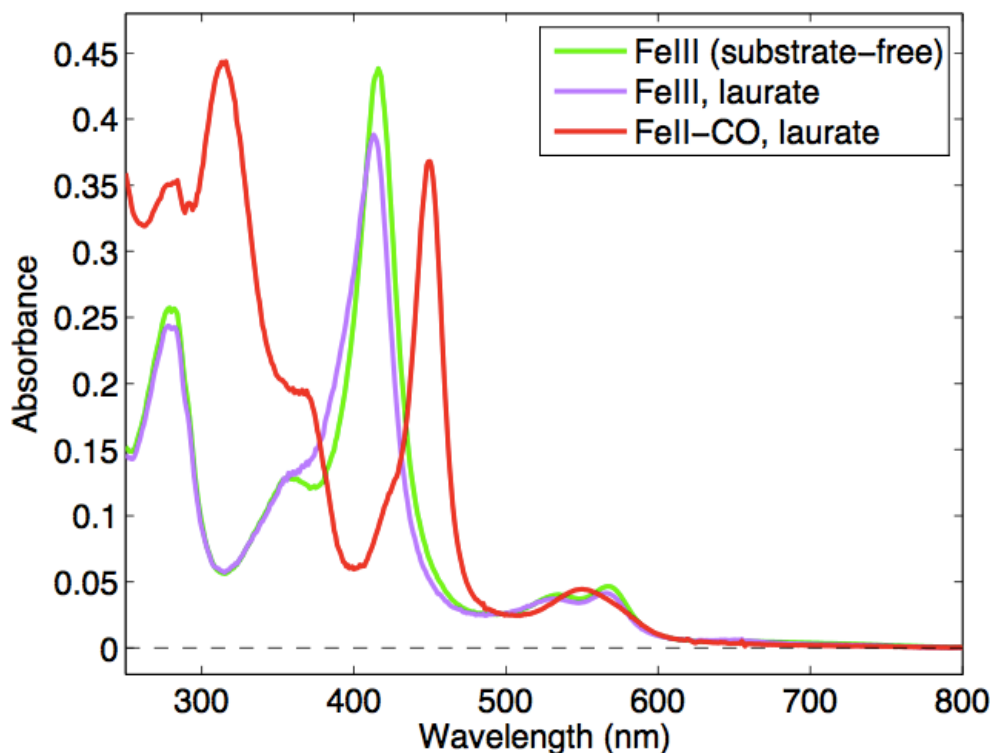


Figure 5.17. UV-visible absorption spectra of WT CYP119 with and without laurate. Green: Ferric, substrate-free. Purple: Ferric, $30 \mu\text{M}$ laurate. Red: Ferrous-CO, with $30 \mu\text{M}$ laurate. Samples have approximately equal concentrations.

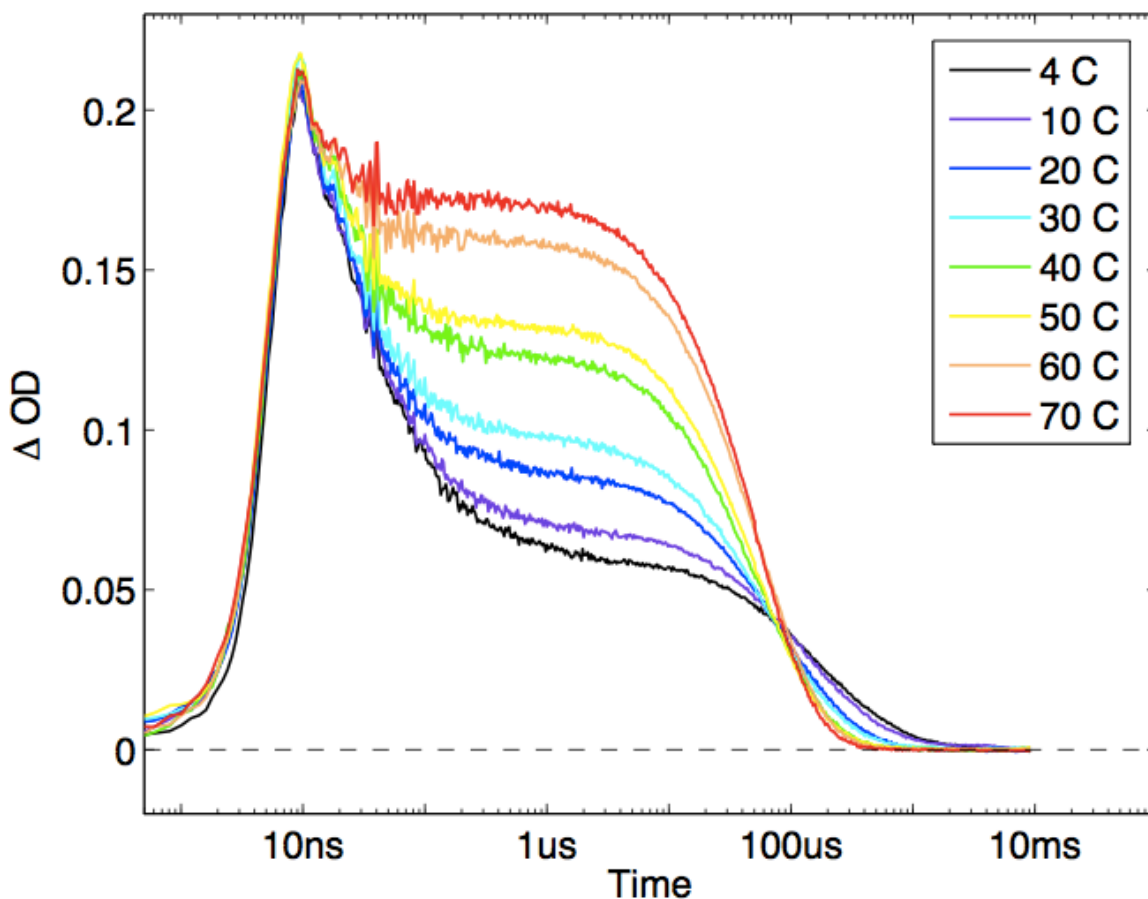


Figure 5.18. Temperature dependence of CO rebinding in the presence of 30 μM laurate. $\text{Abs}(\lambda_{\text{max}}: 449 \text{ nm})=0.37$, $\lambda(\text{excitation}) = 460 \text{ nm}$, 2 mJ/pulse.

A similar temperature dependence of CO rebinding dynamics is observed in the presence of laurate; as temperature increases, there are increases in both the yield of CO escape and the rate of CO rebinding. In contrast to the substrate-free form, there appears to be a greater temperature dependence on yields of CO escape. At lower temperatures, there is a dramatic decrease in CO escape yield for the laurate-bound form (**Figure 5.19**, left); this discrepancy decreases as temperature increases.

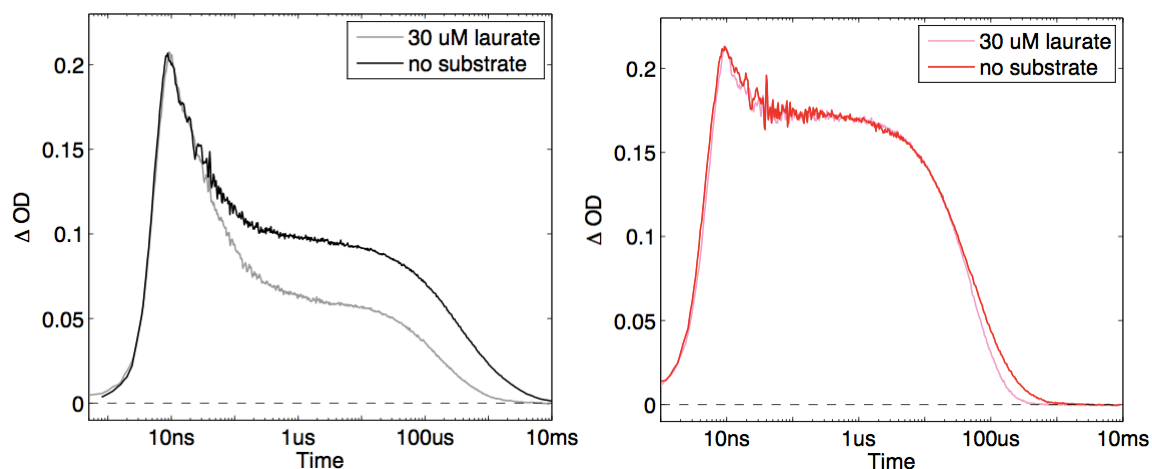


Figure 5.19. Comparison of laurate-free and laurate-bound CO rebinding kinetics (from Figure 5.16 and 5.17). Left: 20 °C. Dark blue, substrate free. Light blue, lauric acid bound; Right: 70 °C. Red, substrate free. Pink, substrate bound. Substrate-free traces have been multiplicatively scaled ($\times 1.06$) to normalize the initial signal magnitude.

Picosecond transient absorption measurements

At high temperatures, geminate recombination appears to be complete within the instrument response in our nanosecond pulsed TA experiments; this is true in both substrate-free and substrate-bound forms. We have investigated the earlier timescales using picosecond-pulsed TA experiments (see appendix B for instrumentation). The signal-to-noise ratios are smaller for picosecond data, but the single-wavelength kinetics traces overlay nicely with nanosecond data (**Figure 5.20**, see Appendix C for a sample overlay).

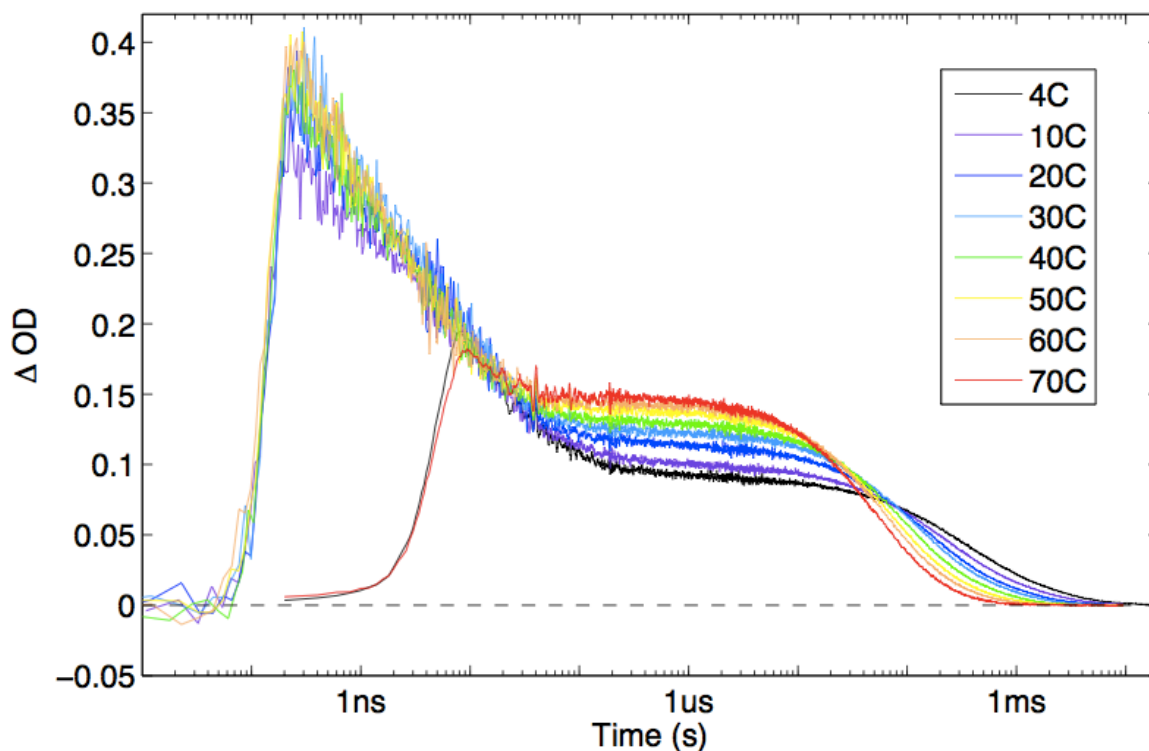


Figure 5.20. Picosecond-to-millisecond TA data for CO rebinding in substrate-free CYP119 at various temperatures. The picosecond data at 70 °C is significantly noisier and has been omitted.

Non-negative least squares fitting

In order to more quantitatively assess the temperature dependence of CYP119 CO rebinding kinetics, we have subjected our transient absorption data to a nonnegative least squares (nnls) fitting procedure. This is similar to the singular value decomposition analysis described in Chapter 2; single-wavelength transient absorption data are fit to a series of rate constants, and the fitting process provides amplitude coefficients corresponding to each rate constant. An additional constraint was added to limit the difference in amplitudes for adjacent rate constants (see Appendix D for matlab scripts).

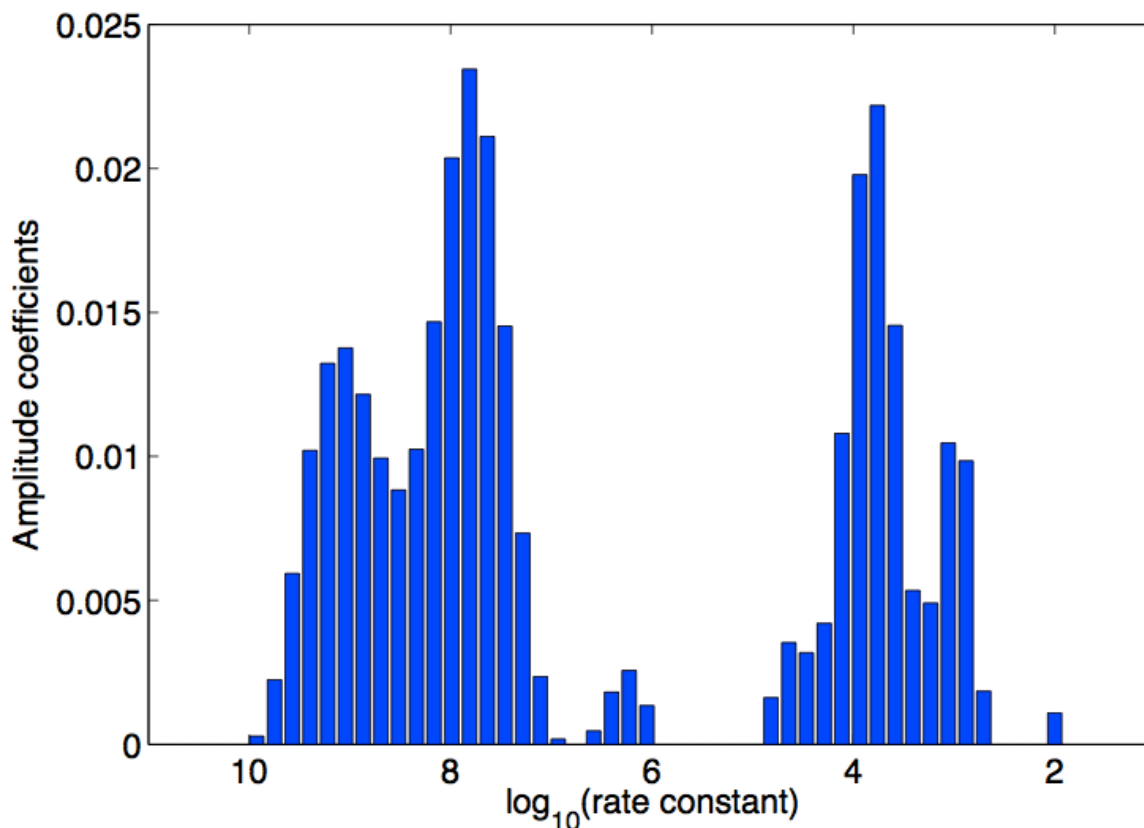


Figure 5.21. Amplitude coefficients derived from nonnegative least squares fitting of CYP119 CO rebinding kinetics. Conditions: 20 °C, no substrate. The lambda value associated with this fit is 1.297.

An example of the amplitude coefficients is shown in **Figure 5.21**; data from analysis of all temperatures can be found in Appendix C. As seen above, the rate constants from nnls fitting are divided into two major populations: the fast population (centered at $\log_{10}(k) \sim 8$) corresponds to geminate recombination, while the slow population (centered around $\log_{10}(k) \sim 4.5$) corresponds to rebinding of the escaped CO.

In order to further analyze the temperature dependence, we have integrated each population, and determined their first moment (mean), and second centered moment (variance).

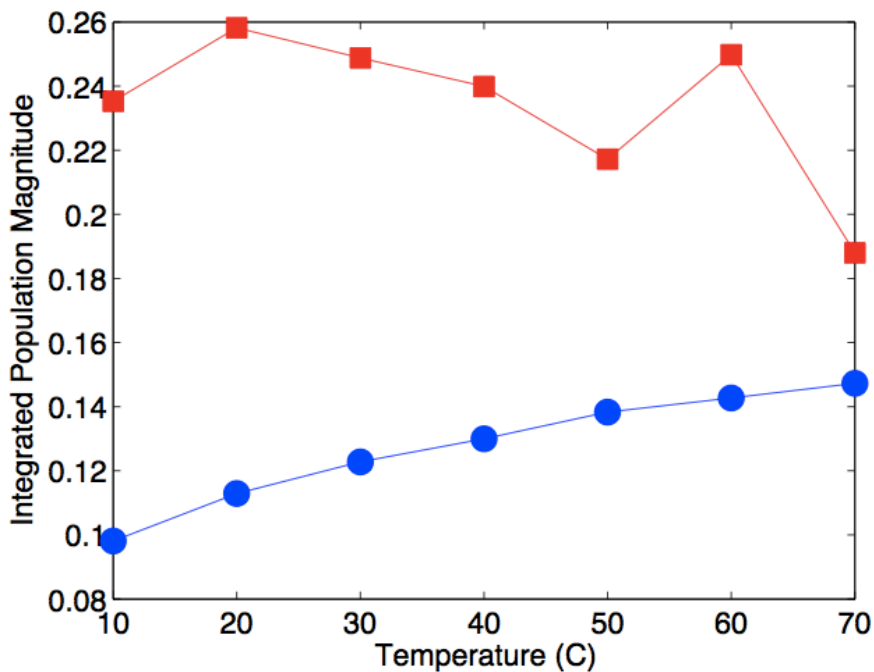


Figure 5.22. Integration of rate constant amplitudes at varying temperature (substrate free). Red: fast population corresponding to geminate recombination. Blue: slow population corresponding to rebinding of escaped CO.

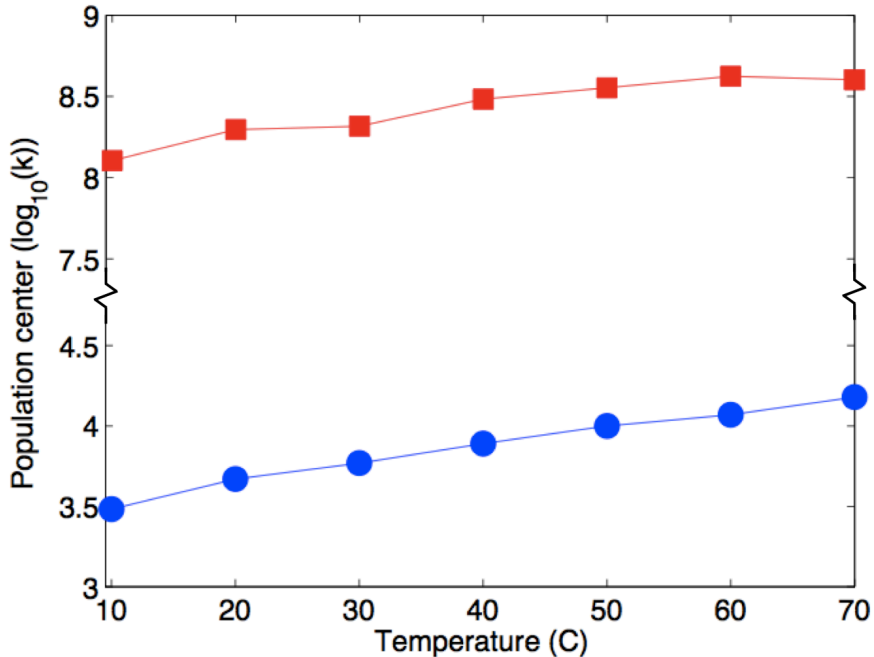


Figure 5.23. First moment of populations at varying temperature (substrate free). Note the break in the y-axis. Red: fast population corresponding to geminate recombination. Blue: slow population corresponding to rebinding of escaped CO.

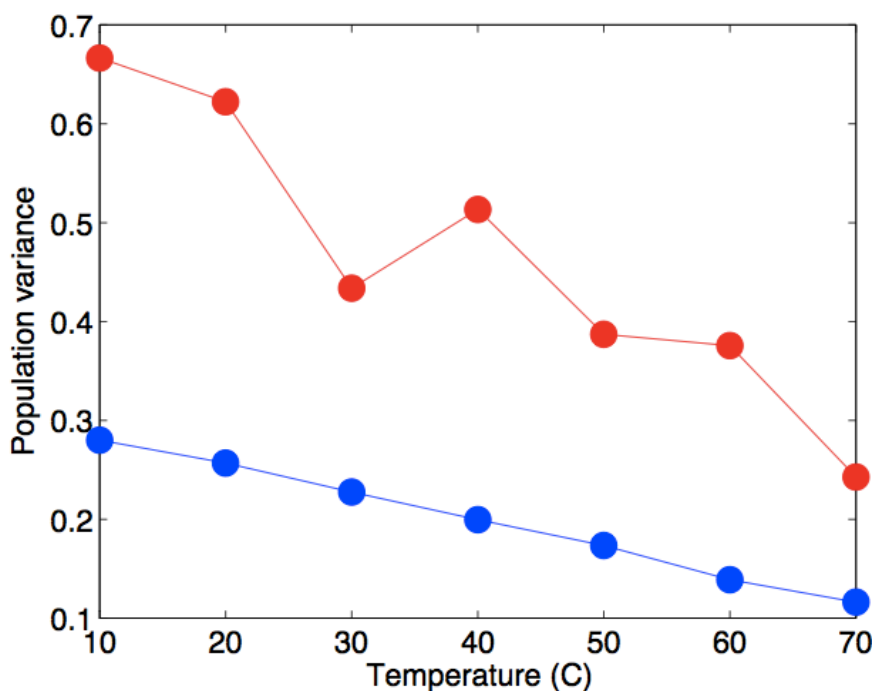


Figure 5.24. Second centered moment of populations at varying temperature (substrate free) Red: fast population corresponding to geminate recombination. Blue: slow population corresponding to rebinding of escaped CO.

As temperature increases, the integrated amplitude associated with the slow population increases in a nonlinear fashion (**Figure 5.22**); this corresponds to the increased yield of escaped CO. Due to increased noise associated with the fast component, it is not clear whether the integrated amplitude remains constant or decreases. The first moment of both the fast and slow components increase with temperature in a linear fashion (**Figure 5.23**). We use these population centers to do an Eyring analysis of the CO rebinding (*vide infra*). The second centered moment of both the fast and slow populations decreases as temperature increases (**Figure 5.24**). Intuitively, one might expect the opposite; as temperature increases, more conformations may become thermally accessed, leading to broadening of the population (and increase in the second centered moment). It is possible that there are multiple sub-populations within the fast and slow components, and that these

populations merge as temperature increases. Investigations into this possibility of subpopulations is ongoing in the Gray group.

The CO rebinding data for laurate-bound CYP119 are more preliminary, and have not been acquired on the picosecond timescale. Nevertheless, we have performed non-negative least squares fitting on the nanosecond-to-microsecond TA data (see **Figure 5.18** for TA data), and provide an initial comparison between rebinding of escaped CO in the presence and absence of laurate.

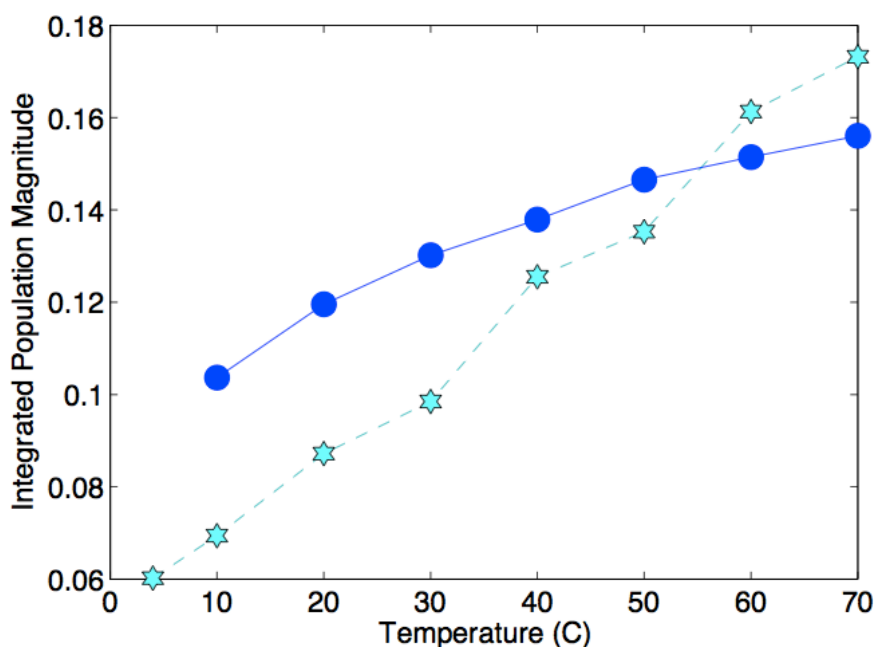


Figure 5.25. Comparison of amplitude integrations for the slow population in substrate-free and laurate-bound CYP119. Integrations of substrate-free data have been scaled multiplicatively by a factor of 1.06 to account for the slight difference in sample concentration and laser power.

As noted earlier, there is a larger temperature dependence for the yield of CO escape in the presence of laurate. It is plausible that the presence of substrate blocks some of the CO escape pathways, lowering the escape yield (and correspondingly lowering the integration of amplitudes). This is observed at lower temperature (< 50 °C). However, at high temperatures, the amplitudes associated

with CO escape appear to be *higher* in the presence of substrate. This intriguing phenomenon has not yet been explained, and deserves additional exploration.

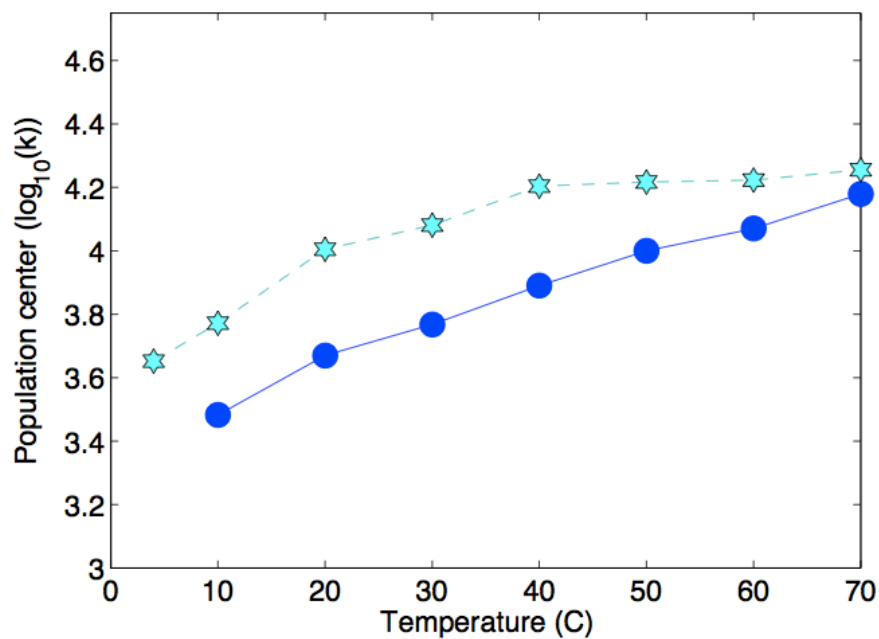


Figure 5.26. Comparison of slow population first moment in substrate-free and laurate-bound CYP119.

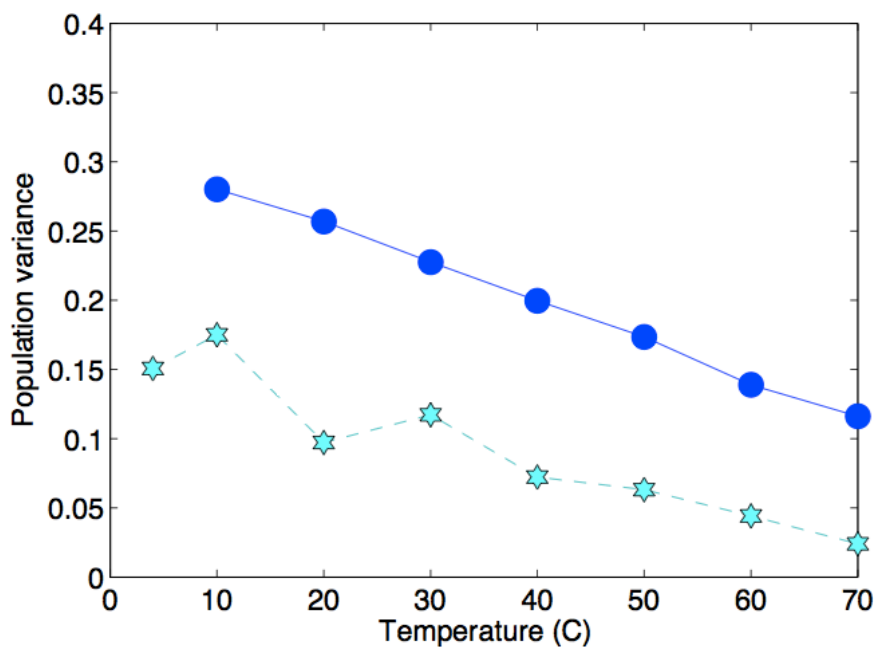


Figure 5.27. Comparison of slow population second centered moment (variance) in substrate-free and laurate-bound CYP119.

The rates of CO rebinding are faster in the presence of substrate; this is true throughout the temperature range, although the effect appears to diminish at higher temperatures. Interestingly, the opposite affect was observed for CO rebinding in P450 BM3¹⁵ and P450cam.³⁰ This may indicate alternate pathways for CO re-entry among different P450 variants.

The final note in the substrate free/bound comparison is that the second moment (variance) in that the slow population distribution is significantly lower in the presence of substrate, over the entire temperature range. This is unsurprising, as tight binding to substrate causes significant structural shifts (see Chapter 1) and generates a single dominant conformation in solution.²⁸

Eyring Analysis

We have performed an Eyring analysis on the kinetics of rebinding for escaped CO (slow population) in the substrate-free form. The data are consistent between samples, and are linear over the range of 10-70 °C (**Figure 5.28**). The extracted activation parameters are listed in **Table 5.3**. These thermodynamic parameters can be compared with those for other heme proteins, including P450_{cam}²⁹ and myoglobin.³¹

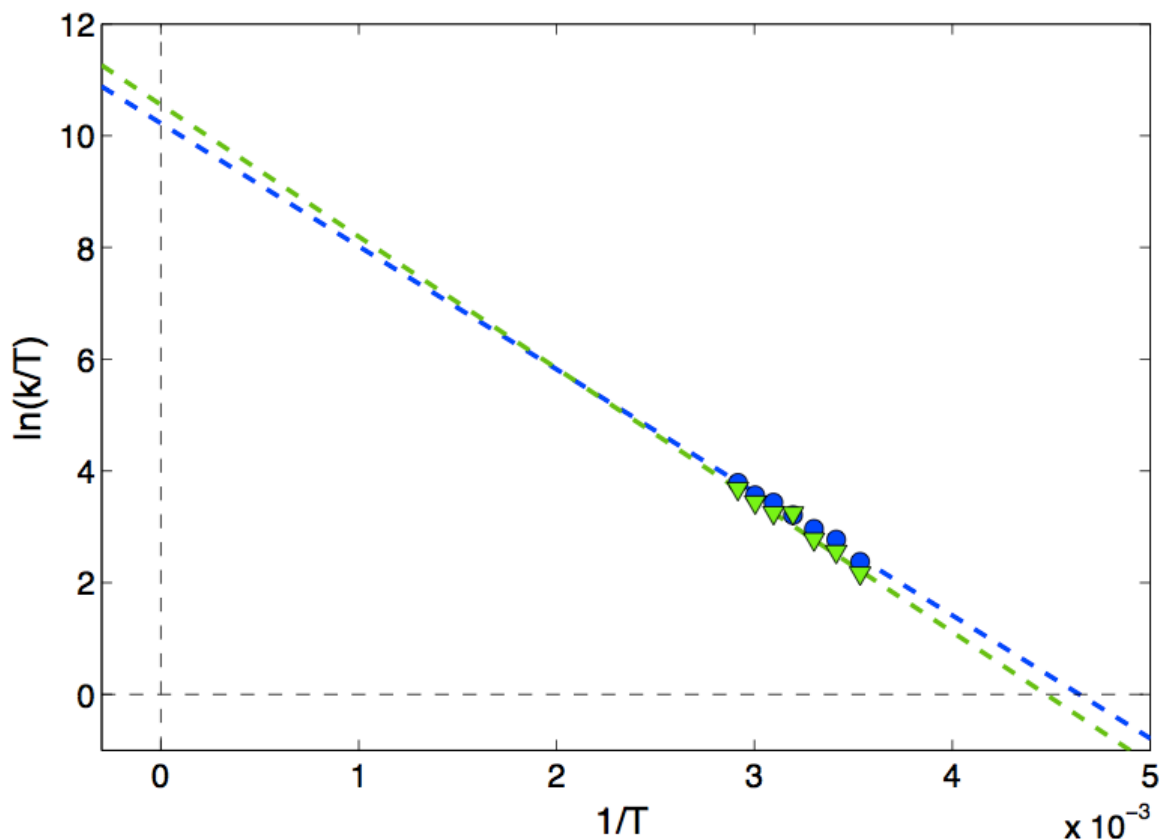


Figure 5.28. Eyring plot for rebinding of escaped CO in CYP119. The green triangles and blue circles represent two separate samples.

Table 5.3. Thermodynamic activation parameters for CO rebinding in CYP119 and various heme enzymes. a: this work. b: Reference 29. c: Reference 31.

Enzyme	ΔH^\ddagger	ΔS^\ddagger
	kcal/mol	cal/molK
CYP119 ^a (substrate free)	4.5	-27
P450 _{cam} ^b (substrate free)	14.2	21.6
P450 _{cam} ^b (with camphor)	7.0	-12.4
Myoglobin ^c	4.1	-19.4

5.3. Discussion, Conclusions and Future works

We achieved rapid, photochemical reduction of the P450 active site of four Ru-P450 conjugates with a rate of $50,000 \text{ s}^{-1}$. By comparison, native ET between the fused reductase and heme domains in P450 BM3 occur at 220 s^{-1} .³² Unlike the

photochemical oxidation discussed in Chapters 2 and 3, this reduction is not sensitive to intervening medium, and proceeds with rapid (microsecond) rates and good yields for all mutants examined. We also used photo-triggered methods to examine the kinetics of CO rebinding to wild type CYP119 following photolysis. We have identified key differences in the yields of CO escape, rates of rebinding, and population variance in the presence and absence of substrate, and have determined thermodynamic activation parameters for the substrate-free form. By selecting appropriate conditions of temperature, excitation wavelength, and buffer composition, we anticipate that these methods can be further refined to examine photochemical formation of ferric hydroperoxo species from chemically generated ferric superoxo, with the goal of observing the rearrangement to form CI.

5.4. Acknowledgments

The design, implementation, data collection, and analysis of picosecond TA were done with Dr. Kana Takematsu, and I am extremely grateful for her expertise, optimism, and perseverance. Discussions with Dr. Jay Winkler have been helpful for fitting, analyzing, and interpreting data. I also would like to thank Dr. Charlotte Whited for samples of the reductive quencher *p*MeODMA, and Professor Jeff Warren for assistance setting up the CO line.

5.5. Materials and Methods

Chemicals

Sodium dithionite (86%) was obtained from Fluka. Other buffer salts were obtained from J.T. Baker. *para*-methoxydimethylaniline (*p*MeODMA) used in these experiments was obtained courtesy of Dr. Charlotte Whited. Solutions were prepared using 18 M Ω cm water unless otherwise noted.

Ru-P450 conjugates

The P450 mutants used for this study are: P450 BM3 C62A/C156S/K97C (C97-BM3(W)), C62A/C156S/K97C/W96H (C97-BM3(wH)); CYP119 D77C (C77-CYP119(H)), D77C/H76W (C77-CYP119(HW)). The selection, mutagenesis, expression, and purification of cytochrome P450 mutants, as well as photosensitizer synthesis, conjugation, and purification, are described in Chapters 2 and 3.

Synthesis/purification of reductive quencher

The reductive quencher *para*-methoxydimethylaniline can be synthesized by previous published methods.⁷ *p*MeODMA used in these experiments was obtained courtesy of Dr. Charlotte Whited, purified by sublimation and characterized by ¹H NMR.

*p*MeODMA is only sparingly soluble in water. 40 mM aqueous stock solutions were prepared by dissolving 5 mg in 200 μ L of dimethylsulfoxide (DMSO), followed by dropwise (10 μ L) addition of aqueous buffer (50 mM sodium borate, pH 8) to a total volume of 500 μ L. Oxygenated solutions of *p*MeODMA change from clear to pinkish/purple in ambient light, with an absorbance increase at 550 nm. For that reason, fresh solutions were prepared immediately prior to use, and protected from light wherever possible.

Preparation of laser samples for flash-quench heme reduction

Laser samples were prepared in a high-vacuum four-sided quartz cuvette, sealed with a high-vacuum valve, and equipped with a small stir bar. Deoxygenation was achieved via gentle pump-backfill cycles with argon. For flash-quench in the presence of carbon monoxide, samples were subsequently pump-backfilled with

CO. Flash-quench samples consisted of approximately $\sim 10 \mu\text{M}$ Ru-P450 (Ru_{C97}-BM3(W), Ru_{C97}-BM3(WH), Ru_{C77}-CYP119(H) or Ru_{C77}-CYP119(HW)) with 10 mM *p*MeODMA in buffered solution: 50 mM sodium borate buffer, pH 8. Samples were excited with 8 ns laser pulses at 480 nm. Luminescence decays were monitored at 630 nm. Single wavelength transient absorption (TA) kinetics were monitored every 10 nm from 390-440 nm, averaging ~ 500 shots per wavelength. Data from five separate timescales (2 μs , 40 μs , 400 μs , 10 ms, and 500 ms) were collected, log-compressed, and spliced together to produce full kinetics traces. See Appendix D for log-compression and splicing scripts in Matlab.

Preparation of samples for Fe^{II}-CO photolysis/rebinding

Flash-photolysis samples were prepared in a specialized high-vacuum 4-sided quartz cuvette containing an attached 10 mL bulb compartment and a 24/40 adaptor; each compartment could be sealed separately by a high-vacuum valve (Kontes) (see diagram in Appendix B). Approximately 1.5 mL of ferric wild-type CYP119 (3-10 μM for ns-pulsed experiments, 30-60 μM for ps-pulsed experiments) in 100 mM potassium phosphate buffer, pH 7.4, was placed in the cuvette portion. A few grains of sodium dithionite were added to the bulb compartment, and the entire apparatus was degassed by gentle pump-backfill cycles with argon. The cuvette was then subjected to gentle pump-backfill cycles with carbon monoxide to obtain a headspace of CO. While sealed from the atmosphere, the ferric protein solution was mixed with sodium dithionite in the bulb, and then returned to the cuvette portion.

For nanosecond-to-millisecond TA experiments, samples were excited with 8 ns laser pulses at either 460 nm (single wavelength TA) or 486 nm (multi-wavelength TA). For single-wavelength transient absorption measurements, a narrow

bandpass filter (centered at 406 nm, Appendix C) was used to block the majority of the white probe light.

For picosecond-to-nanosecond TA experiments, samples were excited with 30 ps laser pulses at 532 nm with 0.5-1 mJ/pulse, and a 405 nm laser diode was used as probe light.

5.6. References

- (1) Noble, M. A.; Miles, C. S.; Chapman, S. K.; Lysek, D. A.; Mackay, A. C.; Reid, G. A.; Hanzlik, R. P.; Munro, A. W. Roles of Key Active-Site Residues in Flavocytochrome P450 BM3. *Biochem. J.* **1999**, *339*, 371–379.
- (2) Rittle, J.; Green, M. T. Cytochrome P450 Compound I: Capture, Characterization, and C-H Bond Activation Kinetics. *Science* **2010**, *330*, 933–937.
- (3) Davydov, R.; Makris, T. M.; Kofman, V.; Werst, D. E.; Sligar, S. G.; Hoffman, B. M. Hydroxylation of Camphor by Reduced Oxy-Cytochrome P450cam: Mechanistic Implications of EPR and ENDOR Studies of Catalytic Intermediates in Native and Mutant Enzymes. *J. Am. Chem. Soc.* **2001**, *123*, 1403–1415.
- (4) Sutin, N.; Creutz, C. Properties and Reactivities of the Luminescent Excited States of Polypyridine Complexes of Ruthenium(II) and Osmium(II). In *Inorganic and Organometallic Photochemistry; Advances in Chemistry; American Chemical Society: Washington, DC, 1978; Vol. 1.*
- (5) Creutz, C.; Chou, M.; Netzel, T. L.; Okumura, M.; Sutin, N. Lifetimes, Spectra, and Quenching of the Excited States of Polypyridine Complexes of Iron(II), Ruthenium(II), and Osmium(II). *J. Am. Chem. Soc.* **1980**, *102*, 1309–1319.
- (6) Coelho, P. S.; Wang, Z. J.; Ener, M. E.; Baril, S. A.; Kannan, A.; Arnold, F. H.; Brustad, E. M. A Serine-Substituted P450 Catalyzes Highly Efficient Carbene Transfer to Olefins in Vivo. *Nat. Chem. Biol.* **2013**, *9*, 485–487.
- (7) Mines, G. A.; Bjerrum, M. J.; Hill, M. G.; Casimiro, D. R.; Chang, I.-J.; Winkler, J. R.; Gray, H. B. Rates of Heme Oxidation and Reduction in Ru(His33)cytochrome c at Very High Driving Forces. *J. Am. Chem. Soc.* **1996**, *118*, 1961–1965.
- (8) Sevrioukova, I. F.; Immoos, C. E.; Poulos, T. L.; Farmer, P. J. Electron Transfer in the Ruthenated Heme Domain of Cytochrome P450BM-3. *Isr. J. Chem.* **2000**, *40*, 47–53.
- (9) Loida, P. J.; Sligar, S. G. Molecular Recognition in Cytochrome-P-450 - Mechanism for the Control of Uncoupling Reactions. *Biochemistry* **1993**, *32*, 11530–11538.
- (10) Martinis, S. A.; Blanke, S. R.; Hager, L. P.; Sligar, S. G.; Hoa, G. H. B.; Rux, J. J.; Dawson, J. H. Probing the Heme Iron Coordination Structure of Pressure-Induced Cytochrome P420(cam). *Biochemistry* **1996**, *35*, 14530–14536.
- (11) Perera, R.; Sono, M.; Sigman, J. A.; Pfister, T. D.; Lu, Y.; Dawson, J. H. Neutral Thiol as a Proximal Ligand to Ferrous Heme Iron: Implications for

- Heme Proteins That Lose Cysteine Thiolate Ligation on Reduction. *Proc. Natl. Acad. Sci.* **2003**, *100*, 3641–3646.
- (12) Dunford, A. J.; McLean, K. J.; Sabri, M.; Seward, H. E.; Heyes, D. J.; Scrutton, N. S.; Munro, A. W. Rapid P450 Heme Iron Reduction by Laser Photoexcitation of Mycobacterium Tuberculosis CYP121 and CYP51B1 - Analysis of CO Complexation Reactions and Reversibility of the P450/P420 Equilibrium. *J. Biol. Chem.* **2007**, *282*, 24816–24824.
- (13) Girvan, H. M.; Heyes, D. J.; Scrutton, N. S.; Munro, A. W. Laser Photoexcitation of NAD(P)H Induces Reduction of P450 BM3 Heme Domain on the Microsecond Timescale. *J. Am. Chem. Soc.* **2007**, *129*, 6647–6653.
- (14) Lange, R.; Heiberlanger, I.; Bonfils, C.; Fabre, I.; Negishi, M.; Balny, C. Activation Volume and Energetic Properties of the Binding of CO to Hemoproteins. *Biophys. J.* **1994**, *66*, 89–98.
- (15) McLean, M. A.; Yeom, H.; Sligar, S. G. Carbon Monoxide Binding to Cytochrome P450(BM-3): Evidence for a Substrate Dependent Conformational Change. *Biochimie* **1996**, *78*, 700–705.
- (16) Rupenyany, A.; Commandeur, J.; Groot, M. L. CO Photodissociation Dynamics in Cytochrome P450BM3 Studied by Subpicosecond Visible and Mid-Infrared Spectroscopy. *Biochemistry* **2009**, *48*, 6104–6110.
- (17) McLean, M. A.; Maves, S. A.; Weiss, K. E.; Krepich, S.; Sligar, S. G. Characterization of a Cytochrome P450 from the Acidothermophilic Archaea Sulfolobus Solfataricus. *Biochem. Biophys. Res. Commun.* **1998**, *252*, 166–172.
- (18) Perera, R.; Sono, M.; Raner, G. M.; Dawson, J. H. Subzero-Temperature Stabilization and Spectroscopic Characterization of Homogenous Oxyferrous Complexes of the Cytochrome P450BM3 (CYP102) Oxygenase Domain and Holoenzyme. *Biochem. Biophys. Res. Commun.* **2005**, *338*, 365–371.
- (19) Castellano, F. N.; Dattelbaum, J. D.; Lakowicz, J. R. Long-Lifetime Ru(II) Complexes as Labeling Reagents for Sulfhydryl Groups. *Anal. Biochem.* **1998**, *255*, 165–170.
- (20) Sassoon, R. E.; Gershuni, S.; Rabani, J. Photochemical Generation and Consequent Stabilization of Electron-Transfer Products on Separate like-Charged Polyelectrolytes. *J. Phys. Chem.* **1992**, *96*, 4692–4698.
- (21) Mines, G. A. Cytochrome c: Folding Triggered by Electron Transfer. Rates of Heme Oxidation and Reduction at High Driving Forces, California Institute of Technology: Pasadena, California, 1997.
- (22) Whited, C. A.; Belliston-Bittner, W.; Dunn, A. R.; Winkler, J. R.; Gray, H. B. Nanosecond Photoreduction of Inducible Nitric Oxide Synthase by a Ru-

- Diimine Electron Tunneling Wire Bound Distant from the Active Site. *J. Inorg. Biochem.* **2009**, *103*, 906–911.
- (23) Dunn, A.; Dmochowski, I.; Winkler, J.; Gray, H. Nanosecond Photoreduction of Cytochrome P450cam by Channel-Specific Ru-Diimine Electron Tunneling Wires. *J. Am. Chem. Soc.* **2003**, *125*, 12450–12456.
- (24) Denisov, I. G.; Makris, T. M.; Sligar, S. G. Cryoradiolysis for the Study of P450 Reaction Intermediates. *Methods Enzymol.* **2002**, *357*, 103–115.
- (25) Pierre, J.; Bazin, M.; Debey, P.; Santus, R. One-Electron Photo-Reduction of Bacterial Cytochrome P-450 by Ultraviolet-Light. 1. Steady-State Irradiations. *Eur. J. Biochem.* **1982**, *124*, 533–537.
- (26) Bazin, M.; Pierre, J.; Debey, P.; Santus, R. One-Electron Photoreduction of Bacterial Cytochrome P-450 by Ultraviolet Light. II. A Study Using Laser Flash Photolysis of the Dynamics of the Reduction of Bacterial Cytochrome P-450 in the Presence of Carbon Monoxide. The Role of the PRotein Conformation. *Eur. J. Biochem.* **1982**, *124*, 539–544.
- (27) Gu, Y.; Li, P.; Sage, T.; Champion, P. M. Photoreduction of Heme-Proteins - Spectroscopic Studies and Cross-Section Measurements. *J. Am. Chem. Soc.* **1993**, *115*, 4993–5004.
- (28) Lampe, J., N.; Brandman, R.; Sivaramakrishnan, S.; de Montellano, P. R. O. Two-Dimensional NMR and All-Atom Molecular Dynamics of Cytochrome P450 CYP119 Reveal Hidden Conformational Substates. *J. Biol. Chem.* **2010**, *285*, 9594–9603.
- (29) Koo, L. S.; Immoos, C. E.; Cohen, M. S.; Farmer, P. J.; Ortiz de Montellano, P. R. Enhanced Electron Transfer and Lauric Acid Hydroxylation by Site-Directed Mutagenesis of CYP119. *J. Am. Chem. Soc.* **2002**, *124*, 5684–5691.
- (30) Tian, W. D.; Wells, A. V.; Champion, P. M.; Di Primo, C.; Gerber, N.; Sligar, S. G. Measurements of CO Geminate Recombination in Cytochromes P450 and P420. *J. Biol. Chem.* **1995**, *270*, 8672–8679.
- (31) Hasinoff, B. B. Kinetic Activation Volumes of the Binding of Oxygen and Carbon Monoxide to Hemoglobin and Myoglobin Studied on a High-Pressure Laser Flash Photolysis Apparatus. *Biochemistry* **1974**, *13*, 3111–3117.
- (32) Munro, A. W.; Daff, S.; Coggins, J. R.; Lindsay, J. G.; Chapman, S. K. Probing Electron Transfer in Flavocytochrome P-450 BM3 and Its Component Domains. *Eur. J. Biochem.* **1996**, *239*, 403–409.

Chapter 6

**AXIAL-LIGAND INFLUENCE ON P450 REDUCTION
POTENTIALS:
IMPLICATIONS FOR CATALYSIS**

Portions of this work are excerpted with permission from:

P. S. Coelho, Z. J. Wang, M. E. Ener, S. A. Baril, A. Kannan,
F. H. Arnold, E. M. Brustad. *Nat. Chem. Biol.* **2013**, 485-487.

Copyright 2013 Nature Publishing Group

6.1. Background: Controlled electron flow through P450

Initiation of catalysis by cytochrome P450 heme enzymes requires the controlled flow of electrons. In the native catalytic cycle, the redox cofactor NAD(P)H supplies necessary reducing equivalents, which are shuttled to the P450 heme active site via the redox cofactors flavin adenine dinucleotide (FAD) and flavin mononucleotide (FMN) that are housed in cytochrome P450 reductases. The self-sufficient enzyme P450 BM3 from the soil bacterium *B. megaterium* contains a flavin reductase domain fused to the heme domain (**Figure 6.1**), which facilitates reduction of the heme¹ and allows for high turnover rates ($> 10^3$ per minute).²

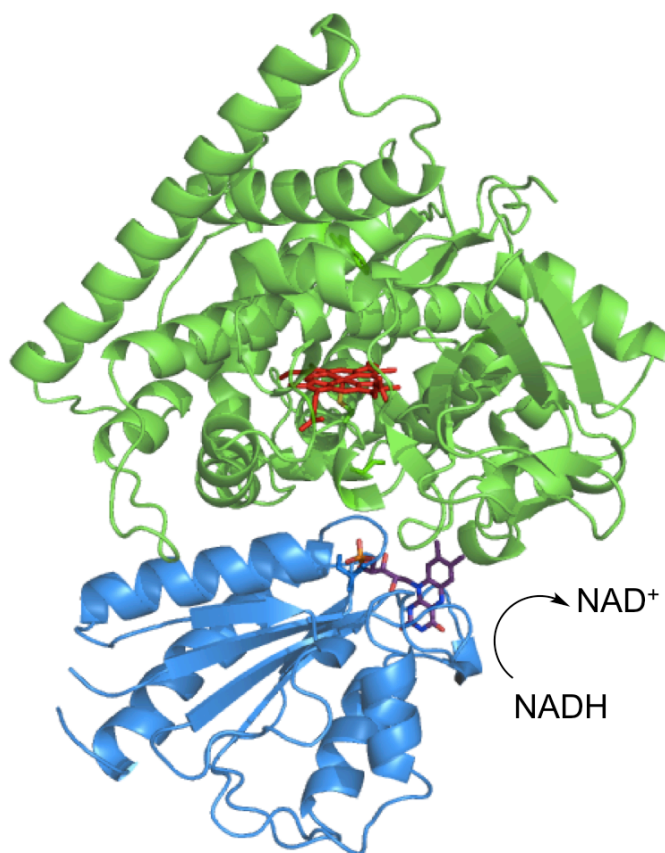


Figure 6.1. Structure of P450 BM3. (PDB: 1BVY) The oxygenase domain is colored green (heme: red), and the reductase domain is colored blue (flavin: purple). All images of protein structures in this Chapter were made using PyMol graphics software for Mac.

In many P450s, including P450 BM3, an important gating mechanism controls this electron flow by modulating the heme reduction potential in the presence or absence of substrate. As described in Chapter 1, the resting state enzyme is low-spin, six-coordinate ferric, where the distal ligation site is occupied by a water molecule; the reduction potential of this species is too negative to be efficiently reduced by NADH via the flavin cofactors. The binding of native substrates displaces the labile water molecule, inducing a positive shift in reduction potential that allows heme reduction.

Controlled electron flow is a critical element of all P450 redox chemistry, including engineered catalytic reactivity. We became interested in electron flow in a series of P450 BM3 mutants designed by Frances Arnold's group at Caltech that catalyze the cyclopropanation of styrene by ethyldiazoacetate (EDA) (**Figure 6.2**). Directed evolution was used to generate P450 mutants that display high levels of regioselectivity (for either *cis* or *trans* isomers) and enantioselectivity in such cyclopropanation reactions.³ In analogy to the native P450 cycle (**Figure 6.3**, left), and by comparison to the mechanisms for small molecule metalloporphyrin-catalyzed cyclopropanations, the Arnold group proposed a catalytic scheme for the reactivity of engineered P450s (**Figure 6.3**, right).

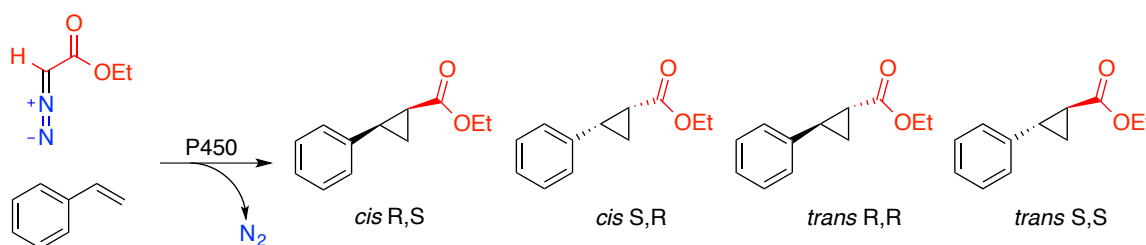


Figure 6.2. P450-catalyzed cyclopropanation of styrene.

Just as in the native catalytic cycle, reduction of the ferric resting state is essential to initiate P450-catalyzed cyclopropanation activity. This is supported

experimentally supported by the inactivity of *ferric* enzyme in the presence of EDA and styrene, and by the requirement of reductant to initiate catalysis. Furthermore, the net reaction is inhibited by carbon monoxide, which readily binds to ferrous hemes, but not ferric.⁴

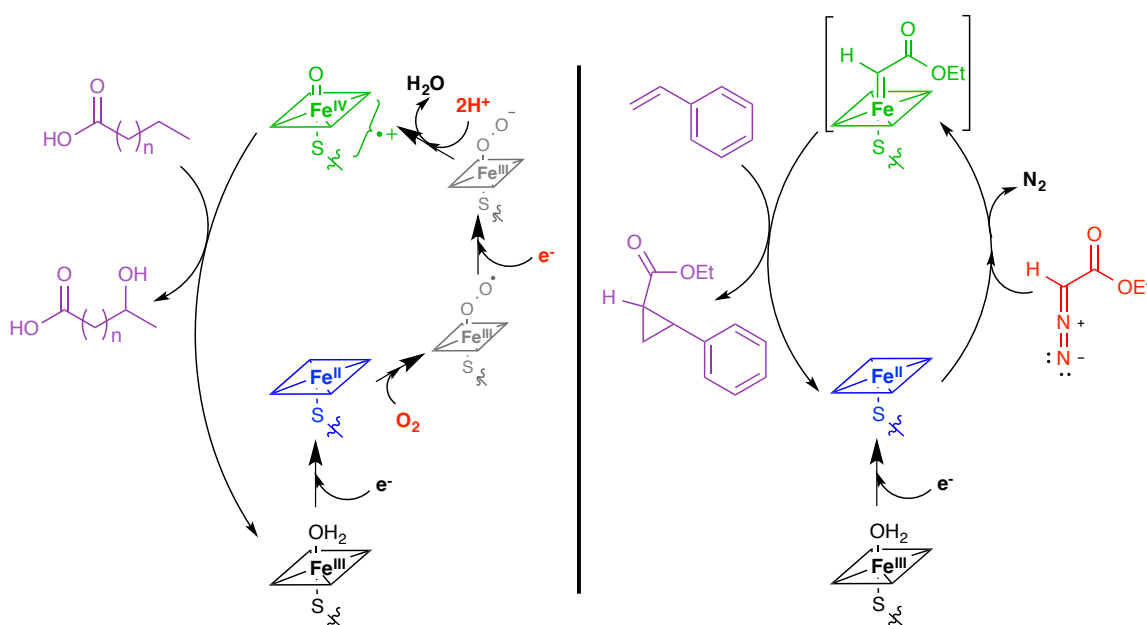


Figure 6.3. Schemes for native and engineered P450 catalysis. **Left:** Consensus P450 catalytic cycle for oxygenations, showing hydroxylation of a fatty acid. **Right:** Proposed catalytic scheme for the cyclopropanation of styrene.

Strong reductants, such as dithionite, are required to initiate catalysis in these mutants; very low levels of activity were observed in the presence of the biological reductant NADH. It was presumed that styrene was ineffective at displacing the labile water molecule and opening the electron gate; a low binding affinity is indicated by the Michaelis-Menten constant ($K_M \sim 5 \text{ mM}$).³ This can be circumvented for solutions of purified enzyme; dithionite can easily be added to solutions. However, the development of enzymatic cyclopropanation for sustainable, industrial scale production would be greatly enhanced by extension to

whole cell biocatalyst systems. In that case, the reductant scope is limited to endogenously produced redox cofactors, including NADH.

Enzyme engineering to more tightly bind styrene could facilitate the substrate gating issue, but this process would need to be repeated for each new substrate, and the P450 catalyst would lose its desirable substrate promiscuity. Alternatively, the enzymes could be engineered with higher resting state reduction potential, effectively propping open the electron gate. Many factors tune the reduction potential of heme enzymes, including the environment in the proximal pocket,⁵ and the nature of the proximal ligand. The reduction potentials of axial mutants of the heme protein cytochrome *c* span a range of 650 mV, from -390 mV for a Cys/His ligated mutant to +262 for the Met/His variant.⁶ Interestingly, the potential of cysteine-ligated cytochrome *c* (-390 mV) is similar to that of P450. Replacement of the strong, axial thiolate with a weakly donating water molecule results in a positive shift of almost 350 mV.

To this end, the Arnold group designed a second generation of mutants in which the axial cysteine ligand (C400) is replaced with other amino acids, including serine. It was hypothesized that the more weakly donating serine ligand would result in a positive shift in reduction potential, similar to the observations for cytochrome *c*. As described in Chapter 1, cysteine ligation is critical for the activation of dioxygen and generation of the ferryl porphyrin radical active species known as compound I (**Figure 6.3** left, highlighted green).⁷ Mutation of the axial cysteine to serine in mammalian P450s abolishes monooxygenation activity.⁸ However, this ligation was not expected to be necessary for cyclopropanation, as free hemein also catalyzes this reaction.

This is in fact the case; serine-ligated P450 BM3 mutants are highly active for cyclopropanation reactions, and show selectivity for cyclopropanation over epoxidation of styrene, even under aerobic conditions (**Figure 6.4**, right).⁹ The Arnold group chose to examine one mutant in particular, which contains 13 mutations to the active site and periphery and the C400S mutation. This mutant catalyzes over 300 turnovers *in vitro*, and is characterized by a ferrous-CO species with an absorbance max at 411 nm.⁹ For the purposes of this Chapter, this particular mutant will be referred to as P411₁₃-Ser. The serine-ligated P450-BM3 heme domain (C400S) has been characterized by X-ray crystallography, which indicates serine-ligation of the heme active site (**Figure 6.4**, left).

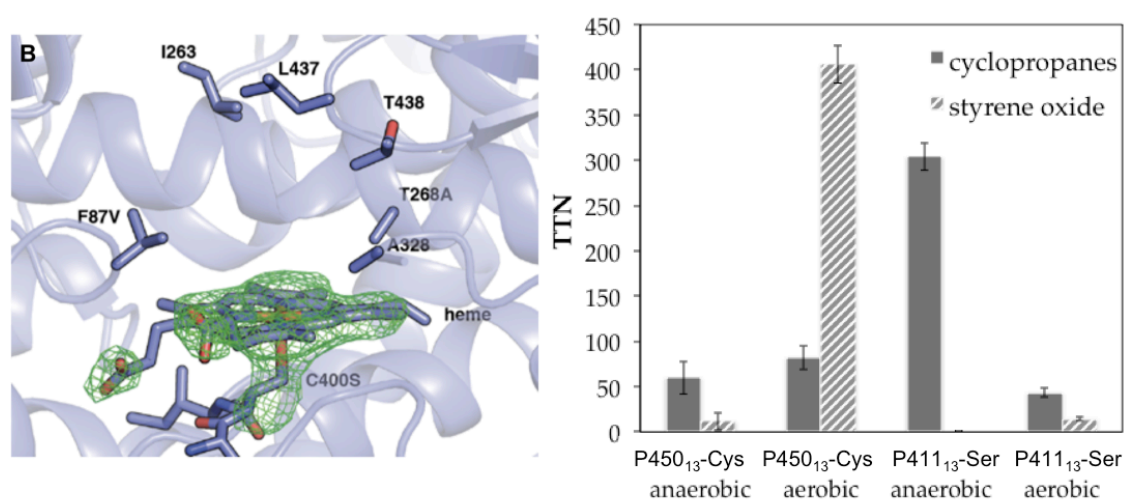


Figure 6.4. P411₁₃-Ser structure and activity.⁹ **Left:** electron density maps show serine ligation to the heme of P411₁₃-Ser heme domain. **Right:** Total turnover numbers (TTN) for P450-catalyzed reactions.

The central question for the function of this catalyst, and improvement to future catalysts is: Does the cysteine-to-serine mutation in P450 also result in a positive shift in reduction potential? Furthermore, is this shift sufficient to make reduction by NADH and flavin cofactors thermodynamically favorable?

Determination of reduction potentials is difficult for enzymes such as P450s. Standard voltammetry techniques are fraught with challenges, including slow diffusion of the large proteins, and poor communication between the buried heme and the working electrode. Additionally, the ferrous state of cytochrome P450 is extremely sensitive to oxygen, and readily auto-oxidizes to ferric. Any method to determine P450 E° (Fe^{III/II}) must be done under strictly anaerobic conditions.

Various methods exist for determining reduction potentials, including spectrophotometric titrations, spectroelectrochemical titrations, potentiometric titrations, and direct electrochemistry of immobilized or freely-diffusing enzymes. However, these techniques result in a wide range of reported potentials. For example, a range of potentials from -368 mV to -427 mV are reported for solution measurements of wild-type (WT),^{5,10} substrate free P450 BM3. Protein film voltammetry has led to even more positive reported values of approximately -133 to $+4$ mV.¹⁰⁻¹² Careful determination of solution reduction potentials and internal comparison between wild type and mutant enzymes is needed.

This Chapter reports the measurement of ferric/ferrous reduction potentials for a variety of P450 mutants. It also describes the advantages and limitations of various techniques that may be used to determine solution ferric/ferrous reduction potentials for P450 variants. In particular, we address whether the ligation change results in a shift in reduction potential within range of biological reductants (NADH, FMN). Unless specified otherwise, all potentials are measured at neutral pH, and are reported versus the normal hydrogen electrode (NHE).

Enzymes

In order to avoid complications with the optically- and redox-active flavin cofactors, all measurements use only the heme domains of all P450 BM3 mutants,

rather than the holo enzyme. To test titration methods and provide an internal reference for reduction potentials, we have examined WT enzymes P450 BM3, and CYP119 from *Sulfolobus acidocaldarius*. To probe the effect of axial ligation on $E^\circ(\text{Fe}^{\text{III/II}})$, we examined BM3 axial mutants: C400S, C400M, C400H, C400Y, C400A, and C400D. We also examined two mutants specifically engineered for cyclopropanation activity. The first mutant, which will be referred to as P450₁₃-Cys, contains the 13 mutations V78A, F87V, P142S, T175I, A184V, S226R, H236Q, E252G, T268A, A290V, L353V, I366V and E442K (Figure 6.5). The second mutant, P411₁₃-Ser, is identical to P450₁₃-Cys except that it contains C400S serine ligation.

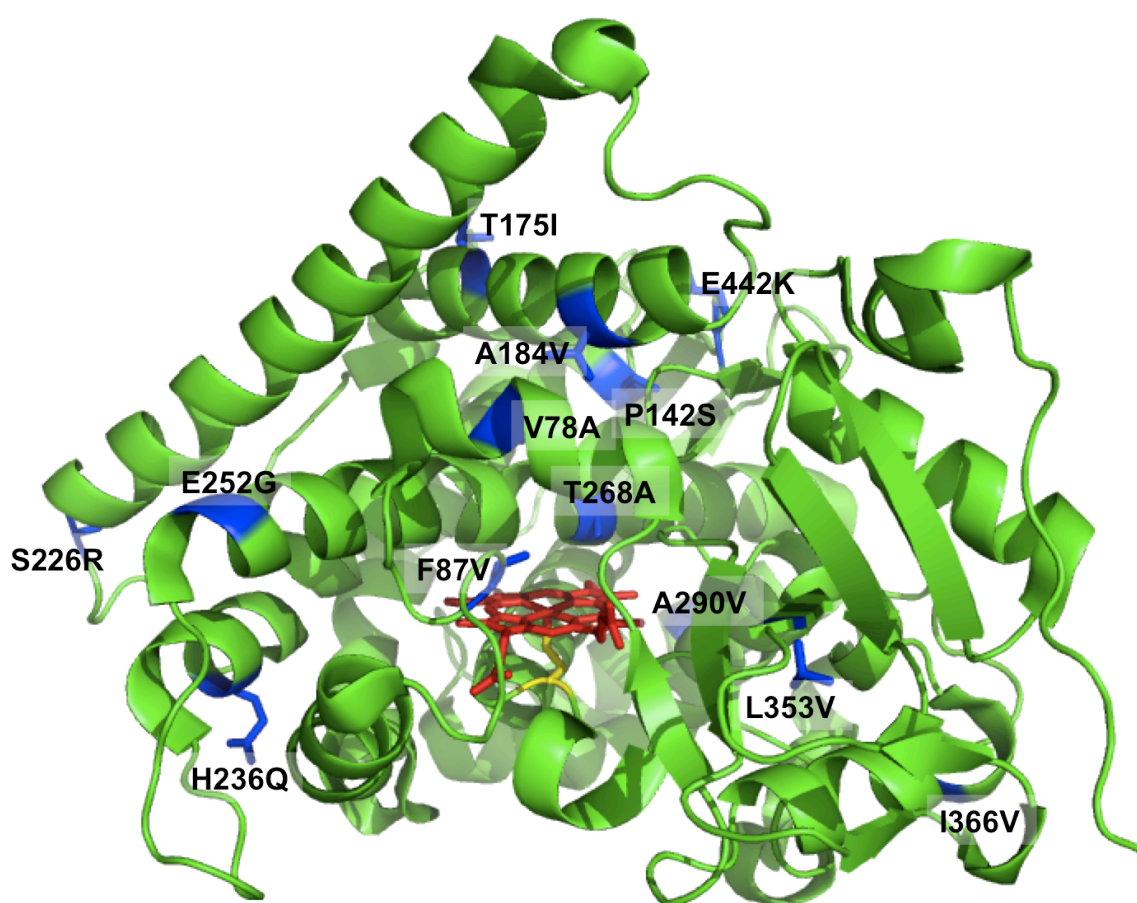


Figure 6.5. Structure of P450₁₃-Cys, highlighting mutations in blue (PDB 4H23).

6.2. Methods Development for Redox Titrations

Spectrophotometric Titration

Spectrophotometric titrations present an experimentally straightforward means to determine reduction potentials. An enzyme sample is titrated by addition of chemical oxidant/reductant of known potential, and absorption spectra are acquired at each point along the titration. Absolute concentrations of reduced and oxidized species are determined based on the absorption profile, to determine K_{eq} (Equation 6.1). The enzyme reduction potential is determined using Equation 6.3, where ΔE° is the reduction potential of the enzyme, and ΔE is the difference in potentials between the enzyme and titrant.

For a reaction: $Enz(ox) + A(red) \rightarrow Enz(red) + B(ox)$

$$K_{eq} = \frac{[Enz(red)][B(ox)]}{[Enz(ox)][A(red)]} \quad 6.1$$

$$\Delta G^\circ = -RT \ln K_{eq} = -nF\Delta E^\circ \quad 6.2$$

$$\Delta E = \Delta E^\circ - \frac{RT}{nF} \cdot \ln \left(\frac{[Enz(red)][B(ox)]}{[Enz(ox)][A(red)]} \right) \quad 6.3$$

The requirements for this method are: 1) Enzyme, in which the reduced and oxidized forms of the protein have distinct absorption profiles with known extinction coefficients; 2) A chemical oxidant/reductant with a known reduction potential within ~100 mV of the enzyme, and in which the reduced and oxidized forms have distinct absorption profiles with known extinction coefficients. Advantages of this method are that low concentrations and volumes of protein can be employed, and no specialized equipment is necessary, other than a

spectrophotometer and cuvette under anaerobic atmosphere (e.g., within a glovebox).

As discussed previously, the $E^\circ(\text{Fe}^{\text{III/II}})$ for WT P450 BM3 is expected to fall within the range of -365 to -430 mV. Methyl viologen radical cation ($\text{MV}^{\bullet+}$) was chosen as the chemical reductant; this species has strong absorbance in the visible region (**Figure 6.6**), and its reduction potential $E^\circ(\text{MV}^{2+}/\text{MV}^{\bullet+}) = -446$ mV^{13,14} falls within 100 mV of the expected P450 potential. $\text{MV}^{\bullet+}$ can be generated from MV^{2+} dichloride, which is optically transparent, by mixing an aqueous MV^{2+} solution with zinc powder under anaerobic conditions.¹⁵ The radical reacts quickly with oxygen to regenerate MV^{2+} ; however, under anaerobic conditions, it is stable for many hours.¹⁶

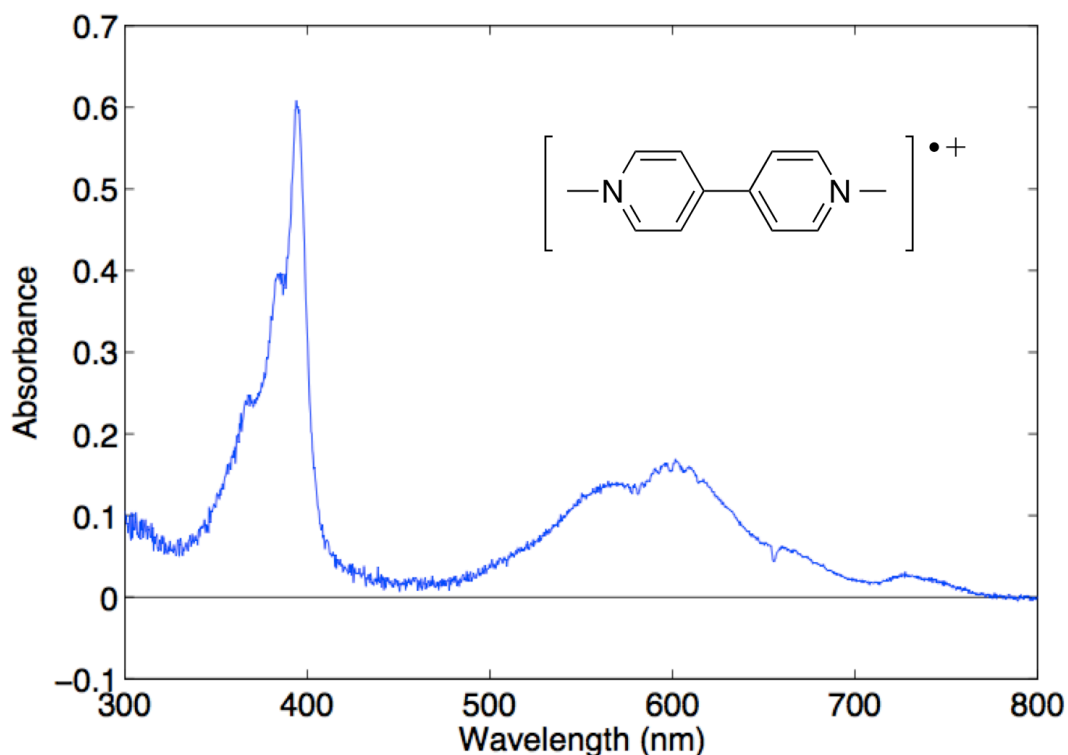


Figure 6.6. Absorption spectrum of the methyl viologen radical cation. Reduction was accomplished by mixing over zinc powder in a glovebox.

Addition of aliquots of $MV^{•+}$ to a solution of ferric, WT P450 results in a series of titration spectra, shown in **Figure 6.7**. There is significant overlap between the $MV^{•+}$ and P450 absorbance spectra in the range of 350-600 nm; this makes spectral deconvolution more difficult.

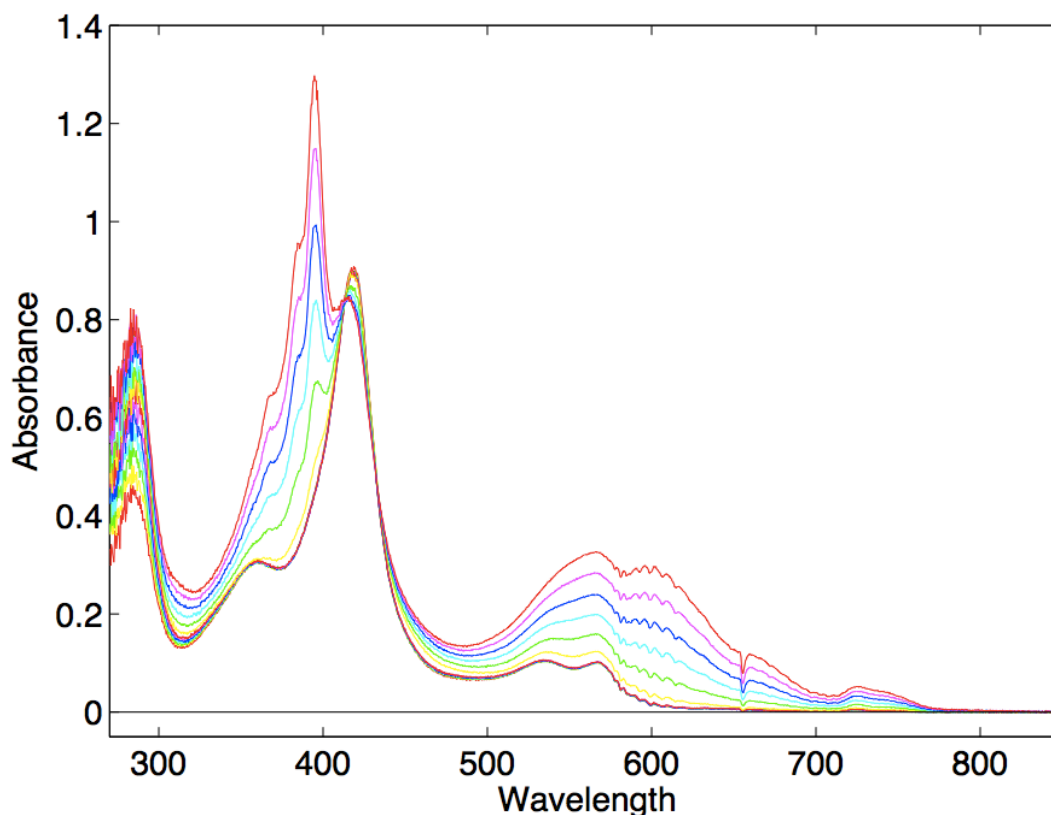


Figure 6.7. Chemical titration of WT P450 BM3 with $MV^{•+}$.

There are other significant concerns with regards to the success of these titrations. Importantly, trace amounts of oxygen can affect the data. Oxygen reacts rapidly with both the ferrous P450 and with $MV^{•+}$. This adds a third redox couple to the reaction, yet there are no optical signals to indicate the concentration of oxygen, or of the oxidized MV^{2+} . It is extremely difficult to remove all traces of oxygen from protein samples; multiple freeze-thaw cycles (e.g., freeze-pump-thaw) or sparging can be detrimental to the protein structure, and therefore, redox properties. There was also a significant amount of error with respect to titrant volumes; the positive

pressure necessary in the glovebox makes accurate pipetting of microliter quantities very difficult. Furthermore, this method requires use of a titrant within ~ 100 mV of the expected reduction potential. A new titrant would need to be found for each mutant, decreasing the generalizability of the method. For all of these reasons, spectrochemical titrations were abandoned for measurement of P450 BM3 reduction potentials.

Electrochemical titration

Electrochemical titrations require a more complex, experimental setup, but determination of ferric/ferrous P450 concentrations and relevant potentials is more straightforward. In this method, reduction of the enzyme is accomplished using a narrow-pathlength spectroelectrochemistry cuvette, with a three-electrode setup (**Figure 6.8**).

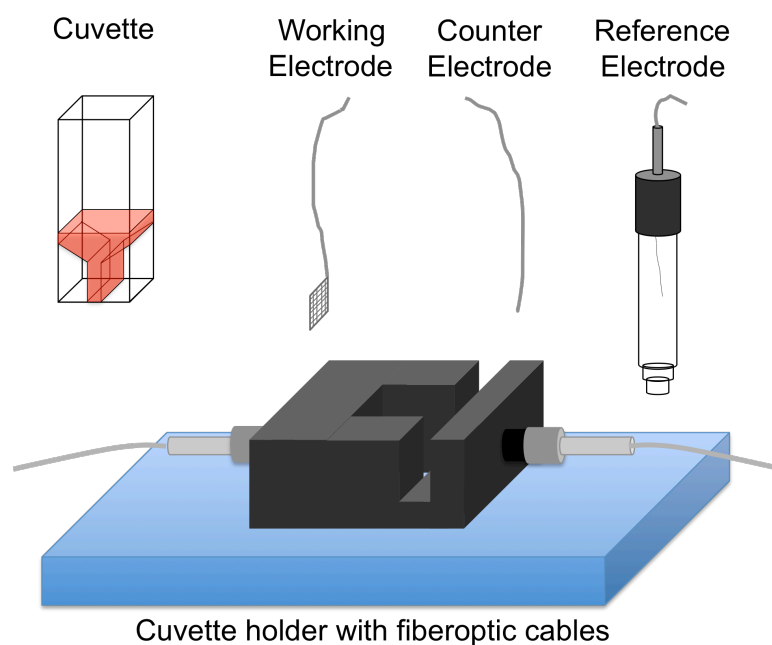


Figure 6.8. Spectroelectrochemical setup. Quartz cuvette with 1mm pathlength, Pt mesh working electrode, Pt wire counter electrode, and AgCl/Ag reference electrode.

When the potential at the electrode approaches the heme reduction potential, electrons flow from the large-surface area working electrode to the P450 heme, relayed via a mixture of small molecule mediators with varying $E^{\circ'}$ (**Figure 6.9**). After equilibration at each potential, spectra are recorded to determine the relative concentrations of reduced and oxidized enzyme (**Figure 6.10**).

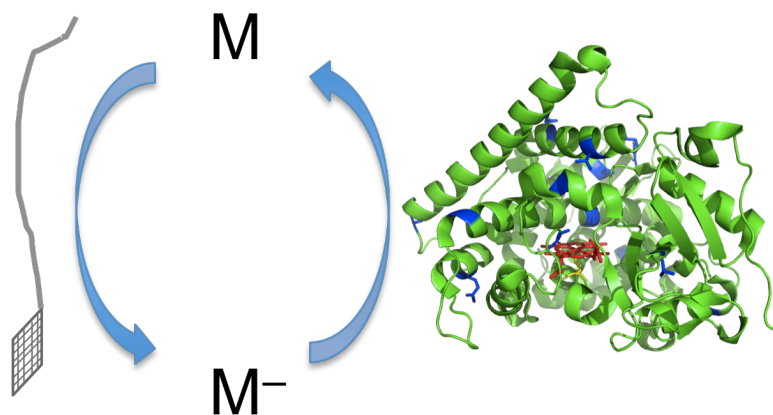


Figure 6.9. Electron relay between the Pt mesh working electrode and the P450 heme (red). “M” represents the small molecule mediators.

For these measurements with short path length (1 mm), the enzyme concentration (~30-70 μM) is greater than that of the mediators. Only the ferric and ferrous P450 species contribute significantly to the visible absorbance spectrum, facilitating spectral deconvolution. A plot of relative %Fe^{II} versus applied electrode potential can be fit to the one-electron Nernst equation to determine $E^{\circ'}$ for the enzyme.

We performed a spectroelectrochemical reduction of the WT BM3 heme using the setup described above, applying electrode potentials over a range of -100 to -530 mV (**Figure 6.10**). Following this reduction, an aliquot of sodium dithionite was added to accomplish complete heme reduction, and the analogous, reverse titration (oxidation) was performed (**Figure 6.11**).

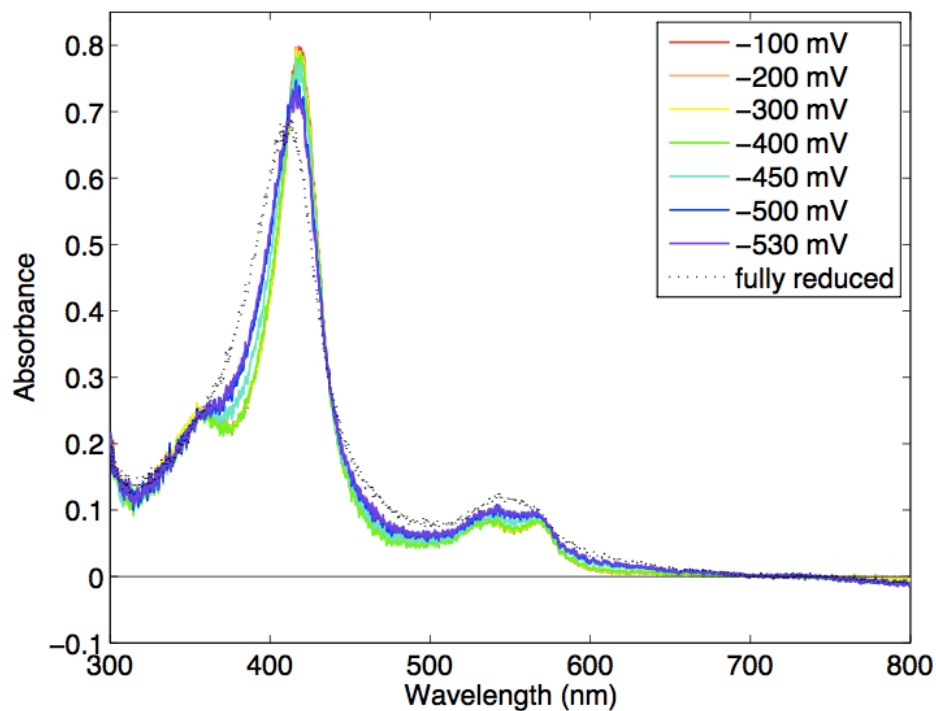


Figure 6.10. Absorption spectra taken during the spectroelectrochemical reduction of WT BM3.

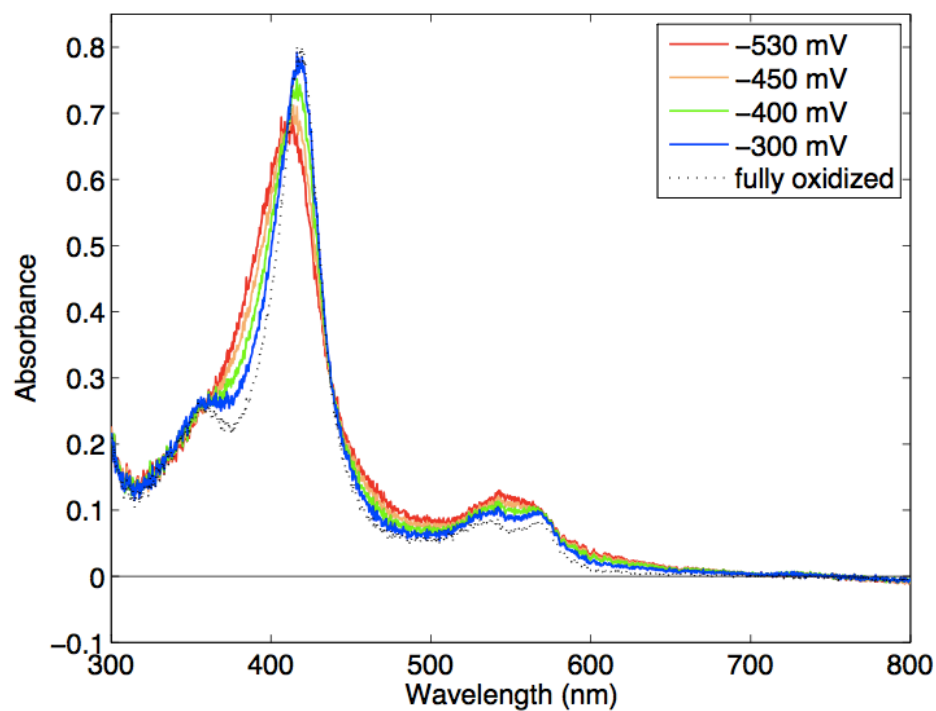


Figure 6.11. Absorption spectra taken during the spectroelectrochemical oxidation of dithionite-reduced WT BM3.

We deconvoluted the spectra (300-600 nm) into ferric and ferrous components using a Matlab program (see Appendix D). A plot of % ferrous P450 versus applied potential is shown in **Figure 6.12**.

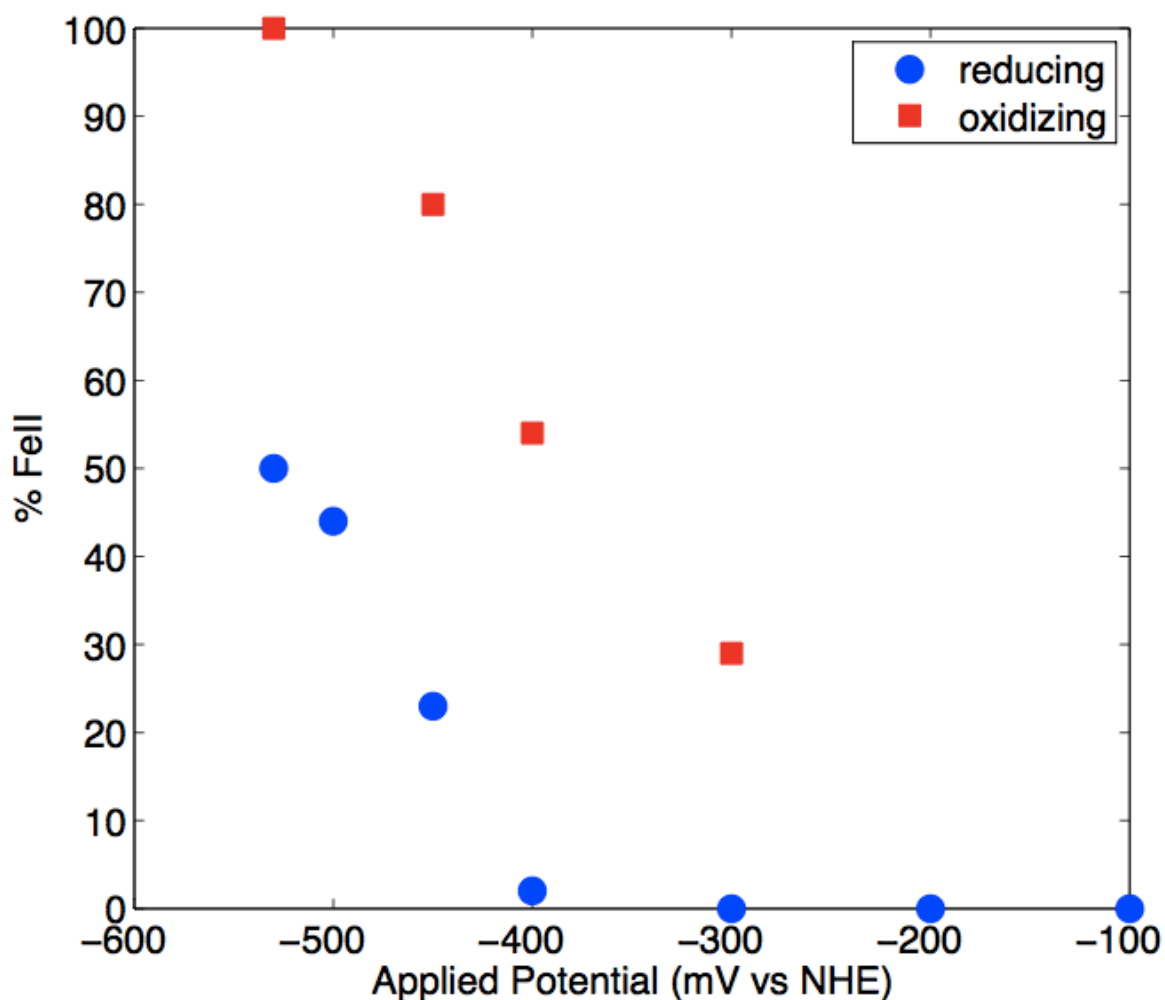


Figure 6.12. Plot of the electrochemical titration of WT BM3. Blue circles: reductive titration. Red squares: oxidative titration.

Significant hysteresis was observed between the reductive and oxidative titrations, making it impossible to fit the data to the Nernst equation. This hysteresis is most likely due to slow equilibration between the electrode and the bulk solution at low concentrations of redox mediators (1-10 μM). Using higher concentrations of

redox mediators is undesirable, as these optically active small molecules interfere with the spectral deconvolution of ferric and ferrous P450 concentrations. Additionally, in these initial experiments (and for space reasons within the spectroelectrochemical cuvette), the counter electrode was not kept in a separate fritted compartment; it is likely that reoxidation/rereduction at the counter electrode precluded full conversion between oxidized and reduced states of the enzyme. For these practical reasons, we have modified this approach, as described below.

Potentiometric titration

Potentiometric titrations are very similar to the electrochemical titrations, except that the supply of reducing/oxidizing equivalents is accomplished by addition of chemical reductants/oxidants. In this case, reduction is accomplished by addition of sodium dithionite, and re-oxidation is accomplished by addition of potassium ferricyanide. The open circuit potential (OCP, potential applied by the electrode at which no current flows) is measured after every chemical addition to determine the solution potential. %Fe^{II} is again determined by deconvolution of absorption spectra into ferric and ferrous components.

Chemical (rather than electrochemical) reduction/oxidation results in faster equilibration of the sample volume upon manual mixing. For these measurements, the electrode need not be high surface area (in contrast to the spectroelectrochemical titration). A single wire working electrode can be used. The reduction potential of aquo-ligated WT P450 BM3 is fairly negative (vide infra), and approaches the thermodynamic potential for proton reduction (at pH 7). Clean platinum wires begin to evolve hydrogen at the relevant potentials, which

complicates the OCP measurements. Implementation of a gold wire working electrode greatly improved potentiometric titrations.

Test: Wild-type P450 BM3

The spectra during titration with dithionite show clean conversion from ferric to ferrous with multiple isosbestic points (**Figure 6.13**). Reoxidation by ferricyanide also proceeds cleanly (**Figure 6.14**).

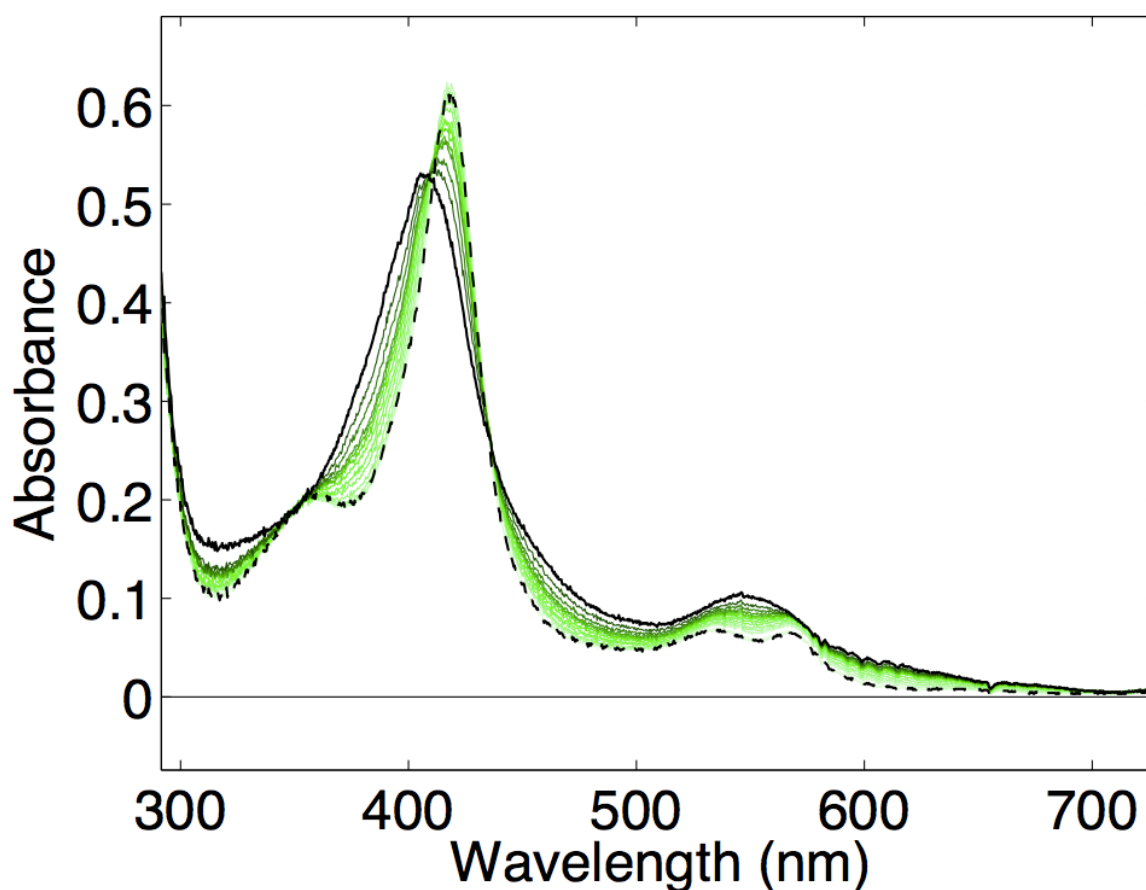


Figure 6.13. Absorption spectra of WT BM3 during reductive potentiometric titration. Ferric: black dashed line. Ferrous: black solid line.

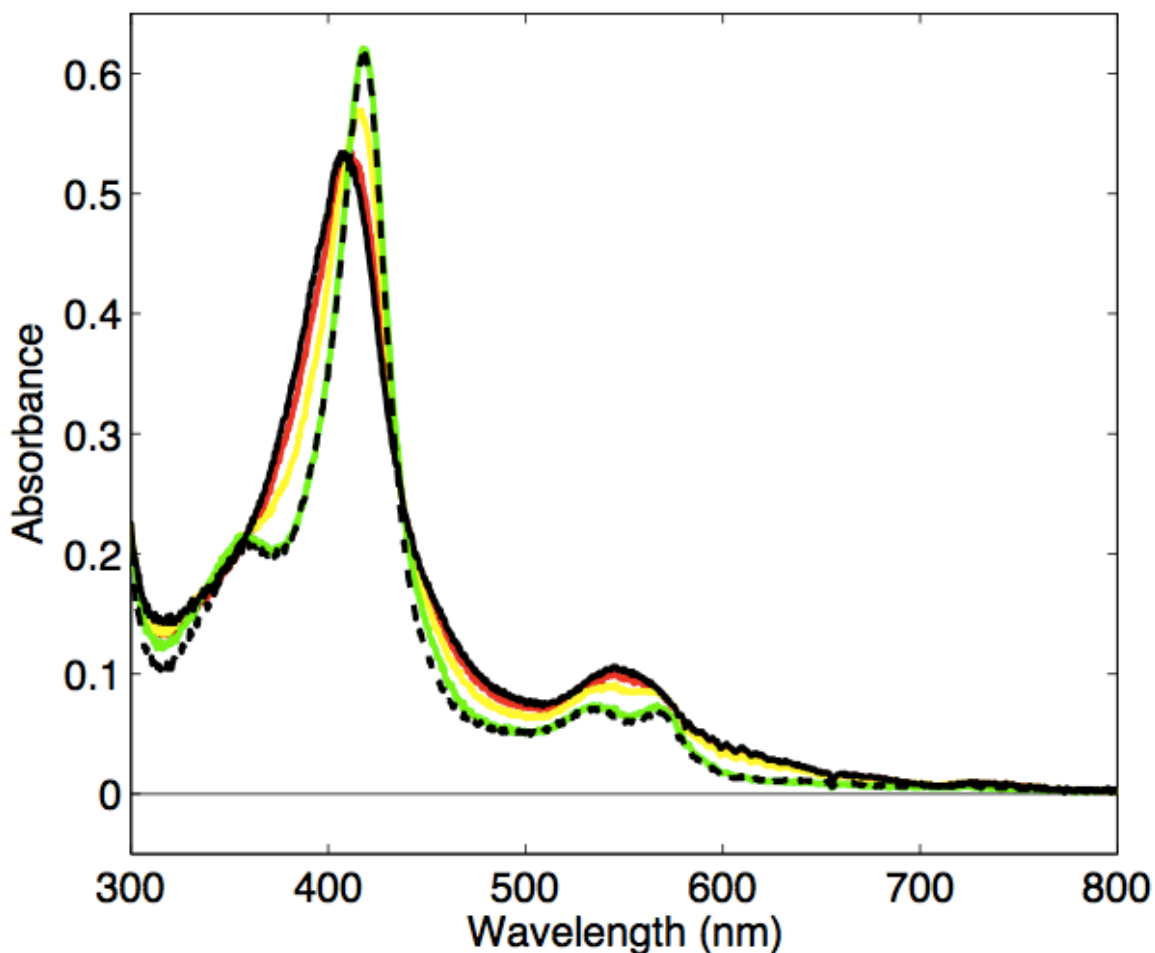


Figure 6.14. Absorption spectra of WT BM3 during oxidative potentiometric titration. Ferrous: black solid line. Ferric (pre-titration): black dashed line.

There is only minor drift in open circuit potentials over the course of the measurement (10 min), almost always toward more positive values (**Figure 6.15**). The drift was generally less than 1.5 mV/min; in cases where drift exceeded this benchmark, an additional 5 minute period was recorded. Excessive amounts of drift (5 mV/min, or more) generally indicated incomplete mixing, the presence of oxygen, sample impurities, or a dirty working electrode. In these cases, manual mixing was repeated, or samples, buffers and electrodes were removed from the box, cleaned/purified and re-deoxygenated, and the titration was attempted again from the beginning.

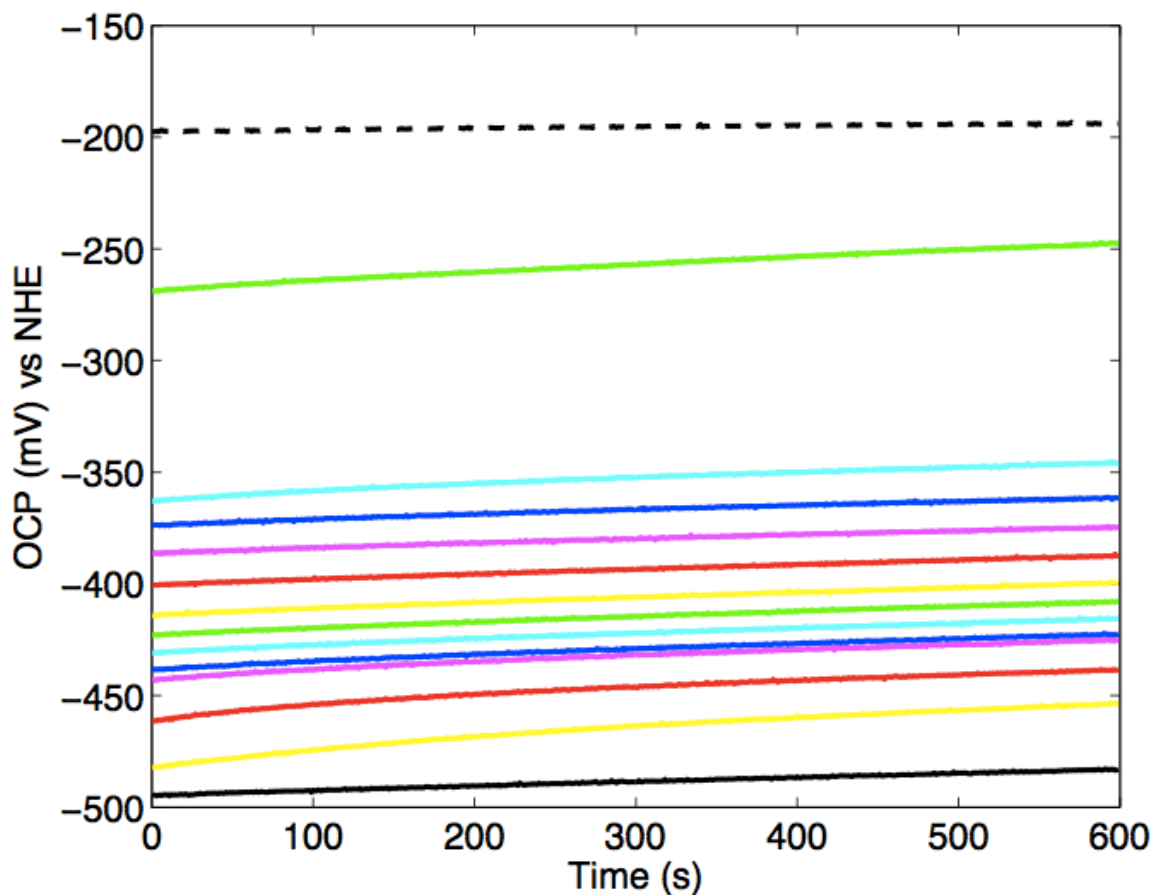


Figure 6.15. Open circuit potential measurements of WT BM3 during potentiometric titration. Dashed black line: first titration point. Solid black line: fully reduced (excess dithionite).

Spectra were deconvoluted to ferric and ferrous components, as discussed previously (see Appendix D). Relative percent ferrous was plotted against the final OCP value at each point in the titration (**Figure 6.16**). No hysteresis is observed between the reductive and oxidative titrations (**Figure 6.16**). An overlay of the one-electron Nernst equation (Equation 6.4) is used to determine reduction potential.

$$E_{cell} = E^{\circ} - \frac{RT}{nF} \left(\frac{[Fe^{II}]}{[Fe^{III}]} \right)$$

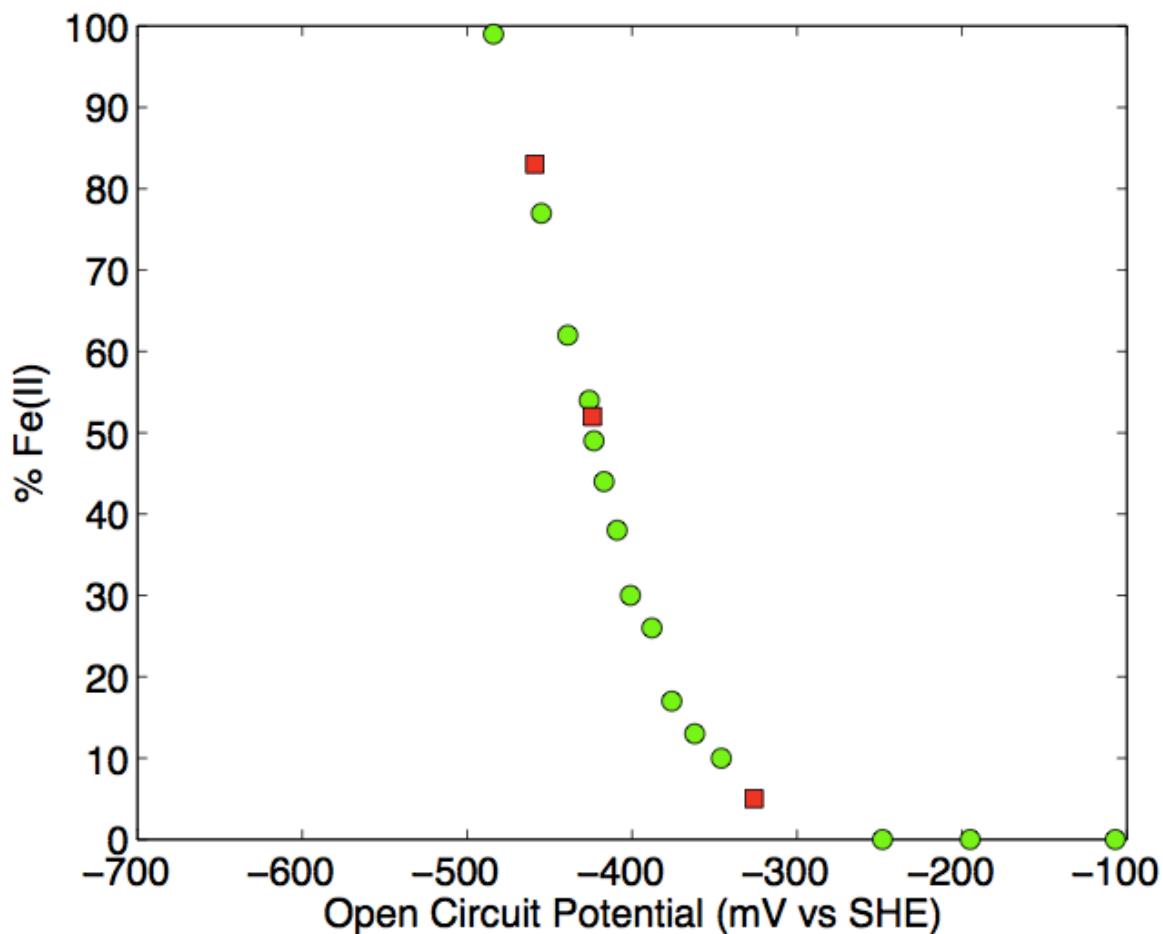


Figure 6.16. Redox titration plot of wild-type P450 BM3. Reduction by sodium dithionite: green circles. Re-oxidation by potassium ferricyanide: red squares.

6.3. Results

6.3.1. Wild-type Enzymes: P450 BM3 and CYP119

Wild Type P450 BM3

The reduction potential for WT P450 BM3 measured by potentiometric redox titration is -420 mV (**Figure 6.17**). This matches closely to the published value of -427 mV.⁵ The authors also note that this value agrees with calculations. Most importantly, this value is repeatable, and provides a benchmark with which to compare other mutants (see Appendix C for discussion of errors and repeatability).

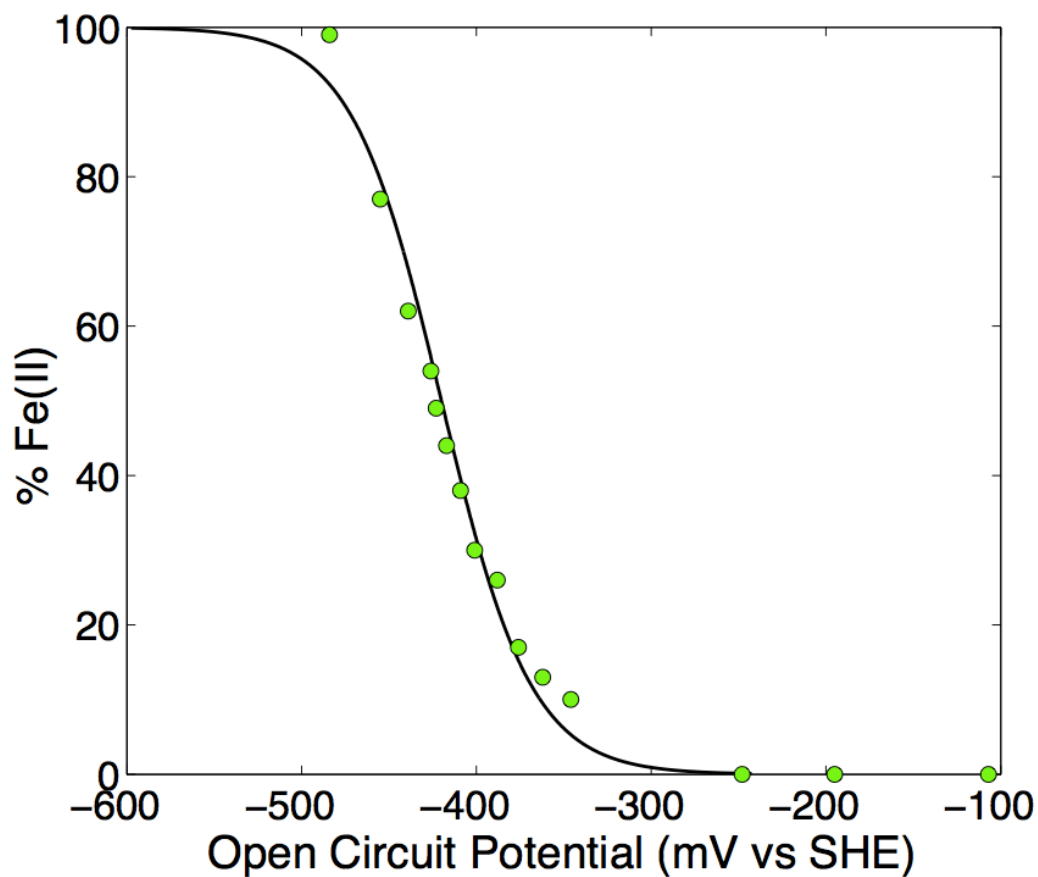


Figure 6.17. Titration curve of WT P450 BM3. The overlaid one-electron Nernst function (black line) has $E^{\circ'} = -420$ mV.

Wild Type CYP119

We also used this titration method to determine the reduction potential of WT CYP119. The only other report of the WT CYP119 reduction potential, to our knowledge, was determined by protein film voltammetry to be $E^{\circ'}(\text{Fe}^{\text{III/II}})$ of -210 mV vs. AgCl/Ag;¹⁷ this corresponds to an anomalously positive value of -10 mV vs. NHE. The same report suggested that CYP119 and myoglobin have the same reduction potential, which is striking as the axial ligation and heme environments of P450 and myoglobin are very different. It is unclear why the CYP119 potential should be 400 mV more positive than other P450s, including P450 BM3.

Potentiometric titration of WT CYP119 with dithionite gives clean conversion from ferric to ferrous, with multiple isosbestic points (Figure 6.18). Open circuit potential measurements are stable and consistent (Figure 6.19).

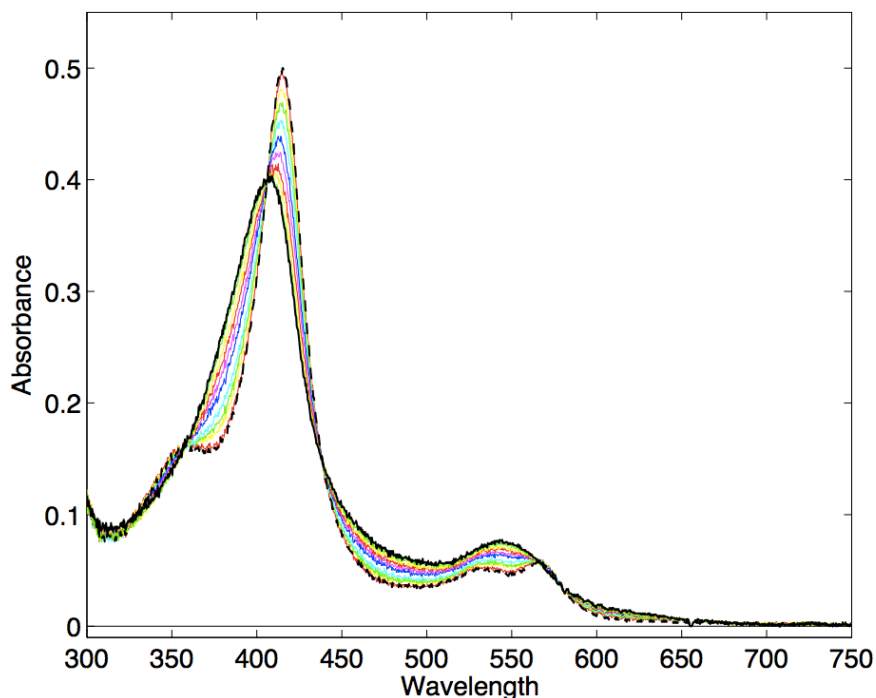


Figure 6.18. Absorbance spectra of WT CYP119 during potentiometric titration with dithionite. Dashed: ferric. Solid black: ferrous.

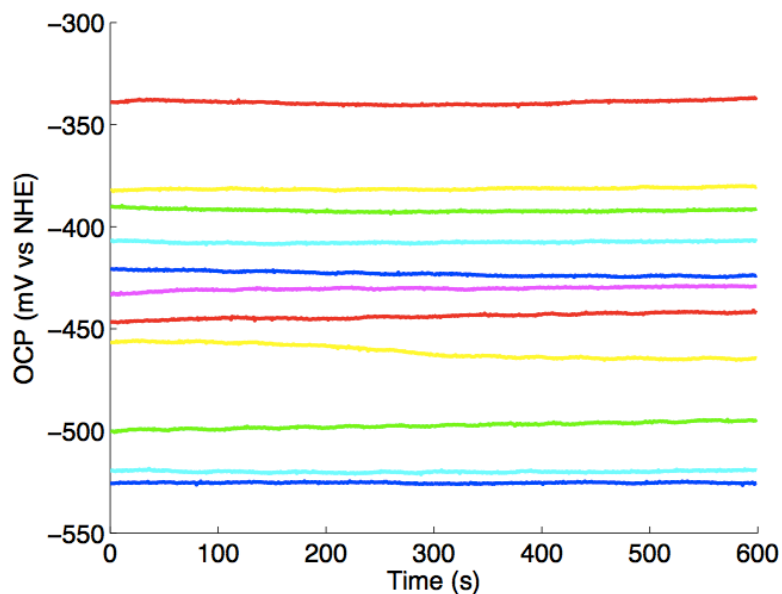


Figure 6.19. Open circuit potential measurements for WT CYP119.

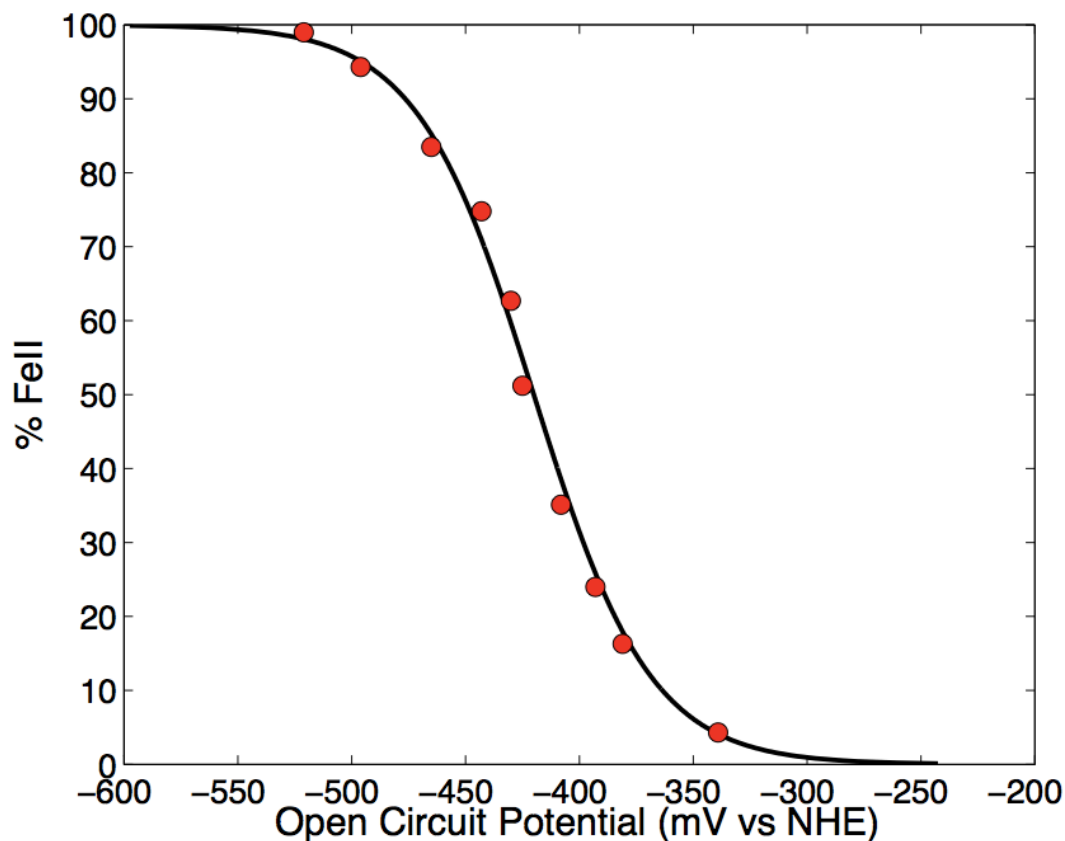


Figure 6.20. Potentiometric titration of WT CYP119 with overlaid Nernst function, $E^\circ = -420$ mV.

The WT CYP119 potential is -420 mV (**Figure 6.20**); this is within error of the value for P450 BM3, and significantly more negative than what was reported by protein film voltammetry.

6.3.2. Potentiometric titration of mutants for *in vivo* cyclopropanation

With a consistent method and reproducible WT BM3 potentials in hand, we set to determine the reduction potentials of P450 BM3 mutants engineered for cyclopropanation. In particular, we were interested in the effect of axial ligation.

C400S axial mutation

The reduction potential of the single mutant C400S was measured by potentiometric titration as described above. Clean isosbestic points are observed in the titration spectra (**Figure 6.21**). The potential for C400S is -290 mV (**Figure 6.22**). This single mutation results in a positive shift of 130 mV compared to WT enzyme, which is sufficient to allow reduction by NAD(P)H.

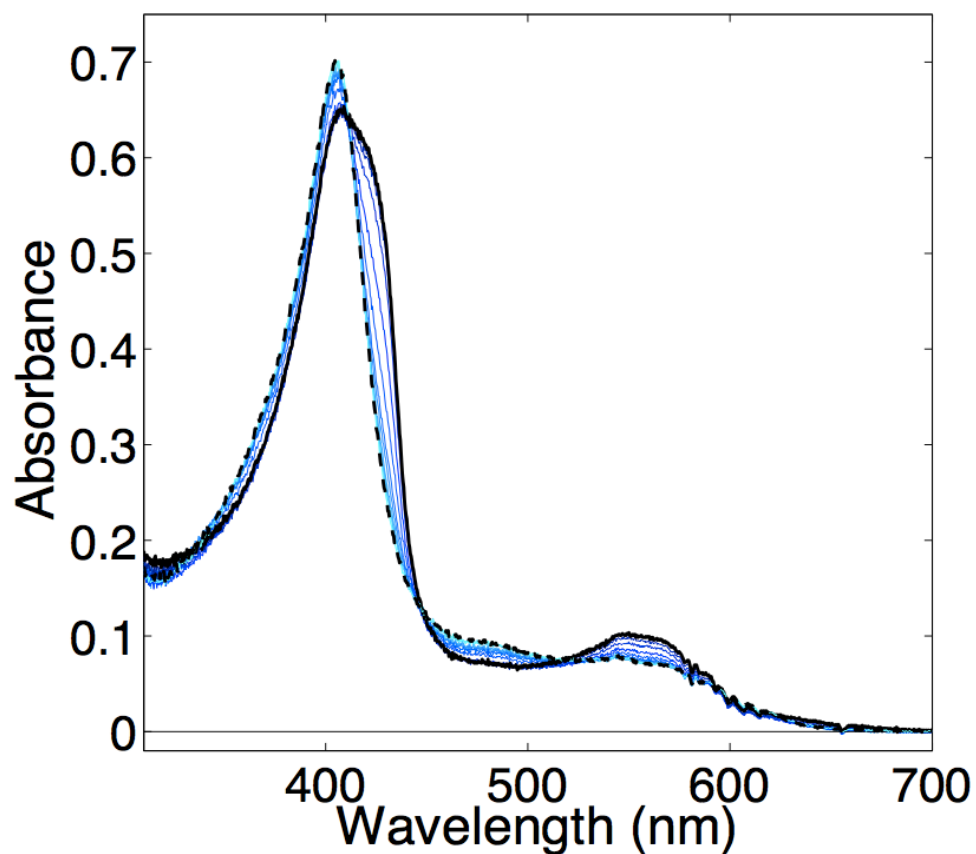


Figure 6.21. Absorption spectra of P450 BM3 C400S. Ferric: dashed; ferrous: solid.

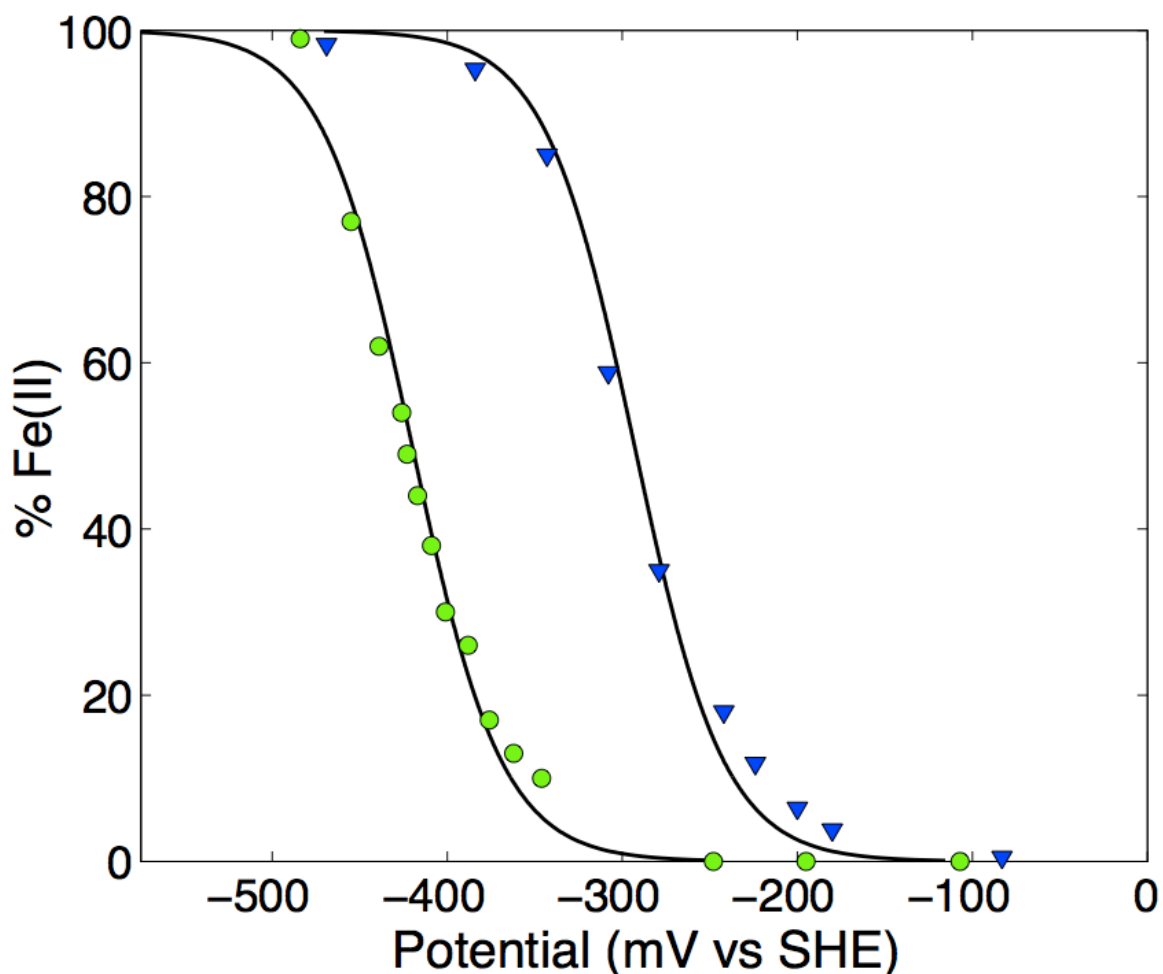


Figure 6.22. Redox titration curves of C400S (blue triangles) and wild-type (green circles), overlaid by the one-electron Nernst function (black line) with $E^{\circ'} = -420$ mV for WT, and -290 mV for C400S.

Engineered cyclopropanation mutants

Reduction potentials were also determined for P450₁₃-Cys and P411₁₃-Ser (**Figure 6.23**). The 13 mutations to the active site and periphery result in a positive shift of 68 mV from that of WT. Of note, these 13 mutations and the C400S mutation are not additive: P411₁₃-Ser is only 148 mV positive of wild type, as opposed to the additive value of 191 mV.

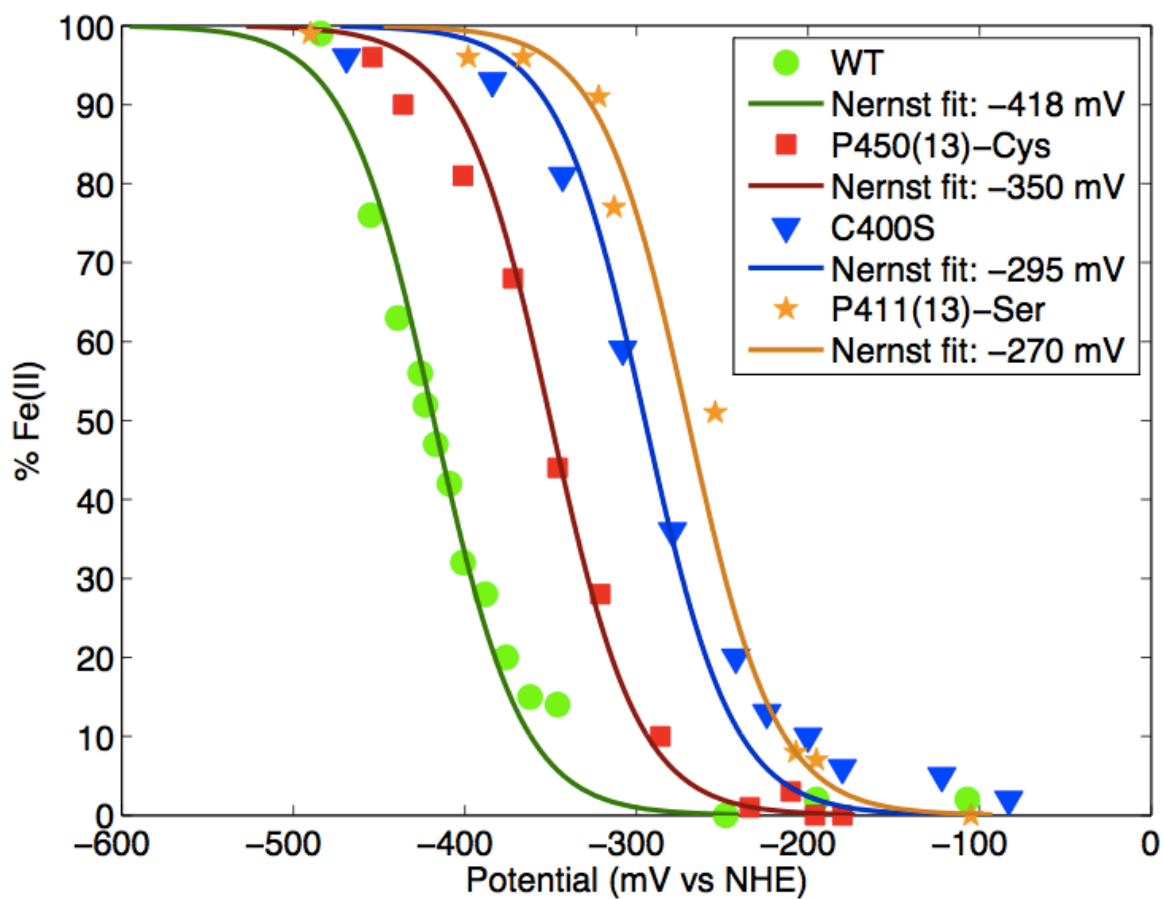


Figure 6.23. Titration curves for four mutants.

6.3.3. Additional axial mutants

The Arnold group also expressed a number of other axial mutants, including: C400M, C400H, C400A, and C400Y.

Titration of C400M yielded a reduction potential of -110 mV (**Figure 6.24**). Somewhat curiously, the titration curve appears to be shallower than the one-electron Nernst function.

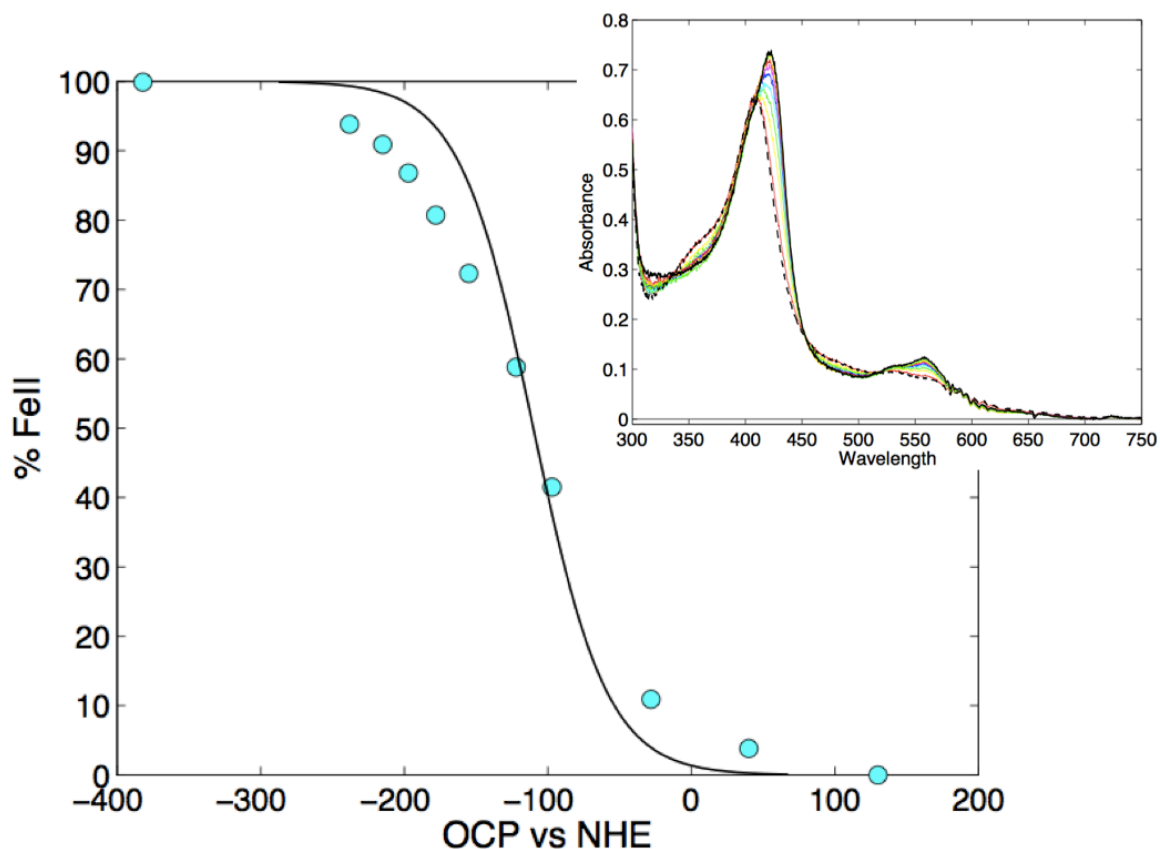


Figure 6.24. Redox titration curve of C400M overlaid by the one-electron Nernst function with $E^{\circ'} = -110$ mV (black line). **Inset:** Titration spectra. Dashed: ferric; solid: ferrous.

We also attempted potentiometric titrations of C400H, C400A, C400D, C400Y. Unfortunately, none of these mutants converts cleanly between ferric and ferrous; isosbestic points are not retained, and reoxidation with ferricyanide does not return the initial spectrum (**Figures 6.25-6.28**). These mutants have not been structurally characterized, and electrochemical measurements may be complicated by the presence of impurities, or heterogeneous populations with mixed ligation.

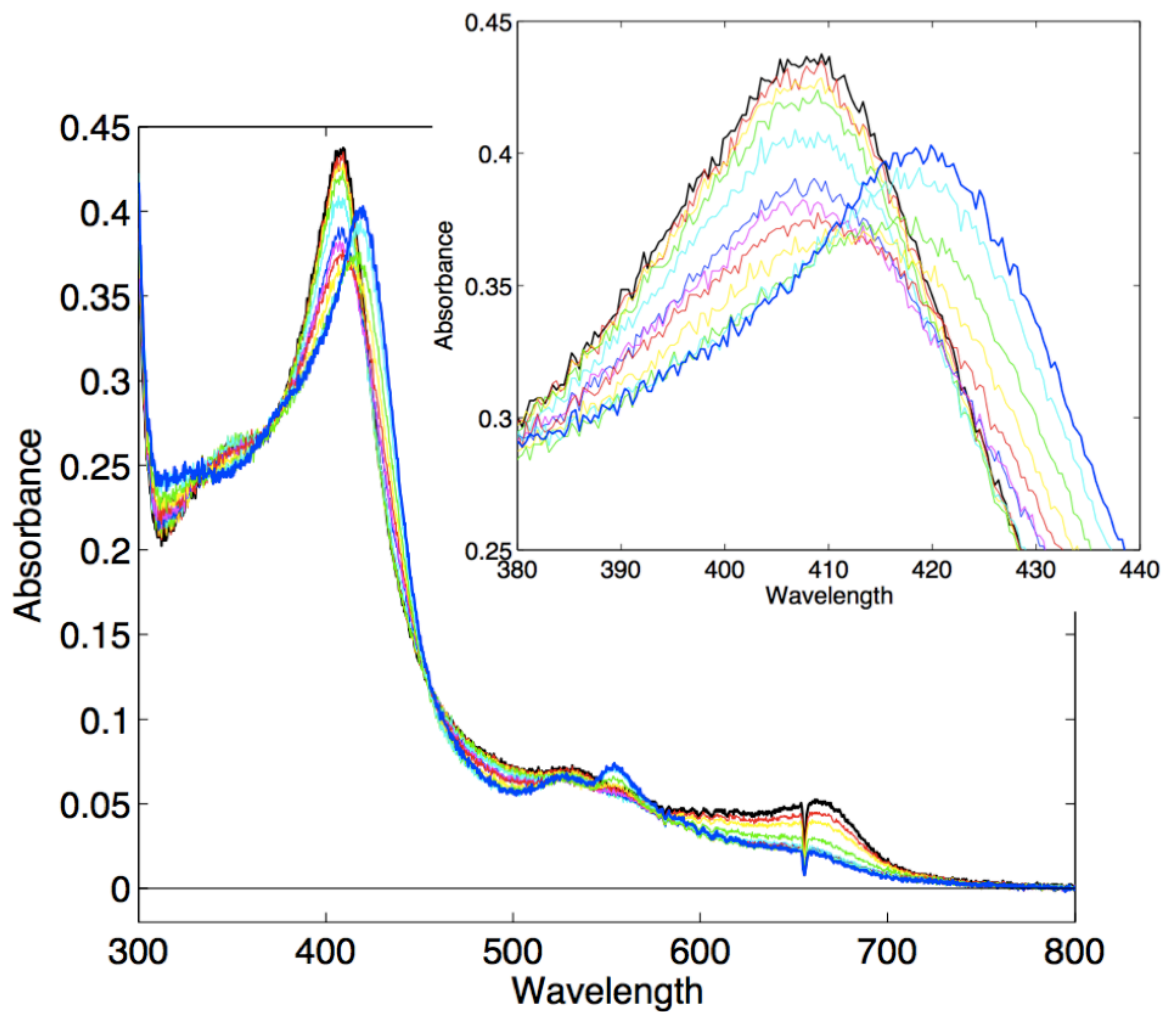


Figure 6.25. Reduction of C400Y shows loss of isosbestic points. Inset: Close-up of Soret region. Ferric: black. Ferrous: dark blue.

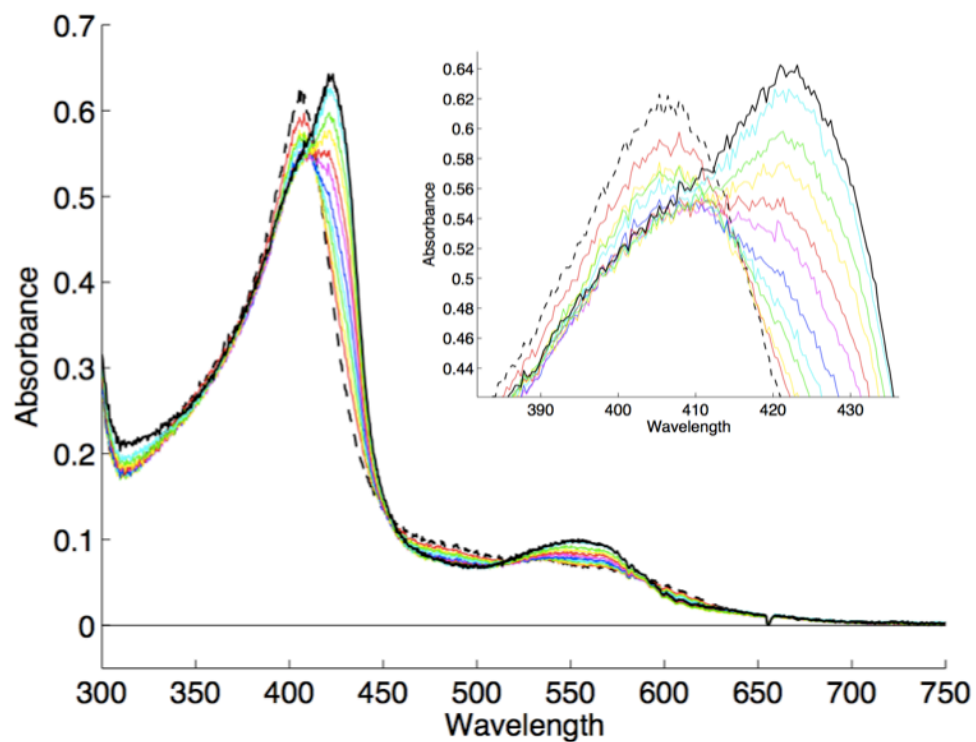


Figure 6.26. Spectra of C400A during potentiometric titration. **Inset:** close-up of Soret region shows non-retention of isosbestic points.

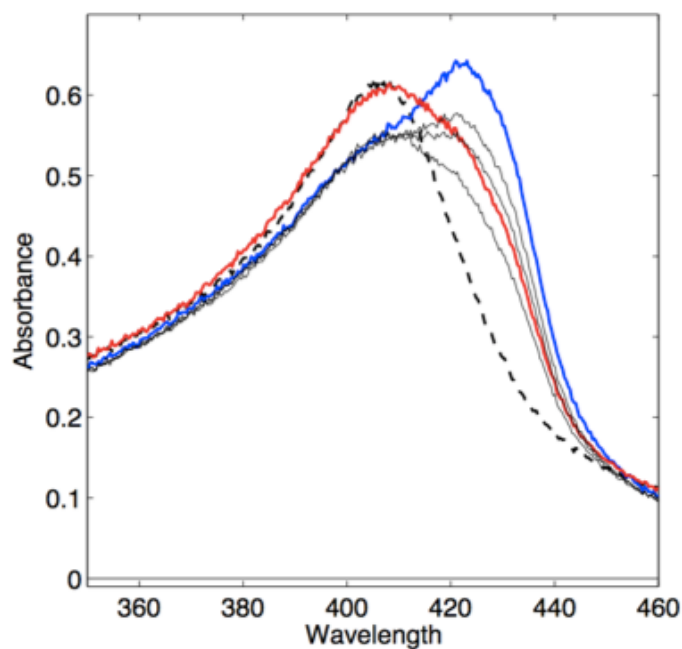


Figure 6.27. Loss of isosbestic points in C400A absorption spectra during titration. Dashed: initial, ferric spectrum. Gray: partial reduction by sodium dithionite. Blue: ferrous spectrum, with excess sodium dithionite. Red: spectrum upon reoxidation with potassium ferricyanide.

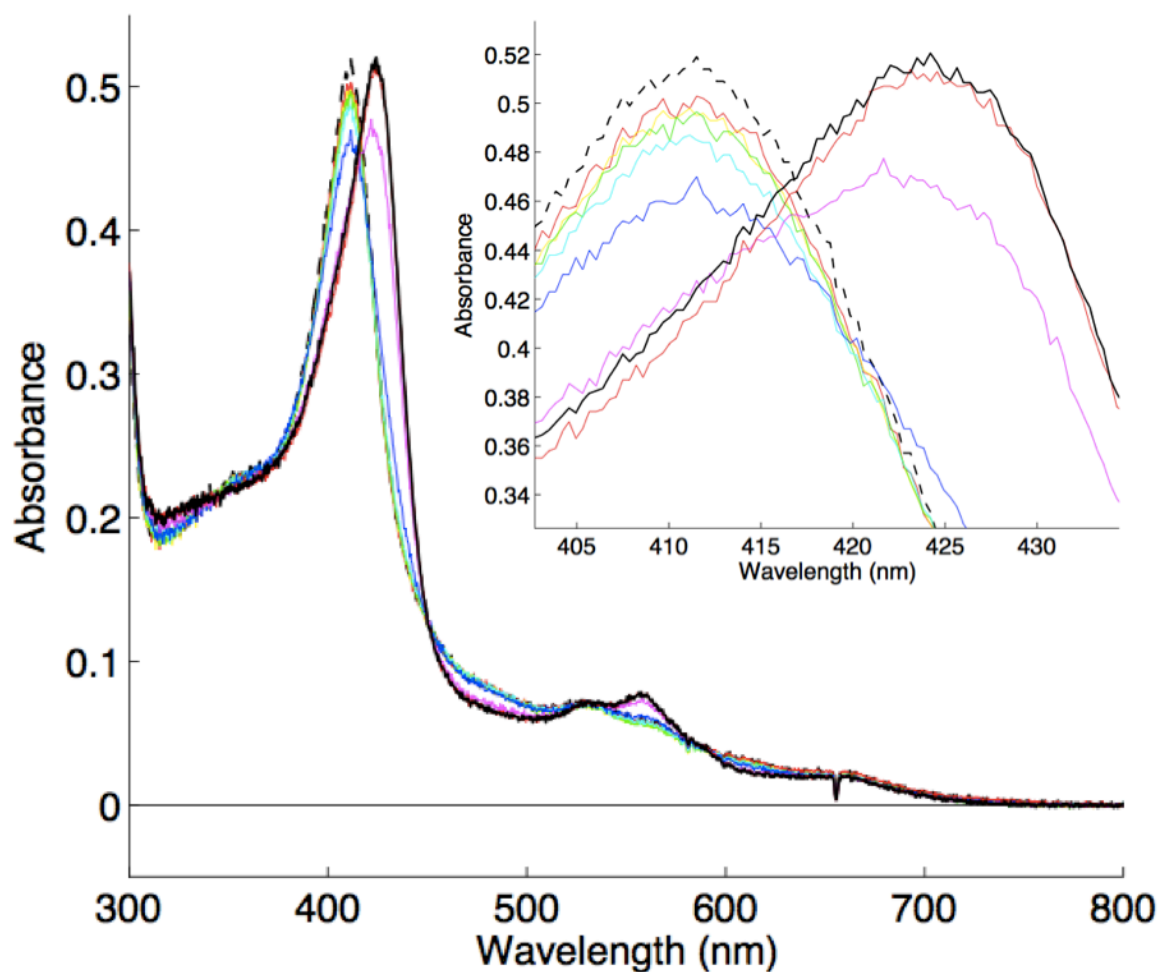


Figure 6.28. Spectra of C400H during potentiometric titration. Inset: close-up of Soret region shows non-retention of isosbestic points.

6.4. Discussion

Using potentiometric redox titration, the reduction potential of wild-type P450 BM3 is -420 mV, in agreement with the more negative reported potential.⁵ The engineered cyclopropanation mutant P450₁₃-Cys has a more positive potential of -360 mV, however this is still too negative to be efficiently reduced by NADH, relayed through the flavin cofactors (**Table 6.1**). The single axial mutation, C400S, raises the WT reduction potential by 130 mV; this shift the same magnitude as the shift conferred by substrate binding to WT BM3. The engineered mutant P411₁₃-

Ser has a similar, positively-shifted reduction potential of -270 mV. Furthermore, this mutant is active in the presence of NADH, and can catalyze cyclopropanation *in vivo*. Whole cell catalysis is capable of generating 27 g/L of cyclopropanes with high enantioselectivity (99% ee_{cis}). *E. coli* cells expressing this mutant can be lyophilized with cryoprotectant and stored for weeks without loss of activity or selectivity.

Table 6.1. Reduction potentials of ferric P450 and redox active cofactors (pH 7)^{5,18,19}

Enzyme/Cofactor	$E^{\circ\prime}$ (mV vs. NHE)
NAD ⁺ /NADH (2e ⁻)	-320 ^a
FAD/FADH ₂ (2e ⁻)	-320 ^b
FAD/FADH•	-264 ^b
FADH•/FADH ₂	-375 ^b
WT BM3 Fe ^{III/II}	-420 to -440 ^{c,d}
WT BM3 Fe ^{III/II} (substrate bound)	-290 ^c
WT CYP119 Fe ^{III/II}	-420 ^d
BM3 C400S	-290 ^d
BM3 P450 ₁₃ -Cys	-360 ^d
BM3 P411 ₁₃ -Ser	-270 ^d
BM3 C400M	-110 ^d

a: ref 18. b: ref 19, c: ref 5, d: this work.

6.5. Conclusions and Future Work

We determined the reduction potentials of wild-type and mutant P450 enzymes using potentiometric redox titrations. Among the enzymes analyzed are a series of P450 BM3 mutants designed for cyclopropanation activity. Mutants containing serine-ligation have a formal reduction potential sufficiently positive to allow reduction by endogenously produced NADH, allowing the development of *in vivo*

cyclopropanation. Other mutations in and around the active site that are beneficial for cyclopropanation also affect reduction potentials more positive, but to a lesser degree; the combined axial and active site mutations are not directly additive. Potentiometric titration is limited to highly pure samples that are stable to reduction by dithionite, and accurate potentials cannot be determined for mutants that do not cleanly convert between ferric and ferrous forms.

6.6. Acknowledgments

This Chapter greatly benefited from the guidance and assistance of a number of people. In particular, I would like to thank Dr. James Blakemore for help with initial setup and electrodes; Professor Jeff Warren for assistance regenerating and maintaining the glovebox, providing reference electrodes, suggestions for chemical titrations, discussions for analysis of titration data; Dr. James McKone for fabrication of mesh electrodes and countless discussions for improving electrochemical technique and for interpreting data; Dr. Wes Sattler for suggestions for MV reduction; and Jay Winkler for discussions regarding data analysis and interpretation of reduction potentials. I also must thank all of the above, with the addition of Megan Jackson and Rocio Mercado, for boosting morale during difficult times.

6.7. Materials and Methods

Chemicals

All chemicals were used as received, without further purification. Buffer salts were obtained from J.T. Baker. Sodium dithionite (86%) was obtained from Fluka. Methyl viologen, benzyl viologen, hydroxynaphthoquinone, and potassium

ferricyanide were obtained from Sigma Aldrich. Solutions were prepared using 18 M Ω cm water unless otherwise noted.

Instrumentation

Electrochemistry was performed using a WaveNow potentiostat (Pine Research Instrumentation). Spectra were recorded using an Ocean Optics spectrometer (USB2000+).

Procedures

A detailed description of experimental protocols can be found in Appendix B. A brief description of the procedures is given below, highlighting any deviations from the general protocol.

Preparation of samples for redox titration

P450 BM3 mutants supplied by the Arnold group at Caltech. Enzyme samples included: wild type, C400S, C400M, C400Y, C400A, C400H, and P450₁₃-Cys, (referred to elsewhere as BM3-CIS: V78A, F87V, P142S, T175I, A184V, S226R, H236Q, E252G, T268A, A290V, L353V, I366V, E442K), P411₁₃-Ser (referred to elsewhere as P411-CIS; the same as P450₁₃-Cys with an additional mutation: C400S).

Enzyme samples were buffer-exchanged into 100 mM KPO₄, 100 mM KCl, pH 7.4, and deoxygenated via 4 x 20 gentle pump-backfill cycles with argon, with care taken to avoid bubbling.

Water was sparged for 2-3 hours, followed by three cycles of freeze-pump-thaw in an ice/salt/water bath (-10 °C). Pre-weighed, dry salts (buffers, mediators) were

pumped into the glovebox, and stock solutions were prepared by addition of deoxygenated water in the anaerobic atmosphere glovebox. To verify buffer pH, a small sample was removed from the glovebox and measured by pH meter. Dithionite solutions were made fresh (within the box) for each titration, and potassium ferricyanide solutions were remade every few days.

Protein samples consisted of approximately 600 μL of 50-100 μM enzyme with the following mediators added to ensure electrochemical communication between the protein and electrode: 4 μM methyl viologen (MV), 8 μM benzyl viologen (BzV), 12 μM 2-hydroxy-1,4-naphthaquinone.

Potentiometric redox titration

Enzyme samples were titrated by addition of ~ 2 μL aliquots of 1-4 mM sodium dithionite stock. The open circuit potential (OCP) of the cell was monitored over a 10-min equilibration period; if the drift was more than 15 mV/ 10 min, the OCP was monitored for an additional 5-10 minutes (or until stable). The final OCP value was used to construct the titration curve. Absorption spectra were recorded at the beginning and end of each OCP measurement to assess enzyme stability; the latter spectrum was used to construct the titration curve. Each spectrum was vertically adjusted to achieve zero baseline in the 750-800 nm region ($\Delta A_{\text{adjust}} < 0.015$ OD). Percent Fe(II) was achieved by using a Matlab script (see Appendix D). The midpoint potential was determined by least-squares fitting to a single one one-electron Nernst curve.

6.8. References

- (1) Munro, A. W.; Daff, S.; Coggins, J. R.; Lindsay, J. G.; Chapman, S. K. Probing Electron Transfer in Flavocytochrome P-450 BM3 and Its Component Domains. *Eur. J. Biochem.* **1996**, *239*, 403–409.
- (2) Miles, J. S.; Munro, A. W.; Rospendowski, B. N.; Smith, W. E.; McKnight, J.; Thomson, A. J. Domains of the Catalytically Self-Sufficient Cytochrome-P-450 BM-3 - Genetic Construction, Overexpression, Purification and Spectroscopic Characterization. *Biochem. J.* **1992**, *288*, 503–509.
- (3) Coelho, P. S.; Brustad, E. M.; Kannan, A.; Arnold, F. H. Olefin Cyclopropanation via Carbene Transfer Catalyzed by Engineered Cytochrome P450 Enzymes. *Science* **2013**, *339*, 307–310.
- (4) Sanders, J. K. M.; Bampos, N.; Clyde-Watson, Z.; Darling, S. L.; Hawley, J. C.; Kim, H.-J.; Mak, C. C.; Webb, S. J. Axial Coordination Chemistry of Metalloporphyrins. In *Inorganic, Organometallic and Coordination Chemistry; The Porphyrin Handbook*; Academic Press: San Diego, CA, 2000; Vol. 3, pp. 1–48.
- (5) Ost, T. W. B.; Miles, C. S.; Munro, A. W.; Murdoch, J.; Reid, G. A.; Chapman, S. K. Phenylalanine 393 Exerts Thermodynamic Control over the Heme of Flavocytochrome P450 BM3. *Biochemistry* **2001**, *40*, 13421–13429.
- (6) Raphael, A. L.; Gray, H. B. Semisynthesis of Axial-Ligand (position-80) Mutants of Cytochrome-C. *J. Am. Chem. Soc.* **1991**, *113*, 1038–1040.
- (7) Dawson, J. H. Probing Structure-Function Relations in Heme-Containing Oxygenases and Peroxidases. *Science* **1988**, *240*, 433–439.
- (8) Vatsis, K. P.; Peng, H. M.; Coon, M. J. Replacement of Active-Site Cysteine-436 by Serine Converts Cytochrome P450_{2B4} into an NADPH Oxidase with Negligible Monooxygenase Activity. *J. Inorg. Biochem.* **2002**, *91*, 542–553.
- (9) Coelho, P. S.; Wang, Z. J.; Ener, M. E.; Baril, S. A.; Kannan, A.; Arnold, F. H.; Brustad, E. M. A Serine-Substituted P450 Catalyzes Highly Efficient Carbene Transfer to Olefins in Vivo. *Nat. Chem. Biol.* **2013**, *9*, 485–487.
- (10) Daff, S. N.; Chapman, S. K.; Turner, K. L.; Holt, R. A.; Govindaraj, S.; Poulos, T. L.; Munro, A. W. Redox Control of the Catalytic Cycle of Flavocytochrome P450 BM3. *Biochemistry* **1997**, *36*, 13816–13823.
- (11) Fleming, B. D.; Tian, Y.; Bell, S. G.; Wong, L.-L.; Urlacher, V.; Hill, H. A. O. Redox Properties of Cytochrome P450_{BM3} Measured by Direct Methods. *Eur. J. Biochem.* **2003**, *270*, 4082–4088.
- (12) Udit, A. K.; Hill, M. G.; Gray, H. B. Electrochemistry of Cytochrom eP450 BM3 in Sodium Dodecyl Sulfate Films. *Langmuir* **2006**, *22*, 10854–10857.
- (13) Michaelis, L.; Hill, E. S. The Viologen Indicators. *J. Gen Physiol.* **1933**, *16*, 859–873.

- (14) Wardman, P. Reduction Potentials of One-Electron Couples Involving Free-Radicals in Aqueous-Solution. *J. Phys. Chem. Ref. Data* **1989**, *18*, 1637–1755.
- (15) Peon, J.; Tan, X.; Hoerner, J. D.; Xia, C.; Luk, Y. F.; Kohler, B. Excited State Dynamics of Methyl Viologen. Ultrafast Photoreduction in Methanol and Fluorescence in Acetonitrile. *J. Phys. Chem. A* **2001**, *105*, 5768–5777.
- (16) Chitose, N.; LaVerne, J. A.; Katsumura, Y. Effect of Formate Concentration on Radical Formation in the Radiolysis of Aqueous Methyl Viologen Solutions. *J. Phys. Chem. A* **1998**, *102*, 2087–2090.
- (17) Immoos, C. E.; Chou, J.; Bayachou, M.; Blair, E.; Greaves, J.; Farmer, P. J. Electrocatalytic Reductions of Nitrite, Nitric Oxide, and Nitrous Oxide by Thermophilic Cytochrome P450 CYP119 in Film-Modified Electrodes and an Analytical Comparison of Its Catalytic Activities with Myoglobin. *J. Am. Chem. Soc.* **2004**, *126*, 4934–4942.
- (18) Harris, D. C. *Quantitative Chemical Analysis*; 6th Edition.; W. H. Freeman and Company: New York, 2003.
- (19) Dunford, A. J.; Girvan, H. M.; Scrutton, N. S.; Munro, A. W. Probing the Molecular Determinants of Coenzyme Selectivity in the P450 BM3 FAD/NADPH Domain. *Biochim. Biophys. Acta* **2009**, *1794*, 1181–1189.

Appendix A

**PHOTOCHEMICAL OXIDATION OF
NITRIC OXIDE SYNTHASE**

A.1. Introduction to Nitric Oxide Synthases

Nitric oxide (NO) is a biological regulator and signaling molecule, and is involved in immune response of eukaryotes.^{1,2} Biological NO production is catalyzed by Nitric Oxide Synthase (NOS), a heme monooxygenase that shares the thiolate-ligation motif with chloroperoxidase and cytochrome P450. Three isoforms of NOS exist in mammals, including endothelial, inducible, and neuronal NOS. All three isoforms exist as homodimers, and are composed of two domains (**Figure A.1**).³ The oxygenase domain contains the thiolate-ligated heme and the redox cofactor tetrahydrobiopterin (THB or H₄B). The calmodulin-linked reductase domain contains the flavin cofactors flavin adenine dinucleotide (FAD) and flavin mononucleotide (FMN); this domain is responsible for delivering electrons to the heme.

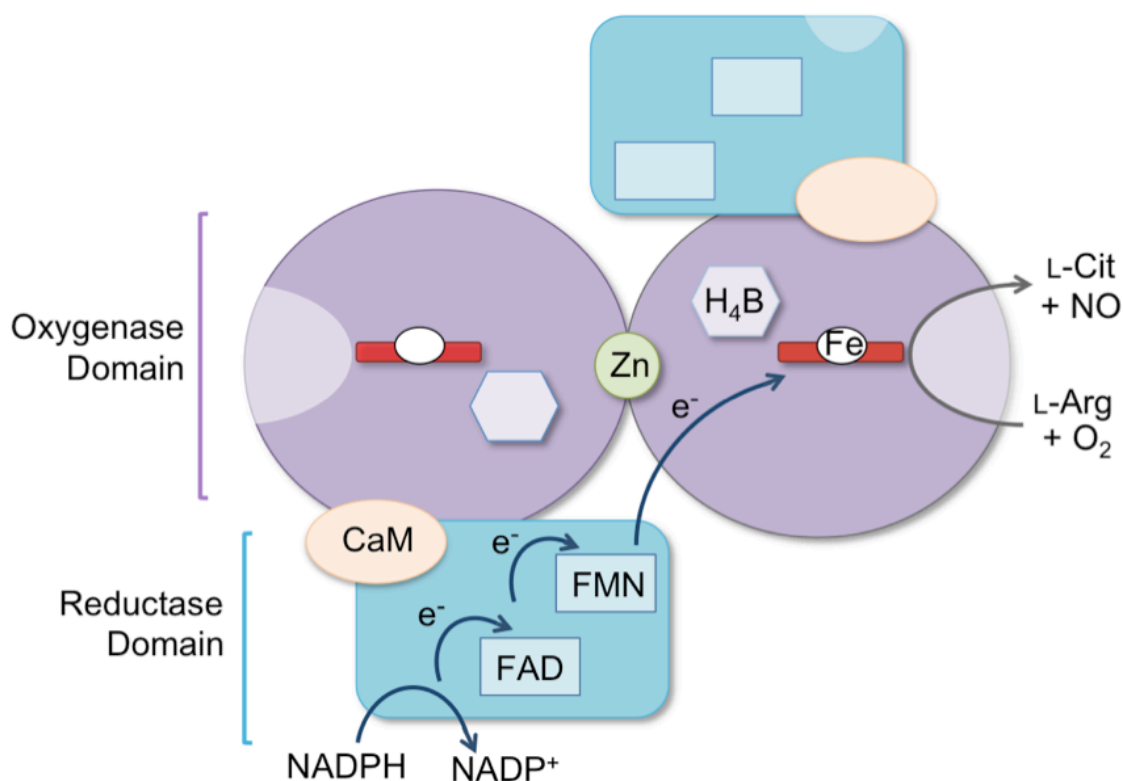


Figure A.1. Cartoon of the NOS homodimeric structure, highlighting pathways for electron flow (reproduced from ref. 10, Thesis by G. E. Keller).

Recently, NOS-like enzymes have also been found in bacteria (**Figure A.2**).^{4,5} These enzymes have strong structural and sequence similarities to their mammalian counterparts, though many are composed solely of the oxygenase domain (and lack the reductase domain).⁶ Bacterial NOS enzymes have been shown to produce NO *in vitro* and *in vivo*,⁶ and can be used as more stable homologues in which to study aspects of NOS catalysis.

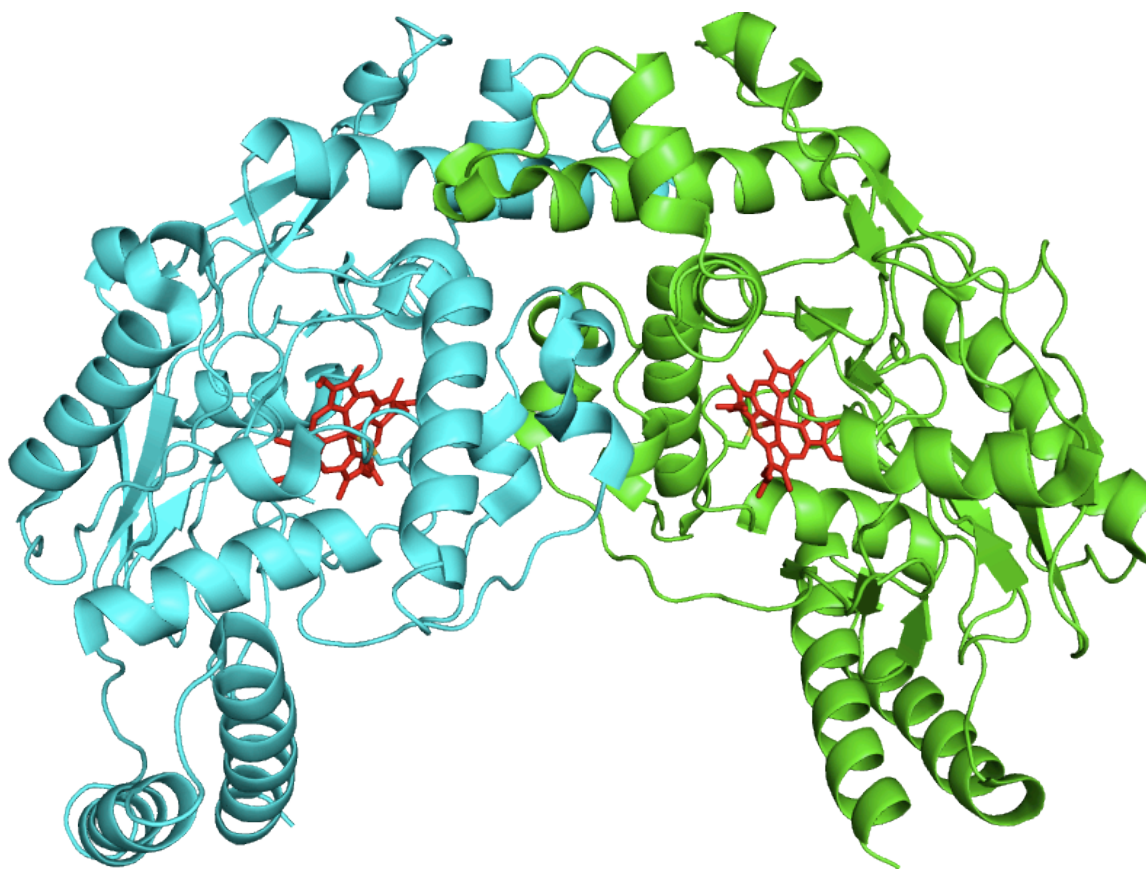


Figure A.2. Dimeric structure of NOS from *Geobacillus stearothermophilus*. PDB: 2FLQ.

NOS catalyzes the production of NO in two turnovers from L-arginine, releasing L-citrulline as a biproduct (**Figure A.3**). Many aspects of the catalytic cycle have yet to be determined for NOS, including the identity of the catalytically active species. However, the first turnover is believed to be similar to P450 catalysis, involving

production of a ferryl-ligand radical cation species known as compound I (CI) (Figure A.4, blue arrows).

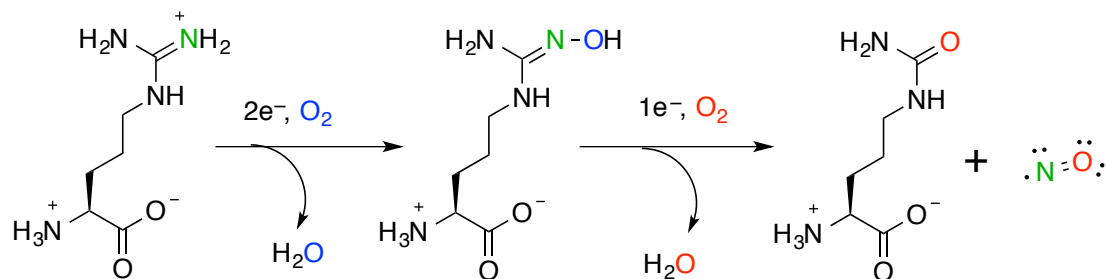


Figure A.3. NOS-catalyzed production of nitric oxide from L-arginine.

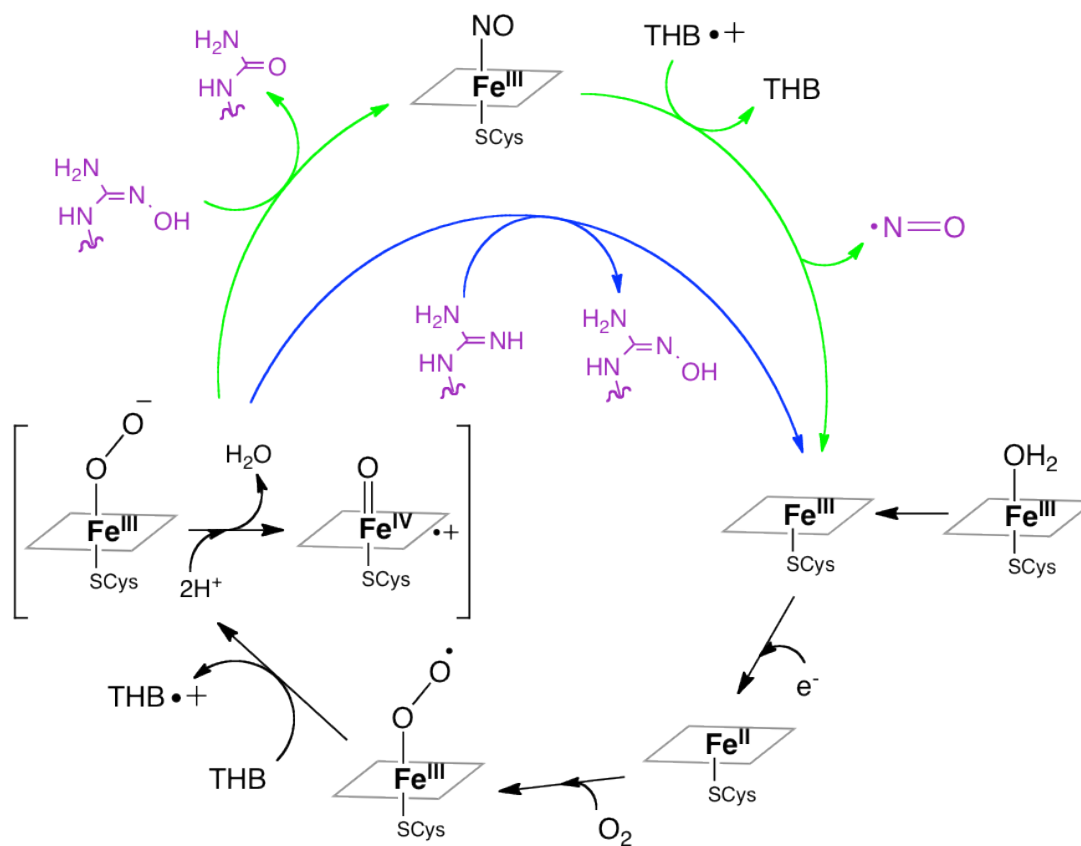


Figure A.4. Proposed catalytic cycle for NOS. Blue arrows indicate the first turnover, green arrows indicate the second turnover. Possible catalytically active species are in brackets.

In both turnovers, two reductive electron transfers (ET) steps activate molecular oxygen (Figure A.4, black arrows). In contrast to cytochrome P450, in which both

electrons are relayed to the heme via flavin cofactors from a reductase domain, the second electron in NOS catalysis is delivered from the bound THB cofactor. The active species (proposed to be CI) hydroxylates the guanidinyll nitrogen of L-arginine, producing N-hydroxy-L-arginine as a stable, bound intermediate, and regenerating the resting (ferric) form of the enzyme. The second turnover, which produce NO, is an odd-electron process that is unique in biology.⁷ Again, an equivalent of molecular oxygen is activated, to form either a CI or ferric-peroxo active species (**Figure A.4**, in brackets). N-hydroxy-L-arginine is oxidized to produce L-citrulline and release nitric oxide. Full NO production requires THB; in the absence of this cofactor, nitrite and cyano-ornithine are produced rather than nitric oxide and citrulline.⁸

As described in Chapters 2-5, we developed photosensitizer-P450 conjugates that replace native ET partners with ruthenium diimine complexes that are bound to the P450 surface at a non-native cysteine. Laser-triggered flash-quench methods (**Figure A.5**, described in Chapter 1) allowed rapid oxidation or reduction of the P450 heme, on the microsecond timescale.

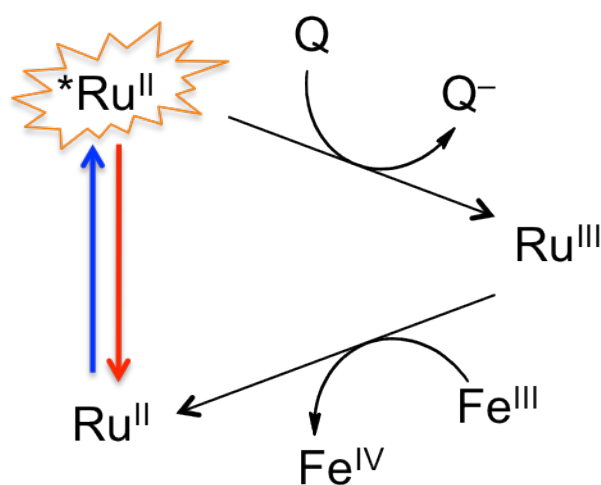


Figure A.5. Flash-quench cycle for oxidizing the heme active site (Fe).

Inspired by the proposed similarities, and intriguing differences, between NOS and P450 catalytic cycles, we set out to determine whether similar flash-quench of Ru-NOS conjugates could be used to probe NOS catalysis. In particular, we were interested in investigating the thermophilic bacterial NOS from *Geobacillus stearothermophilus* (gsNOS), which has been examined by other members of the Gray group.^{9,10} This Appendix describes the development and photophysical characterization of Ru-NOS conjugates, and analysis of photochemical NOS oxidation using time-resolved transient absorption (TA) studies.

A.2. Results

A.2.1. Ru-photosensitizer conjugation

Selection of NOS mutant and Ru photosensitizer

Analogous to the Ru-P450 systems, cysteine-specific labeling was chosen to covalently tether the ruthenium photosensitizer. A mutant enzyme containing a single surface-exposed cysteine was designed by Dr. Charlotte Whited (**Figure A.6**). Two native, surface-exposed cysteines have been removed by mutagenesis: C227S/C269S, and a single cysteine installed: K115C. The exposed cysteine (K115C) is distant from the dimer interface, and it was anticipated that Ru-labeling at this site would not perturb dimer formation.

We have labeled K115C gs NOS with the photosensitizer $[\text{Ru}(2,2'\text{-bipyridine})_2(5\text{-iodoacetamido-1,10-phenanthroline})]^{2+}$ (abbreviated $[\text{Ru}(\text{bpy})_2(\text{IAphen})]^{2+}$), in analogy to studies with cytochrome P450. Ru-NOS conjugation is achieved in high yield within 4 hours at 4 °C.

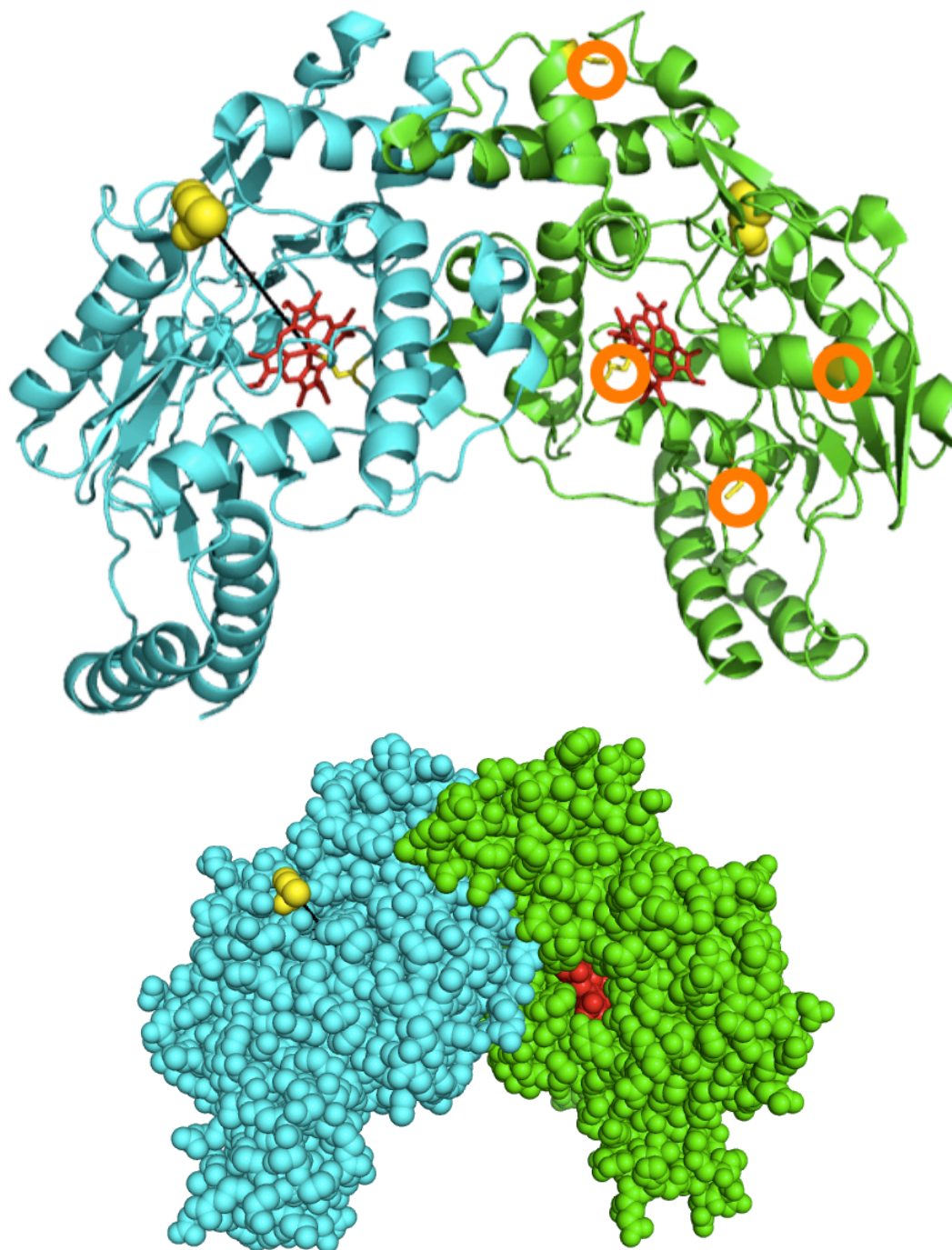


Figure A.6. Location of the photosensitizer tethering site. The NOS heme is colored red, K115C is highlighted in yellow. **Top:** Four native cysteines (including the one that ligates the heme) are circled in orange. **Bottom:** Space filling model, showing surface exposure of K115C, away from the dimer interface.

Characterization of Ru-NOS

The Ru-NOS conjugate has been characterized by mass spectrometry and UV-visible absorption (**Figure A.7**). The mass of Ru-NOS (MW = 44,516 Da) corresponds to that of apo (heme-free) K115C NOS (MW = 43866) plus the mass of the photosensitizer minus the mass of iodide (MW = 652 Da). In addition to typical NOS Soret and Q-bands, the absorption spectrum of Ru-NOS clearly shows a shoulder at 450 nm, which is attributed to photosensitizer absorbance. The crystal structure of this conjugate, Ru_{C115}-NOS, has been obtained by the Crane laboratory in collaboration with Dr. Gretchen Keller (**Figure A.8**).¹⁰

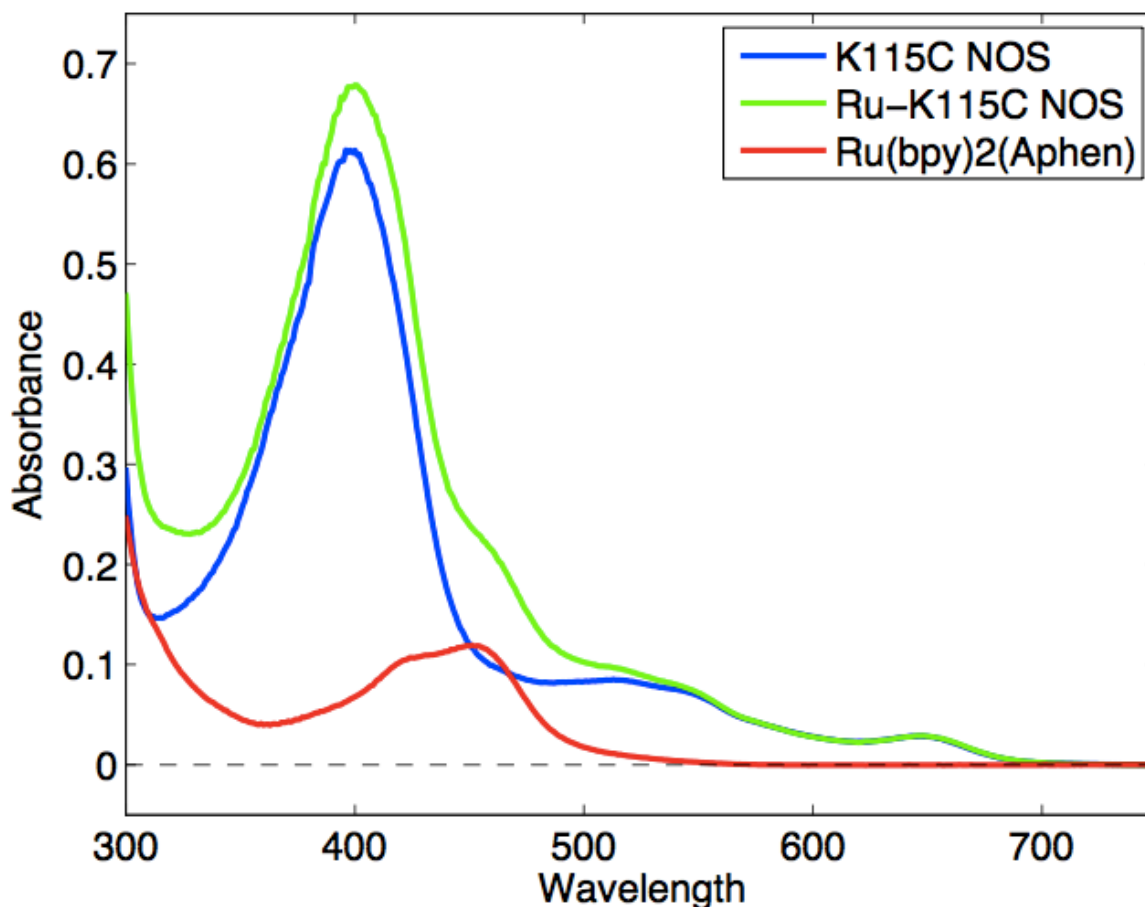


Figure A.7. UV-visible absorption of unlabeled and labeled Ru-NOS and free photosensitizer.

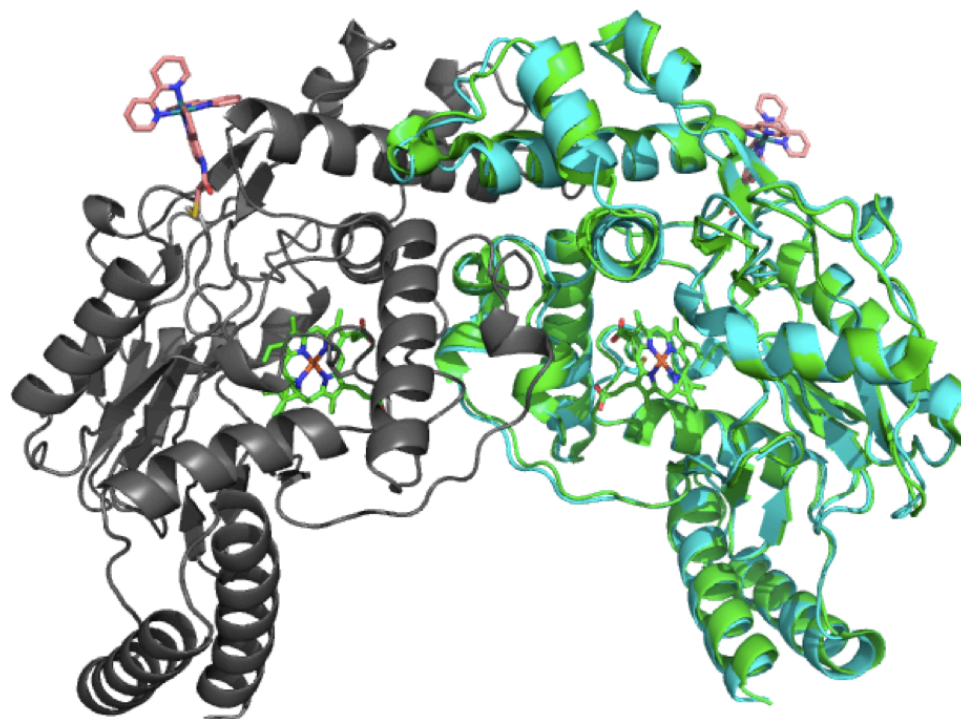


Figure A.8. Structure of Ru-NOS. The Ru-NOS dimer is shown in gray and cyan; the latter monomer is overlaid with wild-type NOS (green, PDB 2FLQ). The tethered Ru complex is colored pink. Figure reproduced from ref 10, G. E. Keller.

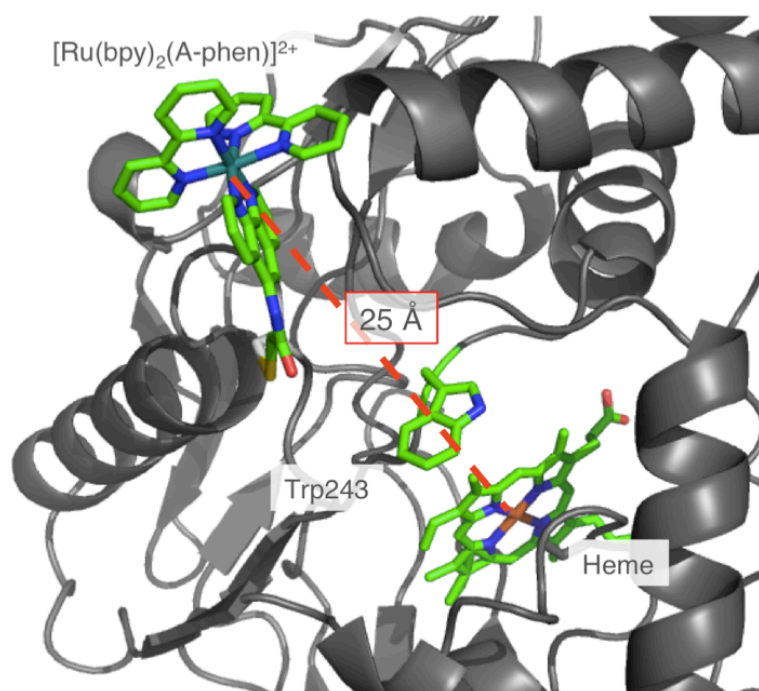


Figure A.9. Tryptophan 243 is located between the photosensitizer and heme in Ru-NOS. The Ru-Fe distance is 25 Å. Figure reproduced from ref 10, G.E. Keller.

A.2.2. Ru-NOS Luminescence

All time-resolved experiments are performed using deoxygenated samples (see sample preparation in Materials and Methods).

As described in Chapters 2, the free $[\text{Ru}(\text{bpy})_2(\text{Aphen})]^{2+}$ photosensitizer is emissive ($\lambda_{\text{max}}=620$ nm) when excited with blue light (e.g., 480 nm). The time-resolved luminescence decay of this complex in deoxygenated water can be fit to a monoexponential decay with a lifetime of 720 ns. In contrast, the time-resolved luminescence decay of Ru-NOS is clearly biexponential (**Figure A.10**). In deoxygenated buffer (50 mM sodium borate, pH 8), the major decay component (~75%) has a decay constant $\tau_A = 150$ ns, while the minor component (~25%) is significantly longer, with $\tau_B = 1100$ ns. Bi-exponential luminescence decay also was observed for Ru-P450 conjugates (see Chapters 2 and 3), and was attributed to multiple conformations of the photosensitizer that do not exchange on the timescale of luminescence decay.

Given the dimeric nature of NOS in solution,⁹ we were interested to investigate whether this biexponential luminescence was related to a monomer-dimer equilibrium. The ratio of major and minor decay components is invariant over a Ru-NOS concentration range of 1-20 μM (**Table A.1**). This ratio and concentration-independence is identical at high ionic strength (500 mM sodium chloride) (**Table A.2**). Interestingly, the luminescence decay rate of the major component is affected by ionic strength, while the minor component is not (**Figure A.11**).

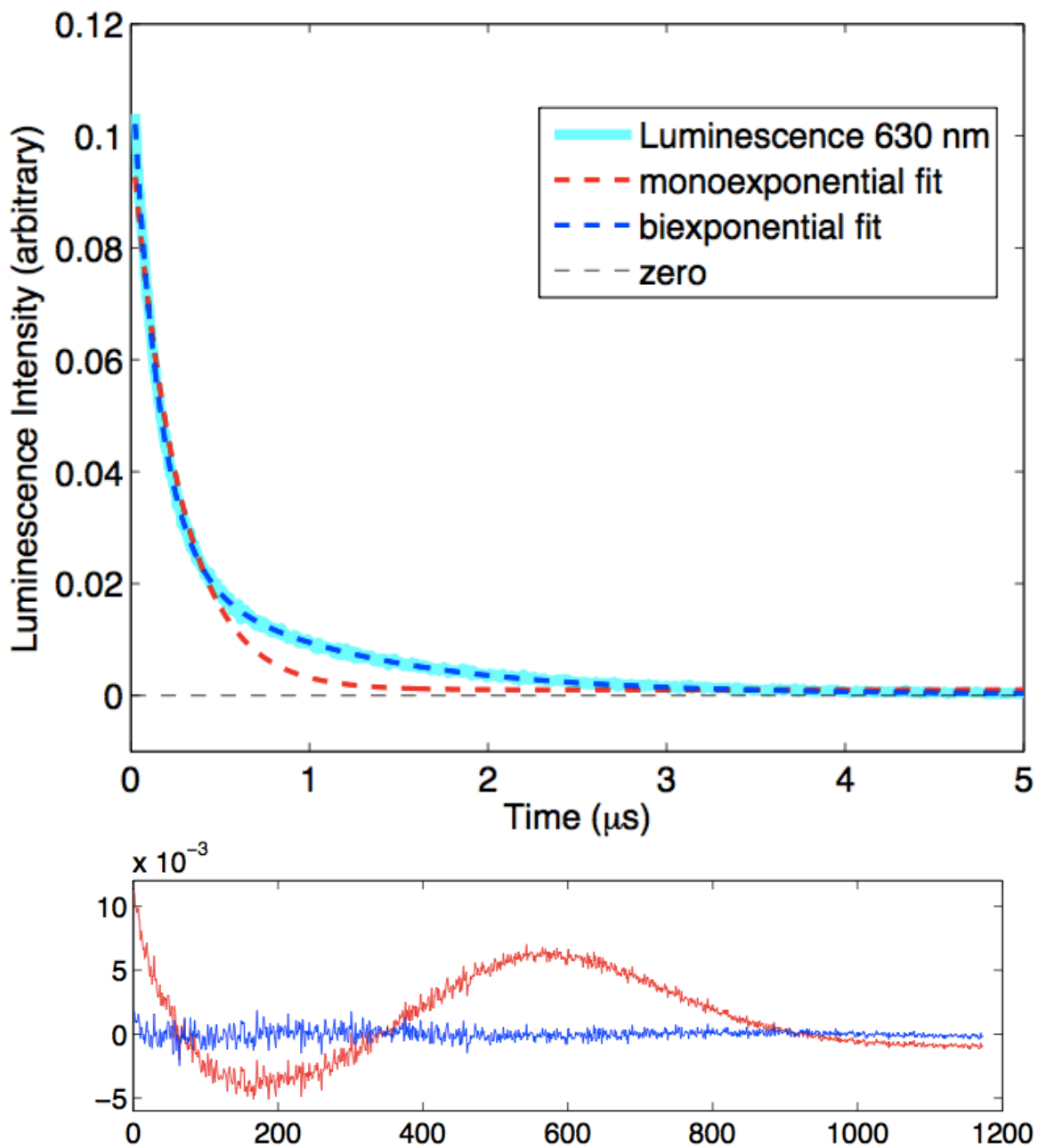


Figure A.10. Top: Luminescence decay of Ru-K115C NOS, fit to a single (red) and double (blue) exponential function. **Bottom:** Residuals from mono- (red) and bi- (blue) exponential fits.

Table A.1. Luminescence lifetimes of Ru-NOS in 50 mM borate buffer, pH 8. A and B are the major and minor components of biexponential decay, respectively.

Conc (μ M)	A: τ (ns) / %	B: τ (ns) / %
1	155 / 77%	1098 / 23%
3	149 / 76%	1042 / 24%
6	154 / 76%	1136 / 24%
9	154 / 76%	1120 / 24%
14	156 / 76%	1151 / 24%
20	155 / 76%	1148 / 24%

Table A.2. Luminescence lifetimes of Ru-NOS in 500 mM sodium chloride, 50 mM borate buffer, pH 8. A and B are the major and minor components of biexponential decay, respectively.

Conc (μ M)	A: τ (ns) / %	B: τ (ns) / %
1	106 / 76%	968 / 24%
3	107 / 75%	962 / 25%
6	107 / 76%	957 / 24%
9	107 / 75%	951 / 25%
13	108 / 76%	965 / 24%
20	111 / 75%	1014 / 25%

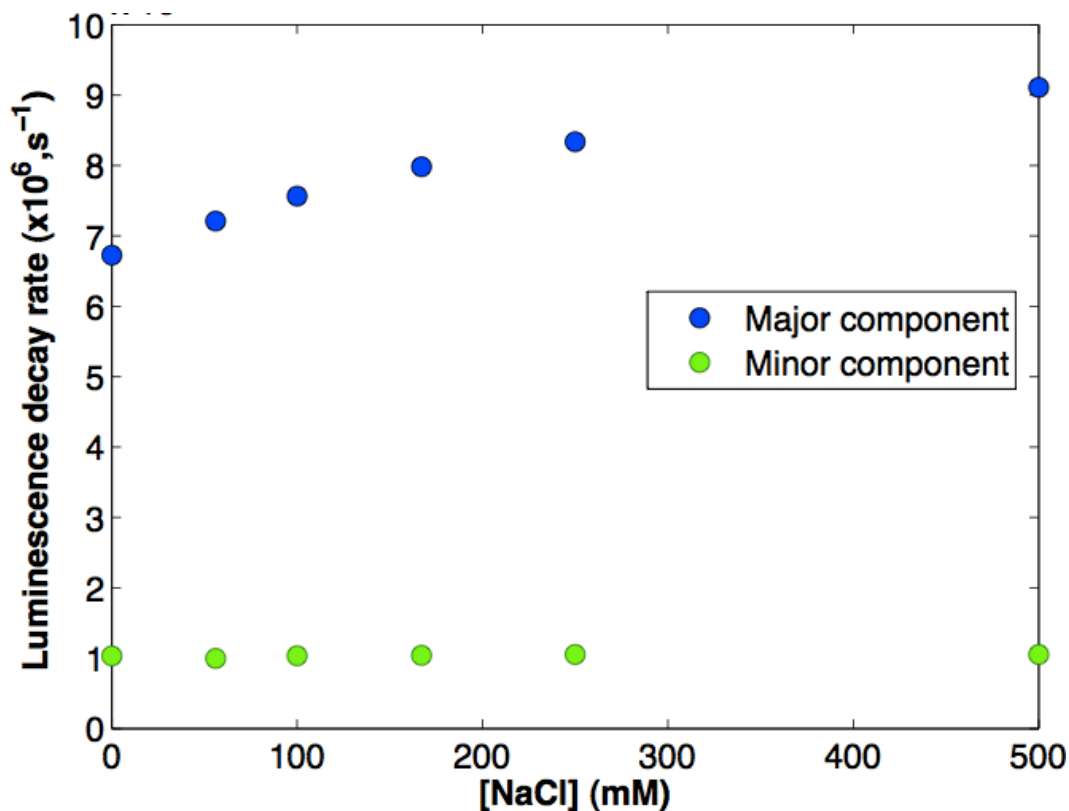


Figure A.11. Luminescence lifetimes of Ru-NOS at varying ionic strengths. Major (blue) and minor (green) decay components are plotted with respect to concentration of sodium chloride.

Luminescence quenching with $[Ru^{III}(NH_3)_6]^{3+}$

We also examined ET quenching of the Ru-NOS excited state by $[Ru^{III}(NH_3)_6]^{3+}$. As observed for P450, addition of $[Ru^{III}(NH_3)_6]^{3+}$ causes protein precipitation in buffers of low ionic strength; this occurs for both Ru-labeled and unlabeled NOS samples. Little or no precipitation is observed for protein samples in buffers of high ionic strength (~ 200 mM sodium chloride). All quenching experiments are performed in buffers with 250 mM sodium chloride, in addition to 50 mM sodium borate, pH 8.

Interestingly, the major component is significantly more affected by $[Ru^{III}(NH_3)_6]^{3+}$ concentration than the minor component (**Figure A.12**).

Additionally, the ratio of major-to-minor decay components increases at high quencher concentration (**Figure A.13**).

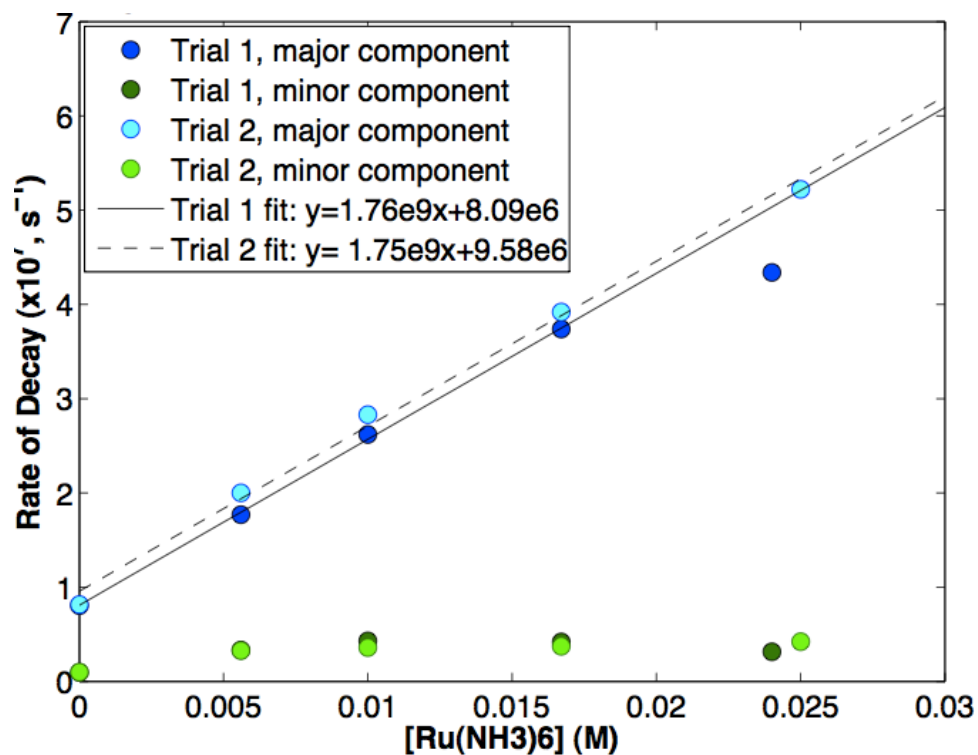


Figure A.12. ET quenching of Ru-NOS with [Ru^{III}(NH₃)₆]³⁺.

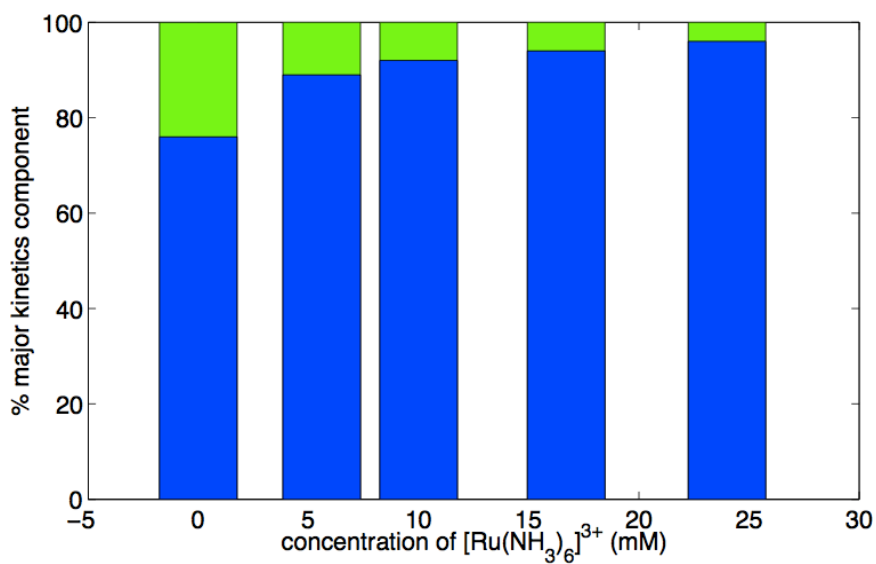


Figure A.13. Relative amplitudes of the major (blue) and minor (green) luminescence decay components for Ru-NOS.

A.2.3. Transient Absorption

As described for Ru-P450, both the Ru photosensitizer and NOS heme have strong electronic absorbance in the 390-440 nm region: NOS Soret $\epsilon(\lambda_{\text{max}}: 400 \text{ nm}) = 79,000 \text{ M}^{-1}\text{cm}^{-1}$;⁹ $[\text{Ru}(\text{bpy})_2(\text{Aphen})]^{2+}$ $\epsilon(\lambda_{\text{max}}: 450 \text{ nm}) = 16,600 \text{ M}^{-1}\text{cm}^{-1}$.¹¹ The shapes and positions of these electronic transitions are sensitive to metal oxidation state and environment; each species has a distinct absorption profile. By monitoring transient absorption (TA) at multiple wavelengths (390-440 nm) over time, we can identify the formation and decay of ET intermediates following laser excitation.

TA data for flash-quench of Ru-NOS is shown in **Figure A.14**. As described in Chapters 2, 3 and 5, the initial transient absorption feature (10 ns) is a bleach ($\Delta\text{OD} < 0$) at all wavelengths examined, with maximum ΔOD at 440 nm. Based on control studies of free photosensitizer, this feature is attributed to the photosensitizer excited state ($^*\text{Ru}^{\text{II}}\text{-NOS}$). This feature decays by ET quenching to form the oxidized, $\text{Ru}^{\text{III}}\text{-NOS}$ species ($\sim 100 \text{ ns}$) that is characterized by a similar, bleached absorption profile. TA at 440 nm recovers to baseline within 20 μs . However, TA at 400 nm (λ_{max} of the NOS Soret) remains bleached up to two orders of magnitude longer (2 ms). This is indicative of heme oxidation.

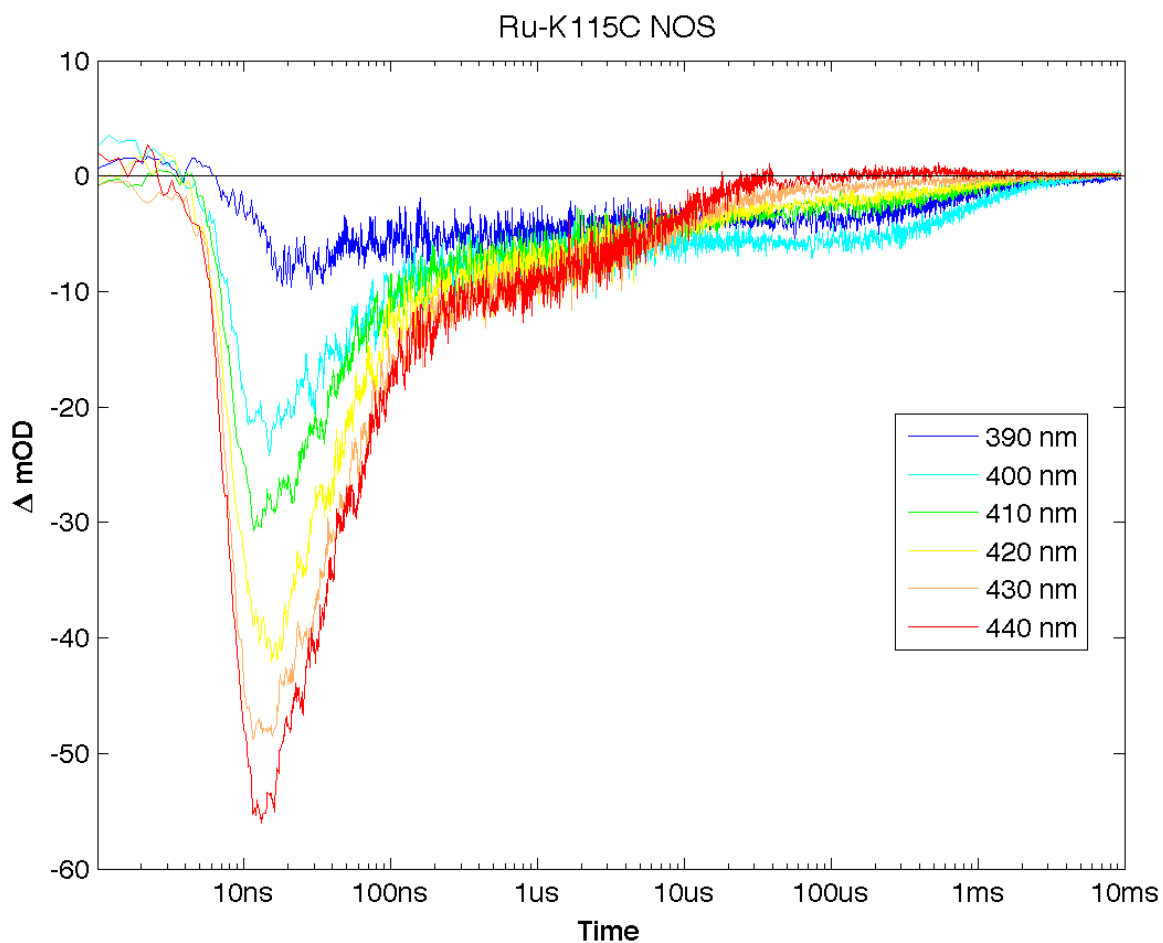


Figure A.14. Transient absorption data at six wavelengths for flash-quenched Ru-NOS.

In order to determine the number of kinetics components associated with Ru-NOS kinetics, and therefore, the number of species, we have subjected TA data at six wavelengths to truncated generalized singular value decomposition analysis (tgSVD) (Regularization Tools, Per Christian Hansen,¹² see sample script in Appendix D). The plot of the tgSVD shows the magnitude (y-axis) of the contribution of each rate constant k (x-axis) to the overall fitting of the transient absorption data. Grouping of the rate constants into three clusters indicates that as many as three distinct kinetic phases contribute to the recovery of TA signals to baseline. This is different from analysis of Ru-P450 TA data, in which 5 kinetics phases were identified.

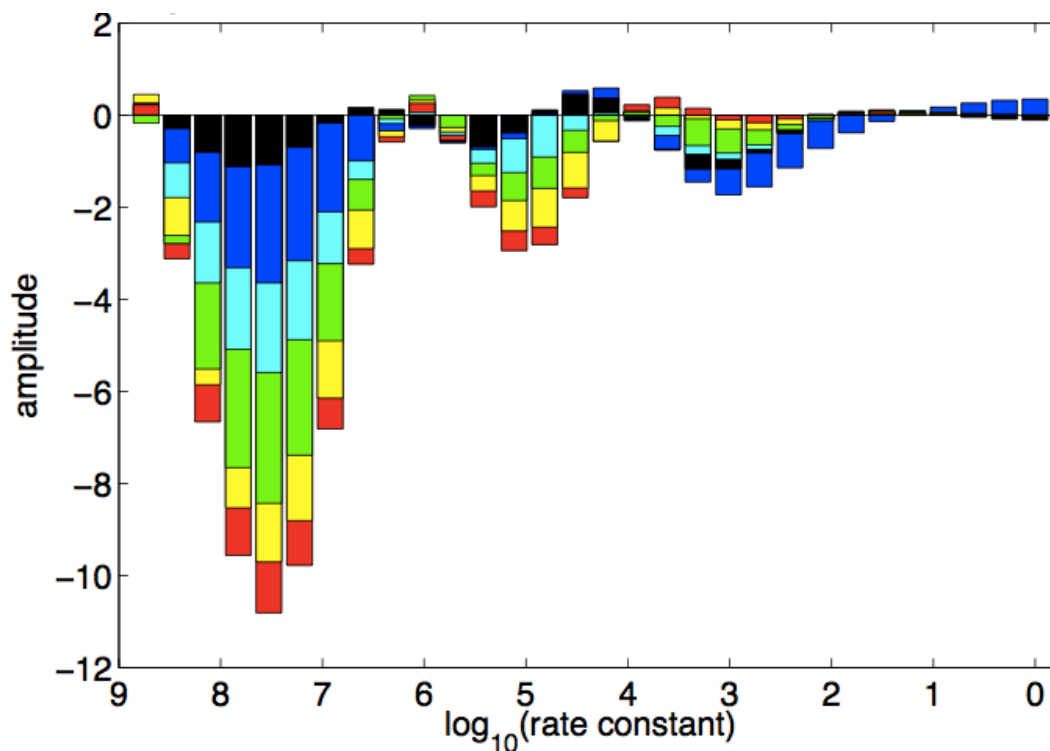


Figure A.15. tgSVD of TA data for flash-quench of Ru-NOS. Red: 440 nm; yellow: 430 nm, green: 420 nm; cyan: 410 nm; blue: 400 nm; black: 390 nm.

We have used the position of each grouping in the tgSVD analysis as an initial guess for multiexponential fitting. Starting with these rate constants, we have performed a global least-squares fitting of the TA data recorded at six wavelengths (390, 400, 410, 420, 430, 440 nm), to a sum of three exponentials with amplitude coefficients ρ_{1-3} and observed rate constants γ_{1-3} (Equation A.1, **Table A.3**) (see a sample fitting script in Appendix D).

$$TA(\lambda_n) = \rho_{n1} \exp(\gamma_1 t) + \rho_{n2} \exp(\gamma_2 t) + \rho_{n3} \exp(\gamma_3 t) \quad \text{A.1}$$

Table A.3. Rate constants extracted from global fitting of TA data.

	γ_1	γ_2	γ_3
Rate (s^{-1})	2.2×10^7	1.5×10^5	9.9×10^2
τ (s)	45 ns	7 μ s	1 ms

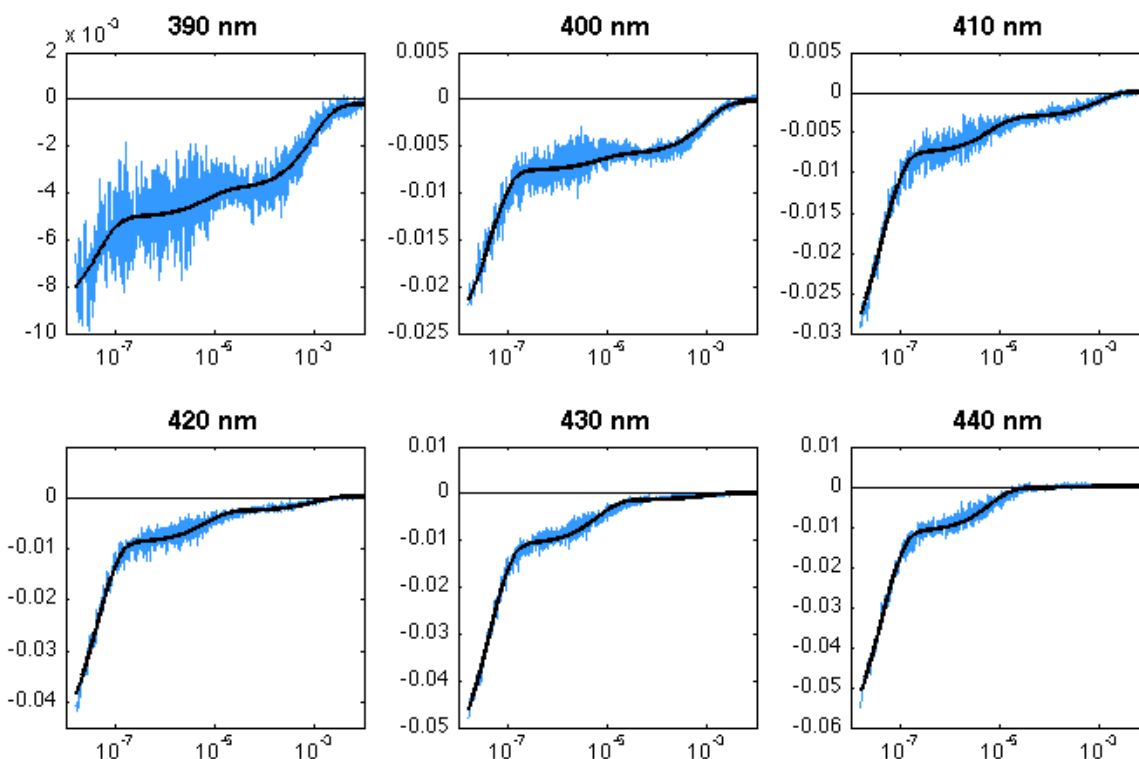


Figure A.16. Global fitting of TA data at six wavelengths.

We can compare the transient features for flash-quenched Ru-NOS to those observed for Ru-P450. In the latter case (see Chapter 2), bleaching of Soret wavelengths on the microsecond-to-millisecond timescale was attributed to formation of porphyrin radical species. These transient intermediates converted to high-valent compound II, which was characterized by a red-shifting of the Soret band. The transient species for flash-quenched Ru-NOS that appears from 10 μ s – 2 ms is characterized by bleaching of the NOS Soret (400 nm). This is consistent with formation of the porphyrin radical. No additional intermediates were observed.

A.3. Discussion

Conjugation of $[\text{Ru}(\text{bpy})_2(\text{Aphen})]^{2+}$ at non-native cysteine115 generates a Ru-NOS conjugate with a Ru-Fe distance of 25 Å; this is very similar to the analogous

distance in Ru-P450 conjugates. Interestingly, there is also an intervening tryptophan (residue 243) between the photosensitizer and heme. This residue may play a role in facilitating oxidative ET in Ru-NOS, as observed for Ru-P450 (see Chapters 3 and 4). Site directed mutagenesis to modify this residue would help elucidate whether transient oxidation of tryptophan₂₄₃ facilitates ET over the 25-Å distance.

The biexponential luminescence decay of Ru-NOS indicates the presence of two photosensitizer conformations that do not exchange on the timescale of the luminescence decay. The relative ratio of major and minor decay components (τ_A and τ_B , respectively) is not affected by Ru-NOS concentration, nor by the ionic strength of the buffer. This suggests that the two conformations are not a result of monomer-dimer equilibrium. τ_A is significantly shorter (150 ns vs. 1100 ns), and its decay rate is more affected by ionic strength and quencher concentration than is τ_B . We suggest that the major component arises from a conformation in which the photosensitizer is more solvent exposed, while the minor component is attributed to a conformation in which the photosensitizer is nestled against the protein framework, possibly through hydrophobic contacts.

ET quenching of the Ru^{II}-NOS excited state with $[\text{Ru}^{\text{III}}(\text{NH}_3)_6]^{3+}$ generates a Ru^{III}-NOS species within 100 ns, which in turn oxidizes the NOS active site (**Figure A.17**). We can compare the transient features for flash-quenched Ru-NOS to those observed for Ru-P450. In the latter case (see Chapter 2), bleaching of Soret wavelengths on the microsecond-to-millisecond timescale was attributed to formation of porphyrin radical species. These transient intermediates converted to high-valent compound II, which was characterized by a red-shifting of the Soret band. The transient species for flash-quenched Ru-NOS that appears from 10 μs – 2 ms is characterized by bleaching of the NOS Soret (400 nm). Thus, we tentatively

assign this species as a porphyrin radical cation. No additional intermediates were observed for Ru-NOS.

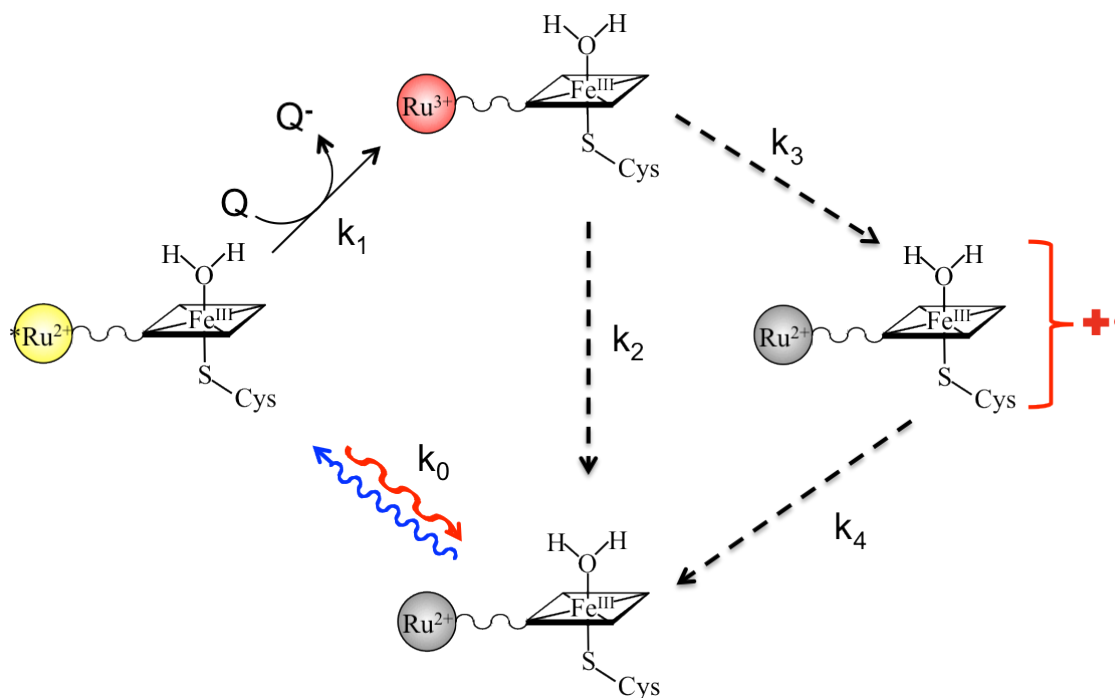


Figure A.17. Scheme for photochemical oxidation of the NOS heme.

A.4. Conclusion

We have developed Ru-NOS conjugates for photo-triggered ET oxidation of the NOS active site. Transient absorption data indicate rapid oxidation of the NOS heme, with a rate constant of (25 μ s). We suggest that this proceeds via formation of the porphyrin radical cation, with no evidence of CII formation. Additional investigations, including pH dependence, are necessary to further characterize this transient species.

A.5. Acknowledgments

I would like to thank Dr. Charlotte Whited for NOS insights and expression protocols, and Dr. Gretchen Keller for crystallization of NOS, and for Team Haem Team.

A.6. Materials and Methods

Plasmid for the triple mutant C227S/C269S/K115C NOS with a 6-histidine tag in the pACYCDuet-1 vector (chloramphenicol resistance) was provided by Dr. Charlotte Whited.

Expression Protocols

Plasmid was transformed into BL21DE3 cells (see Appendix B). Overnight cultures of Luria Bertani broth (LB) (25 mL) containing 34 µg/mL chloramphenicol and a single *E. coli* colony (transformed with the mutant plasmid of interest) were incubated at 37 °C overnight, shaking at 180-200 rpm. Induction cultures of LB (3 x 2L) containing 34 µg/mL chloramphenicol were inoculated with the overnight culture and incubated at 37 °C until reaching an optical density of ~1 at 600 nm (~3 hours). Cultures are induced by addition of 1 mM IPTG, and 0.5 mM α-aminolevulinic acid (a heme precursor) and 1 mM FeCl₃ is added (values refer to final concentrations in the induction flask). After 24 hours of expression, cells were harvested by centrifugation (5000 rpm, 10 min), and cell pellets are stored at -80 °C until needed.

Extraction and purification

Cell pellets were resuspended in cold Resuspension Buffer (50 mM HEPES pH 7.5, 500 mM sodium chloride, 5 mM imidazole). A small spatula tip each of two

protease inhibitors (benzamidine hydrochloride and Pefabloc SC) were added, and cells were lysed by five cycles of probe-tip sonication (2s on, 2s off, repeat for 2 minutes), cooled by an ice-water bath. Centrifugation (16,000 rpm, 1 hr, 8 °C) pelleted cellular debris, the supernatant was filtered through 0.22 µM filters and loaded onto a HiPrep HisTrap Ni FPLC column (GE Healthcare) equilibrated with Wash Buffer (50 mM HEPES pH 7.5, 500 mM sodium chloride, 10 mM imidazole). After thorough washing with Wash Buffer, protein was eluted with Elution Buffer (300 mM imidazole in Wash Buffer), and the colored (red/orange) fractions are collected.

100 µL of thrombin was added, and the solution was gently agitated at 4 °C overnight to cleave the 6-histidine tag. Following cleavage, the enzyme sample was concentrated using 30 kDa centrifugal filters and subjected to gel filtration on a Superdex 200 FPLC column equilibrated with 50 mM Tris, 150 mM sodium chloride, pH 7.5. Samples were buffer exchanged into 20 mM Tris, pH 7.5 with 20 mM dithiothreitol to reduce intermolecular disulfide bonds. Samples were characterized by UV-vis absorption (A_{420}/A_{280}), SDS-PAGE, and mass spectrometry. Protein not intended for immediate use was flash-frozen in liquid nitrogen (with 40% glycerol added to solution as cryoprotectant) and stored at -80°C.

Ru-NOS conjugation and purification

Photosensitizer synthesis and Ru-enzyme conjugation protocols are described in Appendix B. Ruthenium-labeled and unlabeled NOS were separated by FPLC using a HiTrap Q (GE Healthcare). FPLC Buffers A (column equilibration) and B (elution) were 20 mM Tris, pH 8, and 20 mM Tris, 500 mM sodium chloride, pH 8, respectively. After loading the Ru-NOS sample, the column was washed (3

ml/min) with buffer A until absorbance returned to baseline. The gradient was ramped to 25% (5 min), followed by a slow gradient 25-70% Buffer B over 60 min.

Laser sample preparation, and instrument and data acquisition details for transient luminescence and absorption details are described in Appendix B.

A.7. References

- (1) Alderton, W. K.; Cooper, C. E.; Knowles, R. G. Nitric Oxide Synthases: Structure, Function, and Inhibition. *Biochem. J.* **2001**, *357*, 593–615.
- (2) Crane, B. R.; Sudhamsu, J.; Patel, B. A. Bacterial Nitric Oxide Synthases. *Annu. Rev. Biochem.* **2010**, *79*, 445–470.
- (3) Stuehr, D. J.; Santolini, J.; Wang, Z. Q.; Wei, C. C.; Adak, S. Update on Mechanism and Catalytic Regulation in the NO Synthases. *J. Biol. Chem.* **2004**, *279*, 36167–36170.
- (4) Bird, L. E.; Ren, J. S.; Zhang, J. C.; Foxwell, N.; Hawkins, A. R.; Charles, I. G.; Stammers, D. K. Crystal Structure of SANOS, a Bacterial Nitric Oxide Synthase Oxygenase Protein from *Staphylococcus Aureus*. *Structure* **2002**, *10*, 1687–1696.
- (5) Pant, K.; Bilwes, A. M.; Adak, S.; Stuehr, D. J.; Crane, B. R. Structure of a Nitric Oxide Synthase Heme Protein from *Bacillus Subtilis*. *Biochemistry* **2002**, *41*, 11071–11079.
- (6) Gusarov, I.; Starodubtseva, M.; Wang, Z.-Q.; McQuade, L.; Lippard, S. J.; Stuehr, D. J.; Nudler, E. Bacterial Nitric-Oxide Synthases Operate without a Dedicated Redox Partner. *J. Biol. Chem.* **2008**, *283*, 13140–13147.
- (7) Zhu, Y.; Silverman, R. B. Revisiting Heme Mechanisms. A Perspective on the Mechanisms of Nitric Oxide Synthase (NOS), Heme Oxygenase (HO), and Cytochrome P450s (CYP450s). *Biochemistry* **2008**, *47*, 2231–2243.
- (8) Clague, M. J.; Wishnok, J. S.; Marletta, M. A. Formation of N-Delta-Cyanoornithine from N-G-Hydroxy-L-Arginine and Hydrogen Peroxide by Neuronal Nitric Oxide Synthase: Implications for Mechanism. *Biochemistry* **1997**, *36*, 14465–14473.
- (9) Whited, C. A. Tuning Nitric Oxide Synthase: Investigating the Thiolate “Push” and NO Release, California Institute of Technology: Pasadena, California, **2011**.
- (10) Keller, G. E. Phototriggering Nitric Oxide Synthase from *Geobacillus Stearothermophilus*, California Institute of Technology: Pasadena, California, **2013**.
- (11) Castellano, F. N.; Dattelbaum, J. D.; Lakowicz, J. R. Long-Lifetime Ru(II) Complexes as Labeling Reagents for Sulfhydryl Groups. *Anal. Biochem.* **1998**, *255*, 165–170.
- (12) Hansen, P. C. Regularization Tools: A Matlab Package for Analysis and Solution of Discrete Ill-Posed Problems. *Numer. Algorithms* **1994**, *6*, 1–35.

*Appendix B***COMMON PROTOCOLS**

B.1. Instrumentation

Polymerase Chain Reaction (PCR) was performed on a MJ Research PT150 Minicycler. UV-visible absorbance spectra were obtained on an Agilent 8453 diode array spectrophotometer. Mass spectrometry was performed using MALDI-TOF in the Mass Spectrometry Facility at Caltech, or LC-MS at the Caltech Protein/Peptide MicroAnalytical Laboratory (PPMAL). Fast protein liquid chromatography (FPLC) was performed on an AKTApurifier FPLC (GE Healthcare) using HiPrep desalting, HiPrep Q anion exchange, and Superdex 75 gel filtration columns. Steady-state fluorescence spectra were acquired on a Jobin Yvon Spec Fluorolog[®]-3-11 fluorometer.

B.2. Site-directed mutagenesis

Mutations to the P450 gene were made using Qiagen QuikChange site-directed mutagenesis kit. Samples were prepared on ice:

38.5 μ L milliQ water
5 μ L Buffer stock (10X)
2 μ L parent plasmid,
1.25 μ L of forward primer
1.25 μ L of reverse primer
1 μ L dNTPs.

1 μ L of enzyme was added to this mixture as the final component.

The following PCR protocol was used:

1. 95 °C 1 min
2. 55°C 1 min
3. 68°C 8 min
4. Repeat steps 1-3, x 17
5. 4°C 4 hrs (until pickup)

Digestion of methylated DNA (parent plasmid) is achieved by addition of 1 μ L *dpn1* enzyme and incubation at 37 °C for one hour, followed by denaturation at 65 °C for 15 minutes. The PCR mixtures are stored at -20 °C until needed.

B.3. Transformation Protocol

Plasmid for the desired mutant (1-2 μ L) is incubated on ice with (ultra)competent cells (30-50 μ L) for 30 min, followed by 45 seconds of heat shock at 42 °C. Following an additional 2 minute incubation on ice, NZY⁺ broth (250 μ L) is added and the transformation mixture is incubated for 1 hour at 37 °C with gentle agitation. 5-150 μ L of the transformation mixture are plated on LB/Agar culture plates containing 100 μ g/mL ampicillin. These are incubated overnight at 37 °C; BL21-DE3 cells are incubated ~16 hours, XL-1 Blue/Nova Blue are incubated 24 hours.

B.4. Amplification and purification of plasmid DNA

To amplify plasmid DNA, such as for sequencing, the purified plasmid DNA or PCR mixture is transformed into XL-1 Blue or Nova Blue supercompetent cells (see Transformation Protocol).

Overnight cultures containing 5 mL Luria Bertani broth, 100 μ L/mL ampicillin, and a single *E. coli* colony are grown for 16 hours at 37 °C. Cells are pelleted by centrifugation (10 min, 5000 rpm), and supernatant is discarded. Plasmid DNA is extracted using a Qiagen miniprep kit. To verify successful mutagenesis, 10 μ L samples are submitted for sequencing (Laragen) along with sequencing primers. A combination of forward (ptac-ptac promoter: TTGACAATTAATCATCGGC, T_M =53.7 °C) and reverse (pCWrev: CTTTCGTCTTCAAGCAGATCTG, T_M =60.8 °C) primers are used to sequence the entire P450 gene.

B.5. P450 overexpression in *E. coli*, extraction and purification

All P450 mutants were expressed in *E. coli* BL21(DE3) cells, with minor differences for P450-BM3 and CYP119 variants.

Expression

Overnight cultures of Luria Bertani broth (25 mL) containing 100 µg/mL ampicillin and a single *E. coli* colony (transformed with the mutant plasmid of interest) are incubated at 37 °C overnight, shaking at 180-200 rpm. Induction cultures of TB (1x TB for P450 BM3, 2x TB for CYP119; 1L in 4L flask or 2 L in 6L flask) containing 200 µg/mL ampicillin, 1 µM thiamine, 0.4% glycerol, and 250 µL mineral supplements (100 mM FeCl₃, 10 mM ZnCl₂, 8.5 mM CoCl₂, 8.5 mM Na₂MoO₄, 7 mM CaCl₂, 7.5 mM CuCl₂, 8 mM H₃BO₃), are inoculated with the overnight culture and incubated at 37 °C until reaching an optical density of ~1 at 600 nm. Cultures are induced by addition of 1 mM IPTG, and 0.5 mM α-aminolevulinic acid, a heme precursor, is added. The temperature is lowered to 30 °C; the P450 BM3 expression period is 24 hours, CYP119 expression period is 40 hours. Following expression, cells are harvested by centrifugation (5000 rpm, 10 min), and cell pellets are stored at -80 °C until needed.

Extraction and purification

Cell pellets are resuspended in cold Wash Buffer (50 mM Tris pH 8, 300 mM sodium chloride, 20 mM imidazole). A small spatula tip each of two protease inhibitors (benzamidine hydrochloride and Pefabloc SC) are added, and cells are lysed by two to three cycles of probe-tip sonication (0.5 s on, 0.5 s off, for 5 minutes), cooled by an ice-water bath.

Centrifugation (15,000 rpm, 1 hr, 8 °C) pellets cellular debris, and the supernatant is loaded directly onto a Ni batch column. After thorough washing with Wash Buffer (1.5-2 L), protein is eluted (200 mM imidazole in Wash Buffer), and the colored (red/orange) fractions are collected and concentrated in 30 kDa centrifugal filters. Gel filtration chromatography is used to remove fragmented proteins, followed by buffer exchange into 20 mM Tris, pH 8 with 20 mM dithiothreitol (DTT) added to reduce intermolecular disulfide bonds. Purity is determined by UV-vis absorption (A_{420}/A_{280}), SDS-PAGE, and mass spectrometry. Protein not intended for immediate use is flash-frozen in liquid nitrogen (with 40% glycerol added to solution as cryoprotectant) and stored at -80°C.

B.6. Ru-P450 conjugation

The complex $[\text{Ru}(\text{bpy})_2(\text{IA-phen})]^{2+}$ (IA-phen = 5-iodoacetamido-1,10-phenanthroline) was covalently coupled to P450 mutants containing a single, surface exposed cysteine, to afford the respective $\text{Ru}^{\text{II}}\text{-Fe}^{\text{III}}\text{P450}$ conjugates.

Approximately three-fold excess of $[\text{Ru}(\text{bpy})_2(\text{IA-phen})]^{2+}$ is added to a 20 μM solution of P450 mutant in 20 mM Tris buffer (pH 8), and shaken in the dark at 4 °C. Labeling progress can be monitored by MALDI mass spectrometry; no further increase in the peak corresponding to the predicted mass of $\text{Ru}^{\text{II}}\text{-P450}$ is observed after two hours. Excess $[\text{Ru}(\text{bpy})_2(\text{IA-phen})]^{2+}$ is removed during concentration in 30 kDa filters, followed by desalting on an FPLC HiPrep column.

To separate photosensitizer-labeled and unlabeled enzymes, protein samples are loaded onto an anion exchange MonoQ or HiPrep Q column equilibrated with 20 mM Tris buffer, pH 8 (Q Wash Buffer). The column is washed with Q Wash Buffer until UV-visible absorbances return to baseline. The gradient is ramped

quickly to 59% Q Elution Buffer (Q Wash Buffer + 250 mM sodium chloride), followed by a slow gradient of 59-65% Q Elution Buffer over 60 minutes.

B.7. Preparation of laser samples

Laser samples are composed of approximately 10 μM $\text{Ru}^{\text{II}}\text{-Fe}^{\text{III}}\text{P450}$ or the model complex $[\text{Ru}(\text{bpy})_2(\text{IAphen})]^{2+}$, with and without oxidative quencher (17 mM $[\text{Ru}^{\text{III}}(\text{NH}_3)_6]^{3+}$) in buffered solution (pH 6: 20 mM sodium acetate; pH 7: 20 mM sodium acetate; pH 8: 50 mM sodium borate or 50 mM Tris). High ionic strength (100-200 mM sodium chloride) helps to prevent protein precipitation in the presence of quencher. Samples are placed in a specialized, high-vacuum, four-sided quartz cuvette (Starna Cells) with a high-vacuum Teflon valve (Kontes) and 14/20 adaptor (**Figure B.1**), equipped with a small stir bar (1 x 3 mm). Solutions are stirred constantly during deoxygenation and data collection. Deoxygenation is achieved via 3 x 10-15 gentle pump-backfill cycles with argon on a Schlenk line, with 15 minutes of equilibration between each set of cycles.

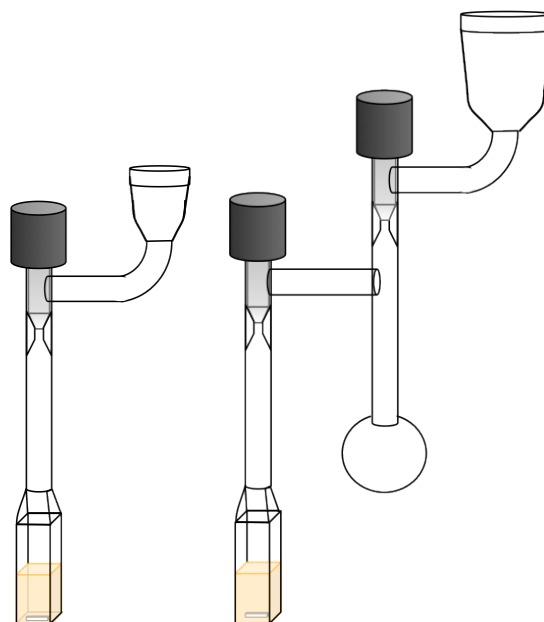


Figure B.1. Two high-vacuum cuvettes for laser studies. Left: typical cuvette for flash-quench. Right: cuvette for $\text{Fe}^{\text{II}}\text{-CO}$ photolysis and rebinding.

B.8. Laser details

Nanosecond-to-second transient spectroscopies

Excitation for nanosecond-to-millisecond transient luminescence and absorption experiments was provided by visible light (e.g., 480 nm) pulses from a tunable optical parametric oscillator (Spectra Physics, Quanta-Ray MOPO-700) pumped by the third harmonic from a Spectra Physics Q-switched Nd:YAG laser (Spectra-Physics, Quanta-Ray PRO-Series, 8 ns pulse width) operated at 10 Hz.

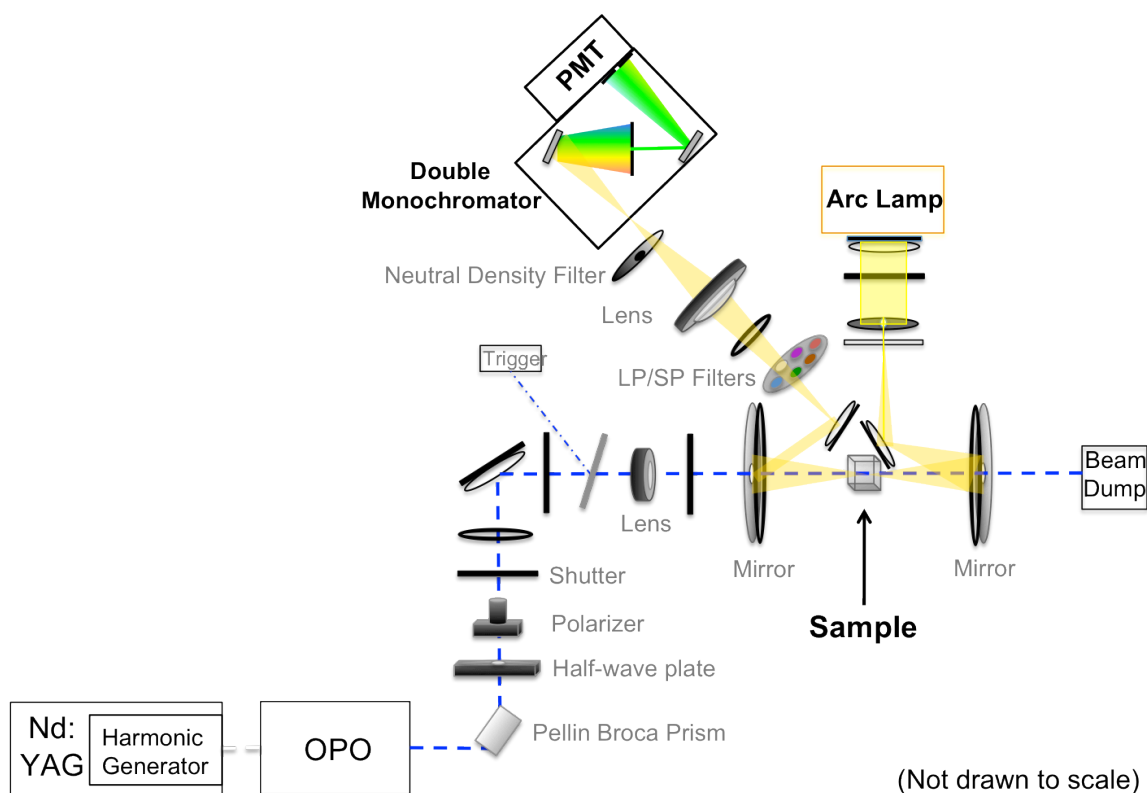


Figure B.2. Nanosecond-pulsed single-wavelength transient luminescence and absorption setup: NSI.

The setup for single-wavelength transient luminescence and absorption studies (“NSI”) is shown in **Figure B.2**. Probe light was provided by a 75-W arc lamp (PTI Model A 1010) that could be operated in continuous or pulsed mode, and passed

through the sample collinearly with the excitation pulse. After rejection of scattered light by appropriate long- and short-pass filters, and intensity modulation by a neutral density filter, probe wavelengths were selected by a double monochromator (Instruments SA DH-10) with 1 mm slits. Transmitted light was detected by a photomultiplier tube (PMT, Hamamatsu R928), and amplified by a 200 MHz wideband voltage amplifier DHPVA-200 (FEMTO).

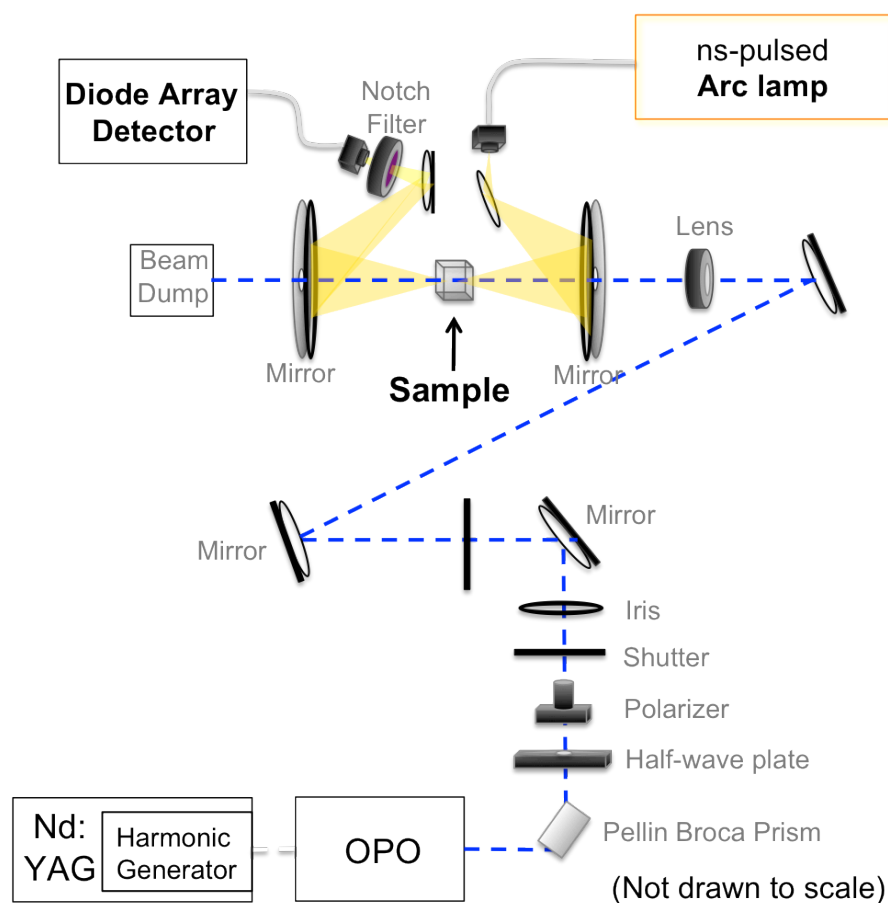


Figure B.3. Nanosecond-pulsed multi-wavelength transient absorption setup: NSII.

The setup for multi-wavelength transient absorption studies (“NSII”) is shown in **Figure B.3**. Probe light was provided by white flashlamp, and transmitted to the sample by fiberoptic cables. A partial reflector directed approximately 30% of the probe light around the sample as a references beam, while the majority was aligned

through the sample, collinearly with the excitation beam. Scattered excitation light was rejected by a narrow notch filter (centered at 486 nm), and the transmitted probe light was detected into two photodiode arrays (Ocean Optics S1024DW Deep Well Spectrometer). Measurements were made with: neither probe light nor excitation light (dark correction), probe light only (background), excitation light only (fluorescence correction), and probe light and excitation light (TA). The timing of laser fire, flashlamp fire, and photodiode array readout were controlled by a series of timing circuits, and the readout was interfaced with a PC via a National Instruments multifunction input/output card. Difference spectra were averaged over approximately 150 shots.

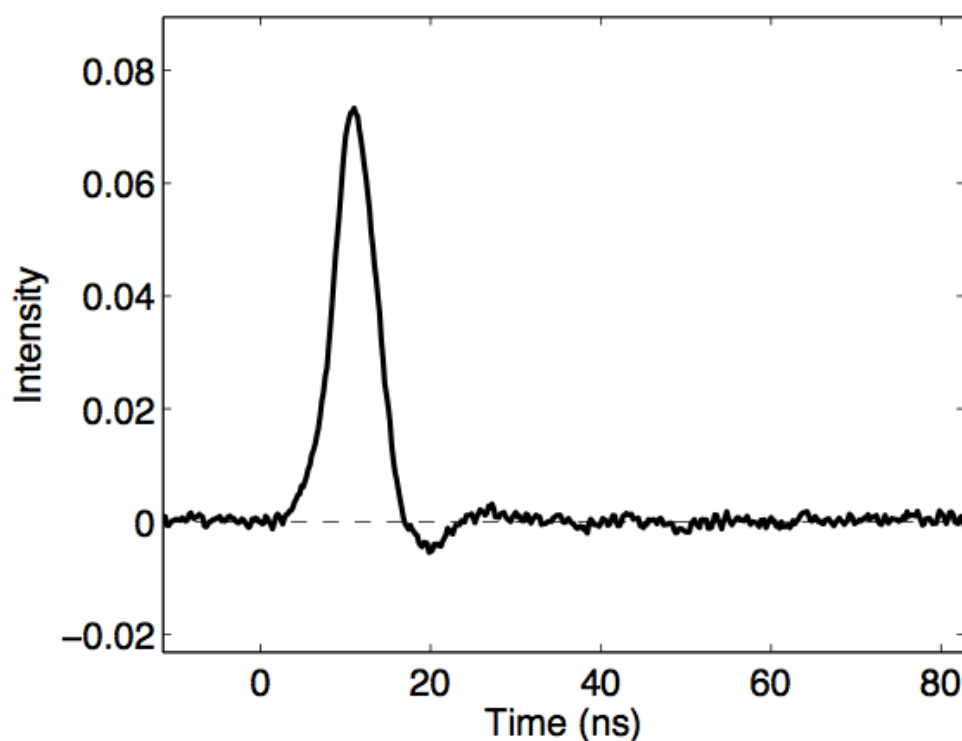


Figure B.4. NSI instrument response to scattered laser light, collected on a 2 μ s window (pulse width: 8 ns).

Picosecond-to-nanosecond transient spectroscopy

The setup for picosecond-pulsed single wavelength transient absorption measurements is shown in **Figure B.5**.

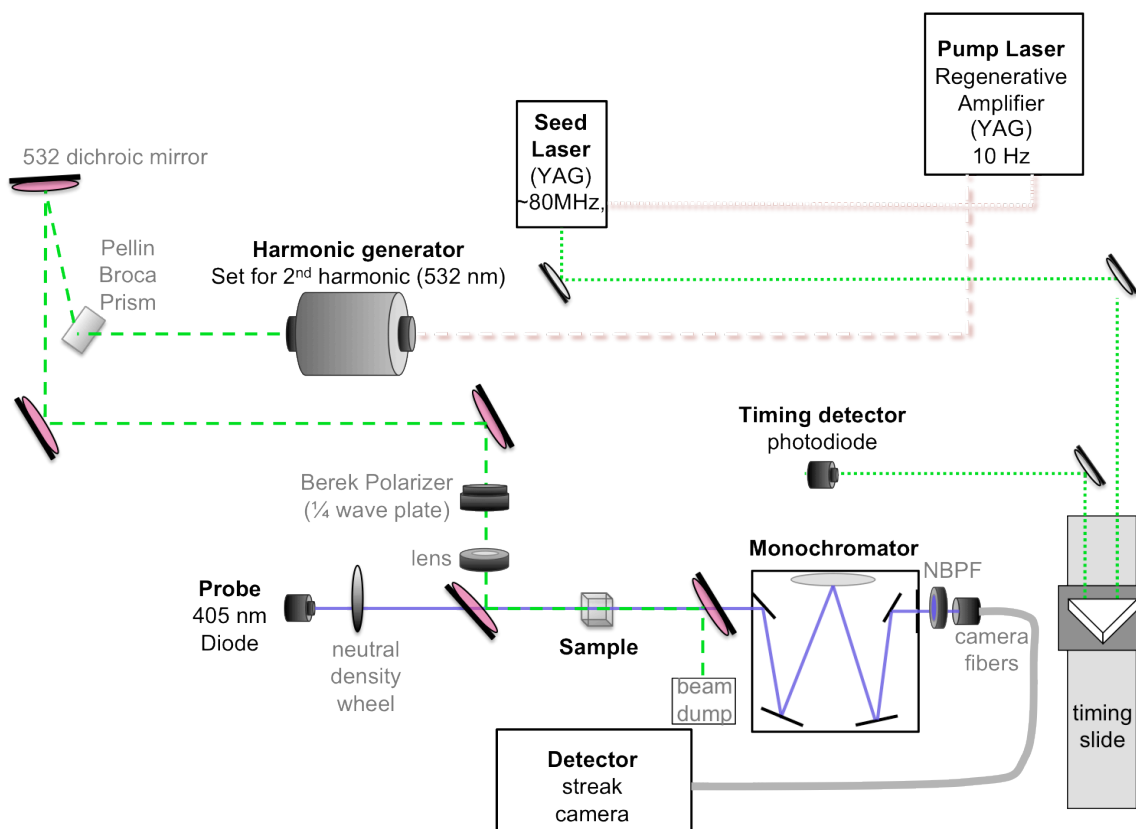


Figure B.5. Picosecond-pulsed single-wavelength transient absorption setup: PSI.

Excitation pulses for picosecond single-wavelength transient absorption measurements were generated by a Continuum Regenerative Amplifier (RGA 60 Series) operated at 10 Hz, seeded by a 70 MHz train provided by the first harmonic (1064 nm) of a mode-locked DPSS Nd:YAG (Spectra Physics Vanguard 2000 HM532). A small portion of the seed laser (2nd harmonic, 532 nm output) was used for timing. The excitation pulse (pulse width ~10 ps) was tuned to the second harmonic (532 nm) by a harmonic generator, and converted to circularly polarized

light by a Berek Retardation Polarizer Compensator (5540) operating in $\frac{1}{4}$ wave plate mode, before being directed through the sample. Continuous probe light was provided by a Sony 405 nm 100 mW focusable laser diode. After passing through the sample, excitation pulses were rejected using a 532 dichroic mirror, and probe light was transmitted through a monochromator and into a picosecond streak camera (C5680 Hamamatsu Photonics) in photon counting mode, operated by a Hamamatsu controller. Samples were stirred continuously, with typical laser powers of 0.5-0.75 mJ/pulse. Kinetics traces were collected on 5 ns and 50 ns time windows, averaged over 10,000 exposures.

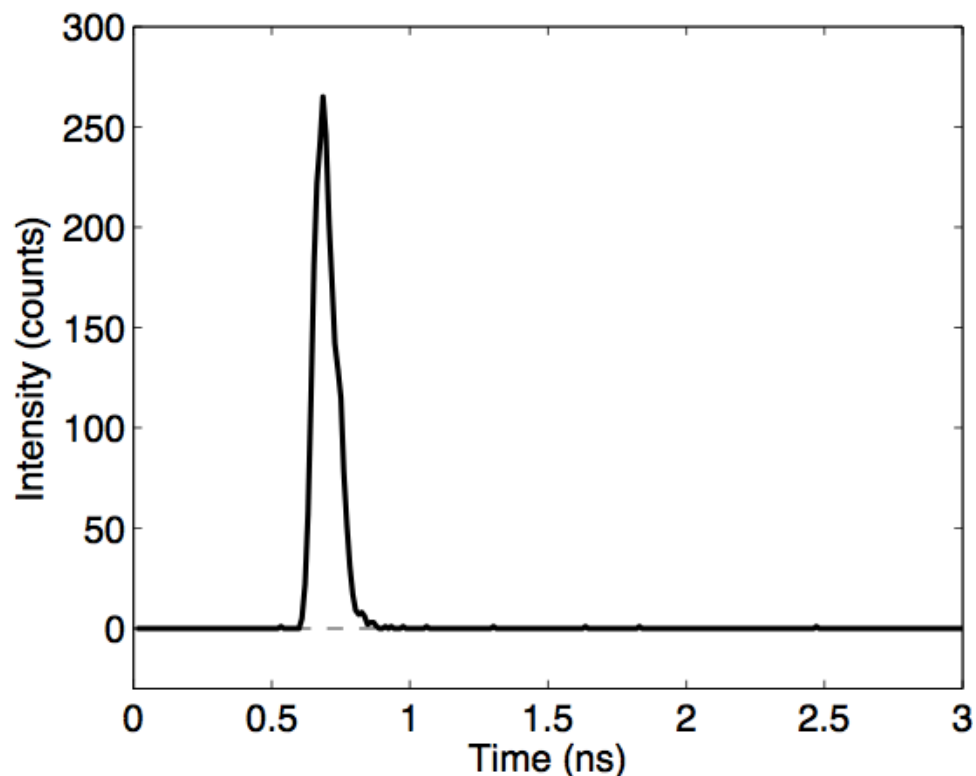


Figure B.6. PSI instrument response to scattered laser light, collected on a 5 ns window.

B.9. Data workup

To generate a complete kinetics picture of TA data on the picosecond-to-second timescale, individual kinetics traces were log-compressed, overlaid, and spliced together.

On the NSI system, timescales 400 μs and shorter were amplified and digitized by the fast amp/digitizer system, while timescales 10 ms and longer are amplified and digitized by the slow amp/digitizer. It was noted that transient absorption data using the slow amp had inconsistent magnitudes that could vary by a factor of 2-3 when compared between different time-windows. Fast-amp traces were more self-consistent. Thus, the magnitude of the fastest trace (2 μs window) was taken as the standard amplitude for each data set; TA data at other time-windows multiplicatively scaled to achieve overlap.

Data collected on the picosecond streak camera had significantly lower signal-to-noise ratios, and showed larger variations in intensity compared to ns1 data. When overlaying ps1 and ns1 data, the magnitude of the ns1 trace from the 2 μs window was taken as the standard amplitude for each data set, and other time-windows were multiplicatively scaled to achieve overlap.

Appendix C

CHAPTER-SPECIFIC NOTES

C.1. Notes for Chapter 2

Ru-P450 luminescence: dependence on concentration

Normalized luminescence decays at four concentrations (2, 4, 8, 12 μM) are superimposable.

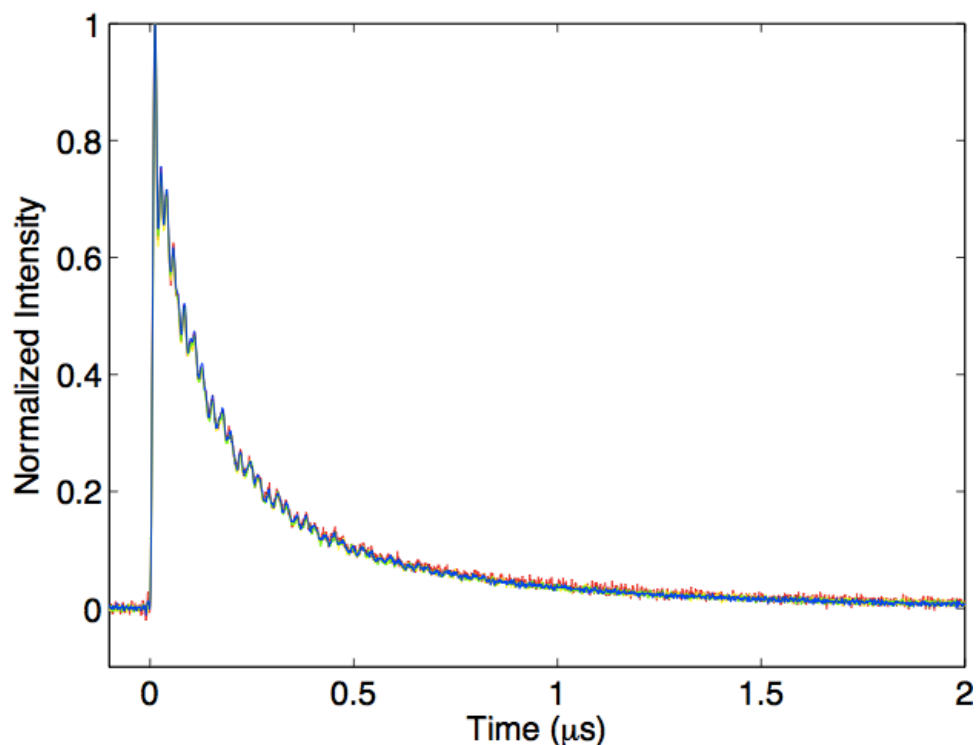


Figure C.1. Luminescence decays of Ru_{K97C}-BM3 at four concentrations. Red: 2 μM ; Yellow: 4 μM ; Green: 8 μM ; Blue: 12 μM .

Low-temperature experiments

We have examined flash-quench of Ru-P450 BM3 at reduced temperatures to try and increase the lifetime of the observed compound II species. Solutions containing 25% glycerol enable examination of temperatures down to $-15\text{ }^\circ\text{C}$. Luminescence lifetimes increase as temperature decreases, for both quenched and unquenched samples (**Figure C.2**). While it does appear that transient absorption features decay more slowly at low temperature, the magnitude of transient features

(and thus, yield of oxidized species) also decreases (**Figure C.3**). This strategy is unlikely to facilitate further characterization of photogenerated compound II.

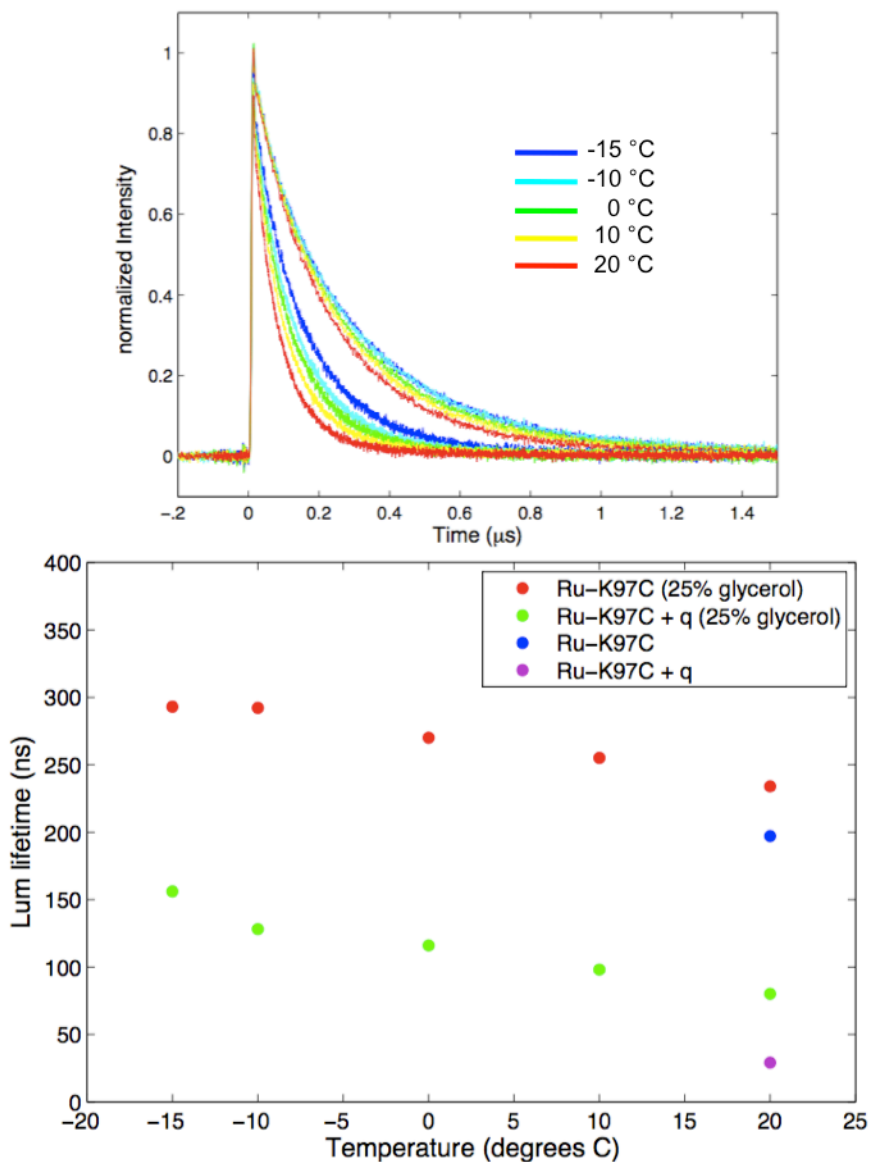


Figure C.2. Luminescence decays at variable temperature. **Top:** Quenched and unquenched luminescence decays of RuC₉₇-BM3(W) at variable temperature. **Bottom:** Luminescence lifetimes at variable temperature.

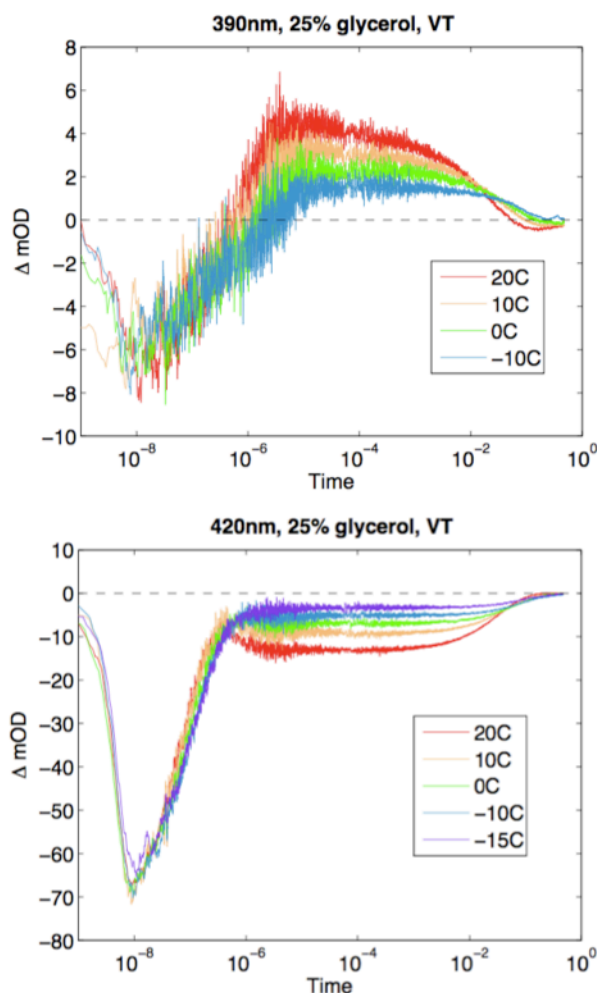


Figure C.3. TA at variable temperature for Ru_{K97C}-P450 BM3(W), pH 6.

C.2. Notes for Chapter 3

Search for the tryptophan radical cation intermediate

Tryptophan radical cation ($W^{\bullet+}$) and neutral radical (W^{\bullet}) species absorb in the visible region, with approximate extinction coefficients of $\epsilon(\lambda_{\text{max}}: 560 \text{ nm}) = 3000 \text{ M}^{-1} \text{ cm}^{-1}$ and $\epsilon(\lambda_{\text{max}}: 510 \text{ nm}) = 2300 \text{ M}^{-1} \text{ cm}^{-1}$, respectively.¹ If such a radical species is indeed formed as a true intermediate along the multi-step electron transfer pathway, it is theoretically possible that we could observe it by transient absorption. Using the Ru_{K97C}-P450_{BM3}(W96) system (in which we have observed

photochemical heme oxidation) we have examined TA of the 500-600 nm region to see if such an intermediate can be identified.

We first examined flash-quench of the photosensitizer model complex $[\text{Ru}(\text{bpy})_2(\text{Aphen})]^{2+}$ to determine absorption components of the photosensitizer in this region. Approximate transient difference spectra at various timepoints were generated using ΔOD from single-wavelength data. We then examined $\text{Ru}_{\text{K97C}}\text{-P450}_{\text{BM3}}(\text{W}_{96})$ and $\text{Ru}_{\text{D77C}}\text{-P450}_{\text{CYP119}}(\text{H}_{76})$, and generated analogous transient difference spectra.

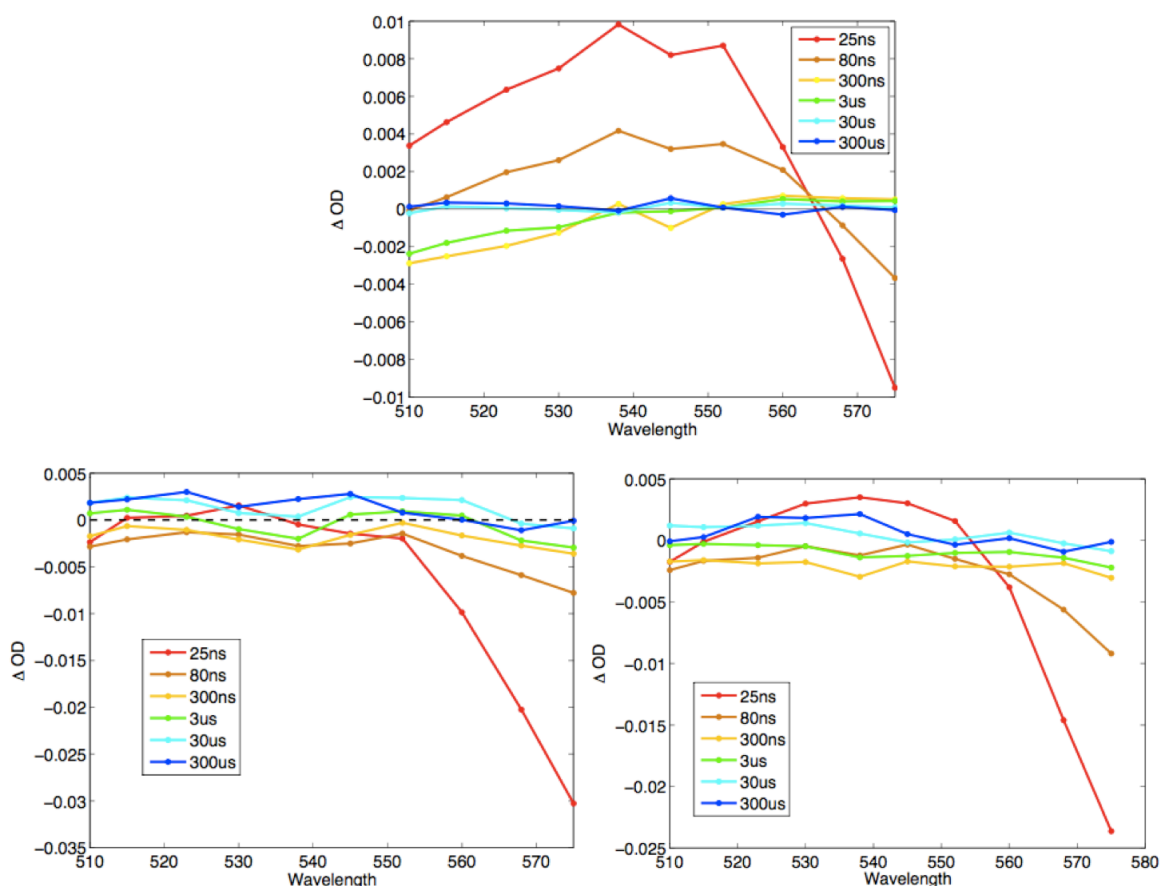


Figure C.4. Transient difference spectra of $[\text{Ru}(\text{bpy})_2(\text{Aphen})]^{2+}$ (top), $\text{Ru}_{\text{K97C}}\text{-P450}_{\text{BM3}}(\text{W}_{96})$ (bottom left) and $\text{Ru}_{\text{D77C}}\text{-P450}_{\text{CYP119}}(\text{H}_{76}\text{W})$ (bottom right) at various time points following excitation at 480 nm and quenching with $[\text{Ru}(\text{NH}_3)_6]^{3+}$.

As seen for $[\text{Ru}(\text{bpy})_2(\text{Aphen})]^{2+}$, the ruthenium excited state ($^*\text{Ru}^{\text{II}}$) absorbs in the 500-570 nm region. Photons from excited state emission give rise to the apparent bleach from 560-580 nm. The Ru^{III} species is characterized by a bleach of the MLCT band, which tails into the 510-540 nm region; this species can be seen at 300 ns and 30 μs timescales. There is no increase at 510 nm or 560 nm associated with the oxidized photosensitizer.

If we are to identify any tryptophan radical species as true intermediates in the electron transfer pathway, we must observe their formation prior to that of heme oxidation (i.e., porphyrin radical cation formation); this occurs within 10 μs . Unfortunately, we are unable to detect any increases in absorbance on this timescale for the W-containing Ru-P450 conjugates. Additionally, TA on longer timescales are complicated by the P450 Q-bands; these also absorb in the 500-600 nm with extinction coefficients $> 10,000 \text{ M}^{-1}\text{cm}^{-1}$, and are expected to shift upon oxidation of the heme. It is quite likely that heme-associated TA signals will obscure any possibility of observing the tryptophan radical.

C.3. Notes for Chapter 5

Selection of probe wavelength for CO rebinding kinetics

For single-wavelength transient absorption measurements, it was observed that the arc-lamp probe light was enough to induce CO-photolysis and generate the inactive form: P420. Thus, a narrow bandpass filter (centered at 406 nm, **Figure C.5**) was used to reject the majority of the probe light. This wavelength has large ΔOD associated with the interconversion between Fe^{II} and $\text{Fe}^{\text{II}}\text{-CO}$ forms, and is far enough from the Soret peak that it causes little photolysis.

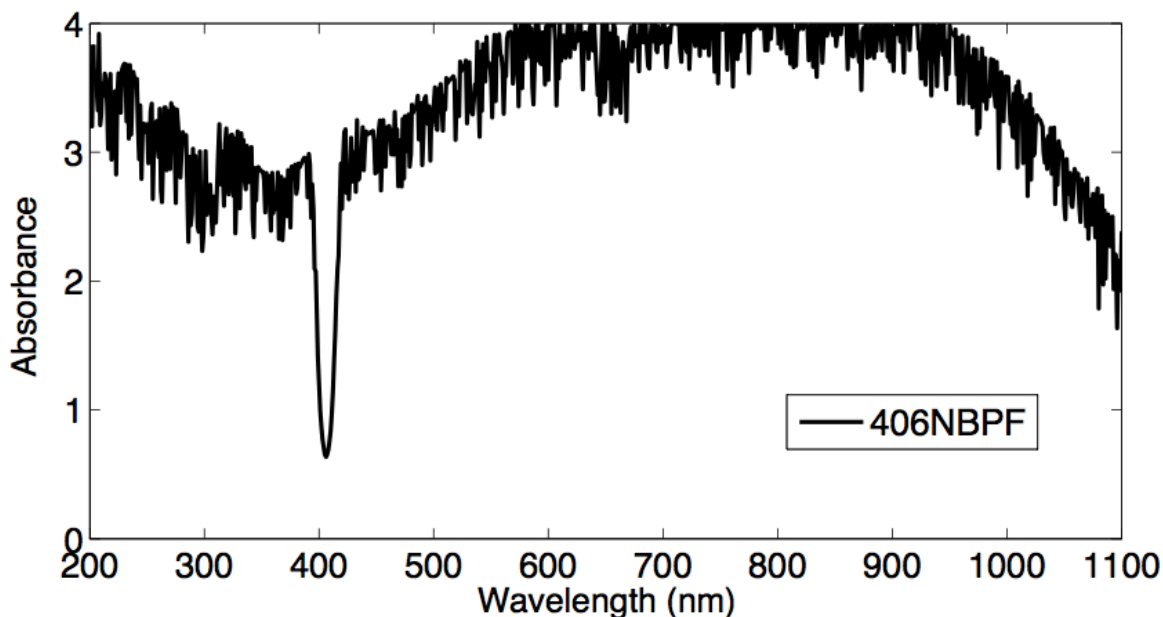


Figure C.5. 406 nm narrow band pass filter.

Overlay of PSI and NSI kinetics traces

Single-wavelength transient absorption data collected on the picosecond-to-nanosecond timescale (“PSI”) and the nanosecond-to-second timescale (“NSI”) overlay well when multiplicatively scaled. PSI data are significantly noisier, with potential variation in laser power or sample integrity over the course of the measurement; therefore, we have scaled PSI data to match the NSI data (**Figure C.6**). Signal averages for each timescale were: 5 ns (10,000); 50 ns (10,000); 2 μ s (150); 2 μ s (150); 100 μ s (150); 10 ms (5).

It is important to note that the scaled signal magnitude at time-zero (**Figure C.6**, magnitude of the red trace) is significantly larger than the maximum signal magnitude expected for this sample (~ 370 mOD vs. 270 mOD). Signal at very early timepoints (< 1 ns) may correspond to an excited state, associated with different absorptivities than the free $\text{Fe}^{\text{II}}\text{-CO}$. Until this magnitude discrepancy is resolved, it is not reliable to take the initial signal magnitude as the photolysis yield.

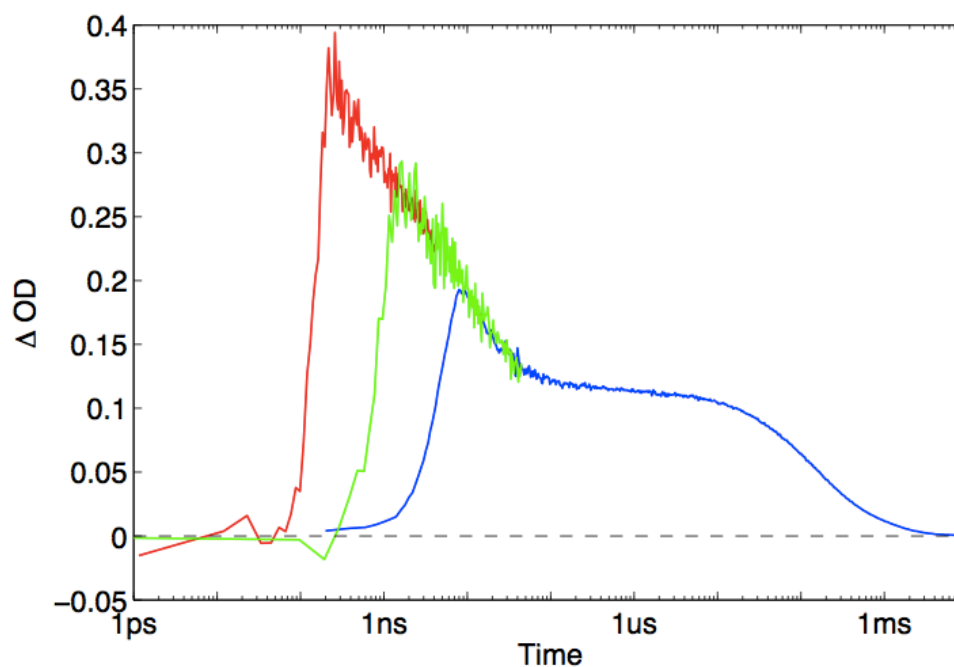


Figure C.6. Overlay of PSI and NSI data for CO rebinding kinetics in CYP119. PSI data (5 ns: red; 50 ns: green) is scaled by ~ 0.5 to overlay with NSI data (2 μ s – 10 ms: blue).

Nonlinear least squares fitting of CO rebinding kinetics at various temperatures

We have subjected picosecond-to-millisecond TA data (collected at temperatures 10-70 °C) to a non-negative least squares fitting method (**Figure C.7**, see Appendix D for sample matlab script). The positive amplitudes at rate constants ($\log_{10}(k)$) greater than 10 are faster than the instrument response; these are an artifact of the fitting procedure, and have been ignored in the remainder of our analysis.

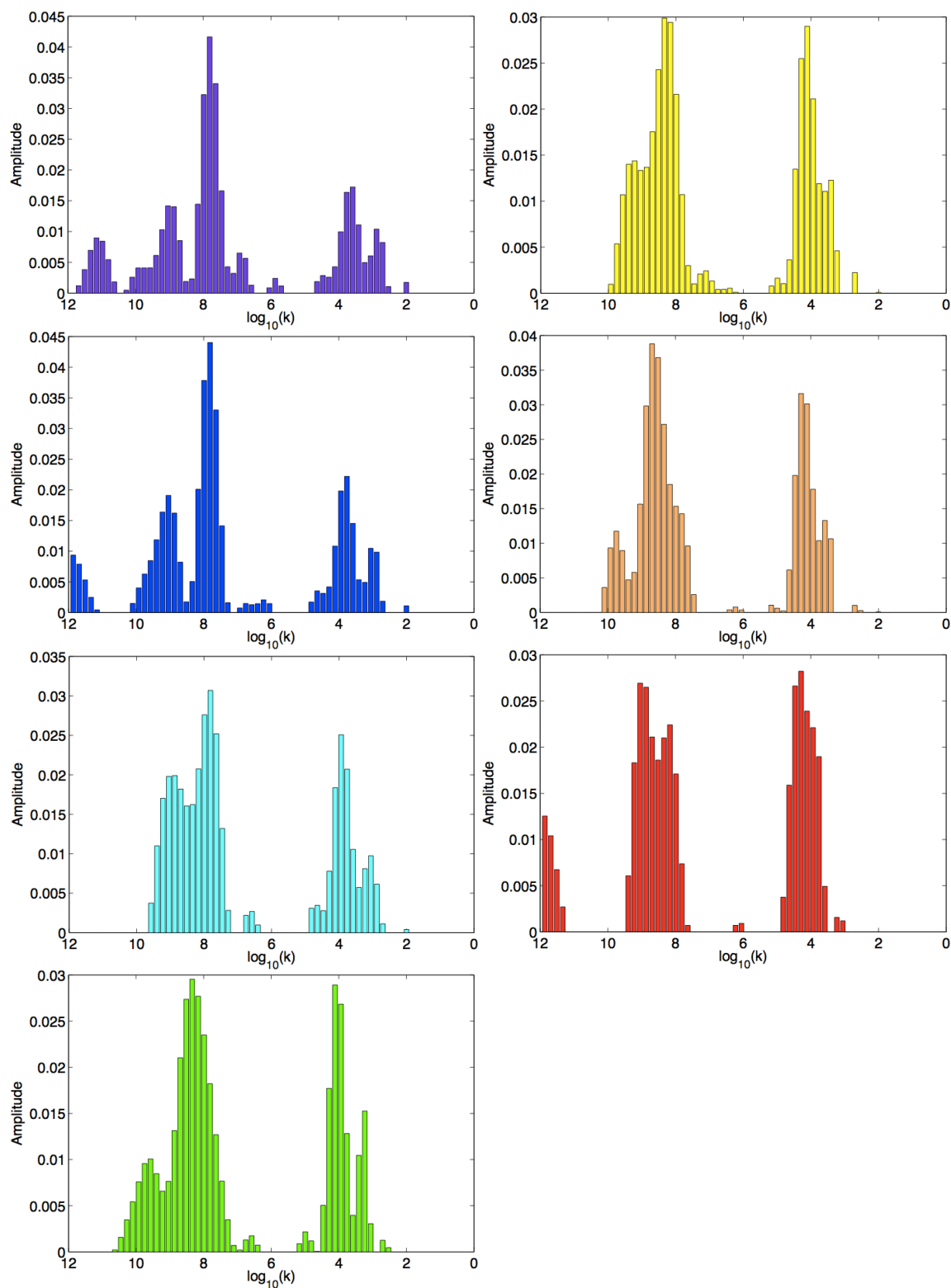


Figure C.7. Rate constant amplitudes from nns fitting of CO rebinding ps-to-ms TA data at various temperatures. Purple: 10 °C; Blue: 20 °C; Cyan: 30 °C; Green: 40 °C; Yellow: 50 °C; Orange: 60 °C; Red: 70 °C.

C.4. Notes for Chapter 6

Determination of ferrous/ferric ratio

We have used a Matlab script (appendix D) to determine the ferrous/ferric ratio in each intermediate spectrum during potentiometric titration. An example is shown below: all ferrous is cyan, all ferric is green, the experimental data is blue, and the model, using 70% of the ferrous component, and 30% of the ferric component, is shown in red dashes.

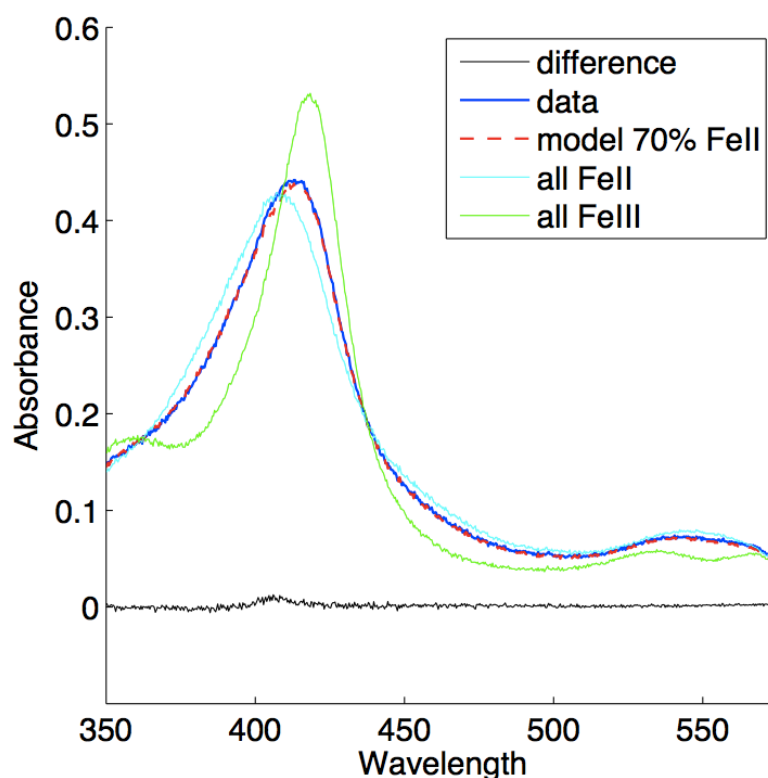


Figure C.8. Decomposition of a spectrum into ferric and ferrous components using the script: `spectraldeconvoluter.m`.

Reproducibility

The figure below shows potentiometric titrations for two batches of wild type P450 BM3. The two protein samples were expressed and purified in separate labs (dark

green: Arnold group; light green: Gray group), measurements were performed 3 months apart, using different electrodes (dark green: Pt mesh working, Pt wire counter, Ag/AgCl reference with vycor frit; light green: Au wire working, Pt wire counter, Ag/AgCl reference with salt bridge). The resulting potentials are within 20 mV of one another.

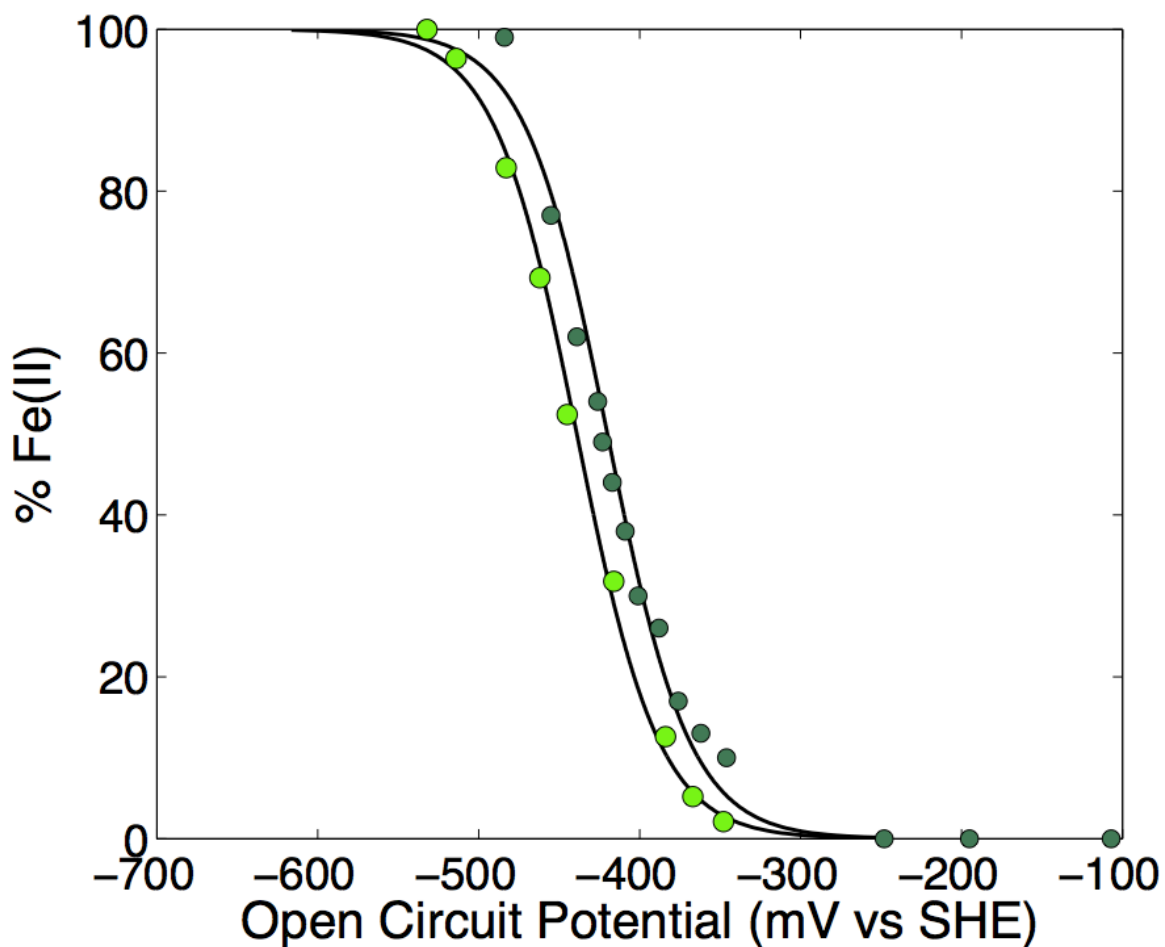


Figure C.9. Two separate potentiometric titrations of wild type P450 BM3.

*Appendix D***MATLAB SCRIPTS**

D.1. Plotting x,y data: MEplotter

The script **MEplotter** plots x and y data, including steady-state absorption spectra and single-wavelength transient absorption kinetics.

MEplotter

```
% TO PLOT WORKED-UP TRACES

i=1;
while i ~= 0
% READ DATAFILE
    [file,dirpath]=uigetfile('*.');
    if isequal(file,0) || isequal(dirpath,0)
        disp('no more')
        i=0;
        return
    end

    filet=[dirpath file];
    data=dlmread(filet);
% EXTRACT X AND Y
    xx=data(:,1);
    yy=data(:,2);
% PLOT
    a=rand(3);
    plot(xx,yy, 'color', a(1:3));
    %semilogx(xx,yy, 'color', a(1:3));

end
disp('voila!')
```

D.2. Time-resolved single-wavelength data workup

Raw data collected on the ns1 (nanosecond pulsed, single-wavelength) system are saved into a “ *.ns1” file. This must first be converted to intensity vs. time (luminescence) or ΔOD vs. time (transient absorption) using the ns1_read.m script provided by Dr. Jay Winkler (available on the bilrc.caltech.edu website.) The ns1_read.m script saves the new, two column data as a .txt file, with time in the first column and intensity/ ΔOD in the second.

D.2.1. Time-zero adjustment

The NSI instrumentation designates a “time-zero”. However, this designated time point is not always accurate, and can fluctuate by as much as 30 ns over the course of several months. All of the kinetics data in this Thesis are time-adjusted using **xadjuster** so that time-zero corresponds to the beginning of the rise in signal (within a few data points).

xadjuster

```
% xadjuster
% To adjust x data to time=0

i=1;
while i ~= 0

% READ DATAFILE
    [file,dirpath]=uigetfile('*.');
    if isequal(file,0) || isequal(dirpath,0)
        disp('no more')
        i=0;
        return
    end
    filet=[dirpath file];
    data=dlmread(filet);

%DETERMINE FILE PROPERTIES
    data=dlmread(filet);           %read raw file to var data
    len=length(filet);           %measure length of file name
    file1=filet(1:len-4);        %remove the .dat
    look=find(file1=='/');       %find all the / in the file
```

```

name
    maxf=max(look)+1;           %find the last / and index 1
value past it (file name)
    file2=file1(maxf:end);      %this was the file name
    file3=double(file2);       %file name converted to ascii

% EXTRACT X AND Y
    xx=data(:,1);
    yy=data(:,2);
% PLOT
    a=rand(3);
    plot(xx,yy,'b');
    hold

% ASK FOR X-ADJUST
    adjfactor=input('input the x offset (in seconds): ');
    disp(adjfactor)
    xnew=xx+adjfactor;
    plot(xnew,yy,'r')
    hold

%WRITE DATA TO FILE
    corcmp=[xnew yy];
    filecmp1=[file3, 100 46    116    120    116]; %Adds 'd.txt' to
the end of the file name
    filecmp2=char(filecmp1);
    dlmwrite(filecmp2,corcmp,'precision',14);      %write a file
of the adjusted xy data
    disp(filecmp2);                                %tell you the
name of the new file

end

```

D.2.2. Log-compression

Data that would be subjected to (multi)exponential fitting protocols were log-compressed, to avoid weighting of longer timepoints. The **compress** script was written to streamline this process. The function **logtimej** was modified from a script provided by Dr. Jay Winkler. In this case, **compress** sets the number of points per decade (ppd) to 600; the TA data in Chapters 2, 3, and most of Chapter 5 used this compression. Picosecond TA data (ps1), and picosecond-to-millisecond data overlays (Chapter 5 CO rebinding studies) were compressed to 200 ppd.

compress

```
%COMPRESSES WORKED UP DATA, AND WRITES A NEW FILE
clear

ans=input('how many traces do you want to compress? -->');
xi=[];
yi=[];

for i=1:ans
    %READ DATAFILE
    [file,dirpath]=uigetfile('/Users/Maraia/MATLAB/0Ahora/.dat');
% -> CHANGE THIS TO YOUR DIRECTORY
    if isequal(file,0) || isequal(dirpath,0)
% So it doesn't give an error if you press cancel
        disp('cancelled!')
        i=0;
        return
    end
    %file=input('enter file path','s');
    filet=[dirpath file];

    %DETERMINE FILE PROPERTIES
    data=dlmread(filet);           %read raw file to var data
    len=length(filet);           %measure length of file

name
    file1=filet(1:len-4);         %remove the .dat
    look=find(file1=='/');       %find all the / in the

file name
    maxf=max(look)+1;           %find the last / and index
1 value past it (file name)
    file2=file1(maxf:end);      %this was the file name
    file3=double(file2);       %file name converted to

ascii
```

```

    %EXTRACT X AND Y
    t=data(:,1); %read the time data out to
var xx          y=data(:,2); %read intensity out to yy
                ppd=600; %points per decade

                [tout,yout,wt] = logtimej(t,y,ppd);
                tout=tout';
                yout=yout';

    %WRITE DATA TO FILE
    corcmp=[tout yout];
    filecmp1=[file3, 99 46 116 120 116]; %Adds 'c.txt'
to the end of the file name
    filecmp2=char(filecmp1);
    dlmwrite(filecmp2,corcmp,'precision',14); %write a file
of the adjusted xy data
    disp(filecmp2); %tell you the
name of the new file
end
disp('compressed!');

```

logtimej

```

function [tout,yout,wt]=logtimej(t,y,ppd)
%
%   function to convert y=f(t) data from linear in time
%   to logarithmic in time
%
%   SYNTAX:
%       [tout,yout,wt]=logtime(t,y,ppd)
%
%       t is the input time vector, linearly spaced
%       y is the input y vector
%       ppd is the number of points per decade for the output
vectors
%       tout is the new time vector space logarithmically
%       yout is the new time vector space logarithmically
%       wt is vector of weights giving the number of points averaged
%           to get the new yout value

%Cut out time<0 data, which can't be plotted on a log scale
ncount=1;
while t(ncount)<=0
    ncount=ncount+1;
end
t=t(ncount:end);
y=y(ncount:end);

zt=length(t);
zy=length(y);
%
%
if zt ~= zy
    fprintf('ERROR: y and t vectors are different lengths')
else

    tmin=min(t);
    tmax=max(t);
%
    ltmin=log10(tmin);
    ltmax=log10(tmax);
%
    tt=ltmin:(1./(2.*ppd)):ltmax;
    tt=10.^tt;
    ztt=length(tt);
%
%
    icount=1;
    jcount=1;
    for i=2:2:ztt
        tout(jcount)=0;
        yout(jcount)=0;
        wt(jcount)=0;
        while (icount < zt) & t(icount) < tt(i)
            tout(jcount)=tout(jcount)+t(icount);
            yout(jcount)=yout(jcount)+y(icount);

```

```
        wt(jcount)=wt(jcount)+1;
        icount=icount+1;
    end
    if wt(jcount) ~= 0
        tout(jcount)=tout(jcount)./wt(jcount);
        yout(jcount)=yout(jcount)./wt(jcount);
        jcount=jcount+1;
    end
end
end
end
%
%
%
```

D.3. Data-splicing

In order to cover the (sub)nanosecond-to-second time range, log-compressed data taken at multiple timescales were spliced together to generate a complete trace. The script **overlayer** was used to import data for three timescales and multiplicatively scale at the users discretion. The function **combine** was used to designate splicing points between timescales, and generate the final combined data.

overlayer

```
%OVERLAYER
%plots fastamp, slowamp, and no-stirring traces, and asks
%for multipliers to adjust the fast and no-stirring traces
%so that they overlay better

tscale=input('To splice 2us, 100us, and 10ms data, enter 1. \n To
splice 100us, 10ms, 500ms data, enter 2. \n To splice 5ns, 50ns, and
2us-500ms data, enter 3 ->');

% READ DATAFILES
disp('select the fastest trace');

    [file,dirpath]=uigetfile('*.txt'); %opens a window to pick my file
    if isequal(file,0) || isequal(dirpath,0)
        disp('cancelled!')
        hold
        i=0;
        return
    end
    file1=[dirpath file];
    data1=dlmread(file1);

disp('select the corresponding middle trace-->');

    [file,dirpath]=uigetfile('*.txt'); %opens a window to pick my file
    if isequal(file,0) || isequal(dirpath,0)
        disp('cancelled!')
        hold
        i=0;
        return
    end
    file2=[dirpath file];
    data2=dlmread(file2);

disp('select the corresponding longest trace-->');
```

```

[file,dirpath]=uigetfile('*.txt'); %opens a window to pick my file
if isequal(file,0) || isequal(dirpath,0)
    disp('cancelled!')
    hold
    i=0;
    return
end
filet=[dirpath file];
data3=dlmread(filet);

% EXTRACT DATA X and Y DATA

x1=data1(:,1);
y1=data1(:,2);
x2=data2(:,1);
y2=data2(:,2);
x3=data3(:,1);
y3=data3(:,2);

% FIRST OVERLAY OF DATA
semilogx(x1,y1,'r');
hold
semilogx(x3,y3,'b');
semilogx(x2,y2,'g');
hold

mult2=1;
mult3=1;

seguir=input('does it need adjustment? (y/n ->)', 's');
if seguir == 'n'
    y1adj=y1;
    y2adj=y2;
    y3adj=y3;
end

while seguir == 'y';
    mult1=input('select a new first trace multiplier (default 1)->');
    if mult1 <= 0
        mult1=1;
        disp('defaulting multf=1');
    end
    mult2=input('select a new second trace multiplier (default 1)->');
    if mult2 <= 0
        mult2=1;
        disp('defaulting mults=1');
    end
    mult3=input('select a new third trace multiplier (default 1)->');
    if mult3 <= 0
        mult3=1;
        disp('defaulting multL=1');
    end
end

y1adj=mult1.*y1;
y2adj=mult2.*y2;
y3adj=mult3.*y3;

```

```
    semilogx(x1,y1adj,'r');
    hold
    semilogx(x3,y3adj,'b');
    semilogx(x2,y2adj,'g');
    hold

    seguir=input('does it need adjustment? (y/n)', 's');
end
disp(mult1);
disp(mult2);
disp(mult3);

datac=combine(tscale,x1,y1adj,x2,y2adj,x3,y3adj);

T=datac(:,1);
Y=datac(:,2);
TY=[T,Y];

keep=input('do you want to keep this combined trace? (y/n)->', 's');
if keep == 'y';
    [Savefile,Savedirpath,Savefilter]=uiputfile([dirpath,'*.txt'],'Save
overlaid traces',[dirpath,file]);
    eval(['save ',Savedirpath,Savefile, ' ' TY -ASCII -DOUBLE']);
end
```

combine

```

function datac=combine(tscale,x1,y1adj,x2,y2adj,x3,y3adj)
%function datac=combine(xf,yfadj,xs,ys)
%TO CREATE A SINGLE DATA SET COMBINING DATA FOR THREE TIMESCALES
% INPUTS
% vectors containing time (x) and delta OD (y) data
% key:f,s & L are fast amp, slow amp, and no stirring.
% yf and yL are adjusted (hence yfadj, yLadj) by a multiplier to
% remove dicontinuities between the data from the three time ranges
%
% OUTPUTS
% datac is a matrix with the combined time values in the first
% column, and delta OD values in the second column

%Timescales for different purposes
if tscale == 1

%For combining the 2us, 100us, 10ms data
    time1l = 1e-9;
    time1u = 1.5e-6;

    time2l=1.5e-6;
    time2u=0.5e-4;      %used to be 0.7e-4/0.4e-4

    time3l=0.5e-4;

elseif tscale == 2

%For combining the 400us, 10ms, 500ms data
    time1l = 1e-9;
    time1u = 5e-5;

    time2l=5e-5;
    time2u=1e-3;

    time3l=1e-3;  %USED to be 2.5e-3

elseif tscale == 3

%For combining the 5ns, 50ns, 2us-500ms data
    time1l = 1e-12;
    time1u = 3.5e-9;

    time2l=3.5e-9;
    time2u=35e-9;

    time3l=35e-9;

end

```

```

%ADJUSTING FIRST TRACE

    %cycles to find indexes of the lower and upper bound times

    xli=1;
    while x1(xli) <= time1l
        xli=xli+1;
    end

    xui=xli;
    while x1(xui) <=time1u
        xui=xui+1;
    end

    newx1=x1(1:xui);
    newy1=y1adj(1:xui);
    newx1=newx1';
    newy1=newy1';

% ADJUSTING SECOND TRACE

    %cycles to find indexes of the lower and upper bound times
    xli=1;
    while x2(xli) <= time2l
        xli=xli+1;
    end

    xui=xli;
    while x2(xui) <=time2u
        xui=xui+1;
    end

    newx2=x2(xli:xui);
    newy2=y2adj(xli:xui);
    newx2=newx2';
    newy2=newy2';

% ADJUSTING THIRD TRACE

    %cycles to find indexes of the lower bound times
    xli=1;
    while x3(xli) <= time3l
        xli=xli+1;
    end

    newx3=x3(xli:(end));
    newy3=y3adj(xli:(end));
    newx3=newx3';
    newy3=newy3';

%creates the combined trace
combx=[newx1 newx2 newx3];
comby=[newy1 newy2 newy3];

combx=combx';
comby=comby';

```

```
hold
semilogx(combx, comby, 'y');
hold

datac=[];
datac(:,1)=combx;
datac(:,2)=comby;
end
```

D.4. Singular Value Decomposition

These scripts use truncated, generalized singular value decomposition (from Regularization Tools, Per Christian Hansen) to determine the number of kinetic components in single-wavelength transient absorption kinetics traces. This can be done for a single kinetics trace using **svder1**, or accomplished and overlaid for six wavelengths using **svderMulti**.

svder1

```
logkpace=0:log10(2):10;
kspace=10.^logkpace;
t=input('define the time vector ');
logAspace=-t*kspace;
Aspace=exp(logAspace);

Adata=input('define the absorbance data vector ');

L=get_l(34,1);
[UU sm XX]=cgsvd(Aspace,L);

figure
trunc=input('enter the truncation value (<34) ');
X_L=tgsvd(UU,sm,XX,Adata,trunc);
bar(log10(kspace),X_L);

Bcalc=Aspace*X_L;
figure
semilogx(t,Adata,'b',t,Bcalc,'r')
```

svderMulti

```

%svderMulti
%Does SVD for 6 wavelengths

logkspace=0:log10(2):10;
kspace=10.^logkspace;
t=input('define the time vector ');
logAspace=-t*kspace;
Aspace=exp(logAspace);

Adata=input('define the absorbance data MATRIX ');

L=get_l(34,1);
[UU sm XX]=cgsvd(Aspace,L);

len=length(kspace);
X_LMat=zeros(len,6);
trunc=input('enter the truncation value (<34) ');

for icount = 1:6
    X_L=sgsvd(UU,sm,XX,Adata(:,icount),trunc);
    X_LMat(:,icount)=X_L;           %put it back in a big matrix
end

%multiplotting
col(1)='k';
col(2)='b';
col(3)='c';
col(4)='g';
col(5)='y';
col(6)='r';
col=col(:);

figure
hold

for ocount=1:30;
    barx(:,1)=X_LMat(ocount,:);
    barx(:,2)=[1; 2; 3; 4; 5; 6];
    barx(:,3)=abs(barx(:,1));
    barz=sortrows(barx,-3);
    for incount=1:6;
        ind=barz(incount,2);
        bar(log10(kspace(ocount)),barz(incount,1),0.25,col(ind));
        %pause(1)
    end
end
end

```

D.5. Multiexponential fitting

A number of scripts are used to fit TA data to a sum of multiexponentials. **nonlinear_fitter4** fits data to a sum of three and four exponentials, to compare fits. It uses the function **autoresider** to plot residuals and autocorrelation of residuals; these are used to determine whether deviations between data and fit are random or systematic (an additional exponent is indicated). **MExpG_Fitter** is used to globally fit data at multiple wavelengths to a sum of exponentials (defined by **MExpG**), using defined upper and lower bounds and initial guesses (**MExpGvalues**).

nonlinear_fitter4

```
%fitting kinetics data to a sum of exponentials

%getting data
xdata=input('define the x data:\n');
ydata=input('define the y data:\n');
figure
semilogx(xdata,ydata,'c');
hold
%defining fitting & parameters
disp('we will be fitting to a sum of 3, 4 exponentials');

ft=fittype('a.*exp(-x.*2.2e7)+b.*exp(-x.*k2)+c.*exp(-x.*k3)+f');
%      a      b      c      f      k2      k3
pu=[ 0.1,   0.3,   1,    1,    1e7,   5e6];
pl=[-0.1,  -0.4,  -1,   -1,   1e5,   5e2];
st=[-0.02, -0.15, 0.1,   0,    1e6,   5e3];

opts=fitoptions(ft);
opts=fitoptions(opts,'lower',pl,'upper',pu,'startpoint',st);
[f,gof]=fit(xdata,ydata,ft,opts);
disp(f);
xcalc=xdata;
ycalc=feval(f,xcalc);
plot(xcalc,ycalc,'r');

%used for all wavelengths
ft2=fittype('a.*exp(-x.*2.2e7)+b.*exp(-x.*k2)+c.*exp(-x.*k3)+d.*exp(-
x.*k4)+f');
%      a      b      c      d      f      k2      k3      k4
pu2=[ 0.1,   0.3,   1,    1,    1,    5e6,   5e5   1e4];
pl2=[-0.1,  -0.4,  -1,   -1,   -1,   5e5,   5e4   1e1];
```

```
st2=[-0.02, -0.15, 0.1, 0, 0, 1e6, 1e5 1e3];
%pu=input('define upper bounds for a-e,k2-k5: 10 parameters\n');
%pl=input('define lower bounds for a-e,k2-k5: 10 parameters\n');
%st=input('define starting values for a-e,k2-k5: 10 parameters\n');

opts=fitoptions(ft2);
opts=fitoptions(opts, 'lower',pl2, 'upper',pu2, 'startpoint',st2);
[f,gof]=fit(xdata,ydata,ft2,opts);
disp(f);

%numpts=length(xdata);
%numpts=1000;
%xmin=log10(min(xdata));
%xmax=log10(max(xdata));
%xcalc=logspace(xmin,xmax,numpts);
ycalc2=feval(f,xcalc);
plot(xcalc,ycalc2, 'b');
hold
autoresider(ydata,ycalc,ycalc2);
```

autoresider

```

function [AC_resid,AC_resid2]=autoresider(y,ycalc,ycalc2)
%
%
%   Calculate and plot the autocorrelation of the residuals between
%   ycalc and y
%
%   Syntax: [AC_resid]=autoresid(y,ycalc);
%
%
y=y(:);
ycalc=ycalc(:);
ycalc2=ycalc2(:);
%
len=length(y);
jlen=floor(len./1.1);
%
resid=y-ycalc;
resid2=y-ycalc2;
%
acorrin=zeros(len,jlen);
acorrin2=zeros(len,jlen);
%
for aij=1:jlen
    acorrin(1:len-aij,aij)=resid(aij+1:len); %
    acorrin2(1:len-aij,aij)=resid2(aij+1:len); %
end
mvect=len-1:-1:len-jlen;
autoc=(resid'*acorrin)./mvect;
autoc2=(resid2'*acorrin2)./mvect;
AC_resid=autoc./((resid'*resid)./len);
AC_resid2=autoc2./((resid2'*resid2)./len);
%
figure
subplot(2,1,1)
plot(y-ycalc,'r')
hold
plot(y-ycalc2,'b')
subplot(2,1,2)
plot(AC_resid,'r')
hold
plot(AC_resid2,'b')

return

```

MExpGFitter

```

%MultiExponential Global Fitter (fits to 6 wavelengths)
%asking for data
tvector=input('define the time vector -> ');
dODdata=input('define the matrix of absorbance data -> ');

x=tvector;
%defining initial values and bounds
[values,ubound,lbound] = MExpGvalues;

%defining fit parameters
fxn=@(values,x) MExpG(values,x);
optm=optimset('lsqcurvefit');
optm=optimset(optm,'Display','iter');
optm=optimset(optm,'TolFun',1e-14);
optm=optimset(optm,'TolX',1e-14);

bfit=lsqcurvefit(fxn,values,tvector,dODdata,lbound,ubound,optm);
bfite=bfit';
ks=bfite(25:end);
display(bfite)
%display(ks)

A=MExpG(bfit,tvector);
for icount = 1:6
subplot(2,3,icount)
semilogx(tvector,dODdata(:,icount),'b',tvector,A(:,icount),'r');
end

```

MExpG

```
function [A]=MExpG(values,tvector)
%UNTITLED Summary of this function goes here
% Detailed explanation goes here
a=values(1:6);
b=values(7:12);
c=values(13:18);
f=values(19:24);
k=values(25:27);
x=tvector;

%lumdec=2.7e7;

A1=(a(1).*exp(-x.*k(1))+b(1).*exp(-x.*k(2))+c(1).*exp(-x.*k(3))+f(1));
A2=(a(2).*exp(-x.*k(1))+b(2).*exp(-x.*k(2))+c(2).*exp(-x.*k(3))+f(2));
A3=(a(3).*exp(-x.*k(1))+b(3).*exp(-x.*k(2))+c(3).*exp(-x.*k(3))+f(3));
A4=(a(4).*exp(-x.*k(1))+b(4).*exp(-x.*k(2))+c(4).*exp(-x.*k(3))+f(4));
A5=(a(5).*exp(-x.*k(1))+b(5).*exp(-x.*k(2))+c(5).*exp(-x.*k(3))+f(5));
A6=(a(6).*exp(-x.*k(1))+b(6).*exp(-x.*k(2))+c(6).*exp(-x.*k(3))+f(6));

A=[A1, A2, A3, A4, A5, A6];
end
```

MExpGvalues

```

function [values,ubound,lbound] = MExpGvalues
%UNTITLED2 Summary of this function goes here
% Detailed explanation goes here

%defining initial values and bounds
%'a' defines six pre-exponential terms corresponding to the first rate
%constant, 'b' defines those pre-exponentials for the second rate
constant,
%and the same for 'c'
a=[-0.2, -0.2, -0.2, -0.2, -0.2, -0.2];
b=[-0.15, -0.15, -0.15, -0.15, -0.15, -0.15];
c=[0.1, 0.1, 0.1, 0.1, 0.1, 0.1,];
f=[0.01, 0.01, 0.01, 0.01, 0.01, 0.01];
k=[2e7, 6e4, 1e3];           %these are the three exponential terms

values=[a b c f k];

%upper bounds
ua=[1, 1, 1, 1, 1, 1];
ub=[1, 1, 1, 1, 1, 1];
uc=[1, 1, 1, 1, 1, 1];
uf=[1, 1, 1, 1, 1, 1];
uk=[3e8, 5e6, 1e4];

ubound=[ua ub uc uf uk];

%lower bounds
la=[-1, -1, -1, -1, -1, -1];
lb=[-1, -1, -1, -1, -1, -1];
lc=[-1, -1, -1, -1, -1, -1];
lf=[-1, -1, -1, -1, -1, -1];
lk=[1e6, 5e3, 5e0];

lbound=[la lb lc lf lk];

end

```

D.6. Nonnegative least squares analysis

Multiexponential kinetics data (with all positive magnitudes), such as fluorescence decays or CO rebinding in substrate-free P450 CYP119, can be examined using nonnegative least squares (nnls) fitting. This procedure requires that the data be log-compressed, and that the first time point be exactly zero. The **nnls_prep** script sets the initial time to zero and can be used to normalize data; the script **nnls_grad_reg_r2_KT** (written by Jay Winkler and modified by Kana Takematsu) does the fitting analysis. To further analyze the nnls outputs, the script **Panalyzer** and function **Pmoments** allow the user to define populations within the nnls histogram of rate constants and amplitude, and determine statistics (integrated amplitudes, first moment, and second and third centered moments) for each population.

nnls_prep

```
% nnls_prep
% This script selects the maximum absorbance data point from x,y TA
data, sets that time point to t=0, and
% normalizes Y (absorbance) data

i=1;
while i ~= 0

% READ DATAFILE
    [file,dirpath]=uigetfile('*.');
    if isequal(file,0) || isequal(dirpath,0)
        disp('no more')
        i=0;
        return
    end
    filet=[dirpath file];

%DETERMINE FILE PROPERTIES
    data=dlmread(filet);
    len=length(filet);
    file1=filet(1:len-4);
    look=find(file1=='/');
name
    maxf=max(look)+1;
value past it (file name)
    file2=file1(maxf:end);

%read raw file to var data
%measure length of file name
%remove the .dat
%find all the / in the file
%find the last / and index 1
%this was the file name
```

```

file3=double(file2);           %file name converted to ascii

% EXTRACT X AND Y
xx=data(:,1);
yy=data(:,2);

% DATA ADJUSTMENTS
% [myy,indmyy]=max(yy);      %find value and index of max
Y-data point
indmyy=21;
xadj=xx(indmyy);             %find time value of max Y-data
point
xtrunc=xx(indmyy:end);      %truncating rise from X-data
ytrunc=yy(indmyy:end);      %truncating rise from Y-data
xnew=xtrunc-xadj;           %setting first data point as
time zero
% ynorm=ytrunc/myy;         %normalizing Y-data to max Y-
data point

% PLOT
plot(xx,yy,'r')
plot(xnew,ytrunc,'b');

%WRITE DATA TO FILE
corcmp=[xnew ytrunc];
filecmp1=[file3, 95 116 48 110 46 116 120 116];
%Adds '_t0n.txt' to the end of the file name
filecmp2=char(filecmp1);
dlmwrite(filecmp2,corcmp,'precision',14); %write a file
of the adjusted xy data
disp(filecmp2); %tell you the
name of the new file

end

```

nmls_grad_reg_r2_KT

```

% Script to read [t,y] data from a file
% Fit using chisq and first derivative constraint
% with lsqnonneg and scan lambda to maximize breadth.
%
%
clear all
close all
%
%lambda_min_def=0.001;
%lambda_max_def=10;
lambda_min_def=0.01;
lambda_max_def=50;
lambda_inc_def=1.5;
k_inc_def=1.5;
%
H0=figure;
%
[FileName,PathName] = uigetfile('*.txt') ;
filet=[PathName FileName];
xy=dlmread(filet);
%[a,b]=size(xy);
%if (a~=2)&(b~=2)
% return
%elseif (a==2)
% xy=xy';
%end
%
x=xy(:,1);
y=xy(:,2);
warning off
wt=1./sqrt(y);
wttest=isfinite(wt);
wttest=isinf(1./wttest);
sqrt(y+wttest);
wt=1./sqrt(abs(y+wttest));
wt=[wt(1:214); 3*wt(215:length(y))];
%kana: add abs and define new wt
%MUST REMEMBER TO change this value for each data set!!!
warning on
%
%
chk3=-1;
while chk3 < 0
chk=-1;
prompt={'Enter the minimum value for \lambda',
'Enter the maximum value for \lambda',
'Enter the ratio of adjacent \lambda values',
'Enter the ratio of adjacent rate constants'};
dlg_title='Fitting Parameters (enter ? for help)';
numlines=1;
options.Resize='on';
options.WindowStyle='normal';
options.Interpreter='tex';
helpstr1=['The program minimizes the sum of the squared deviations

```

```

between calculated and experimental intensities (chi-squared) AND the
sum of the squared gradient of the P(k) function. The weighting factor
between these two functions is lambda. Small \lambda values give more
weight to chi-squared minimization. Large lambda values give more
weight to P(k) gradient minimization. The program will scan from a
minimum to a maximum value of lambda. The scanned lambda values are
logarithmically spaced. This query asks for the maximum and minimum
values of lambda as well as the ratio of adjacent lambda values.'];
helpstr2=['The k-space vector is logarithmically spaced. This query
asks for the raio of adjacent k values.'];
help1=' ';
help2=' ';
while chk < 0

defanswer={num2str(lambda_min_def),num2str(lambda_max_def),num2str(lamb
da_inc_def),num2str(k_inc_def),,};
    answer=inputdlg(prompt,dlg_title,numlines,defanswer,options);
    ans1=cell2mat(answer(1));
    ans2=cell2mat(answer(2));
    ans3=cell2mat(answer(3));
    ans4=cell2mat(answer(4));
    %
    chk=1;
    hep1=0;
    hep2=0;
    if ishandle(help1)==1
        close(help1);
    end
    if ishandle(help2)==1
        close(help2);
    end
    %
    if (isempty(ans1))
        chk=-1;
    elseif ans1(1) == '?'
        hep1=1;
        chk=-1;
    else
        lambda_min=str2num(ans1);
        if isempty(lambda_min)
            chk=-1
        else
            lambda_min_def=lambda_min;
        end
    end
    %
    if (isempty(ans2))
        chk=-1;
    elseif ans2(1) == '?'
        hep1=1;
        chk=-1;
    else
        lambda_max=str2num(ans2);
        if isempty(lambda_max)
            chk=-1
        else
            lambda_max_def=lambda_max;
        end
    end
end

```

```

end
%
if (isempty(ans3))
    chk=-1;
elseif ans3(1) == '?'
    hep1=1;
    chk=-1;
else
    lambda_inc=str2num(ans3);
    if isempty(lambda_inc)
        chk=-1
    else
        lambda_inc_def=lambda_inc;
    end
end
%
if (isempty(ans4))
    chk=-1;
elseif ans4(1) == '?'
    hep2=1;
    chk=-1;
else
    k_inc=str2num(ans4);
    if isempty(k_inc)
        chk=-1
    else
        k_inc_def=k_inc;
    end
end
%
if (hep1 == 1)
    help1=helpdlg(helpstr1,'Lambda Values')
    hpos1=get(help1,'Position');
    set(help1,'Position',[hpos1(1)+0.5.*hpos1(3),
hpos1(2)+0.5.*hpos1(4), hpos1(3), hpos1(4)]);
end
%
if (hep2 == 1)
    help2=helpdlg(helpstr2,'k-ratio')
    hpos2=get(help2,'Position');
    set(help2,'Position',[hpos2(1)+0.5.*hpos2(3),
hpos2(2)+0.5.*hpos2(4), hpos2(3), hpos2(4)]);
end
%
end
%
%lambda_max
%lambda_min
%lambda_inc
%k_inc
%
%
loglambda=log10(lambda_min):log10(lambda_inc):log10(lambda_max);
lambda=10.^loglambda;
lenlam=length(lambda);
%
%
Off_set=0;

```

```

chk=-1;
menprompt='Offset Rate Constant';
menopt1='YES';
menopt2='NO';
menopt3='Help';
helpstr3='If the data do not decay to zero, a slow rate constant can be
added to the k-space vector to produce an offset in the data. This
query asks if you want to include that offset rate constant.';
help3=' ';
while chk < 0
    %
    choice=menu(menprompt,menopt1,menopt2,menopt3);
    %
    if ishandle(help3)==1
        close(help3);
    end
    if choice == 1
        Off_set=1;
        chk=1;
    elseif choice == 2
        Off_set=0;
        chk=1;
    elseif choice ==3
        help3=helpdlg(helpstr3,'Weighting');
    end
end
%
%
iwt=0;
chk=-1;
menprompt='Data Weighting';
menopt1='No weighting';
menopt2='Weight y(i) values by 1/sqrt(yi)';
menopt3='Weight y(i) values by 1/yi';
menopt4='Help';
helpstr4='No weighting minimizes sum of {yi(exp)-yi(calc)}^2; higher
intensity values carry more weight. The uncertainty in each yi(exp)
value is approximately sqrt(yi(exp)). The sum of {[yi(exp)-
yi(calc)]/sqrt(yi(exp))}^2 is used to generate reduced chi-squared
values. The optimum result is reduced chi-squared = 1. The sum of
{[yi(exp)-yi(calc)]/yi(exp)}^2 minimizes the fractional deviations of
experiment from calculated values.';
help4=' ';
while chk < 0
    %
    choice=menu(menprompt,menopt1,menopt2,menopt3,menopt4);
    %
    if ishandle(help4)==1
        close(help4);
    end
    %
    if choice == 1
        WT=eye(length(y));
        chk=1;
    elseif choice == 2
        WT=diag(wt);
        chk=1;
    elseif choice == 3

```

```

        WT=diag(wt);
        WT=WT.^2;
        chk=1;
    elseif choice == 4
        help4=helpdlg(helpstr4,'Weighting');
    end
end
%
chk=-1;
menprompt='Gradient Method';
menopt1='Two-point';
menopt2='Three-point';
menopt3='Help';
helpstr5='The two-point gradient for P(ki) is [P(k(i+1))-
P(k(i))]/delta. The three-point gradient for P(ki) is calculated by
fitting the three points, [P(k(i-1)), P(k(i)), P(k(i+1))] to a second
order polynomial and calculaing the gradient from the polynomial
coefficients.';
help5=' ';

while chk < 0
    %
    choice=menu(menprompt,menopt1,menopt2,menopt3);
    %
    if ishandle(help5)==1
        close(help5);
    end
    %
    if choice == 1
        grad=1;
        chk=1;
    elseif choice == 2
        grad=2;
        chk=1;
    elseif choice == 3
        help5=helpdlg(helpstr5,'Weighting');
    end
    %
end
%
%kana: what is the appropriate kmax?
len=length(y);
kmax=5./(x(2)-x(1));
kmax=min(kmax,1e12);
kmin=0.2./x(len);
kmin=1.0./x(len);
%
%
lkmin=log10(kmin);
lkmax=log10(kmax);
incr=log10(k_inc);
%
lkmin=floor(lkmin);
lkmax=ceil(lkmax);
logk=lkmin:incr:lkmax;
%
k=10.^logk;
if (Off_set == 1)

```

```

    k=[k(1)./100,k];
end
%
%
lenk=length(k);
jlen=floor(len./2);

%
%
A=x*k;
A=exp(-A);
%
if (grad == 1)
    P_reg=2.*ones(lenk,1);
    P_reg(1,1)=1;
    P_reg(lenk,1)=1;
    P_reg_3=zeros(lenk,1);
    AA=diag(P_reg);
    P_reg_2=-1.*ones(lenk-1,1);
    AA1=diag(P_reg_2,1);
    AA2=diag(P_reg_2,-1);
else
    P_reg=2.*ones(lenk,1);
    P_reg(1,1)=1;
    P_reg(lenk,1)=1;
    P_reg_3=zeros(lenk,1);
    AA=diag(P_reg);
    P_reg_2=-1.*ones(lenk-2,1);
    AA1=diag(P_reg_2,2);
    AA2=diag(P_reg_2,-2);
end
%
AA=AA+AA1+AA2;
%
%
for ijk=1:lenlam
    %
    AA_lam=lambda(ijk).*AA;
    %
    Aw=WT*A;
    AAA=[Aw; AA_lam];
    yw=WT*y;
    YY=[yw; P_reg_3];
    %
    Pr=lsqnonneg(AAA,YY);
    gradsq(ijk)=(AA*Pr)'*(AA*Pr);
    %
    chisq(ijk)=(yw-Aw*Pr)'*(yw-Aw*Pr);
    chisq(ijk)=chisq(ijk)./(length(y)-length(Pr)-1);
    %kana: deleted as necessary?
    ycalc(:,ijk)=A*Pr;
    resid(:,ijk)=y-ycalc(:,ijk);
    resid(:,ijk)=resid(:,ijk).*wt;
    %kana: wt is okay sometimes? the autocorrelation makes more sense
if it
    %is weighted?
    %

```

```

acorrin=zeros(len,jlen);
for aij=1:jlen
    acorrin(1:len-aij,aij)=resid(aij+1:len,ijk); %"ijk" added
4/27/2010 jrw
end
mvect=len-1:-1:len-jlen;
autoc(ijk,:)=(resid(:,ijk)*acorrin)./mvect;
autoc(ijk,:)=autoc(ijk,:)./((resid(:,ijk)*resid(:,ijk))./len);
%
Pok(:,ijk)=Pr;
%
subplot(3,2,1)
semilogx(x,y-ycalc(:,ijk),'r',[min(x) max(x)],[0 0],'k')
%semilogx(x,resid(:,ijk),'r',[min(x) max(x)],[0 0],'k')
%kana replace
A331=axis;
axis([min(x) max(x) A331(3) A331(4)]);
xlabel('time');
ylabel('y_{obsd}-y_{calc}');
title(['Residuals: {\chi}^2 = ',num2str(chisq(ijk),'%4g'),';
(grad(P))^2 = ',num2str(gradsq(ijk),'%4g')]);
%
subplot(3,2,3)
[aa,bb]=size(autoc(ijk,:));
plot([1:bb],autoc(ijk,:),'r',[1,bb],[0 0],'k')
xlabel('Correlation Channel');
ylabel('Cr(j)');
title('Autocorrelation of Residuals');
%
subplot(3,2,5)
semilogx([min(x) max(x)],[0 0],'k',x,y,'r',x,ycalc(:,ijk),'k')
xlabel('time');
ylabel('Intensity');
title(['{\lambda} = ',num2str(lambda(ijk),'%4g')]);
%
subplot(3,2,4)
HH=loglog(lambda(1:ijk),chisq(1:ijk),'ro-');
xlabel('\lambda');
ylabel('{\chi}^2');
title('{\chi}^2 vs. \lambda');
%
subplot(3,2,2)
bar(log10(k),Pr,'r')
axis([min(log10(k)), max(log10(k)), 0, 1.025.*max(Pr)])
xlabel('log(k)');
ylabel('P(k)');
title(['{\lambda} = ',num2str(lambda(ijk),'%4g')]);
%
subplot(3,2,6)
loglog(chisq(1:ijk),gradsq(1:ijk),'ro-')
xlabel('{\chi}^2');
ylabel('(grad(P))^2');
title(['L-curve: {\lambda} = ',num2str(lambda(ijk),'%4g')]);
%
drawnow
end
%
subplot(3,2,4)

```

```

title('LEFT-CLICK on a point to see its fit, residual, and
distribution.', 'FontSize', 12, 'Color', 'b', 'FontWeight', 'Bold');
drawnow
%
chk2=-1;
menprompt='Select an Option';
menopt1='Chose a different point';
menopt2='Refit the data';
menopt3='EXIT THE PROGRAM';
while chk2 < 0
    [xtest,ytest, button]=ginput(1);
    %
    while (button == 1)
        %
        [lambdatest,ijktest]=min(abs(lambda-xtest));
        %
        subplot(3,2,1)
        semilogx(x,y-ycalc(:,ijktest),'r',[min(x) max(x)], [0 0], 'k')
        %semilogx(x,resid(:,ijktest),'r',[min(x) max(x)], [0 0], 'k')
        %kana
        A331=axis;
        %axis([min(x) max(x) A331(3) A331(4)]);
        axis([x(450) x(length(y)) -0.005 0.005])
        %kana: manually adjust 0.1 to 0.005.
        xlabel('time');
        ylabel('y_{obsd}-y_{calc}');
        title(['Residuals: {\chi}^2 =
',num2str(chisq(ijktest),'%4g'),' (grad(P))^2 =
',num2str(gradsq(ijktest),'%4g')]);
        %
        subplot(3,2,3)
        plot([1:bb], autoc(ijktest,:), 'r', [1,bb], [0 0], 'k')
        %axis ([1 bb -0.1 0.1])
        %kana
        xlabel('Correlation Channel');
        ylabel('Cr(j)');
        title('Autocorrelation of Residuals');
        %
        subplot(3,2,5)
        semilogx([min(x) max(x)], [0
0], 'k', x, y, 'r', x, ycalc(:,ijktest), 'k')
        xlabel('time');
        ylabel('Intensity');
        title(['{\lambda} = ', num2str(lambda(ijktest), '%4g')]);
        %
        subplot(3,2,4)
        loglog(lambda(1:ijk), chisq(1:ijk), 'ro-')
        hold on
        h1=loglog(lambda(ijktest), chisq(ijktest), 'bo');
        set(h1, 'MarkerFaceColor', 'b');
        hold off
        xlabel('\lambda');
        ylabel('{\chi}^2');
        title('LEFT-CLICK on a point to see its fit, residual, and
distribution; RIGHT-CLICK to
proceed.', 'FontSize', 12, 'Color', 'b', 'FontWeight', 'Bold');
drawnow
%

```

```

subplot(3,2,2)
bar(log10(k),Pok(:,ijktest),'r')
axis([min(log10(k)), max(log10(k)), 0,
1.025.*max(Pok(:,ijktest))])
xlabel('log(k)');
ylabel('P(k)');
title(['{\lambda} = ',num2str(lambda(ijktest),'%4g')]);
%
subplot(3,2,6)
loglog(chisq(1:ijk),gradsq(1:ijk),'ro-')
hold on
h2=loglog(chisq(ijktest),gradsq(ijktest),'bo');
set(h2,'MarkerFaceColor','b');
hold off
xlabel('{\chi}^2');
ylabel('(grad(P))^2');
title(['L-curve: {\lambda} = ',num2str(lambda(ijk),'%4g')]);
%
drawnow
%
[xtest,ytest, button]=ginput(1);
%
%
end
%
choice=menu(menprompt,menopt1,menopt2,menopt3);
%
if choice == 1
    chk2=-1;
elseif choice == 2
    chk2=1;
    chk3=-1;
elseif choice == 3
    chk2=1;
    chk3=1;
end
%
close(H1);
%
close(H2);
%
close(H3);
%kana
end
%
end
%kana: insert saving
pause(3)
[filename2,PathName2] = uiputfile('*.txt','choose directory','bozo');
[pathstr1,name1,ext1] = fileparts(filet);
filet2=[PathName2,name1];
dlmwrite(strcat(strcat(filet2,'_kPok'),' .dat'),[log10(k)',Pok])
dlmwrite(strcat(strcat(filet2,'_residual'),' .dat'),[x,repmat(y,1,size(y
calc,2))-ycalc])
dlmwrite(strcat(strcat(filet2,'_lambda'),' .dat'),[lambda'])
dlmwrite(strcat(strcat(filet2,'_autoc'),' .dat'),[autoc'])
close all hidden
%
%
```

Panalyzer

Written to determine population statistics, given a histogram (such as the population distributions from fitting of CO rebinding data, Chapter 5).

```
%Panalyzer

% READ DATAFILE
[file,dirpath]=uigetfile('*.');
if isequal(file,0) || isequal(dirpath,0)
    disp('no more')
    i=0;
    return
end
filet=[dirpath file];
data=dlmread(filet);

% EXTRACT X AND Y
ks=data(:,1);
Poks=data(:,2:end);

% GET INDEX
%ind=17;
ind=input('what is the index for the desired P values? ');
desPoks=Poks(:,ind);

% PLOT
%a=rand(3);
figure
bar(ks,desPoks,'r');
hold
%semilogx(xx,yy,'color',a(1:3));

% SELECT POPULATIONS
klen=length(ks)
n=0;

    seguir=input('would you like to analyze a population? (y/n):
','s');

    col(1)='y';
    col(2)='g';
    col(3)='c';
    col(4)='b';
    col(5)='m';
    col(6)='k';

    while seguir=='y'
        redo='y';
        n=n+1;
        while redo=='y'
```

```

        hold
        bar(ks,desPoks,'r');
        hold
        Plow(n)=input('enter the lower k(index) for the population:
');
        Pup(n)=input('enter the upper k(index) for the population:
');
        bar(ks(Plow(n):Pup(n)),desPoks(Plow(n):Pup(n)),col(n))
        redo=input('would you like to select a different region for
this population? (y/n): ','s');
        end
        seguir=input('would you like to select another population?
(y/n): ','s');
        end

        %DETERMINE STATISTICS (MOMENTS)
        for m=1:n

[tempint,tempcentro,tempcmoms]=Pmoments(desPoks(Plow(m):Pup(m)),ks(Plow
(m):Pup(m)));
        Pint(m)=tempint;
        Pcentro(m)=tempcentro;
        Pcmoms(:,m)=tempcmoms;
        end

Pint
Pcentro
Pcmoms

```

Pmoments

```

function [Plint,centro,cmoms] = Pmoments(Ps,ks)
%UNTITLED Summary of this function goes here
% Detailed explanation goes here

%Ps are the populations
%ks are the log10 of the rate constants

centro=sum(Ps.*ks)./sum(Ps);
centks=ks-centro;

Plint=trapz(Ps);           %Integrating the population distribution

%uncentered moments
% for n=1:4
%     moms(n)=sum(Ps.*(ks.^n))./sum(Ps);
%     moms=moms';
% end

%centered moments
for n=1:4
    cmoms(n)=sum(Ps.*(centks.^n))./sum(Ps);
    cmoms=cmoms';
end

end

```

D.7. Hopping Maps

The script **MapMaker** generates Hopping Maps using **MapPlotter**, **MapValues**, **tauM**, and **tauETM**.

MapMaker

```
%MapMaker - A GUI

%MapMaker takes user input for various electron transfer parameters,
%and a desired map range, and runs the hopping mapper programs
(MapValues,MapPlotter)

numlines=1;
halt1=0;
halt2=0;

%Acquiring Electron Transfer Parameters
prompt1={'temperature (K)', 'A-I distance (A)', '\beta step 1
(1/A)', '\lambda step 1 (eV)', 'I-B distance (A)', '\beta step 2
(1/A)', '\lambda step 2 (eV)', 'A-B distance (A)', '\beta single step
(1/A)', '\lambda single step (eV)'};
defaults1={'298', '8.1', '1.1', '0.8', '12.8', '1.1', '0.8', '19.4', '1.1', '0.8
'};
options.Interpreter='tex';

ETparams=inputdlg(prompt1, 'ET Parameters', numlines, defaults1, options);

%Acquiring the Hopping Map Range
prompt2={'\Delta G(total) min (eV)', '\Delta G(total) max
(eV)', '\Delta G(1^s^t step) min (eV)', '\Delta G(1^s^t step) max
(eV)', 'resolution (eV)', 'contour interval (-log(sec))'};
defaults2={'-1.5', '0', '-0.4', '0.3', '0.005', '0.2'};
options.Interpreter='tex';
mapRange=inputdlg(prompt2, 'Map Parameters', numlines, defaults2, options);

%THE LOOP - repeats until the user presses 'cancel'
while halt1~= 1 && halt2~=1

%converting user input values to useable numbers
conv1=char(ETparams);
convETparams=str2num(conv1);
conv2=char(mapRange);
convmapRange=str2num(conv2);

%Making the HoppingMap
[dGT, dG1, taoslog]=MapValues(convETparams, convmapRange);
%generates map values
MapPlotter(dGT, dG1, taoslog, convETparams, convmapRange);
%plots the map
```

```
%Repeating the cycle
ETparams=inputdlg(prompt1, 'ET Parameters', numlines, ETparams, options);
halt1=isempty(ETparams);

mapRange=inputdlg(prompt2, 'Map Parameters', numlines, mapRange, options);
halt2=isempty(mapRange);

end
```

MapPlotter

```

function MapPlotter(dGT,dG1,taoslog,convETparams,convmapRange)
%Mapper3 Plots the hopping map
% Detailed explanation goes here

etValues={'', '\bfET Parameters', '', ['\rmT =
', num2str(convETparams(1)), ' K'], '', ['r (A-I) =
', num2str(convETparams(2)), ' A'], ['\beta (A-I) =
', num2str(convETparams(3)), ' A^-^1'], ['\lambda (A-I) =
', num2str(convETparams(4)), ' eV'], '', ['r (I-B) =
', num2str(convETparams(5)), ' A'], ['\beta (I-B) =
', num2str(convETparams(6)), ' A^-^1'], ['\lambda (I-B) =
', num2str(convETparams(7)), ' eV'], '', ['r (A-B) =
', num2str(convETparams(8)), ' A'], ['\beta (A-B) =
', num2str(convETparams(9)), ' A^-^1'], ['\lambda (A-B) =
', num2str(convETparams(10)), ' eV']];
contourSpacing=convmapRange(6);

loglines=(1:contourSpacing:15); %defines the position and spacing of
contour lines

scrsz = get(0, 'ScreenSize');
figure1=figure('Position', [scrsz(3)/1.8 scrsz(4)/4 scrsz(3)/2.3
scrsz(4)/2]);
annotation(figure1, 'textbox', [0.81 0.3 0.187
0.53], 'FitBoxToText', 'on', 'Interpreter', 'tex', 'String', etValues, 'Backgr
oundColor', [1,1,1])
axes1=axes('Parent', figure1, 'XDir', 'reverse', 'Position', [0.13
0.122249388753056 0.68
0.802750611246944], 'Layer', 'top', 'FontSize', 12);
xlim(axes1, [-1.5 0]);
ylim(axes1, [-0.4 0.3]);
box(axes1, 'on')
hold(axes1, 'all');

contour(dGT,dG1,taoslog,loglines, 'LineColor', [0 0
0], 'Fill', 'on', 'Parent', axes1);
xlabel('\Delta G^0_T_o_t_a_l (eV)', 'FontSize', 14);
ylabel('\Delta G^0_l_s_t_s_t_e_p (eV)', 'FontSize', 14);
colorbar('peer', axes1);
annotation(figure1, 'textbox', [0.72 0 0.187
0.1], 'FitBoxToText', 'on', 'Interpreter', 'tex', 'String', '\bf-
log(\tau)', 'Edgecolor', 'none', 'FontSize', 11)

end

```

Map Values

```

function [dGT,dG1,taosNEWlog]=MapValues(ETparams,mapRange)
%MapValues - CALCULATES HOPPING MAP VALUES

%General parameters
temp=ETparams(1);

%First step (A->I) parameters
r1=ETparams(2);
beta1=ETparams(3);
lamda1=ETparams(4);

%Second step (I->B) parameters
r3=ETparams(5);
beta2=ETparams(6);
lamda2=ETparams(7);

%Single step (A->B) parameters
rT=ETparams(8);
betaT=ETparams(9);
lamdaT=ETparams(10);

%The range for the x axis (dGT)
dGTmin=mapRange(1);
dGTmax=mapRange(2);

%The range and step for the y axis (dG1)
dG1min=mapRange(3);
dG1max=mapRange(4);

%The map resolution
dGstep=mapRange(5);

%creates vectors for x (dGT) and y (dG1) axes of the Hopping Map
dGT=(dGTmin:dGstep:dGTmax);
dG1=(dG1min:dGstep:dG1max);
lenx=length(dGT);
leny=length(dG1);

%GENERATING THE VALUES OF TAO: THE "Z" AXIS OF THE PLOT

%Creates the matrix taos of dimensions lenx & leny which holds the "z"
values for the Hopping Map, at
%each (dG1,dGT) point
taos=zeros(leny,lenx);      %defines the empty matrix taos of
appropriate size
ycount=1;
while ycount<=leny
    xcount=1;
    dG1now=dG1(ycount);
    while xcount<=lenx
        dGTnow=dGT(xcount);
        %this if statement defines the "sink" region

```

```

        if dG1now < dGTnow
            taoVal=1e100;
        else

taoVal=tauM(dGTnow,dG1now,r1,r3,beta1,beta2,lamda1,lamda2,temp);
        end

        taos(ycount,xcount)=taoVal;
        xcount=xcount+1;
    end
ycount=ycount+1;
end

%Creates a vector taosET with length lenx holding values of taoET at
%each dGT and dG1
taosET=zeros(lenx);      %defines the empty matrix taosET of appropriate
size
tcount=1;
while tcount<=lenx
    dGTnow=dGT(tcount);
    taoETVal=tauETM(dGTnow,rT,betaT,lamdaT,temp);
    taosET(tcount)=taoETVal;
    tcount=tcount+1;
end

%HOPPING ADVANTAGE

%Where taoET/tao > 1, two step hopping is faster than single-step
tunneling.
%The values of a new matrix taoNEW are set to 1 if there is
%no advantage - otherwise the values are transfered, untouched.

taosNEW=zeros(leny,lenx);
rcount=1;
while rcount<=leny
    ccount=1;
    while ccount<=lenx
        taoETC=taosET(ccount);
        taoC=taos(rcount,ccount);
        advantage=taoETC/taoC;
        if advantage<1
            taosNEW(rcount,ccount)=1;      %Only displays hopping areas
        else
            taosNEW(rcount,ccount)=taoC;
        end
        ccount=ccount+1;
    end
    rcount=rcount+1;
end

%Puts tao values on a log scale to make things easier
taosNEWlog=-log10(taosNEW);

```

tauM

```

function [tauVal] = tauM(dGT,dG1,r1,r3,B1,B3,lam1,lam3,T)
%this function

%Values for the constants
h=4.13574*10^-15;    %planck's constant (eV*s)
R=8.61733*10^-5;    %gas constant (eV/K)
Hab02=0.0005323;    %Hab(r0)^2 (eV^2)
r0=3;                %r0 (A)

dG3=dGT-dG1;

eB1=exp(-B1.*(r1-r0));
eB3=exp(-B3.*(r3-r0));

eG11=exp((-dG1+lam1)^2/(4.*lam1.*R.*T));
eG31=exp((-dG3+lam3)^2/(4.*lam3.*R.*T));

eG1=exp(dG1/(R.*T));
eG3=exp(dG3/(R.*T));
eGT=exp(dGT/(R.*T));

c0a=((4*pi())^3)/((h^2).*lam1.*R.*T)^0.5)*Hab02;
c0b=((4*pi())^3)/((h^2).*lam3.*R.*T)^0.5)*Hab02;

taunum=c0a*eB1*eG11*(1+eG1)+c0b*eB3*eG31*(1+eG3);
tauden=c0a*c0b*(eB1*eG11*eB3*eG31*(1+eG3+eGT));

tauVal=taunum/tauden;

```

tauETM

```

function [tauETVal] = tauETM(dGT,rT,BT,lamT,T)
%Returns taoVal - the value of tao, for a given dG1 and dGT

%Values for the constants
h=4.13574*10^-15;    %planck's constant (eV*s)
R=8.61733*10^-5;    %gas constant (eV/K)
Hab02=0.0005323;    %Hab(r0)^2 (eV^2)
r0=3;                %r0 (A)

%values for recurring sets of constants
c0=sqrt((4*pi^3)/((h^2)*lamT*R*T))*Hab02;    %the constants in front
of the exponents in tao

%piece by piece putting together the function taoET(dGT)

%the denominator...
t1=exp(-BT*(rT-r0));
t2=exp(-((dGT+lamT)^2)/(4*lamT*R*T));
t3=exp(-((dGT-lamT)^2)/(4*lamT*R*T));
tauETden=c0*t1*(t2+t3);

%taoET!
tauETVal=1/tauETden;

```

D.8. Ferric/ferrous deconvolution

The *SpectralDeconvoluter* script is used to deconvolute a two-component absorption spectrum and determine the percent of each parent component (e.g., ferric and ferrous components during potentiometric titration). Each spectrum must use the same wavelength data (and have the same number of points).

SpectralDeconvoluter

```
%SpectralDeconvoluter

%Ask for data
xInt=input('Enter the wavelength data (must be the same for all
spectra) ');
yInt=input('Enter the intermediate spectrum to deconvolute ');
yFe3=input('Enter the parent FeIII spectrum data ');
yFe2=input('Enter the parent FeII spectrum data ');

%Compare FeIII to data
error1=yInt-yFe3;
error1=error1.^2;
error1_tot=sum(error1);

%Make the midpoint n=0.5, compare to data
n=0.4;
yMid=n.*yFe2+(n-1).*yFe3;

%compare to data
error2=yInt-yMid;
error2=error2.^2;
error2_tot=sum(error2);

nInc=n;
nNew=n;
lastError_tot=error1_tot;
errorTest_tot=error2_tot;
rebound=0;
turn=1;
counter=0;
vals=[];

%iterate to find deconvolution
while nInc > 0.001 && rebound < 20

if errorTest_tot > lastError_tot
    turn=-1*turn;
    nInc=nInc/2;
end
```

```

lastError_tot=errorTest_tot;

nNew=nNew+turn.*nInc;
if nNew < 0
    nNew=0;
    disp('lbounded!')
    rebound=rebound+1;
    turn=-1*turn;
    nInc=nInc/2;
end

if nNew > 1
    nNew=1;
    disp('ubounded!')
    rebound=rebound+1;
    turn=-1*turn;
end

[errorTest1,errorTest_tot,yTestNew]=errorTester(nNew,yFe2,yFe3,yInt);

%optimization visualization
counter=counter+1;
vals(1,counter)=lastError_tot;
vals(2,counter)=nNew;
vals(3,counter)=errorTest_tot;

end

%display optimization
xvals=1:1:counter;

%Output answers
disp(nNew)
figure
hold
%plot final residuals
plot(xInt,errorTest1,'k')
plot(xInt,yInt,'b')
plot(xInt,yTestNew,'r')
hold
figure
plot(xvals,vals(1,:), 'r')
figure
plot(xvals,vals(2,:), 'b')
figure
plot(xvals,vals(3,:), 'g')

```